Using Lunar Apatite to Assess the Volatile Inventory of the Lunar Interior

Thesis

Using lunar apatite to assess the volatile inventory of the lunar interior

Nicola Jane Potts
MSc Geochemistry, University of Leeds
BSc(hons) Geological Sciences, University of Leeds

Planetary & Space Sciences, The Open University, Milton Keynes, UK
Faculty of Earth & Life Sciences, Vrije Universiteit, Amsterdam, NL

Supervisors: Mahesh Anand, Wim van Westrenen, Ian Franchi, Romain Tartése

July 2016

This thesis was submitted to The Open University for the degree of Doctor of Philosophy

ABSTRACT

Recent *in situ* measurements of volatiles (H_2O, Cl, F) within lunar melt inclusions, glass beads, and the mineral apatite have challenged the previously held notion that the Moon is depleted in volatiles. As the most widespread volatile-bearing phase, apatite has been the focus of many studies aiming to constrain the volatile inventory of the lunar interior. The thermodynamics of volatile partitioning into apatite, however, are poorly constrained. Here, Apollo mare basalts were investigated to provide an accurate composition for which apatite is found to crystallize under lunar conditions. This composition was used high temperature, high pressure experiments which constrained volatile partitioning between apatite and silicate melt. Combining experiments from this study, and those of the literature, an empirical model was developed to back-calculate melt volatile contents, at the time of apatite formation. Conservative estimates and preliminary findings suggest the amount volatiles in the at the time of apatite crystallization is highly variable but ranges up to 3.6 wt.% H_2O, 5 wt.% F and 5.3 wt.% Cl. One of the reasons volatiles contents, in apatite and melt, vary so much is likely a result of degassing, as apatite is a late-stage mineral formed after ∼95 % melt solidification. Degassing, under lunar conditions, utilizing low-Ti and high-Ti compositions was constrained experimentally. The results from this investigation suggest that degassing is melt composition dependant and, as such, requires a thorough investigation of late-stage melt pockets to determine the amount of degassing that may occur prior to apatite growth. In addition, vapor-phase interaction was found to also alter volatile contents and δ^{37}Cl isotope signatures in apatites from Apollo 14 samples. This vapor-phase is thought to be from volatile-release during a major impact event, similar to other old (sim4 Ga) samples found on the lunar nearside. To constrain whether this process was a global phenomenon samples from regions previously unexplored (including the lunar farside) are required. A mission scenario, optimising sample return from Schödinger basin is proposed here where volcanics and potentially mantle material could be collected. These samples would provide key insight into indigenous lunar mantle volatile contents and global differentiation processes.

What matters most is how well you walk through the fire

CHARLES BUKOWSKI

Acknowledgements

First and foremost I have to thank my supervisors for giving me the chance to tackle such an interesting PhD topic. Although the path wasn't always smooth, I'm so grateful for the experiences and opportunities provided to me during my PhD.

I was fortunate to be part of two groups during my PhD and, as such, my thanks are divided.

In Amsterdam, I cant thank Wim van Westrenen enough for his help and support in (and out of) the lab! Im also eternally grateful to Nachiketa Rai for all his technical help, being a good office mate (if only for a short time) and sharing his experimental expertise. The same goes to Aureila Colin who always found time to help me and share experimental nightmare stories to make me feel better. Thanks also to Edgar, Jurrien, Wouter, and Yanhao for being good friends and making the lab a very fun place to be! I also have to thank everyone who came through the XP lab during my time there for putting up with my cleaning obsession and momentary thermocouple breakdowns!

Whenever in Amsterdam I was always made to feel extremely welcome and part of the group! Thank you so much to Gareth Davies, Lara Font, Esther Velasco, Janna Koornneef, Sergie Matveev. And of course I am forever grateful to Jessica Flahaut and Esther Plomp. Thank you for being such great friends, giving me somewhere to stay, and making my time in Amsterdam amazing! A very special thanks also goes to Wynanda Koot and Bouke. They were always extremely nice to me when I was making unreasonable demands and made my samples look beautiful!

In the UK, I am grateful to Pete Landsberg for also helping with sample prep (and unreasonable demands), being a good friend, and sounding-board. Everyone in the student office is thanked for morale, banter, and Christmas songs. I'm especially grateful to my corner-buddy Tom for letting me ramble random apatite nonsense to him without complaint (and his whiskey supply) and Katie Robinson for coming in at the end and giving me lots of moral support. Thanks for everyone for Friday beer time and making Milton Keynes that little bit bearable.

I was very fortunate to get training on a wonderfully complex instrument without Ian Franchi and Romain Tartése I would have been lost, so thank you for your patience and time! Thanks also to my main supervisor, Mahesh, for encouraging me to strive for excellence and for support when times got tough.

During my PhD I got to spend an amazing summer at the Lunar and Planetary Institute, Houston. This experience really developed me as a research and built my understanding of the Moon. For allowing me the experience and being an amazing mentor I thank David Kring. I also thank Natalie Curran and Amber Gullikson for making that summer perfect and being great lunar friends for life. The summer also wouldnt have been the same without Eve, Dayl Martin, Kelsey Williams, Laura Corley, Alastair Tait, Andrea Bruck, Michael Bouchard, Caitlin, Anthony Frushour, Mona, and of course Ross Potter. Thanks also Ross for the LaTex help and proofreading!

I also thank Andrew Cunningham for always believing in me and never losing patience with my incessant talking about my PhD. I really couldn't have done this without his love and support. And finally, I'm grateful to Riley for the dancing, waggy bums, and general dog-love that kept me happy and sane throughout my PhD!

Contents

List of Figures

List of Tables

Chapter 1

Introduction

1.1 To the Moon (and back)

Prior to the Apollo (1969 –1972) and Luna (1970 –1976) missions little was known about the surface, and interior, composition of the Moon. The six crewed Apollo missions and three robotic Luna missions returned 382 kg and 326 g (respectively) of lunar rocks and soils that became instrumental in understanding the origin and evolution of Earth's only satellite. Almost five decades have passed since the return of these samples, and they are still providing a wealth of information that is constantly reshaping our understanding of the Moon and its formation.

At a present-day average distance of 3.845×10^5 km the Moon is the Earth's nearest neighbour, yet, the two planetary bodies differ considerably. The Moon is a single plate, geologically inactive, body that lacks liquid water and a significant atmosphere. It has a small iron-rich core, thought to be between 200 and 450 km in diameter, identified by geophysical measurements (e.g. Wieczorek, 2006). Recent re-evaluation of Apollo-era lunar seismograms have gone as far to suggest the presence of a solid inner core and fluid outer core overlain by a partially molten silicate lower mantle (Weber et al., 2011), although this has yet to be confirmed with additional data. The Moon is known to have a segregated mantle and single, heavily cratered, primary crust (Figure 1.1). The crust has an average thickness between 34 km and 43 km (Wieczorek et al., 2013). Ancient volcanic deposits are concentrated on the nearside and found mostly within maria regions of the Moon.

1.2 Moon formation

A prominent recent discovery, made from the Apollo samples, is the isotopic similarity between the silicate Earth and Moon for nearly all elements. The list of matching isotopes, within analytical uncertainty, for the Earth-Moon system is ever increasing; calcium (Dauphas et al., 2015; Valdes et al., 2014), chromium (Lugmair and Shukolyukov, 1998), iron (Beard and Johnson, 1999), potassium (Humayun and Clayton, 1995), stable strontium isotopes (Charlier et al., 2012), silicon (Armytage et al., 2011, 2012; Zambardi et al., 2013), titanium (Meier, 2012; Zhang et al., 2012), tungsten (Touboul et al., 2007), and zirconium (Schönbächler et al., 2003) are all identical among lunar and terrestrial rocks. Oxygen isotopes (Figure 1.2) were long thought

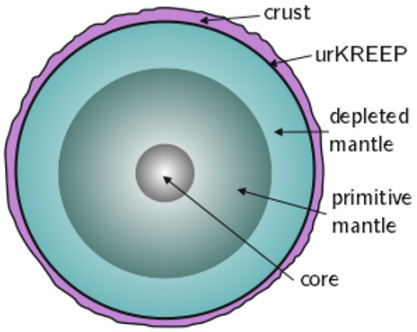

Figure 1.1: Sketched cross-section of the Moon at ~4.4 Ga illustrating the metallic core, segregated mantle, last dregs of the solidified lunar magma ocean (urKREEP layer) and plagioclase-rich crustal layer prior to impact erosion of the crust.

to be identical (Hallis et al., 2010; Wiechert et al., 2001), however, a very small difference was recently detected in $\Delta^{17}O$ (Herwartz et al., 2014). This finding has been disputed (Kohl et al., 2015; Young et al., 2016), yet, even if the difference is confirmed, it is so small as to be easily explained by post-Moon formation impacts on the Moon. Differences in chlorine (Boyce et al., 2015; Sharp et al., 2010b; Tartèse et al., 2014a), copper (Herzog et al., 2009), hydrogen (Barnes et al., 2014; Saal et al., 2013), and zinc (Paniello et al., 2012) isotopes between the silicate Earth and lunar samples have been explained by isotope fractionation as a consequence of volcanic degassing (Hauri et al., 2015), and do not reflect primary differences between Earth and Moon.

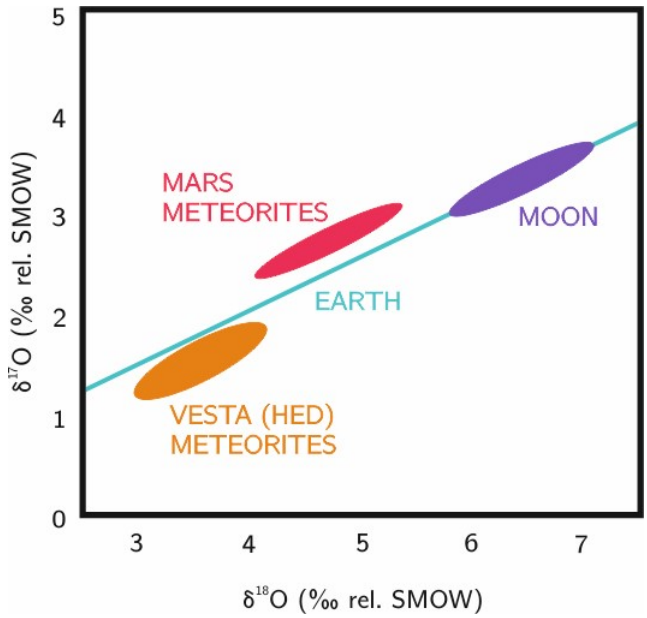

Figure 1.2: Oxygen isotope data for Earth, Mars, Moon, and HED meteorites. *After Vitz et al., 2010.*

Recent developments in the separation and measurement techniques of W isotopes have highlighted that the Moon has an $^{182}W/^{184}W$ ratio ~25 ppm higher than the Earth (Kruijer et al., 2015; Touboul et al., 2015); suggested to be a consequence of a disproportionate amount of chondritic material being delivered to the Earth during the late veneer (Kruijer et al., 2015). Immediately after Moon formation the Earth and Moon are thought to have had an identical W isotope signature; an important implication as W isotopes are fractionated during planetary differentiation, making them unique to individual differentiated bodies (Touboul et al., 2007).

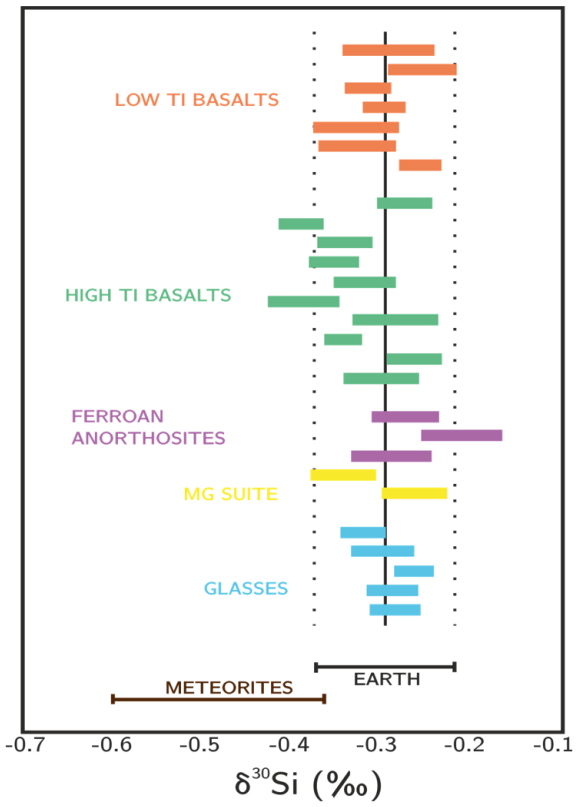

Figure 1.3: Silicon isotope data for a variety of lunar samples samples compared to Earth and meteorite samples. *After Armytage et al., 2012.*

Lunar samples have the same, heavy, $^{30}Si/^{28}Si$ signature as the bulk silicate Earth (BSE; Armytage et al., 2012, Figure 1.3). Based on differences in $^{30}Si/^{28}Si$ isotopes between meteorites and terrestrial rocks (Armytage et al., 2011, and references therein), and experimental studies of silicon isotope fractionation (Kempl et al., 2013; Shahar et al., 2009) the Earth's core is thought to be enriched in ^{28}Si (Shahar et al., 2009). Given the small size of the lunar core, the similarities in Si isotopes between the BSE and lunar rocks indicate the Moon is derived from BSE material; thus explaining the similarities in isotopes between the Earth and Moon system (de Meijer et al., 2013).

A BSE-derived Moon, however, creates issues for models of the giant impact hypothesis. The classical theory on how the Moon formed is a collision between a Mars-sized impactor (often named Theia) and the Earth (Canup, 2008, 2012; Ćuk and Stewart, 2012). This formation mechanism can only account for a large degree of sim-

ilarity between the Moon and the silicate Earth if the Earth-Moon system contained far more angular momentum, soon after it formed, than it does at present (Canup, 2012; Ćuk and Stewart, 2012). Early suggestions of the Earth and Moon being isotopically homogenized in the aftermath of the giant impact were disproved by refractory Ti isotopes that would not have been easily re-equilibrated in the Earth-Moon accretion disk. All terrestrial rocks have identical $^{50}Ti/^{47}Ti$, re-equilibrated, signatures that differ from those measured in meteorites and, yet, are the same as lunar rocks (Zhang et al., 2012, Figure 1.4); thus supporting the hypothesis of a BSE-derived Moon. Based on current models, the optimal way to form the Moon from a giant impact requires an impactor of the same composition as the Earth (Dauphas et al., 2014; Mastrobuono-Battisti et al., 2015).

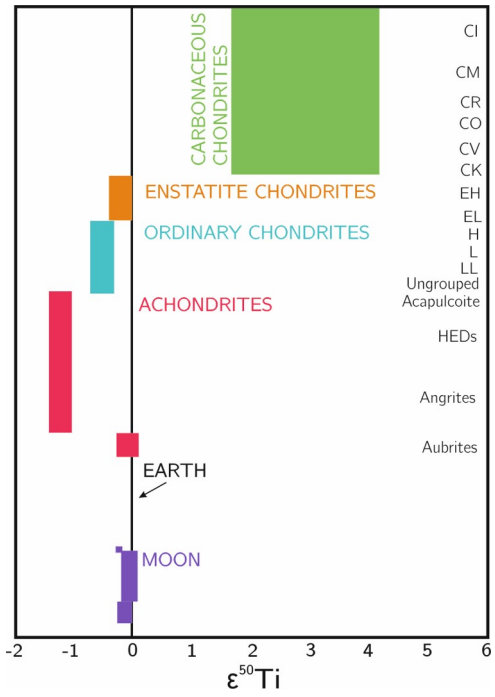

Figure 1.4: Titanium isotope data for a variety of extra-terrestrial samples compared to Earth and lunar samples. *After Zhang et al., 2012.*

During Earth's accretion the material being contributed to the proto-Earth was geochemically similar, presumably due to a uniform isotopic composition within the inner protoplanetary disk (Dauphas et al., 2014). If the Moon-forming impactor originated in the same region of the disk as other-Earth forming embryos, it would have a similar isotopic composition to the Earth (Dauphas et al., 2014). Simulations of planetary accretion found that giant impactors were statistically more similar to the planets they impact, with some pairs having identical compositions, supporting the hypothesis of an isotopically twinned impactor/Earth (Mastrobuono-Battisti et al., 2015). While some evidence suggests that the heavy $\delta^{30}Si$ of BSE and lunar samples is a consequence of fractionation in the solar nebular not core formation (Dauphas et al., 2014); this hypothesis, however, cannot explain the similarities in W isotopes.

An additional caveat to Moon formation models has been the suggestion that lunar

samples are more volatile depleted than terrestrial mantle rocks, given that expected disk conditions do not favour the mechanism of evaporative escape (Canup et al., 2015). Dynamical models have suggested that the Moon initially accreted at the outer disk before further accretion of melt that originated in the inner disk. Recent models have shown that volatile-rich melt is preferentially accreted from the inner disk to the Earth as the disk cools. At this time the Moon's orbit has begun to expand away from the disk, terminating lunar accretion before condensation of volatile elements (Canup et al., 2015), thus leaving the Moon volatile depleted; although a volatile-rich inner region is conceded to be possible. It should be noted that the extent of volatile depletion of the Moon compared to the Earth may be smaller than commonly assumed, in the above-mentioned models, if segregation of volatile elements into metallic liquid during core formation is taken into account (e.g. Steenstra et al., 2016).

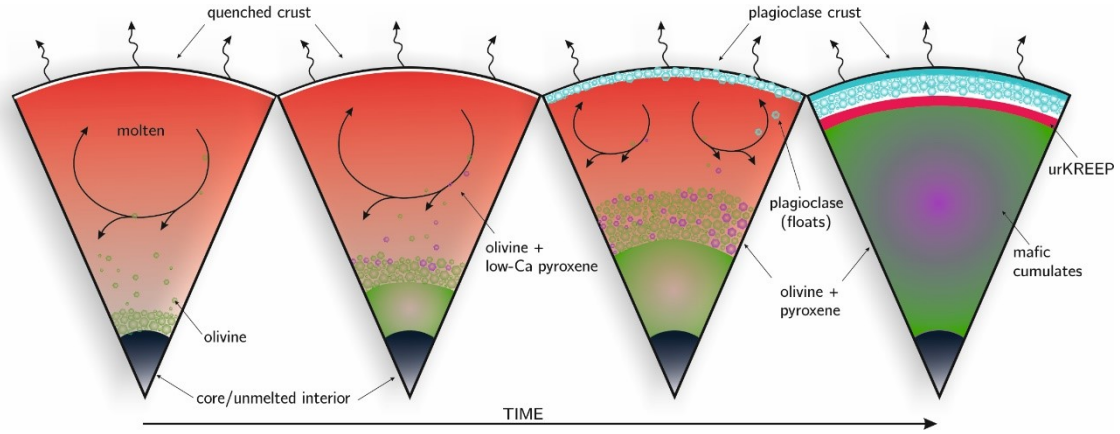

Figure 1.5: Diagram illustrating solidification of the Lunar Magma Ocean.

1.3 Lunar Magma Ocean

Immediately after accretion the Moon is thought to have undergone a period of planetary-scale melting, referred to as the Lunar Magma Ocean (LMO Shearer et al., 2006). A thin, discontinuous, quenched protocrust allowed significant radiative heat transfer from the LMO (Spera, 1992), leading to very high cooling rates during the early stages of magma ocean crystallization (Shearer and Papike, 1993). It is likely that crystallization started as equilibrium crystallization, followed by fractional crystallization for the last half of solidification (Snyder et al., 1992). Although the initial composition strongly affects the fractionation sequence of the LMO (Snyder et al., 1992) the sequence has been summarized as follows: 1) olivine; 2) olivine + orthopyroxene; 3) olivine + pigeonite + plagioclase; 4) pigeonite + clinopyroxene + plagioclase, and 5) pigeonite + clinopyroxene + plagioclase + ilmenite. The density of the first forming mafic minerals is higher than that of surrounding melt and initiated sinking of these minerals towards the base of the cooling LMO. After ∼80% bulk crystallization anorthitic plagioclase began to crystallize, inheriting the bulk Eu component of the Moon (Snyder et al., 1997). The lower density of anorthitic plagioclase allowed for efficient flotation through the surrounding dense melt, creating the lunar crust. Plagioclase flotation has been shown not to be dependant on existing crystal fractions

or networks (Grove and Krawczynski, 2009). The final few percent of the LMO melt became enriched in incompatible elements forming the urKREEP (potassium, rare earth elements, phosphorous) layer (Figure 1.5).

Crystallization of the late, Ti-rich, cumulates created a gravitational instability within the cumulate pile (Shearer and Papike, 1993). It is commonly assumed that this instability led to cumulate overturn, although the exact mechanics of this are poorly constrained (de Vries et al., 2010; Hess and Parmentier, 1995; Snyder et al., 1992) and its existence has even been disputed (Elkins-Tanton et al., 2002). If mantle overturn occurred, it is thought this led to re-melting of the cumulate pile leading to the eruption of mare basalts and pyroclastic glass deposits (Shearer et al., 2006; van Kan Parker et al., 2011, 2012).

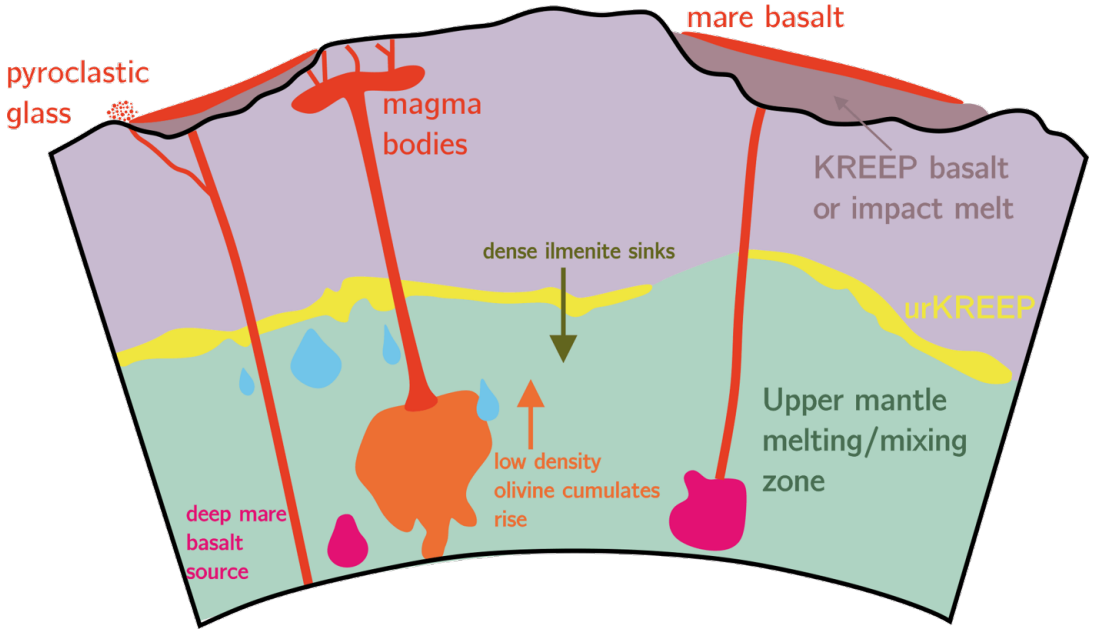

Figure 1.6: Sketch of magmatism within the lunar interior.

There is an indirect correlation between the composition of basalts and the composition and depth of their source regions. Low-pressure crystallization, assimilation, and the melting process itself have obscured initial signatures making direct observations difficult (Hess and Parmentier, 1995). It can be deciphered that the high-TiO_2 basalts must have been in equilibrium with a shallow cumulate pile, originating as remelts of the final stages of cumulate formation (Grove and Krawczynski, 2009). While the low-TiO_2 basalts are saturated with olivine and pyroxene and, as such, have origins in the deeper mantle within the cumulate pile (Grove and Krawczynski, 2009); basalts rich in KREEP material are expected to have assimilated material from the urKREEP layer during ascent. Lunar basalts are volatile-poor and very reduced (Nicholis and Rutherford, 2009) suggested to be inherited from mantle sources. Yet, the Apollo 15 and 17 pyroclastic glass deposits are thought to originate from volatile-driven fire-fountaining (Shearer et al., 2006, Figure 1.6).

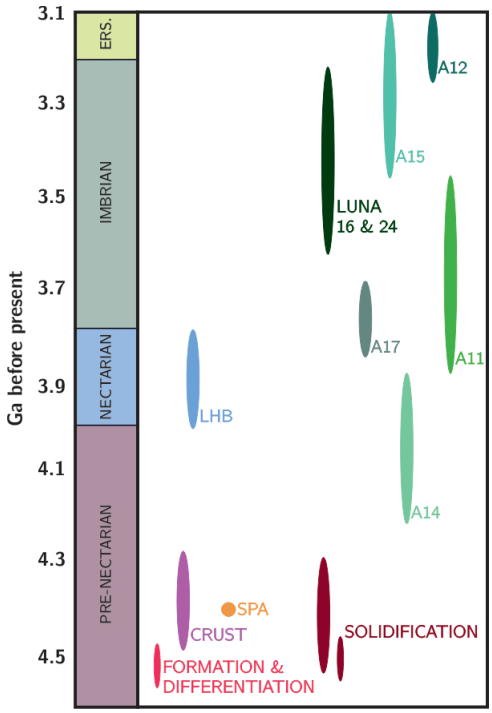

Figure 1.7: Timeline of key lunar events including volcanism (A= Apollo mission), Late heavy bombardment (LHB), South-pole Aitkin basin formation (SPA) with geological periods for reference. ERS. = Eratosthenian.

1.4 Volatiles in the Moon

Understanding the volatile budget of the lunar interior is not a straight forward task. We, ideally, require pristine mantle specimens (such as peridotites on Earth), however, this is not something currently held in the lunar sample collection. This leaves us limited to studying lunar volcanic rocks, which have undergone various degrees of alteration (i.e. fractionation, degassing) before/during eruption, with modified initial volatile contents. The most primitive of these samples are the pyroclastic glass beads, however, their distribution on the lunar surface and in the lunar rock collection is limited. The recent development of *in situ* microbeam techniques has changed the view of an anhydrous Moon (Anand et al., 2014). Varying amounts of hydrogen-species have been detected in lunar volcanic glasses (Füri et al., 2014; Hauri et al., 2011; Saal et al., 2008), melt inclusions in lunar basalt phenocrysts (Chen et al., 2015), and lunar apatites (see McCubbin et al., 2015b, and references therein). The small quantities of measured water found in bulk lunar samples was originally credited to solar wind implantation (Wieczorek, 2006) or terrestrial contamination (Epstein and Taylor, H. P., 1973). Ion microprobe based spatial profiles of H_2O contents peaking in the cores of glass beads and decreasing towards their rims provides strong evidence that the water in these glasses is indigenous and not surface implanted or terrestrial contamination (Saal et al., 2008). The discovery of volatiles indigenous to the lunar interior could have large implications for the LMO hypothesis, Moon formation, and/or evolution theories. It is also important to note that water, in the context of lunar studies, is a polyseme in that it is not liquid water or molecular H_2O which is being referred to.

Water is a term used to describe H-species in lunar samples; apatite for instance does not have the capability to include H_2O in its crystal structure, but it is able to incorporate the OH^- anion. This has important implications for the origin and evolution of water in the lunar interior as, for example, molecular H_2 is thought to diffuse more effectively through lunar melts than H_2O or OH^- (Zhang, 2011).

The plethora of measurements of volatiles in lunar rocks has led to a new, widely-held, belief that the Moon is not as volatile depleted as initially thought (Anand et al., 2014). The next important steps in the field of lunar volatiles are 1) to understand what the measured volatile contents in lunar surface samples mean for the lunar interior volatile budget; and 2) to assess the extent to which volatile-rich samples reflect the composition of rare, heterogeneous parts, of the lunar mantle rather than being representative of the bulk Moon (Sharp et al., 2010b).

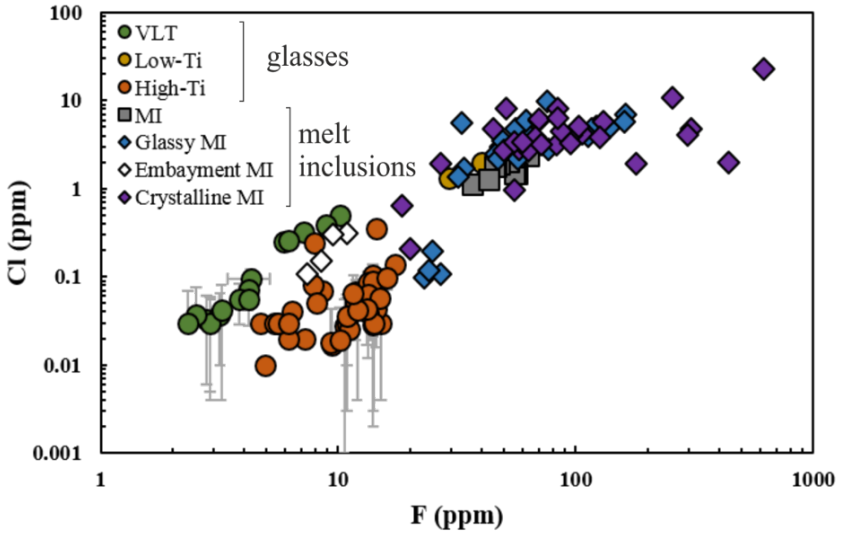

Figure 1.8: F and Cl contents (ppm) of lunar glass beads (circles), olivine-hosted melt inclusions in glass beads (squares), and phenocryst-hosted melt inclusions from glasses and basalts (triangles). VLT = Very-Low-Ti. Glassy, embayment, and crystalline refer to the textural descriptions and classifications of Chen et al. (2015). Note no errors available for Chen et al. (2015) data.

1.5 Apatite Structure

Apatite in *senso stricto* refers to a group of minerals which share a common atomic arrangement (Figure 1.9). The most common apatite minerals are the calcium phosphate apatites which have the general formula, $Ca_5(PO_4)_3(F, Cl, OH)$. In relation to lunar samples, it is this calcium phosphate apatite which is referred to, most commonly the fluroapatite end member.

For the most part, apatite is hexagonal, $a = 9.4 - 9.6\mathring{A}, c = 6.8 - 6.9\mathring{A}$, with a space group symmetry of $P6_3/m$ and two [001] mirror planes perpendicular to the 6_3 screw axis, at $Z = \frac{1}{4}$ and $\frac{3}{4}$. There are three cation sites within the apatite structure (red, orange, and yellow atoms in Figure 1.9). A PO_4 tetrahedron site within the

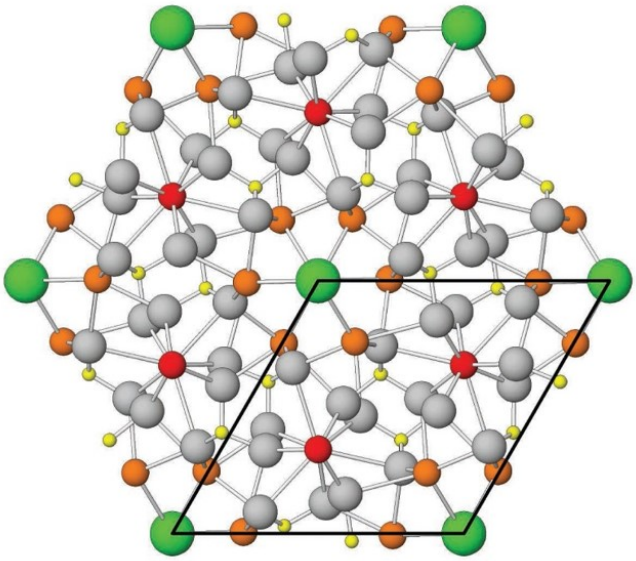

Figure 1.9: Atomic arrangement of apatite, projected down the c axis with the unit cell outlined in black. The T sites are in yellow, *M1* sites in red, *M2* sites in orange, while the green ions at the corners are the F-Cl-OH anion column. *After Hughes and Rakovan (2002)*).

tetrahedral (T site) site with a P - O distance of $\sim$1.53 $\mathring{A}$. The metal sites (*M1* and *M2*) are synonymous with calcium (Ca1 and Ca2) in apatite. The *M1* or Ca1 site is bonded to three O atoms to create CaO_9 tricapped-triagonal prisms. The *M2* sites form an irregular CaO_6X_1 polyhedron where X is F, Cl, and OH (Figure 1.10). In a given apatite unit cell there are six tetrahedron, four *M1*, and six *M2* sites with a half unit cell stoichoimetry of $Z = 2$. At the edges of the unit cell sit the F, Cl, OH anions [0,0,z] in columns (anion column), which allows for a rare anion solid solution to occur.

Interestingly, the column anions significantly differ in size requiring a structural response from the *M2* site. There is little to no structural response, to the anion column, from *M1* and T cation sites (Hughes and Cameron, 1989). As shown in Figure 1.10, there are three *M2* cations that form a triangle around the anion column, with an *M2* triangle on each mirror plane in the unit cell. The F anion is coplanar with the three *M2* sites, meaning that it sits at the center of the cation triangle. The Cl and OH anions, however, are too large to fit at the center of the triangle. This means that Cl and OH are forced either above or below the triangle ($\sim$1.3 $\mathring{A}$ for Cl and $\sim$0.35 $\mathring{A}$ for OH). As the anion moves above the triangle it enforces vacancies in the mirror plane below (or vice versa).

This, therefore, means that symmetry is only achieved in the fluroapatite system and thus only fluroapatite has the expected hexagonal $P6_3/m$ shape. If there are no anion substitutions, pure chlorapatite or hydroxylapatite will have Cl or OH anions ordered above the triangle/mirror plane, with anions in adjacent columns ordered below the plane. The destruction of this mirror symmetry leads to a $P2_1/b$ monoclinic symmetry (Candela, 1986). A $P6_3/m$ symmetry can exist on a whole crystal scale if Cl or OH anions occupy only half the anion sites above and below the mirror plane with impurities occupying the other sites within the anion column. Although less than

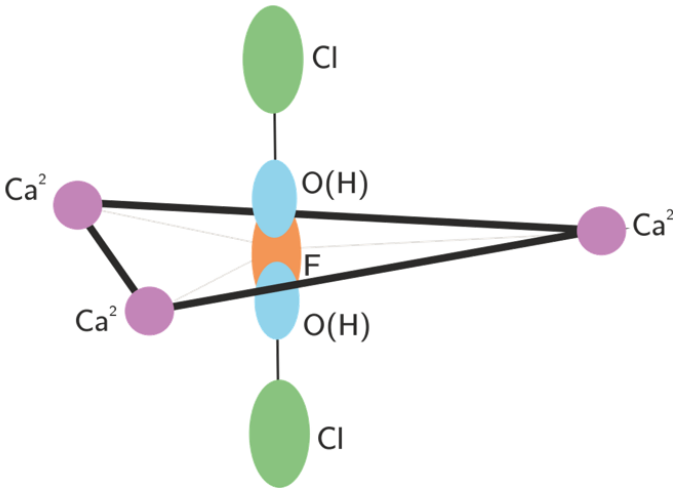

Figure 1.10: *M2* triangle and mirror plane showing how F anions sit perfectly centered within the mirror plane while Cl and OH anions are too large for the site and sit either above or below the plane.

10 % substitution of F (or impurities) or vacancies is sufficient to destroy this ordering leading to a disordered, hexagonal $P6_3/m$ symmetry (Hughes and Rakovan, 2015).

Furthermore, steric interactions between F, Cl, and OH require structural changes not seen in end-member structures, namely in the addition of anion sites. To achieve solid solution between the anions in a ternary or binary system a new Cl site that relaxes at ~0.4 Å toward the associated mirror plane is required, which allows space for an adjacent OH (Hughes and Cameron, 1989). The implications of this are that 1) end-member atomic arrangements can not be used to predict mixed-anion atomic arrangements, 2) direct anion substitution cannot occur thus impacting or understanding of anion diffusion.

1.6 Thesis objectives

The primary aim of this thesis is to provide a better understanding of the volatile content of the lunar interior. To achieve this, experimental petrology was combined with high precision *in situ* measurements of experimental and Apollo samples. The focus of this thesis is the mineral apatite, because of its abundance and distribution in lunar rocks, especially mare basalts. The first study in this thesis characterized the late-stage melts from which lunar apatite crystallised. Mesostasis regions in four Apollo mare basalts were analysed and compared with petrogenetic modelling to provide information on the bulk composition from which apatite would be expected to crystallise under lunar conditions (Chapter 2). The main findings of this Chapter addressed the variability across thin sections and samples of late-stage melts. These melts were found to be more silicic than previously assumed for lunar apatite growth. A representative bulk-mesostasis composition was then synthesised and subjected to high pressures and high temperatures in the presence of volatiles, to quantify volatile partitioning between apatite and silicate melt (Chapter 3).

Apatite found in lunar samples is mostly fluorapatites with varying amounts of Cl

and OH. We, therefore, began by characterising F partitioning within a Cl and OH depleted system. This provided a baseline for future experiments in which varying amounts of Cl and OH were added to fluorapatite, thus allowing the effects of all three volatiles in the fluorapatite system to be fully identified (Chapter 3). A model to back-calculate melt H_2O contents at the time of apatite formation was derived by combining experimental data from this work and that of the literature. This empirical model was applied to Apollo apatite abundance values to provide estimates of up to $\sim$0.5 wt.% melt H_2O at the time of apatite formation.

Given that apatite is a late-stage mineral, it is likely that some degree of volatile degassing has taken place prior to apatite growth. Volatile degassing experiments were performed, under lunar conditions, to provide information on how back-calculated volatile contents in late-stage melts relate to initial lunar interior values (Chapter 4). Higher rates of degassing were found in experiments performed here compared to literature studies (Ustunisik et al., 2015, 2011). Additionally, volatile degassing was found to be composition dependant, adding further complexity to the study of volatiles within late-stage basaltic melts.

Understanding gained from experiments on Cl partitioning into apatite and Cl degassing, under lunar conditions, was then applied to studies of Cl isotopes measured from lunar apatites. Volcanic rocks and impact melts from the Apollo 14 collection, abundant in apatite, were analysed for Cl isotopes (Chapter 5) to provide understanding on the heavy δ^{37}Cl signature of the Moon. Vapor-induced volatile alteration was found to be the most likely cause of the wide spread in chlorine isotope signatures found in these samples. Highlighting how, after partitioning and degassing, further volatile alteration is possible, that can mask original abundance values. The results from this study also point to active volatile release on the lunar surface during a period which coincides with the late-heavy bombardment.

The overall results of this thesis, and their implications for the volatile budget of the lunar interior, are summarised in the final section of this work, as are my suggestions for future research (Chapter 7).

Chapter 2

Characterising mesostasis regions within mare basalts: Understanding late-stage melt evolution and its influence on apatite formation

Nicola J. Potts[1,2*], Romain Tartése[1,3], Mahesh Anand[1,4], Wim van Westrenen[2], Alexandra A. Griffiths[1,5], Thomas J. Barrett[1], Ian A. Franchi[1]

[1]Planetary & Space Science, The Open University, Walton Hall, Milton Keynes, MK7 6AA, UK
[2]Faculty of Earth & Life Sciences, Vrije Universiteit Amsterdam, 1081 HV Amsterdam, NL
[3]Institut de Minralogie, de Physique des Matriaux et de Cosmochimie, Musum National dHistoire Naturelle, Sorbonne Universits, CNRS, UPMC & IRD, 75005 Paris, France
[4]Department of Earth Sciences, The Natural History Museum, London, SW7 5BD, UK
[5]School of Earth, Atmospheric, & Environmental Sciences, University of Manchester, Manchester, UK

This chapter has been published as Potts et al. (2016) *Meteoritics and Planetary Sciences.* **51**, 1555-1575. doi: 10.1111/MAPS.12681

ABSTRACT

Recent studies geared towards understanding the volatile abundances of the lunar interior have focused on the volatile-bearing accessory mineral apatite. Translating measurements of volatile abundances in lunar apatite into the volatile inventory of the silicate melts from which they crystallized, and ultimately of the mantle source regions of lunar magmas, however, has proved more difficult than initially thought. In this contribution, we report a detailed characterization of mesostasis regions in four Apollo mare basalts (10044, 12064, 15058, 70035) in order to ascertain the compositions of the melts from which apatite crystallized. The texture, modal mineralogy, and reconstructed bulk composition of these mesostasis regions vary greatly within and between samples. There is no clear relationship between bulk-rock basaltic composition and that of bulk-mesostasis regions, indicating that bulk-rock composition may have little influence on mesostasis compositions. The development of individual melt pockets, combined with the occurrence of silicate liquid immiscibility, exerts greater control on the composition and texture of mesostasis regions. In general, the reconstructed late-stage lunar melts have roughly andesitic to dacitic compositions with low alkali contents, displaying much higher SiO_2 abundances than the bulk compositions of their host magmatic rocks. Relevant partition coefficients for apatite-melt volatile partitioning under lunar conditions should, therefore, be derived from experiments conducted using intermediate compositions instead of compositions representing mare basalts.

2.1 Introduction

In order to constrain the volatile inventory of the lunar interior many studies have focused on measuring structurally bound OH in apatite [$Ca_5(PO_4)_3$(F,Cl,OH)] from Apollo and lunar meteorite samples (e.g. Barnes et al., 2013, 2014; Boyce et al., 2010; McCubbin et al., 2011, 2010a,b; Tartèse et al., 2013a, 2014a,b). Yet, translating volatile measurements in apatite to volatile abundances in co-existing melt has proved troublesome, leading many studies to focus on improving understanding on the partitioning behavior of volatiles between apatite and melt (Boyce et al., 2014; McCubbin et al., 2015a). Few studies, however, have focused on constraining the petrographic context in which apatite forms in lunar melts. Apatite begins to crystallize after ∼95 % melt solidification in typical mare magmas (McCubbin et al., 2010b), but is likely to start crystallizing earlier (∼85 % melt solidification) in KREEP (enriched in incompatible elements such as K, REE and P) basalts (Tartèse et al., 2014b). Apatite, therefore, does not form from bulk basaltic melts but instead forms from differentiated late-stage melts, which are represented by mesostasis regions within lunar samples (Henderson, 1970). Although mesostasis regions have been observed within many Apollo basalts and lunar basaltic meteorites, few studies have focused on constraining the silicate melt compositions from which they formed. To provide better understanding on the bulk composition of melts from which lunar apatite crystallized, we have characterized the mineralogy and geochemistry of apatite-bearing mesostasis areas in four Apollo mare basalts (samples 10044, 12064, 15058, and 70035) representative of the high-Ti and low-Ti mare basalts. Knowledge of the melt-compositions from which apatite crystallized will inform experimental studies aiding in the determination of appropriate apatite-melt partition coefficients of volatile elements in geochemical models of lunar magma evolution.

2.2 Samples

2.2.1 10044

Lunar sample 10044 is a high-Ti ilmenite basalt with a low-K content (Beaty and Albee, 1978). It is a subophitic basalt (James and Jackson, 1970) that is sometimes described as a microgabbro (Anderson et al., 1970). A similarity between 10044, 10047, and 10058 has been noted (Beaty and Albee, 1978) with a suggestion that these samples could be fragments of a larger block. Geochronological studies carried out on this sample yielded Rb-Sr dates of ∼3.7 Ga (Papanastassiou et al., 1970), $^{40}Ar/^{39}Ar$ dates of 3.73 ± 0.04 Ga (Guggisberg et al., 1979; Turner, 1970) and a tranquillityite $^{207}Pb/^{206}Pb$ date of 3.72 ± 0.01 Ga (Tartèse et al., 2013b). Cosmic-ray exposure (CRE) ages of ∼70 Ma were determined using the abundance of cosmogenic ^{81}Kr (Hohenberg et al., 1970), ^{126}Xe (Srinivasan, 1974) and ^{38}Ar (Guggisberg et al., 1979). 10044 contains subhedral to anhedral zoned pyroxene phenocrysts (∼45 % modal abundance) surrounded by a matrix of subophitic plagioclase (∼35 %), and ilmenite (∼13 %) (McGee et al., 1977). Mesostasis areas in this sample are composed of silica (∼7 %), troilite (∼0.5 %) associated with metallic iron, K-rich glass, and accessory minerals including apatite (∼0.1 %) and Zr-rich minerals such as baddeleyite and tranquillityite (McGee et al., 1977). We have examined mesostasis areas in thin

section 10044,645, which is 6 × 10 mm in size. The mineralogy of this section is consistent with that of the main rock sample described above, containing anhedral pyroxene phenocrysts (∼1 × 2 mm), plagioclase laths (∼1 × 0.2 mm) and ilmenite (∼3 × 0.5 mm). Multiple mesostasis regions are found throughout the 10044,645 section and are further described in section 2.4.1.

2.2.2 12064

Sample 12064 is a coarse-grained low-Ti ilmenite basalt that displays a subophitic texture containing anhedral pyroxene crystals (∼56 % modal abundance) intergrown with anhedral plagioclase laths (∼29 %) (Klein et al., 1971). It is characterized by coarse-grained mesostasis areas (∼9 %) that contain fayalite, Fe-rich pyroxene, troilite, K-feldspar, K-rich glass, Zr-rich phases, merrillite and apatite (Kushiro and Haramura, 1971). Plagioclase compositions range from An_{93} to An_{86} while pyroxene compositions are close to the Fe-rich end-member hedenbergite (Kushiro and Haramura, 1971). The sample also contains coarse-grained laths of ilmenite (∼3.5 %) associated with ulvspinel (∼2 %). Small, sporadic grains of pyroxferroite are observed coexisting with clinopyroxene (Klein et al., 1971). Rb-Sr (Papanastassiou and Wasserburg, 1971a) and $^{40}Ar/^{39}Ar$ (Horn et al., 1975) dating studies for sample 12064 yielded dates of 3.18 ± 0.09 Ga and 3.18 ± 0.01 Ga, respectively, which have been interpreted as crystallization ages. An exposure age of 255 Ma has been reported by Horn et al.(1975), while exposure ages determined from abundances of cosmogenic ^{3}He, ^{21}Ne, and ^{38}Ar cluster around 200 Ma (Hintenberger et al., 1970). We have examined mesostasis areas in thin section 12064,130, which is ∼8 × 4 mm in size. The mineralogy of the studied sample is consistent with modal abundances reported for the bulk-rock, containing anhedral pyroxenes (>2 × 2 mm), intergrown with anhedral plagioclase (∼2 × 1 mm) and with minor ilmenite (∼1 × 0.2 mm). Multiple mesostasis regions are found across the 12064,130 section and are further described in section 2.4.1.

2.2.3 15058

Apollo 15 sample 15058 is one of the largest basalts returned from the Moon. It is a coarse-grained low-Ti pigeonite basalt (Ryder, 1985). Olivine (∼2 % modal abundance) in this sample is found only in the cores of large pigeonite grains (∼71 %). This sample also contains radiating plagioclase (∼24 %) clusters (Butler, 1971). Dates determined for sample 15058 range from ∼3.36 ± 0.03 Ga ($^{40}Ar/^{39}Ar$; Husain 1974) to ∼3.46 ± 0.04 Ga (Rb/Sr; Birck et al., 1975). 15058 is characterized by a multistage exposure history with increased ^{81}Kr near the surface of the sample but constant at depth (Eugster et al., 1984). We have studied mesostasis areas in thin section 15058,20, which is ∼6 × 8 mm in size. The mineralogy of this section, consistent with that of the main rock sample, comprises anhedral pyroxene phenocrysts (>2 × 2 mm), plagioclase (∼1 × 0.5 mm) and minor ilmenite (<0.5 × 0.2 mm). Mesostasis regions in 15058,20, which are further described in section 2.4.1, are observed mostly in a few clusters in the center of this thin section.

2.2.4 70035

Apollo 17 sample 70035 is a medium-grained, vesicular, high-Ti basalt (Ridley and Brett, 1973). It is a large crystalline basalt with large (>1mm) anhedral clinopyroxene crystals (∼46 % modal abundance) enclosing armalcolite, ilmenite, and spinel (∼22 %). Interstitial plagioclase (∼26 %) is found together with ilmenite and olivine (∼2.5 % Weigand, 1973). The mesostasis regions (∼2 %) include silica, K-feldspar, tranquillityite, ilmenite, ulvospinel, troilite, K-rich glass and apatite (McGee et al., 1977; Papike et al., 1974). Metallic iron is found in the cracks and cleavage of opaque oxides and silicates in this sample (El Goresy and Ramdohr, 1975). Plagioclase composition in sample 70035 varies from An_{88} to An_{83} (Weigand, 1973). The Rb/Sr dates of 3.82 ± 0.06 Ga and 3.73 ± 0.11 Ga determined for 70035 are consistent with each other (Evensen et al., 1973; Nyquist, 1977) and with a $^{40}Ar/^{39}Ar$ date of 3.75 ± 0.07 Ga (Stettler et al., 1973). Exposure ages determined from abundance of cosmogenic ^{38}Ar (Stettler et al., 1973) and ^{81}Kr (Drozd et al., 1977) are 95 to 100 Ma and 122 ± 3 Ma, respectively. We have studied mesostasis areas in thin section 70035,195. This section is ∼14 × 3 mm in size and has a mineralogy consistent with that of the main rock sample, comprising anhedral plagioclase phenocrysts (>2 × 1 mm), pyroxene (∼1 × 1 mm) and ilmenite (∼0.5 × 0.2 mm). Small mesostasis pockets are found throughout the studied section and are further described in section 2.4.1.

2.3 Methods

2.3.1 Identifying mesostasis regions

The aim of this study was to characterize the regions in which apatite is found in lunar basalts, therefore, mesostasis regions containing apatite were primarily investigated. Using whole section element maps of the studied samples, mesostasis regions were identified by the presence of small (<1 mm) anhedral and amorphous phases that crystallized between larger surrounding crystals. The presence of symplectite assemblages and/or silicate liquid immiscibility textures was also used to identify mesostasis regions. These regions are rich in fayalite, silica, and glass and host a wide variety of smaller phases (i.e. sulphides, phosphates) compared to the surrounding major minerals. Pernet-Fisher et al. (2014) suggested that coarse-grained silica in mare basalts (>100 μm) is likely a pseudo-eutectic mineral and, therefore, should not be included as a mesostasis phase. For the majority of mesostasis regions investigated here this is not a concern as silica within the regions is fine-grained (<100 μm), and intergrown with other mesostasis phases. For mesostasis regions containing large (>100 μm), elongate silica grains, intergrown with other mesostasis phases, we have considered this as a product of crystallization of the late-stage melt and, therefore, as part of the mesostasis region. In the basalts studied here silica is only found associated with mesostasis regions.

A large variety of textures and mineral phases were observed in the different mesostasis regions. We determined the two-dimensional extents of the different regions in multiple ways. For silica-rich mesostasis regions the boundary was drawn around the area including silica. Pernet-Fisher et al. (2014) proposed that up to 30 vol.% of mesostasis melt could have been equilibrated with larger surrounding phases.

Re-equilibration of pre-existing plagioclase and pyroxene grains with mesostasis melt modified their chemistry and created chemical zonations. In some mesostasis regions clear modification of pre-existing pyroxene associated with overgrowth of mesostasis phases was observed on back-scattered electron (BSE) and false-color X-ray images, and later confirmed with electron probe microanalysis (EPMA). In regions with no clear modification of pre-existing phases, mesostasis boundaries were drawn around mesostasis phases only. Compositional differences between phases within and outside mesostasis regions are detailed in section 2.5. For modal abundance estimates, where possible, mesostasis regions were limited to areas that included late-stage phases with limited incorporation of surrounding pre-existing phases. It is worth noting that thin sections only provide 2D sections through 3D mesostasis regions, which likely implies a sampling bias. To try and mitigate the possible effects associated with this sampling bias, we analyzed multiple mesostasis regions $>50 \times 50$ μm.

2.3.2 Electron Microscopy

The BSE maps were collected using the FEI Quanta 3D dual beam scanning electron microscope (SEM) at The Open University. The instrument is fitted with an Oxford Instruments 80 mm X-MAX energy dispersive X-ray detector, which allowed X-ray maps of each sample to be obtained by using the SEM in Energy Dispersive Spectroscopy (EDS) mode. Elemental mapping was carried out using a 20 kV accelerating voltage and a 0.60 nA beam current. X-ray maps were acquired at resolutions of 512×448 and 1024×896 pixels with a magnification of 200 to 300.

Quantitative mineral compositions were determined using a CAMECA SX-100 Electron Probe Micro Analyzer (EPMA) at The Open University. An accelerating voltage of 20 kV and a beam current of 20 nA were used except for plagioclase and glass analyses where the beam current was reduced to 10 nA. The beam diameter varied from 1 μm to 10 μm, depending on the dimensions of the analyzed phase. Standard count rates of 20 to 40 s per element were used, with a background counting time of half the peak counting time before and after peak analysis. A selection of natural standards were used for calibration, including feldspar (Si, Al, K), jadeite (Na), forsterite (Mg), hematite (Fe), rutile (Ti), and apatite (P). The apatite compositions used here for bulk-mesostasis composition calculations are those reported by Tartèse et al. (2013a) for apatite grains located in the same thin sections but not necessarily in the same mesostasis regions. For 70035, the average apatite composition of those analyzed in the other samples by Tartèse et al. (2013a) was used as these authors did not analyze apatite in this sample. The modal mineralogy and the quench glass abundances, for each mesostasis area, were calculated using pixel histograms from BSE-images in the ImageJ software. For each mesostasis region a bulk composition was calculated using average EPMA compositions for each phase and the modal mineralogy within individual regions.

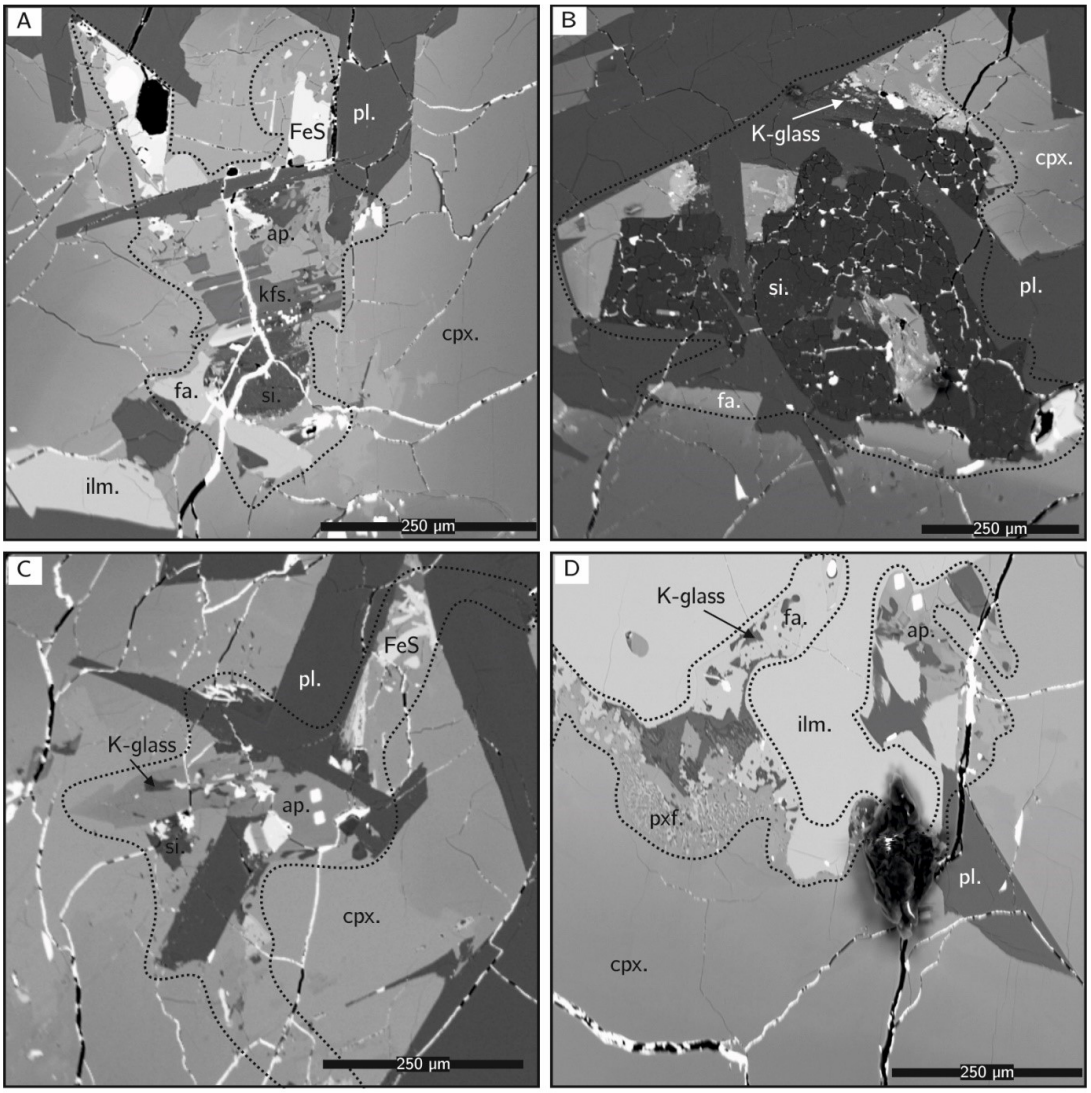

Figure 2.1: BSE images of mesostasis regions from 10044,645. The extent of mesostasis regions are outlined with a black dashed line. ap. = apatite, cpx. = clinopyroxene, fa. = fayalite, ilm. = ilmentite, kfs. = K-feldspar, mrl. = merrillite, pl. = plagioclase, pxf. = pyroxferroite, si. = silica

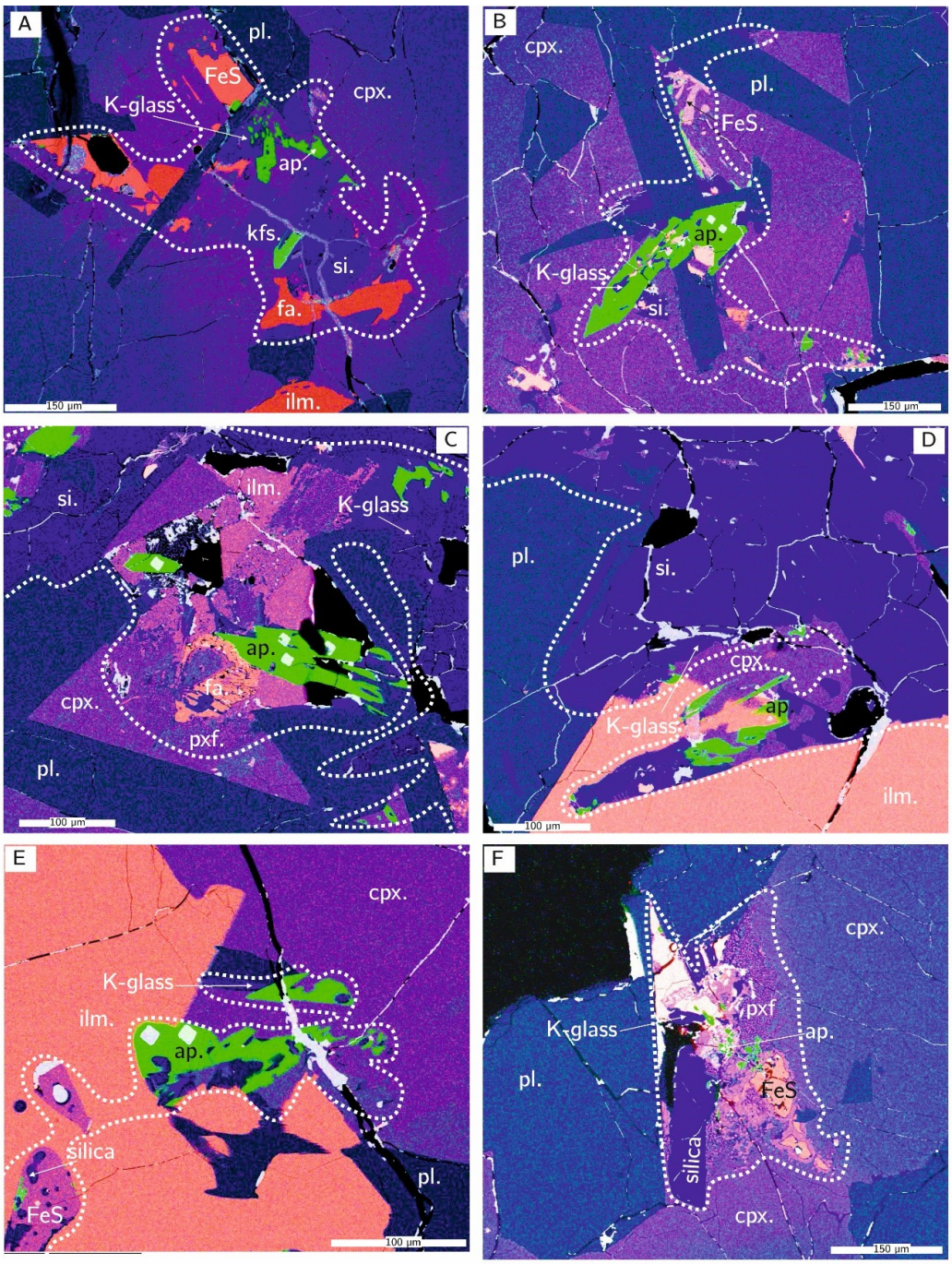

Figure 2.2: False-color (Si = purple, Ca = green, Fe = red) compositional maps of mesostasis regions in 10044,645. A and B correspond to BSE images A and C, respectively, shown in Figure 2.1. Mesostasis regions are outlined with a white dashed line. Mineral abbreviations are the same as in Figure 2.1. The white squares are NanoSIMS sputter pits.

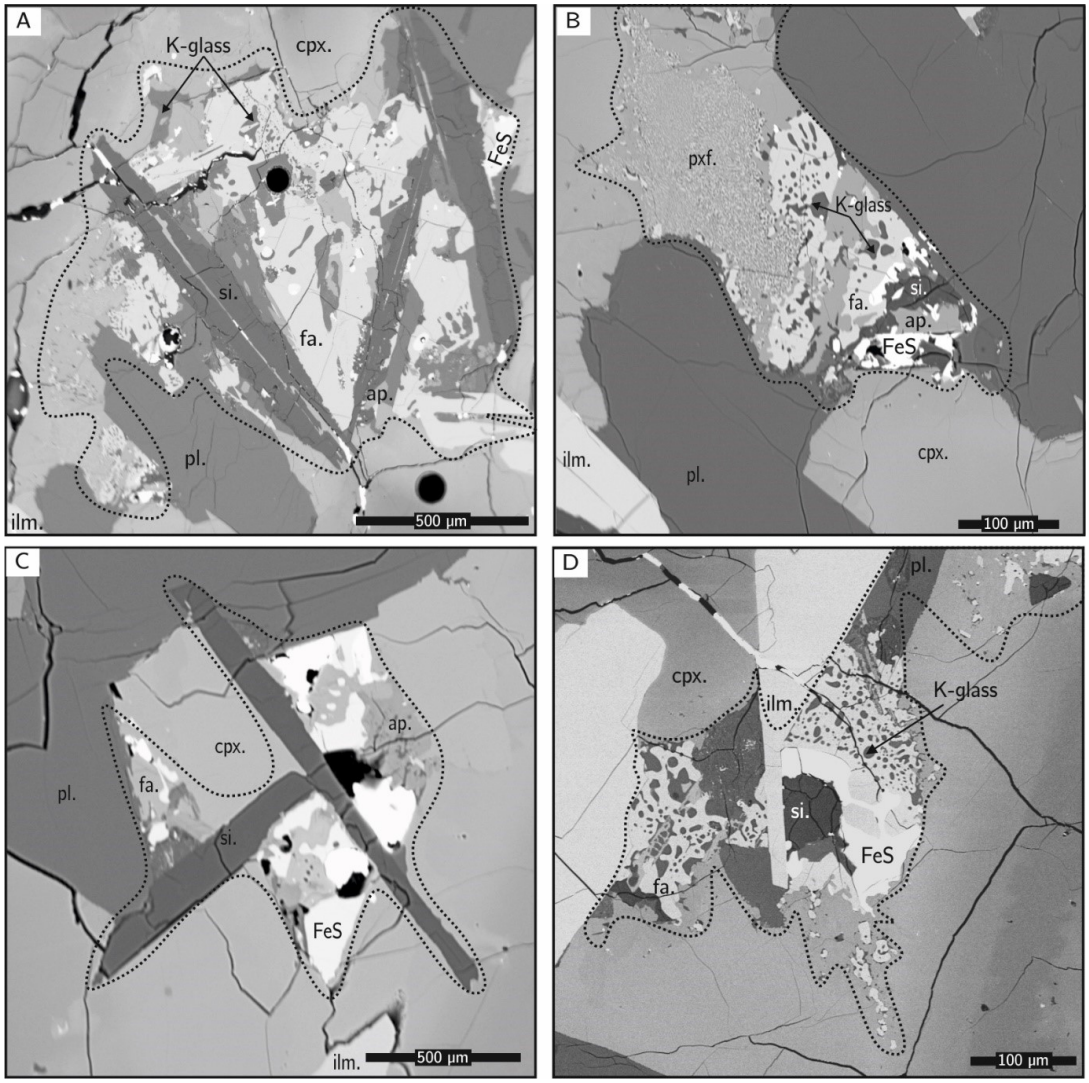

Figure 2.3: BSE images of mesostasis regions from 12064,130. The extent of mesostasis regions are outlined with a black dashed line. Mineral abbreviations are the same as in Figure 2.1

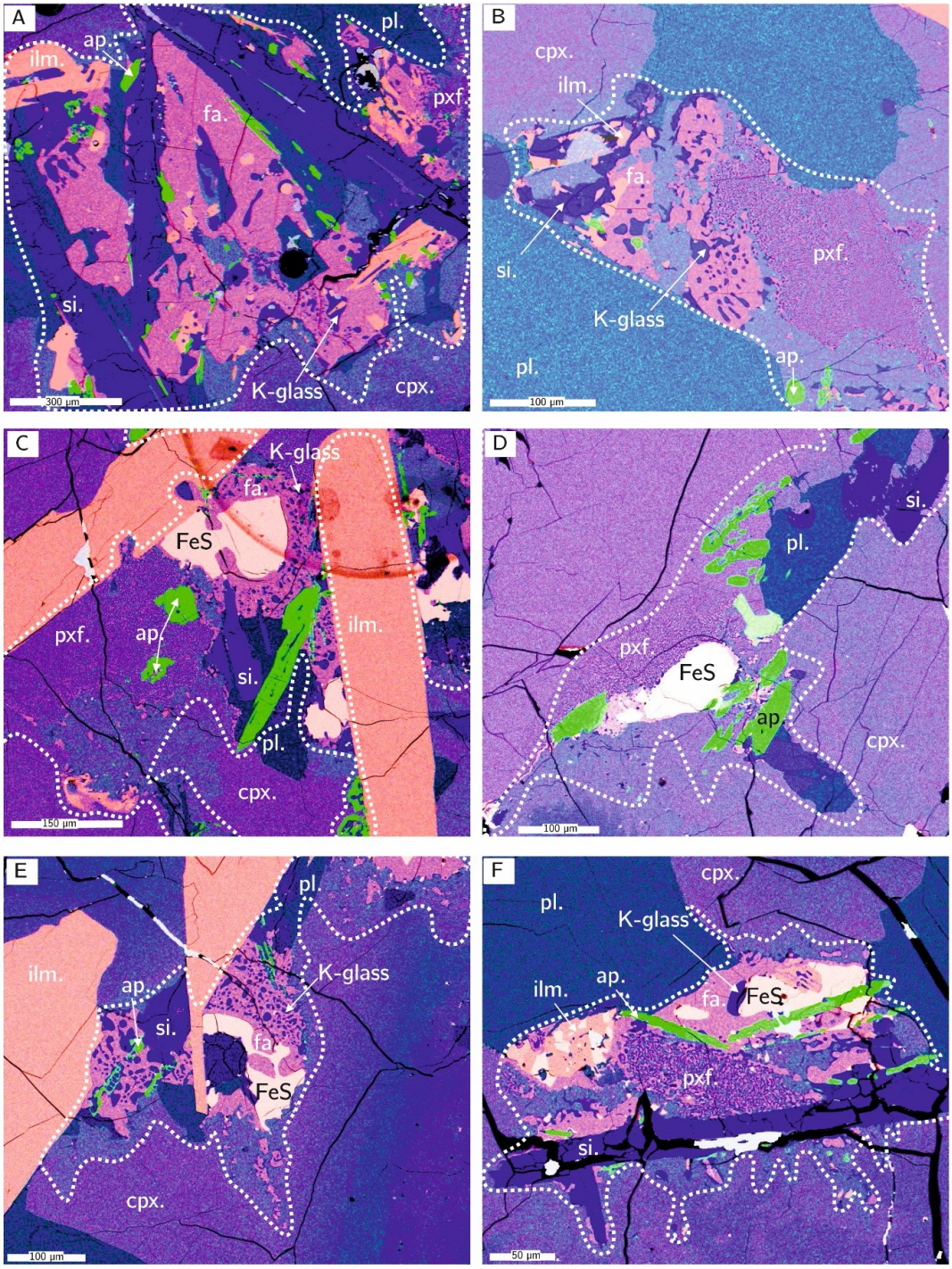

Figure 2.4: False-color composite (Si = purple, Ca = green, Fe = red) compositional maps of mesostasis regions in 12064,130. A, B and E correspond to BSE images A, B and D, respectively, shown in Figure 2.5. Mesostasis regions are outlined with a white dashed line. Mineral abbreviations are the same as in Figure 2.1

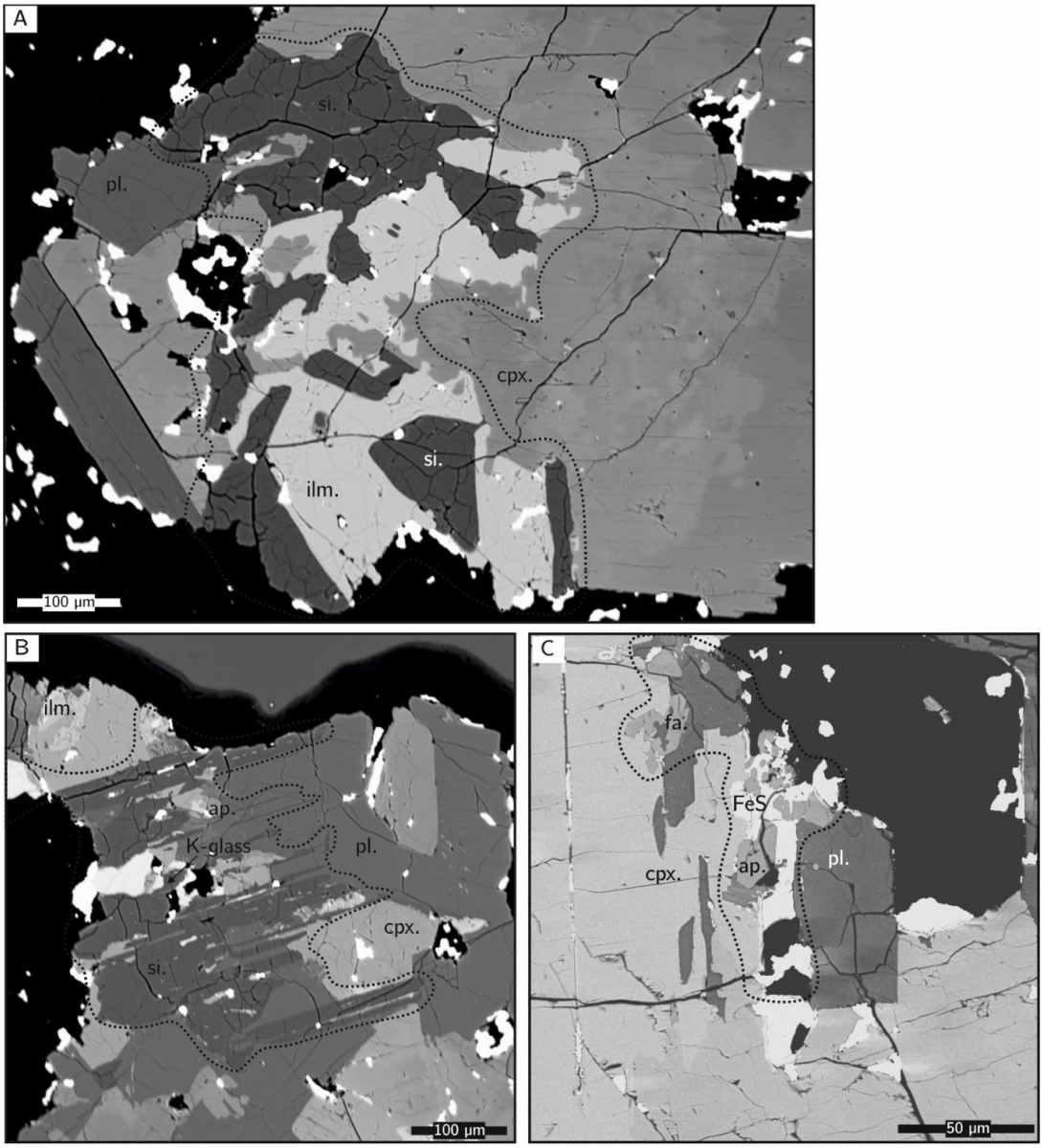

Figure 2.5: BSE images of mesostasis regions from 15058,20. The extent of mesostasis regions are outlined with a black dashed line. Mineral abbreviations are the same as in Figure 2.1

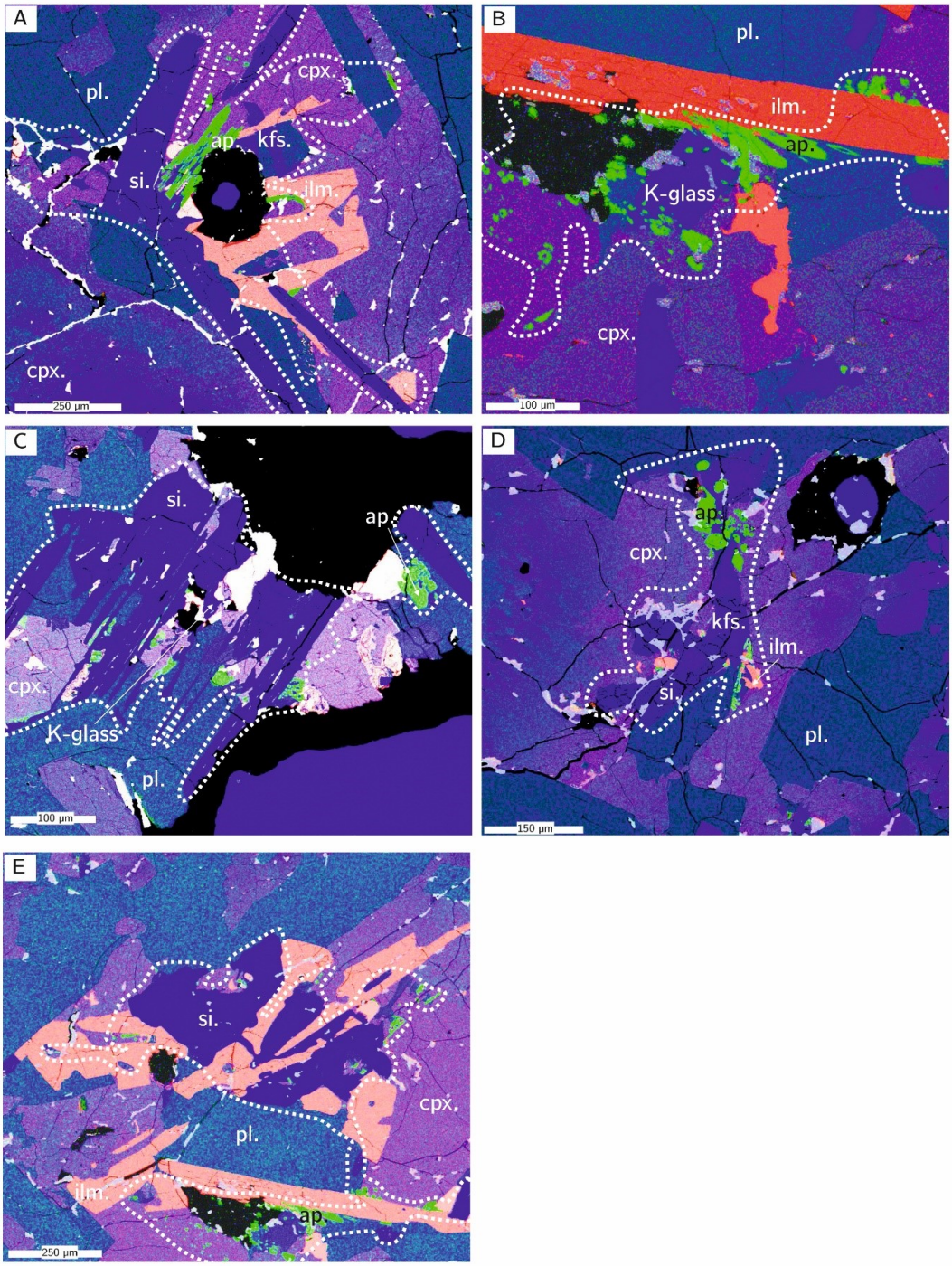

Figure 2.6: False-color composite (Si = purple, Ca = green, Fe = red) compositional maps of mesostasis regions in 15058,20. C and E correspond to BSE images B and A, respectively, shown in Figure 2.5. Mesostasis regions are outlined with a white dashed line. Mineral abbreviations are the same as in Figure 2.1

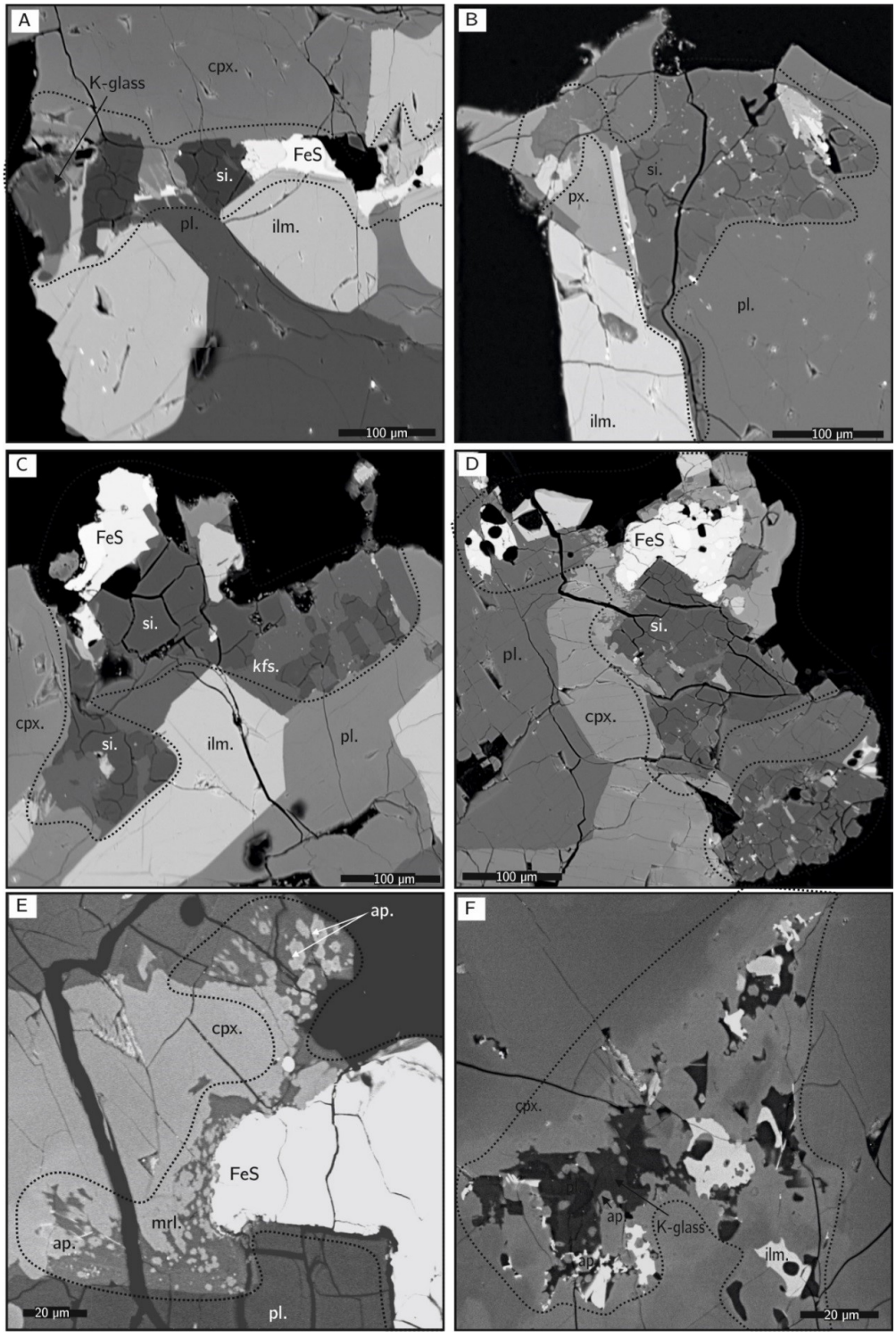

Figure 2.7: BSE images of mesostasis regions from 70035,195. The extent of mesostasis regions are outlined with a black dashed line. Mineral abbreviations are the same as in Figure 2.1

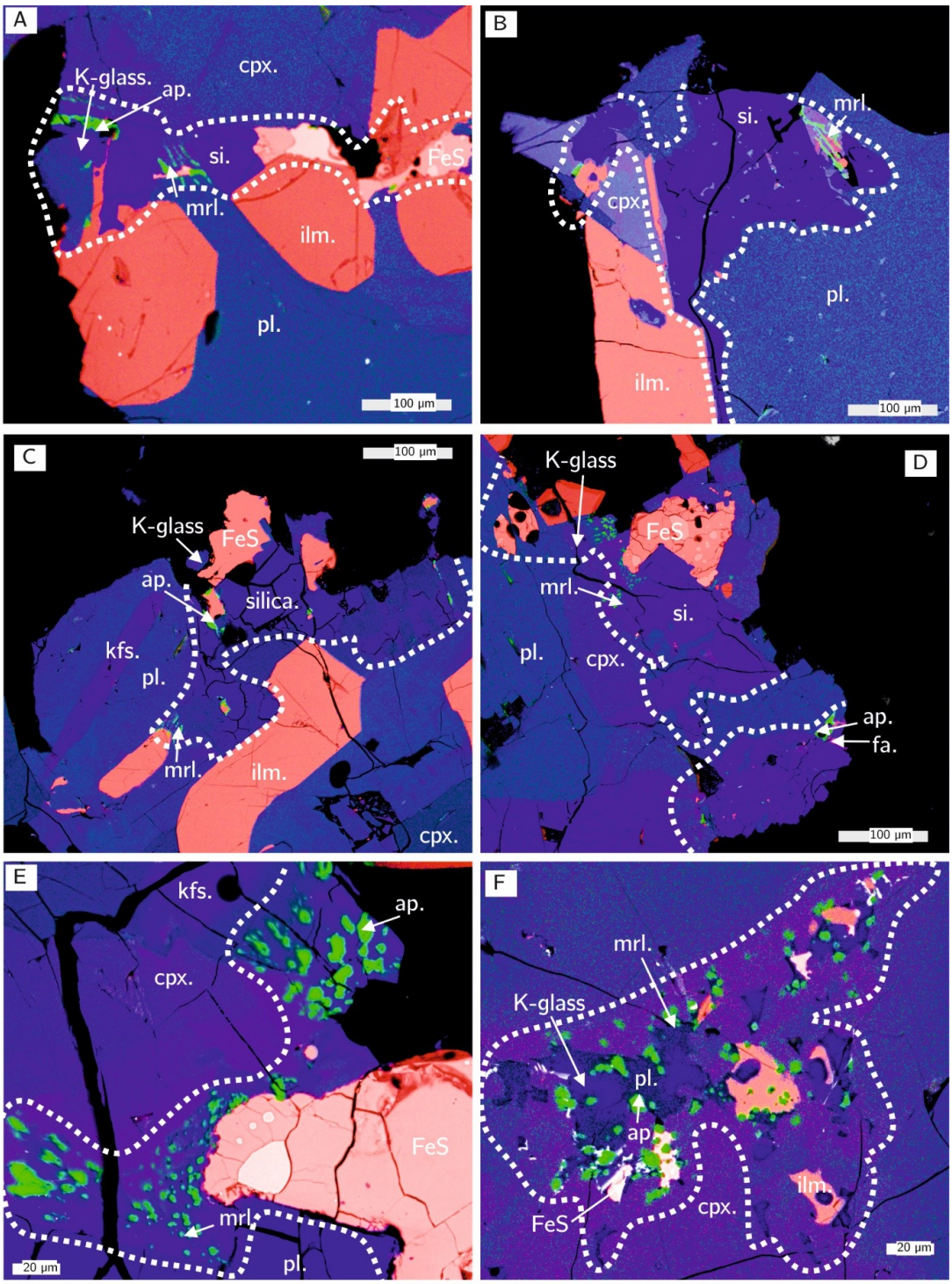

Figure 2.8: False-color composite (Si = purple, Ca = green, Fe = red) compositional maps of mesostasis regions in 70035,195. Mesostasis regions are outlined with a white dashed line. Mineral abbreviations are the same as in Figure 2.1

	10044 (n = *10*)	12064 (n = *7*)	15058 (n = *6*)	70035 (n = *7*)
Plagioclase	33 (*11*)	25 (*28*)	37 (*15*)	10 (*15*)
Pyroxene	27 (*11*)	28 (*12*)	33 (*5*)	30 (*17*)
Silica	36 (*24*)	30 (*4.8*)	15 (*6*)	24 (*18*)
Ilmenite	2 (*19*)	3 (*3*)	8 (*8*)	26 (*17*)
Fayalite	1 (*2*)	8 (*19*)	-	-
Glass	1 (*10*)	6 (*3.5*)	7 (*4*)	10 (*13*)
Phosphate	0.3 (*1.5*)	1 (*2*)	0.3 (*1*)	0 (*5*)
Total	100	100	100	100

Table 2.1: Average modal abundances of mesostasis regions for Apollo samples normalized to 100. n refers to number of regions analyzed. *(1σ). Note analysis do not include metal, troilite, or K-feldspar*

2.4 Results

2.4.1 Mesostasis textural descriptions

The BSE images and false-color compositional maps of representative mesostasis regions for the four samples are shown in Figures 2.1 - 2.8, and the modal mineral abundances in Table 2.1.

In sample 10044,645, ten mesostasis regions were analyzed, and representative BSE images of some of these regions are shown in Figure 2.1, while Figure 2.2 displays false-color X-ray elemental maps combining Si, Ca and Fe. These regions are $\sim$200 $\times$ 200 μm and are located between pre-existing plagioclase laths (Figures 2.1B & 2.1C) and pyroxene phenocrysts (Figures 2.1A, 2.1C, & 2.1D). All of the regions contain apatite, pyroxene and ilmenite, while silica, plagioclase, K-glass, and K-feldspar were found in the majority of areas. Two mesostasis regions contained fayalite grains large enough (i.e. $>$10 μm) for multiple microprobe spot analyses (Figures 2.1A & 2.1D). Symplectite texture (labelled as pxf in accompanying figures), formed from the breakdown of pyroxferroite into fayalite, silica, and hedenbergite, was observed in two regions within 10044,645 (Figures 2.1D & 2.2C). Two regions within this sample contained coarse-grained silica (Figures 2.1B & 2.2D). Spheroidal textures comprising of Si-K-Ba-rich glass (hereafter referred to as K-glass) enclosed by fayalite, characteristic of silicate-liquid immiscibility (SLI; Pernet-Fisher et al. 2014), were observed in five of the regions and shown in Figure 2.1D. Such textures were described by Pernet-Fisher et al. (2014) as sieve textures and classified as mature (large glass droplets) or immature (small glass droplets). The mesostasis region in Figure 2.1D displays immature sieve texture, with fine-grained droplets of K-glass trapped within host fayalite.

Seven mesostasis regions within basalt 12064,130 were analyzed. These regions are $\sim$100 $\times$ 100 μm and found mostly between pyroxene phenocrysts (Figures 2.3A, 2.3C, & 2.3D) and plagioclase laths (Figure 2.3B). Mesostasis regions contain varying amounts of apatite, silica, pyroxene, K-feldspar, fayalite, and ilmenite (Figures 2.3 & 2.4). Pyroxferroite breakdown products are present in some regions (Figures 2.3B, 2.4B, 2.4C, 2.4D & 2.4F). Both mature (Figure 2.3A) and immature (Figures 2.3B & 2.3D) sieve textures, indicative of SLI, were observed in all but two mesostasis region of 12064 (Figures 2.3C & 2.3D). One region within 12064 contained both mature and immature SLI textures (Figure 2.3A & 2.3A).

In sample 15058,20, six mesostasis regions were analyzed. These regions are ∼300 × 300 μm and found between pre-existing plagioclase (Figure 2.5B) and pyroxene (Figures 2.5A & 2.5C). Most of these regions contain a high abundance of silica (Figures 2.5A, 2.5B, 2.6A, 2.6C, 2.6E & 2.6F). Five of the regions contained apatite, pyroxene, plagioclase, and ilmenite, while one area did not contain apatite. K-glass was found in some of these regions. Textures indicative of SLI or pyroxferroite breakdown products were not observed in this sample.

Seven mesostasis regions within sample 70035,195 were analyzed. The mesostasis regions in this sample are ∼100 × 100 μm, and found between pre-existing pyroxene and plagioclase grains, and they generally contain silica, pyroxene, plagioclase, ilmenite, and K-glass (Figures 2.7 & 2.8). These regions contain small (<2 to 10 μm) apatite crystals co-existing with merrillite grains (e.g., Figure 2.8A). Out of the nineteen areas initially investigated we found that most of the regions contained merrillite. Apatite was not widespread but instead found concentrated within a few of the mesostasis regions.

2.4.2 Composition of mesostasis phases

For all four samples plagioclase compositions vary from An_{93} to An_{68} (Figure 2.9A). The K-rich plagioclase feldspars are those firmly within mesostasis regions (Figure 2.9A). Most of the pyroxene analyses in samples 10044 and 12064 plot close to the Hd –Fs binary (Figure 2.9B). In contrast, all pyroxene analyses for 70035 are more Mg-rich, plotting towards the En and Di regions (Figure 2.9B). The few analyses of pyroxene compositions in 15058 range between those in 70035 and in samples 10044/12064 (Figure 2.9B).

Glass compositions from mesostasis regions are displayed in a Total-Alkali-Silica (TAS) diagram in Figure 2.10, together with compositions of the bulk-rock mare basalts studied and of lunar granites (Beaty and Albee, 1978; Kushiro and Haramura, 1971; Rhodes and Hubbard, 1973; Rhodes et al., 1976; Seddio et al., 2013). In general, the glass compositions plot in a similar region of the diagram to the lunar granites (∼4 - 10 wt.% alkali and ∼68 wt.% to 78 wt.% SiO_2).

2.4.3 Reconstructed bulk-mesostasis compositions

Average modal abundances for mesostasis regions in the four studied samples are given in Table 2.1, while average compositions of mesostasis mineral and glass phases are given in Tables 2.2 to 2.5. Histograms within the ImageJ software were combined with this chemical data to produce modal abundance values given here. Mesostasis regions, as outlined, where restricted to regions with small (< 20 μm) phases. These data were combined to calculate the bulk-mesostasis compositions, and average compositions for the latter are given in Table 2.6, while an average apatite composition taken from Tartèse et al. (2013a) where used to include phosphorous in bulk reconstructed compositions. Compositional variations between different mesostasis regions within individual samples are generally larger than variations between different samples. Bulk SiO_2 contents within 10044 mesostasis regions, for example, varied from 57 wt.% to 83 wt.%, while SiO_2 contents varied by about 12 wt.% across the different mesostasis regions in 70035. Large variations between bulk compositions of mesostasis

regions were also observed for TiO_2 in sample 70035 for example, which varied by 14 wt.%. Significant variations in CaO contents (6.2 wt.% difference) in sample 12064 were also observed between different mesostasis regions. Very little variation within regions was observed for MnO, Na_2O, K_2O, and P_2O_5 contents, which is related to the lower abundance of these oxides in the calculated meostasis compositions.

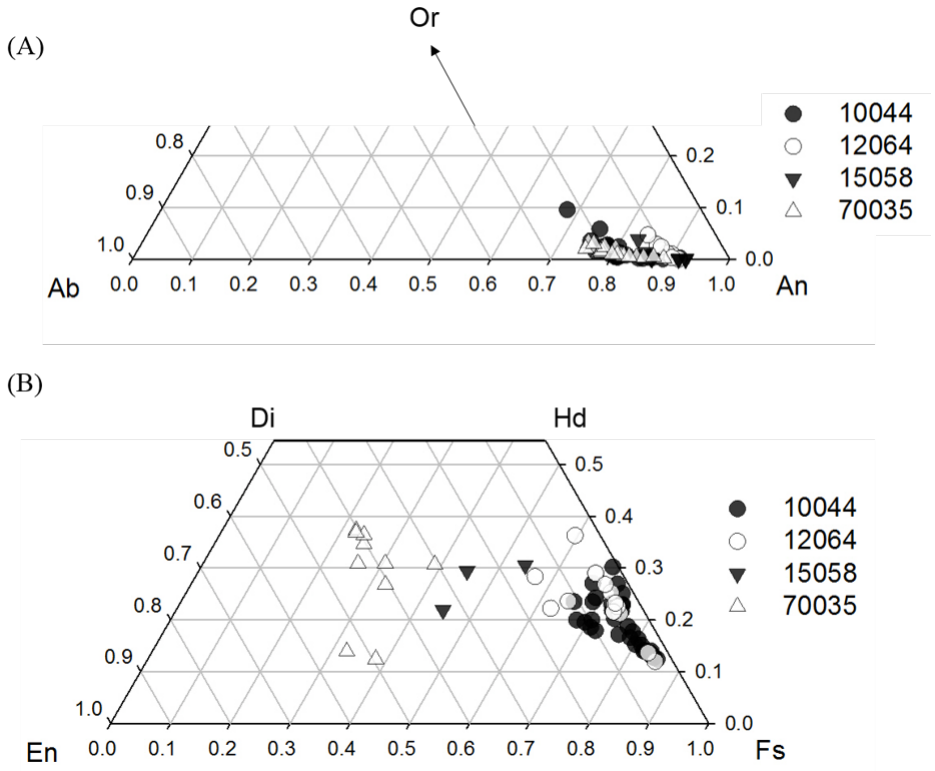

Figure 2.9: (A) Feldspar ternary diagram for analyses in mesostasis regions. (B) Pyroxene quadrilateral for pyroxenes measured in mesostasis regions.

The reconstructed bulk-mesostasis compositions display large variations between each sample. The largest variation is observed for SiO_2, which varies from 70 wt.% (10044) to 56.2 wt.% (70035). There is no correlation between the reconstructed SiO_2 content of the mesostasis regions and the SiO_2 content of the bulk sample. Sample 70035 does have the lowest bulk-rock SiO_2 content (37.8 wt.%; Rhodes et al., 1976) out of the four samples studied here, but 10044 has a lower bulk-rock SiO_2 content (42.2 wt.%; Beaty and Albee 1978) than both 12064 (46.0 wt.%; Scoon, 1971) and 15058 (47.8 wt.%; Rhodes and Hubbard, 1973) and, yet, the highest bulk-mesostasis SiO_2 content. The reconstructed mesostasis compositions for the four samples also display large variations in TiO_2 content. Sample 70035, a high-Ti basalt, has the highest mesostasis TiO_2 content (7.0 wt.%), however, high-Ti basalt 10044 has a relatively low mesostasis TiO_2 content (1.5 wt.%). TiO_2 contents of mesostasis regions in low-Ti basalts 12064 and 15058 are 0.9 wt.% and 3.6 wt.%, respectively. FeO contents of mesostasis regions in samples 10044 (10.8 wt.%), 15058 (11.1 wt.%) and 70035 (11.2 wt.%) are fairly similar, while it is much higher in 12064 (23.0 wt.%). The CaO contents of bulk-mesostasis are similar in samples 10044 and 15058 (6.4 wt.% CaO), while bulk-mesostasis in 12064 and 70035 have varying CaO contents (5.7 8.8 wt.%

CaO). The Al_2O_3 contents of mesostasis regions in 10044, 15058, and 70035 are similar (9.3, 9.2, and 10.1 wt.%), while 12064 has a lower Al_2O_3 content of 4.1 wt.%. The MgO contents of the mesostasis regions are highly variable between the four samples, ranging between 4.9 wt.% (70035) and 1.7 wt.% (15058), down to 0.8 wt.% (12064) and 0.3 wt.% (10044). The Na_2O contents of the mesostasis regions display little variation, ranging from 0.1 wt.% to 0.7 wt.%. The K_2O contents, however, show relatively large variation between 0.1 wt.% (70035) and 0.4 wt.% (12064), and up to 0.9 wt.% for sample 15058 and 0.5 wt.% for 10044.

	Feldspar *n = 33*	Pyroxene *n = 36*	Ilmenite *n = 2*	Silica *n = 25*	Glass *n = 8*	Fayalite *n = 1*
SiO_2	49.35 (*1.29*)	46.15 (*0.48*)	0.02	99.28 (*0.51*)	76.79 (*1.36*)	29.55
TiO_2	0.08 (*0.07*)	0.75 (*0.28*)	52.34 (*0.11*)	0.25 (*0.07*)	0.33 (*0.07*)	0.12
Al_2O_3	31.82 (*0.91*)	0.71 (*0.25*)	0.08 (*0.01*)	0.72 (*0.13*)	11.61 (*0.69*)	
MgO	0.11 (*0.05*)	1.50 (*0.92*)	0.21 (*0.09*)			0.55
CaO	15.87 (*0.97*)	7.97 (*2.11*)			0.01 (*0.01*)	0.87
MnO	0.01 (*0.01*)	0.65 (*0.09*)	0.40 (*0.01*)		0.01 (*0.01*)	0.87
FeO	0.76 (*0.23*)	41.35 (*2.95*)	45.59 (*0.17*)	0.13 (*0.10*)	0.92 (*0.26*)	66.47
Na_2O	1.93 (*0.32*)	0.02 (*0.02*)		0.20 (*0.06*)	0.41 (*0.15*)	0.06
K_2O	0.28 (*0.30*)			0.17 (*0.17*)	8.26 (*0.72*)	
Total	100.2 (*0.44*)	99.2 (*0.25*)	98.7 (*0.17*)	100.8 (*0.51*)	99.8 (*0.53*)	98.1
Si	2.26 (*0.05*)	1.97 (*0.01*)		0.99	1.28 (*0.02*)	1.01
Ti		0.02 (*0.01*)	1.00			
Al	1.71 (*0.05*)	0.04 (*0.01*)		0.01	0.12	
Mg		0.09 (*0.06*)	0.01			0.03
Ca	0.78 (*0.05*)	0.36 (*0.09*)			0.02 (*0.01*)	0.01
Mn		0.02	0.01		0.01	0.03
Fe	0.03 (*0.01*)	1.48 (*0.12*)	0.97		0.01	1.90
Na	0.17 (*0.03*)				0.01	
K	0.02 (*0.02*)				0.09 (*0.01*)	
Total	4.95 (*0.01*)	3.99	1.99	1.00		2.99
Ab	17.76 (*3.00*)					
An	80.54 (*4.26*)					
Or	1.70 (*1.86*)					
Wo		18.79 (*4.88*)				
En		4.91 (*2.96*)				
Fs		76.30 (*6.14*)				

Table 2.2: Average mineral compositions for mesostasis phases in 10044,645. Values in wt.%. Numbers in parenthesis are standard deviation on average compositions. *n* refers to number of analyses. Structural formulae based on 8 oxygen atoms for feldspars, 6 oxygen atoms for pyroxenes, 4 oxygen atoms for fayalite, 13 oxygen atoms for glass, and 2 oxygen atoms for silica and ilmenite.

	Feldspar	Pyroxene	Ilmenite	Silica	Glass	Fayalite
	n = 12	*n = 17*	*n = 2*	*n = 7*	*n = 1*	*n = 2*
SiO_2	47.07 (*0.71*)	46.22 (*0.53*)	0.03 (*0.01*)	98.98 (*1.00*)	74.86	29.45 (*0.03*)
TiO_2	0.04 (*0.03*)	0.87 (*0.20*)	51.39 (*0.17*)	0.21 (*0.03*)	0.50	0.11
Al_2O_3	32.98 (*0.54*)	0.88 (*0.24*)	0.06 (*0.03*)	0.45 (*0.16*)	11.78	
MgO	0.08 (*0.07*)	1.79 (*1.25*)	0.16			0.83 (*0.04*)
CaO	17.35 (*0.57*)	10.15 (*2.47*)	0.08 (*0.09*)	0.07 (*0.10*)	1.55	0.73 (*0.48*)
MnO	0.01 (*0.01*)	0.45 (*0.07*)	0.31		0.02	0.71
FeO	0.84 (*0.12*)	38.43 (*3.64*)	45.26 (*0.28*)	0.20 (*0.18*)	2.27	66.47 (*0.51*)
Na_2O	1.05 (*0.08*)	0.01 (*0.01*)	0.01 (*0.01*)	0.06 (*0.05*)	0.27	0.02 (*0.03*)
K_2O	0.24 (*0.22*)			0.23 (*0.10*)	7.90	
Total	99.7 (*0.23*)	98.8 (*0.34*)	97.3	100.2 (*0.70*)	99.2	98.4 (*0.02*)
Si	2.18 (*0.03*)	1.96 (*0.01*)		0.99 (*0.01*)	1.25	1.00
Ti		0.03 (*0.01*)	1.00		0.01	
Al	1.80 (*0.03*)	0.04 (*0.01*)		0.01	0.12	
Mg		0.11 (*0.08*)	0.01			0.04
Ca	0.86 (*0.03*)	0.46 (*0.11*)			0.03	0.03 (*0.02*)
Mn		0.02	0.01			0.02
Fe	0.03	1.37 (*0.14*)	0.98 (*0.01*)		0.03	1.89 (*0.02*)
Na	0.09 (*0.01*)					
K	0.01 (*0.01*)				0.08	
Total	4.98 (*0.01*)	3.99	2.00	1.01		2.99
Ab	9.76 (*0.85*)					
An	88.76 (*2.51*)					
Or	1.48 (*1.37*)					
Wo		23.76 (*5.62*)				
En		5.82 (*3.96*)				
Fs		70.42 (*7.36*)				

Table 2.3: Average mineral compositions for mesostasis phases in 12064,130. Values in wt.%. Numbers in parenthesis are standard deviation on average compositions. *n* refers to number of analyses. Structural formulae based on 8 oxygen atoms for feldspars, 6 oxygen atoms for pyroxenes, 4 oxygen atoms for fayalite, 13 oxygen atoms for glass, and 2 oxygen atoms for silica and ilmenite.

	Feldspar	Pyroxene	Silica	Glass
	n = 7	*n = 3*	*n = 13*	*n = 1*
SiO_2	46.88 (*1.47*)	48.20 (*0.90*)	98.29 (*0.50*)	76.61
TiO_2	0.05 (*0.01*)	1.02 (*0.21*)	0.27 (*0.06*)	
Al_2O_3	32.81 (*1.21*)	1.20 (*0.09*)	0.57 (*0.16*)	12.20
MgO	0.21 (*0.10*)	8.02 (*3.05*)		
CaO	17.56 (*0.95*)	12.23 (*1.95*)	0.12 (*0.06*)	0.14
MnO	0.01 (*0.01*)	0.39 (*0.02*)		
FeO	0.67 (*0.19*)	27.37 (*2.58*)	0.16 (*0.15*)	0.19
Na_2O	1.18 (*0.29*)	0.05 (*0.06*)	0.15 (*0.05*)	0.15 (*7.36*)
K_2O	0.12 (*0.20*)		0.09 (*0.12*)	8.13
Total	99.5 (*0.23*)	98.5 (*0.11*)	99.7 (*0.48*)	100.1
Si	2.17 (*0.06*)	1.95 (*0.01*)	0.99	1.28
Ti		0.03 (*0.01*)		
Al	1.79 (*0.07*)	0.06	0.01	0.12
Mg	0.01 (*0.01*)	0.48 (*0.18*)		
Ca	0.87 (*0.05*)	0.53 (*0.01*)		
Mn		0.01		
Fe	0.03 (*0.01*)	0.93 (*0.10*)		
Na	0.11 (*0.03*)			
K	0.01 (*0.01*)			0.09
Total	4.99 (*0.01*)	3.99	1.01	
Ab	9.76 (*0.85*)			
An	88.76 (*2.51*)			
Or	1.48 (*1.37*)			
Wo		23.76 (*5.62*)		
En		5.82 (*3.96*)		
Fs		70.42 (*7.36*)		

Table 2.4: Average mineral compositions for mesostasis phases in 15058,20. Values in wt.%. Numbers in parenthesis are standard deviation on average compositions. *n* refers to number of analyses. Structural formulae based on 8 oxygen atoms for feldspars, 6 oxygen atoms for pyroxenes, 4 oxygen atoms for fayalite, 13 oxygen atoms for glass, and 2 oxygen atoms for silica and ilmenite.

	Feldspar *n = 22*	Pyroxene *n = 10*	Ilmenite *n = 3*	Silica *n = 12*	Glass *n = 3*
SiO_2	49.20 (*1.34*)	50.15 (*0.58*)	0.02 (*0.03*)	97.85 (*0.52*)	76.06 (*1.38*)
TiO_2	0.11 (*0.08*)	1.47 (*0.38*)	53.44 (*0.01*)	0.37 (*0.08*)	0.76
Al_2O_3	31.08 (*1.15*)	1.77 (*0.47*)	0.03 (*0.01*)	0.89 (*0.16*)	11.52 (*0.11*)
MgO	0.20 (*0.05*)	14.02 (*2.29*)	2.37 (*0.16*)		0.91 (*0.68*)
CaO	15.60 (*1.00*)	13.62 (*4.19*)	0.02 (*0.02*)	0.19 (*0.09*)	0.58 (*0.99*)
MnO	0.01 (*0.01*)	0.32 (*0.06*)	0.38 (*0.01*)		0.01 (*0.01*)
FeO	0.66 (*0.27*)	17.48 (*3.60*)	41.83 (*0.16*)	0.17 (*0.08*)	0.88 (*0.47*)
Na_2O	2.03 (*0.33*)	0.07 (*0.03*)	0.02 (*0.03*)	0.26 (*0.07*)	0.88 (*0.10*)
K_2O	0.25 (*0.14*)			0.10 (*0.13*)	6.35 (*0.16*)
Total	99.2 (*0.47*)	98.9 (*0.24*)	98.1 (*0.08*)	99.9 (*0.48*)	97.9 (*0.70*)
Si	2.27 (*0.06*)	1.93 (*0.02*)		0.99	1.27 (*0.02*)
Ti		0.04 (*0.01*)	1.01 (*0.01*)		
Al	1.69 (*0.06*)	0.08 (*0.02*)		0.01	0.11
Mg	0.01	0.80 (*0.13*)	0.10 (*0.02*)		0.02 (*0.02*)
Ca	0.77 (*0.05*)	0.56 (*0.17*)			0.01 (*0.02*)
Mn		0.01	0.01		
Fe	0.03 (*0.01*)	0.56 (*0.12*)	0.88		0.01 (*0.01*)
Na	0.18 (*0.03*)			0.01	0.01
K	0.01 (*0.01*)				0.07
Total	4.98 (*0.01*)	3.99 (*0.01*)	1.99	1.01	
Ab	18.79 (*3.21*)				
An	79.67 (*3.93*)				
Or	1.54 (*0.87*)				
Wo		29.18 (*9.03*)			
En		41.63 (*6.24*)			
Fs		29.19 (*6.14*)			

Table 2.5: Average mineral compositions for mesostasis phases in 70035,645. Values in wt.%. Numbers in parenthesis are standard deviation on average compositions. *n* refers to number of analyses. Structural formulae based on 8 oxygen atoms for feldspars, 6 oxygen atoms for pyroxenes, 4 oxygen atoms for fayalite, 13 oxygen atoms for glass, and 2 oxygen atoms for silica and ilmenite.

	10044	12064	15058	70035
SiO_2	70.0 (*14.9*)	61.1 (*8.8*)	65.1 (*6.0*)	56.2 (*11.9*)
TiO_2	1.5 (*1.0*)	0.9 (*0.7*)	3.6 (*1.6*)	7.0 (*6.9*)
Al_2O_3	9.3 (*4.1*)	4.1 (*0.5*)	9.2 (*2.6*)	10.1 (*4.8*)
FeO	10.8 (*7.9*)	23.0 (*6.2*)	11.1 (*6.8*)	11.2 (*3.7*)
MnO	0.2 (*0.1*)	0.3 (*0.1*)	0.1 (*0.1*)	0.2 (*0.1*)
MgO	0.3 (*0.2*)	0.8 (*0.4*)	1.7 (*0.1*)	4.9 (*2.5*)
CaO	6.4 (*2.9*)	5.7 (*0.9*)	6.4 (*0.7*)	8.8 (*3.1*)
Na_2O	0.6 (*0.2*)	0.1 (*0.0*)	0.4 (*0.0*)	0.7 (*0.3*)
K_2O	0.5 (*0.6*)	0.4 (*0.4*)	0.9 (*1.2*)	0.1 (*0.1*)
P_2O_5	0.5 (*0.8*)	0.4 (*0.6*)	0.02 (*0.1*)	0.01 (*0.01*)
Total	99.0	98.4	98.8	99.2

Table 2.6: Average bulk compositions of mesostasis regions in Apollo samples based on EMPA data and modal abundances from ImageJ. All values in wt. *(2σ)*. Compositions do not include FeS.

2.5 Discussion

2.5.1 Relationships between bulk-rock chemistry and mesostasis composition

Analysis of mesostasis regions in samples from this study and those studied by Pernet-Fisher et al. (2014) show that these regions have distinct mineralogy and textures, which vary greatly across a single sample, and display both mature (Figures 2.3A & Figure 2.4A) and immature (Figures 2.4B, 2.4C, & 2.4E) SLI-related sieve textures. Mesostasis compositions appear to be more dependent on the composition of surrounding mineral phases than on bulk-rock composition, which is consistent with the observations of Pernet-Fisher et al. (2014). The similarity of Al_2O_3, CaO, and K_2O concentrations of the mesostasis regions of 10044 and 15058 on one hand, and of 12064 and 70035 on the other hand, is a reflection of surrounding pre-existing grains. The majority of mesostasis regions within 10044 and 15058 are mostly surrounded by pre-existing pyroxenes and smaller plagioclase grains, while mesostasis regions in 12064 are found between pre-existing plagioclase and pyroxene grains, and those in 70035 are commonly observed between pre-existing plagioclase grains. Phase boundaries in contact with mesostasis melt are thought to re-equilibrate with this melt. However, precisely quantifying the extent of diffusion into pre-existing phenocrysts is not possible from our dataset. It is worth noting, however, that mesostasis areas surrounded by pre-existing plagioclase that were not included in melt reconstructions may lead to modeled melts having lower Al_2O_3, contents for example, assuming some of the melt Al_2O_3 is lost as diffusion into pre-existing grains.

Mineral compositional variations between different mesostasis regions within a sample also support fractional crystallization as an important process in controlling mesostasis bulk compositions and explaining differences for different mesostasis regions. For example, Figure B.3 highlights how feldspar and pyroxene compositions within different mesostasis regions in sample 10044 vary. It is important to note that in addition, sampling bias, notably due to the 2D nature of mesostasis regions observed in thin sections while they are in fact 3D objects, can also be responsible for part of the variations observed between different mesostasis regions in individual samples.

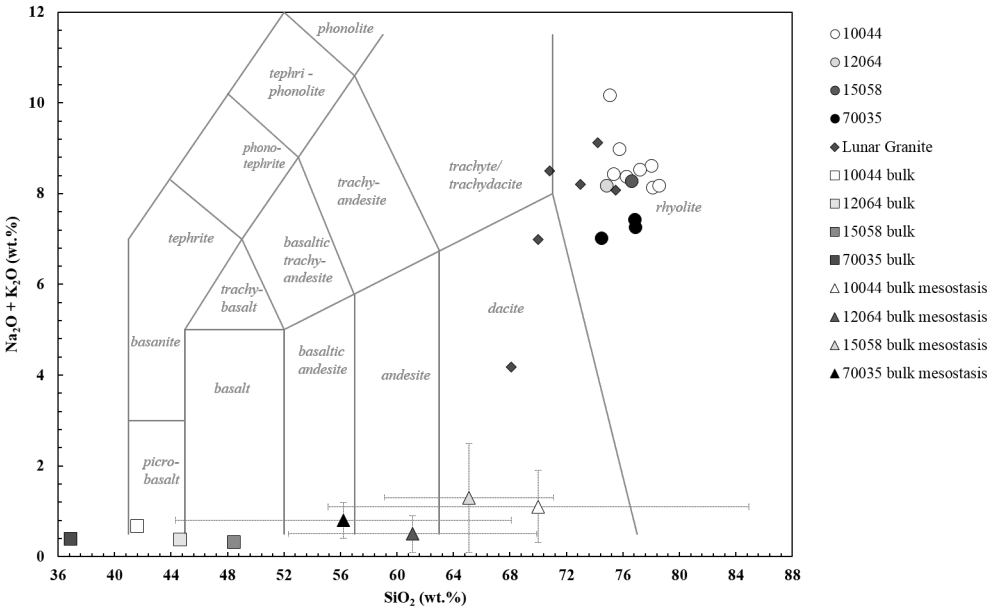

Figure 2.10: Total-alkali-silica (TAS) diagram for glasses measured in mesostasis regions in this study plus bulk-mesostasis calculated compositions. Bulk compositions of the studied mare basalts (Dymek et al. 1975, Hallis et al., 2014, and Rhodes and Hubbard, 1973) and of lunar granites (Seddio et al., 2013) are plotted for comparison.

The bulk-rock samples from this study are all relatively enriched in Fe (Mg# = 37 for 12064, 38 for 10044 and 44 for 15058), the less differentiated being sample 70035 (Mg# = 48). Sample 12064 has the lowest Mg# and the highest mesostasis FeO content. Sample 10044 has a similar Mg# but a lower bulk-mesostasis FeO content compared to 12064. Pernet-Fisher et al. (2014) have suggested that lunar basalts with low Mg# (<50) are more likely to undergo SLI than those with higher Mg# (>50). Even though all the studied samples have low-Mg#, the two samples that do not display evidence of SLI, 15058 and 70035, have the highest Mg#, which supports the observation of Pernet-Fisher et al. (2014). Also, Pernet-Fisher et al. (2014) found that their low Mg# basalts displayed the largest range in pyroxene compositions. In the studied samples, pyroxene have more restricted compositions. Pyroxene in samples 70035 and 15058 displays the largest range in compositions (Figure 2.9B), which is opposite to the observation of Pernet-Fisher et al. (2014) since these two samples have the highest Mg#.

The SiO_2 contents of K-rich glass for all samples cluster together at around 74-78 wt.%, while the Na_2O + K_2O contents of glass in 70035 (∼7.0 - 7.5 wt.%) are slightly lower than in basalts 10044, 12064 and 15058 (>8 wt.%; Figure 2.10). This may suggest that mesostasis regions in 70035 generally crystallized earlier than in other mare basalts, having slightly less evolved chemical compositions (Table 2.6), which is also reflected in the more Mg-rich nature of pyroxene in 70035 mesostasis regions. In general there is no relationship between SiO_2 in the bulk-rock, bulk-mesostasis, and mesostasis glasses, supporting the hypothesis that fractional crystallization of major silicate minerals may not be the main process controlling the compositional characteristics of mesostasis regions.

2.5.2 Fractional crystallization modeling and the influence of bulk-rock composition on late-stage melts

To provide further understanding on the evolution of these lunar basalts, crystallization modeling was undertaken using whole-rock major element compositions for each of the four samples. Liquid lines of descent (LLD) were calculated using the Simulating Planetary Igneous Crystallization Environments package (SPICEs Davenport et al., 2014), which incorporates the FXMOTR, MAGFOX, and MAGPOX programs (Longhi, 1991). The use of MELTS for modeling basaltic systems is well demonstrated in the literature (Ghiorso et al., 2002; Ghiorso and Sack, 1995; Gualda et al., 2012) and has been used for extraterrestrial applications (e.g. Anand et al., 2003; Day et al., 2006; Fagan et al., 2014; Liu et al., 2009). However, the SPICEs program has the unique advantage of being calibrated for extra-terrestrial systems. Here, the MAGFOX program was used to model fractional crystallization of the four Apollo samples under lunar relevant conditions. The MAGFOX program has been widely utilized for modeling Apollo basalt evolution (Neal et al., 1994a,b) and more recently to investigate SLI in late-stage melts (Pernet-Fisher et al. 2014). Results from the MAGFOX algorithm are plotted on the AFM 2D pseudo-ternary (Na_2O + K_2O –FeO –MgO; Figure 2.11). It is worth noting that the MAGFOX calculates temperature for each run that varies between ∼1200 °C and ∼900 °C.

For each sample, all available bulk compositions were input into the MAGFOX algorithm. The LLD for each sample varies with composition indicating the sensitivity of the model to relatively minor changes in bulk composition (Figure 2.11). To investigate the possible effect of pressure, we used the bulk composition from Engel and Engel (1970) for sample 10044 and varied the pressure between 1 kb, 5 kb, and 10 kb, which had very little effect until the final stages of crystallization (Figure 2.11A). When MgO becomes exhausted in the system, the 1 kb LLD moves towards lower FeO contents while the 10 kb moves in the opposite direction on the AFM (the run at 5 kb did not crystalize to the point of MgO exhaustion (Figure 2.11A). Based on modeling for sample 10044, we considered the effect of pressure much less significant than the effect of the bulk-rock composition, and runs were only performed at a pressure of 1 kb for the remaining samples.

MAGFOX was unable to model crystallization up to 100 % fractionation for any of the samples. The volume of crystals fractionated for 10044 was 64 % using the bulk composition from Wänke et al. (1970), 98 % using that of Engel and Engel (1970) and Beaty and Albee (1978), and 99 % using those from Agrell et al. (1970), Wakita et al. (1970), and Dymek et al. (1975) (Figure 2.11B). For sample 12064, the volume of crystals fractionated ranged from 88 % using the composition from LSPET (1970) to 99 % with those from Kushiro and Haramura (1971) and Scoon (1971) (Figure 2.11C). Finally, the volume of crystals fractionated for sample 15058 varied from 97 % using the composition of Rhodes and Hubbard (1973) to 99 % with that of Willis et al. (1972) (Figre 2.11D) while the crystallization of 70035 reached 96 % (Rhodes et al. 1976).

For all the samples the LLDs plot within the mare basaltic field on the AFM (Fagan et al. 2014). The LLDs for 10044 are in good agreement with some of the compositions of late-stage melts calculated in this study (Figure 2.11B). The bulk-rock composition from Beaty and Albee (1978) has a low initial bulk alkali content

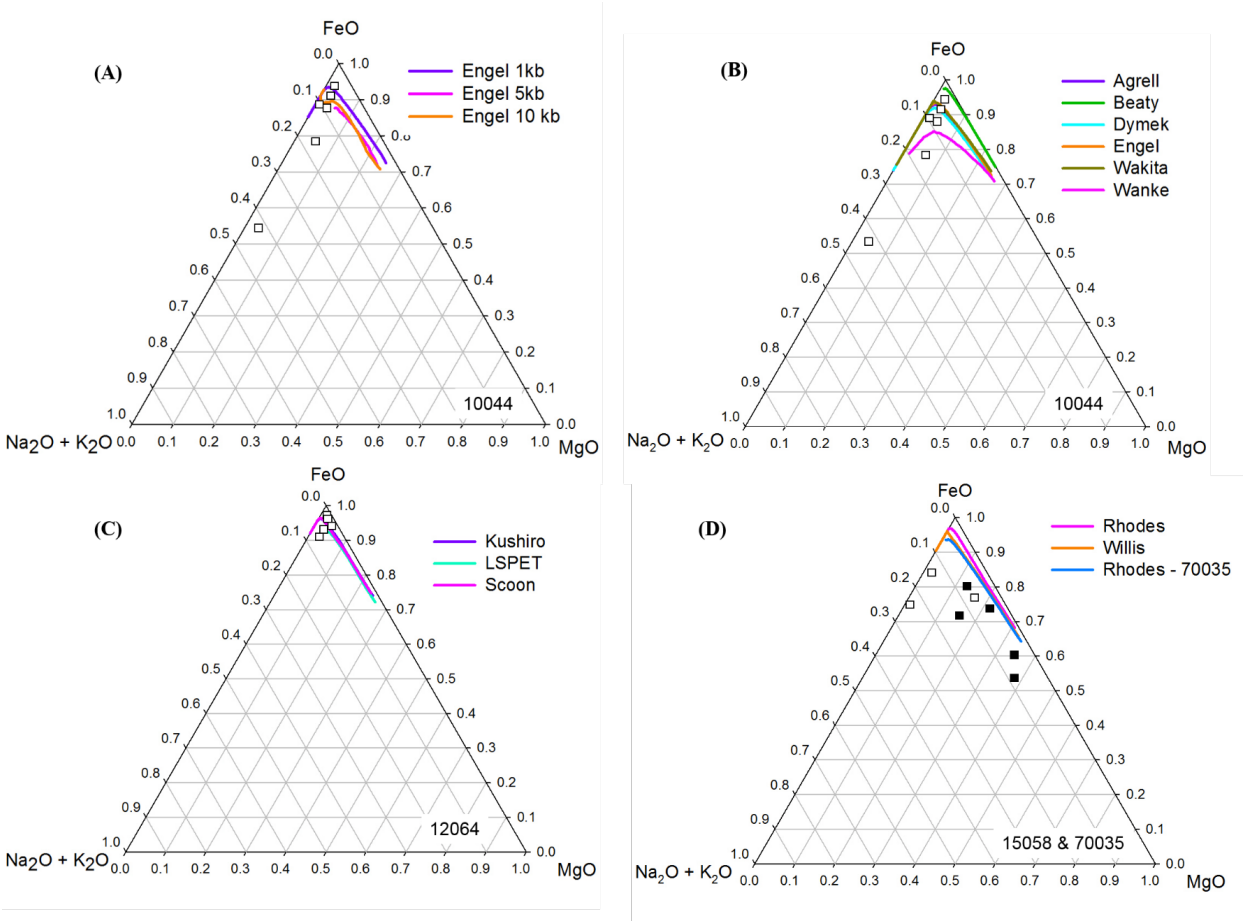

Figure 2.11: AFM ternary diagrams ([Na_2O + K_2O] –MgO –FeO) for (A) varying pressure runs for the bulk-rock composition of mare basalt 10044 of Engel and Engel, 1970 (B) all bulk-rock compositions for sample 10044, (B) all bulk-rock compositions for sample 12064, and (D) all bulk-rock compositions for samples 15058 and 70035. Lines indicate liquid lines of descent as modeled by SPICEs. Bulk mesostasis compositions calculated here plotted also as white squares (black squares in D for sample 70035).

(Na_2O + K_2O = 0.02 wt.%), resulting in a LLD which is too depleted in Na_2O and K_2O to correspond with any of the late-stage melt calculated compositions. The LLD calculated using the bulk-rock composition of Wänke et al. (1970), which has an initial alkali content much higher than the other compositions, also has alkali contents which are higher than the majority of the mesostasis region calculated compositions. There is good agreement for the majority of calculated mesostasis regions and the compositions of Dymek et al (1975), Engel and Engel (1970), and Wakita et al. (1970). The LLDs for 12064 plot closely together and show fairly good agreement with the calculated late-stage melt compositions (Figure 2.11C). For samples 15058 and 70035, the LLDs do not correspond with calculated mesostasis region compositions (Figure 2.11D)

The overall broad agreement between petrological and modeling estimates of mesostasis melt compositions in sample 12064, and to a lesser extent 10044, suggests that SPICEs may be an efficient tool for calculating the composition of late-stage melts (Figure 2.11). However, SPICE modeling was unable to reconcile compositions in samples 15058 and 70035. Additionally, AFM diagrams only considers Na_2O + K_2O, FeO, and MgO contents modeled using SPICEs, and other chemical parameters may differ in their reconciliation. Petrological estimates of mesostasis regions compositions for 15058 appear to slightly overestimate MgO and Na_2O + K_2O contents (Figure 2.11D). This is similar for 70035, which shows a large discrepancy between the reconstructed bulk-mesostasis compositions and those modeled by SPICEs, as the reconstructed bulk-mesostasis compositions are Mg-rich and would plot near the beginning of the LLD, when SPICEs modeling suggests that mesostasis compositions should be similar to those in sample 10044. The high MgO content calculated for the bulk-mesostasis regions in 70035 (Table 2.6) presumably results from the high proportion of pyroxene relative to plagioclase surrounding mesostasis regions in this sample. The pyroxene grains in 70035 have also higher Mg contents than those of the other samples (Figure 2.9B). As highlighted by the other samples, however, the bulk-rock composition inputted in SPICE can have a significant influence on the calculated LLDs and with only one available composition for 70035 it is difficult to make strong conclusions. Overall the outcome of SPICEs modeling indicates that fractional crystallization can produce the compositions seen for some late-stage melts but not all. This suggests, therefore, that other processes such as equilibrium crystallization and/or alteration of early-crystallized pyroxene and/or plagioclase phenocrysts are also affecting late-stage melt compositions. The variability of late-stage melts also highlights that apatite within lunar mare basalts does not crystalize from a fixed melt composition.

2.5.3 Silicate liquid immiscibility

We have argued that the composition of phases between which mesostasis regions become trapped and crystallize have a large influence on these late-stage melt compositions. After these late-stage melts become trapped, SLI is thought to exert additional control on the compositions of these melts (Pernet-Fisher et al., 2014). It is not known, however, if SLI commonly operates in all late-stage melts. There are many regions, in the samples studied here, where SLI has obviously occurred. Where present, however, the extent of SLI appears limited and has no influence on the bulk composition of these regions as both fractions remain. It should be noted, however,

that the absence of SLI-related textures, such as sieve textures, does not indicate that SLI did not occur, only that it was not followed by immediate quenching if it occurs. In the sections studied here, apatite was not found in direct contact with textures directly related to SLI within mesostasis regions, preventing a thorough investigation of whether apatite crystallized before, during or after SLI. Volatiles, such as F, Cl and OH, can be fractionated during SLI (Lester et al. 2013), which, therefore, could add further uncertainty into reconstructing volatile abundances in silicate melts based on analysis of volatiles in apatite. It is worth noting, that SLI is thought to be an important process in lunar granite formation after extensive fractional crystallization (Seddio et al., 2013). This not only highlights how important it is to understand SLI on a global lunar scale but could explain the overlap between glasses within mare basalt mesostasis regions and the bulk composition of lunar granites.

2.6 Summary

The lack of relationship between bulk-rock chemistry and reconstructed mesostasis melt composition argues for distinct chemical evolution of the different mesostasis regions within a single crystallizing basalt. Mesostasis regions within a single sample can vary in composition and textural maturity, which suggests that volatile contents could also vary within these regions. Our study also shows that mesostasis regions have bulk compositions that differ significantly from those of the initial basaltic melts that formed the bulk sample. As such, partition coefficients derived from experimental studies of apatite-melt partitioning designed for basaltic melts may not be fully applicable. Future experiments on apatite-melt volatile partitioning should, therefore, be conducted with more silicic starting compositions given the strong dependence that melt composition has on partitioning in this system (Mathez and Webster, 2005).

The mineralogy and petrology of mare basalts are well characterized in the literature, yet detailed analyses of mesostasis regions in Apollo samples have been largely overlooked. This study has highlighted the variability of mesostasis regions in lunar basalts. Once a mesostasis melt is trapped between pre-existing grains, its evolution becomes distinct and separated from the evolution of melts trapped in other mesostasis regions. It is expected that volatile evolution in these mesostasis regions is equally distinct, and as such, detailed petrographic information of apatite surroundings should be collected when conducting apatite analysis. In general, the mesostasis melts are elevated in SiO_2, slightly enriched in alkali elements, and contain varying amounts of TiO_2 and FeO. The bulk-mesostasis compositions calculated here may also be used to guide future experimental work on apatite-melt volatile partitioning under lunar conditions.

2.7 Acknowledgements

We wish to thank Tim Fagan and Steve Elardo for their helpful comments and suggestions, and Randy Korotev for his editorial handling of the manuscript. We thank NASA CAPTEM for allocation of Apollo samples to MA. This work was funded by an STFC Studentship awarded to NJP and research grant to MA (Grant no. ST/I001298/1). The Paneth Trust for Meteorite Research is thanked for a bursary

awarded to MA, which funded AAG for a summer internship at the Open University. Jesse Davenport is thanked for assistance with SPICEs modeling and Jessica Barnes is thanked for helpful comments on the manuscript.

Chapter 3

An empirical model to estimate the volatile contents (F, Cl, H_2O) of lunar melts using measured volatile abundances in apatite

Nicola J. Potts[1,2,3*], Wim van Westrenen[2], Romain Tartése[1,4], Ian A. Franchi[1], Jessica J. Barnes[1,*], Mahesh Anand[1,5]

[1]Planetary & Space Science, The Open University, Walton Hall, Milton Keynes, MK7 6AA, UK
[2]Faculty of Earth & Life Sciences, Vrije Universiteit Amsterdam, 1081 HV Amsterdam, NL
[3]School of GeoSciences, Kings Buildings, University of Edinburgh, Edinburgh, EH9 3JW, UK
[4]Institut de Minralogie, de Physique des Matriaux et de Cosmochimie, Musum National dHistoire Naturelle, Sorbonne Universits, CNRS, UPMC & IRD, 75005 Paris, France
[5]Department of Earth Sciences, The Natural History Museum, London, SW7 5BD, UK

This chapter is a revised version of a manuscript originally submitted to *American Mineralogist*.

ABSTRACT

Apatite is the main volatile-bearing phase in lunar samples and is common throughout most of the lunar rock collection, making it an ideal candidate to serve as a proxy to reconstruct the volatile content of the interior of the Moon. Translating measurements of hydroxyl, fluorine, and chlorine in apatite to volatile abundances in the parent melt, however, remains a major challenge. In this study, high-pressure experiments were performed to quantify apatite-silicate melt volatile partitioning using, for the first time, silicate melt compositions that are similar to those from which lunar apatite crystallizes. Fluorapatite was equilibrated with silicate melt to constrain the partitioning of added volatiles. Melt and apatite volatile (F, Cl and H_2O) contents were measured by ion microprobe analysis. In experiments, run at temperatures between 1350 and 1500 °C and at a pressure of 1 GPa, we obtained a range of apatite-melt D_{OH} values between 0.26 ± 0.004 and 1.00 ± 0.009, D_{Cl} between 0.23 ± 0.020 and 8.00 ± 0.002, and D_F from 1.80 ± 0.062 to 7.70 ± 0.039. The calculated K_D^{F-OH} values range between 2.8 ± 0.063 and 11.9 ± 0.040, K_D^{F-Cl} values between 0.4 ± 0.7 and 7.9 ± 0.1, K_D^{Cl-OH} values between 0.4 ± 0.02 and 10.5 ± 0.01. Our results confirm that apatite with similar F, Cl, and H_2O contents can crystallize from silicate melts with variable H_2O contents, and show that significant amounts of H_2O can be partitioned into apatite while F is still available in the melt. Combining results from this study with literature data allows for new empirical predictive models to be constrained. These models relate the F, Cl, or H_2O contents of melts from which apatite crystallizes to the volatile contents of apatite. Applying our model to literature data for lunar apatite we calculate up to 5 wt.% F, 5.3 wt.% Cl, and 3.6 wt.% H_2O present in the melt during apatite formation. Further experiments encompassing a larger range of melt H_2O contents are recommended to refine this model. In addition, future measurements aimed at constraining lunar melt water contents using apatite should be focused on measuring at least both water and chlorine contents, with limited value for measurements focusing on water only.

3.1 Introduction

Many recent investigations into the presence and abundance of indigenous lunar volatiles (F, Cl, and hydrogen) have focused on the mineral apatite [$Ca_5(PO_4)_3$(F,Cl,OH)] as it contains volatiles as major constituents in its crystal structure and is ubiquitous in a wide range of lunar samples. Measurements of apatite F, Cl, and hydrogen abundances, as well as H and Cl isotopic compositions, have been made on a large suite of lunar rocks; including mare and KREEP basalts (Barnes et al., 2013, 2016; Boyce et al., 2010, 2015; Greenwood et al., 2011; McCubbin et al., 2011, 2010a,b; Sharp et al., 2010b; Tartèse et al., 2013a, 2014b), highland rocks (Barnes et al., 2015, 2014; Robinson et al., 2016; Treiman et al., 2014), and brecciated meteorites (Tartèse et al., 2014a). Calculating the volatile abundances in the silicate melts from which apatite crystallized, based on apatite volatile contents, however, has proven difficult. This is because variations in the extent to which F, Cl and hydrogen partition into apatite as a function of intrinsic variables including pressure, temperature, apatite and melt composition, and oxygen fugacity, remain poorly constrained for lunar conditions. Previous, terrestrial-focused, experimental studies on F, Cl, and hydrogen partitioning between apatite and silicate melt have attempted to tackle this issue using various approaches, such as constraining the thermodynamics (Candela, 1986), structure (Fleet et al., 2000; Hughes and Cameron, 1989; Hughes et al., 1990; Pan and Fleet, 2002) or free energy of the apatite system (Duff, 1972; Hovis and Harlov, 2010; Hovis et al., 2014), assessing diffusion during F, Cl, and OH exchange (Brenan, 1993b), and determining the distribution of F, Cl, OH (Edgar and Pizzolato, 1995) in apatite. Many studies have focused on partitioning within chlorapatite systems (Brenan, 1993a; Doherty et al., 2014; Konzett et al., 2011; Kusebauch et al., 2015; Li et al., 2015; Mathez and Webster, 2005; Webster et al., 2009) or have focused on rare earth element (REE) partitioning into apatite (Fleet, 1995; Jolliff et al., 1993; Prowatke and Klemme, 2006; Watson, 1979; Watson and Green, 1981), with only one recent study looking at volatile partitioning in some F-rich apatite (McCubbin et al., 2015a).). In most lunar basalts, apatite are Cl-poor and have volatile compositions extending along the F-OH join of the F-Cl-OH apatite ternary diagram, with the majority of apatite compositions clustering close to the fluorapatite end-member (e.g. McCubbin et al., 2015a). Experimental studies focused on chlorapatite may, therefore, not be directly applicable to lunar basaltic systems given the structural differences between the F-rich and Cl-rich apatite end-members (Hughes and Rakovan, 2002). Some hydrogen-rich apatite, containing the equivalent of 1.7 wt.% H_2O, have been reported from the brecciated portion of lunar meteorite Northwest Africa (NWA) 773 (Tartèse et al., 2014a) but these remain uncommon in the majority of lunar samples investigated to date. Synthesizing fluorapatite has been a lower priority in experimental investigations, with no study focused on detailing F, Cl, OH partitioning in F-rich apatite, although recent investigations have started to characterize thermodynamic mixing along the F-OH binary (Hovis et al., 2014).

Previous experimental investigations of volatile partitioning between apatite-melt have mostly used bulk basaltic compositions (Mathez and Webster 2005; Prowatke and Klemme 2006; McCubbin et al. 2015a). Apatite, however, does not reach saturation until ∼95 % melt crystallization in lunar basaltic magmas and ∼85 % melt crystallization in case of KREEP-rich basalts (Tartèse et al., 2014b). The crystalliza-

tion of major silicate and oxide phases in lunar basaltic magmas produces late-stage liquids chemically distinct from the initial basaltic melt, reflected by notably higher silica contents (Chapter 2; Pernet-Fisher et al. 2014) This is important as (i) apatite saturation is known to vary with melt SiO_2 and CaO contents (Bea et al., 1992; Harrison and Bruce, 1984; Tollari et al., 2006) and (ii) experiments on terrestrial apatite have shown that apatite/melt partitioning of trace elements varies with silicate melt composition (Mathez and Webster, 2005; Prowatke and Klemme, 2006; Watson and Green, 1981).

The dependency of F-Cl-OH partitioning, between apatite and silicate melt, on the relative abundances of these three volatile species in the melt was highlighted in a recent study by Boyce et al. (2014). These authors argued that F-Cl-OH partitioning into apatite is primarily a function of their availability in the melt from which apatite crystallizes, and that simple Nernst partition coefficients (D) are not applicable to apatite/melt systems. The observation that the apatite X site, containing F, Cl and OH, needs to be stoichiometrically filled (Candela, 1986) also suggests the unsuitability of using Nernstian D values in apatite-melt partitioning studies. An experimental study by McCubbin et al. (2015a) using a Martian meteorite bulk composition showed that D values were dependent on apatite volatile contents (which points to non-Nernstian behavior), and concluded that exchange coefficients (K_D) describing exchange between F and OH, Cl and OH, and F and Cl were much less variable.

At present, it is not clear to what extent partitioning of volatiles in apatite-melt systems vary as a function of pressure, temperature, melt composition, and oxygen fugacity. In this study, we present results of an experimental study aimed at improving such constraints for lunar apatite. We investigated the volatile contents of magmatic fluorapatite containing variable amounts of Cl and OH and co-existing silicate melt under lunar high-pressure, high-temperature conditions. Apatite crystals were grown from a silicate melt similar in composition to reconstructed melt compositions from mesostasis regions in which apatite is most commonly found in lunar basalts (Chapter 2). We compare our results with previous data and assess to what extent lunar apatite volatile contents can be used to accurately quantify the volatile content of the melts from which they formed.

3.2 Experimental methods

3.2.1 Starting materials

Starting materials were prepared by mixing appropriate amounts of high purity (99.5 –99.99 %, Alfa Aesar) powdered oxides and carbonates (Fe_2O_3, $CaCO_3$, Na_2CO_3, K_2CO_3, Al_2O_3, TiO_2, SiO_2), as well as CaF_2 and $Ca_3(PO_4)_2$. Al_2O_3, TiO_2, and SiO_2 were initially fired overnight at 1000 °C to remove any residual moisture before storage with the other oxides and the carbonates at 110 °C. The starting materials were mixed under ethanol in an agate mortar to promote homogeneity and left to air-dry overnight. The dry mixtures were then transferred to a Pt crucible and decarbonated in a box furnace by gradually raising the temperature from 650 °C to 900 °C, over a period of three hours. The mixtures were then removed from the furnace, which

was subsequently heated to 1580 °C. Once the furnace reached final temperature the mixtures were placed in the center of the box furnace for 60 minutes and subsequently quenched to a glass by immersing the bottom of the Pt crucibles in water.

Once cooled, the glasses were ground to a fine powder under ethanol in an agate mortar and air-dried. Small fragments of the glasses were separated to measure their bulk composition. CaF_2 and $Ca_3(PO_4)_2$ were subsequently added and mixed with the starting glasses under ethanol in an agate mortar without additional melting to prevent degassing of P and F. The resulting final starting materials (labeled L2a, L3a and L4a) were stored in powdered form at 110 °C, enabling nominally dry high-pressure experiments. A portion of the L2a starting material was stored in air at ambient temperature conditions to allow some water into the system (L2a OH). For Cl-bearing experiments NaCl was added to starting material without additional heating. A SiO_2-free mixture was made so that various proportions of SiO_2 and H_2SiO_3 could be added to a series of OH-bearing experiments.

3.2.2 Experimental methods

Experiments were conducted in an end-loaded Boyd and England type piston-cylinder (PC) at the Faculty of Earth and Life Sciences, Vrije Universiteit Amsterdam, using a 1/2 inch diameter talc-pyrex cell assembly. The pressure correction for this assembly was determined to be 3 % (van Kan Parker et al., 2011) in line with previous work (McDade et al., 2002). For each experiment a hand-machined graphite bucket, with an inside diameter (ID) of 0.7 mm, an outside diameter (OD) of 1.7 mm and a length of ∼3 mm was filled with starting material powder under a binocular microscope. A graphite lid of ∼1 mm in length was made to close the bucket. The closed graphite bucket was inserted into a Pt capsule, with an ID of 1.7 mm, an OD of 2 mm, and a length of ∼8 to 9 mm. The Pt capsule was closed at one end with a triple crimp, then welded shut and flattened. After insertion of the graphite bucket in the Pt capsule, the other extremity was also crimped and welded shut and placed in an alumina inner tube. Graphite-lined Pt capsules impose an oxygen fugacity (fO_2) close to the C-CO buffer of IW +1.5 at 1360 °C and 1.5 GPa (where IW ± X is the value of fO_2 relative to the iron-wüstite buffer in log10 units at a given temperature), as reported by Medard et al. (2008). The oxygen fugacity of the lunar interior is thought to vary from ∼ IW -2.5 to IW (Wadhwa, 2008), with more reduced estimates made for lunar glass beads (Karner et al., 2006; Krawczynski and Grove, 2012) and the more oxidized estimates for lunar basalts (Haggerty and Meyer, 1970; Sato, 1976). Low fO_2 ensures that Fe is dominantly in the Fe^{2+} valence state and that the fH_2/fH_2O ratio of the experimental liquids lies in the parameter space applicable to lunar basalts (Zhang, 2011). $H_2/(H_2+H_2O)$ solubility, however, varies as a function of fO_2 with a difference of 20 % between IW and IW-2 at 1 GPa (Hirschmann et al., 2012). Although, $H_2/(H_2+H_2O)$ solubility shows a greater dependence on H content of the melt (∼24 % difference across the range of water compositions in our experiments) than on fO_2. As the H contents of lunar melts are poorly constrained this remains an unknown parameter in any experimental study applicable to lunar apatite. As all H-species are measured in this study we do not consider H-speciation further but argue that the fO_2 of our experiments provides a good first order investigation into apatite-melt volatile

partitioning under relatively reducing conditions.

A $W_{97}Re_3$ –$W_{75}Re_{25}$ (type D) thermocouple was inserted axially into the talc-pyrex assembly using four-bore high purity alumina tubing to measure the sample temperature (T), which was controlled with a Eurotherm 2404 controller with a resulting T uncertainty of ± 3 °C. The sample was placed in the hotspot of the assembly, ∼2 mm from the thermocouple tip end, shown to be 10 °C from the thermocouple reading (Watson et al., 2002). The runs were performed at a pressure of 1 GPa using a hot piston-in technique (McDade et al., 2002). Samples were initially heated to 1500 or 1550 °C at 100 °C/minute. The pressure (P) was initially kept low, at ∼300 psi, until a temperature of approximately 700 °C was reached. P was then gradually raised to ∼715 psi (equivalent to the target sample pressure of 1 GPa) during further heating. The samples dwelled at their maximum temperature for ten minutes before being cooled (at a rate of 50 °C/hour, following Prowatke and Klemme (2006)) to final temperatures of 1500 °C, 1450 °C, 1400 °C, and 1350 °C after which the experiments were left to dwell for between 7 and 72 hours. The runs were quenched by turning off the power to the furnace. Experimental temperatures were higher than experienced by lunar apatite —our focus was on performing experiments in chemical systems of relevance to the Moon, rather than performing experiments at appropriate temperatures. This is a common approach in mineral-melt partitioning studies.

3.3 Analytical methods

3.3.1 Sample imaging

Starting material glasses and experimental run products were mounted in Epo-Cure resin, chosen for its low volatile content and, therefore, low background signal during volatile abundance analyses. After grinding and polishing, the samples were carbon coated for imaging using the Open University FEI Quanta 3D dual beam Secondary Electron Microscope (SEM), fitted with an Oxford Instruments 80 mm X-MAC energy dispersive X-ray detector. Back-scattered electron (BSE) and secondary electron (SE) images were acquired using a 20 kV accelerating voltage and 0.6 nA beam current to identify areas within apatite grains that were clean and crack-free for NanoSIMS analysis. Selected grains were further examined using short-exposure energy dispersive spectroscopy (EDS) to confirm that they were apatite and not merrillite/whitlockite.

3.3.2 NanoSIMS analysis

Following SEM imaging, the carbon coat was removed with isopropanol, and the samples were further cleaned in isopropanol for ten minutes in an ultrasonic bath and dried in a vacuum oven at ∼55 °C for ∼48 hours. Samples were subsequently coated with ∼30 nm of gold using an EMITECH K575X Peltier cooled gold sputter coat and immediately transferred into the Cameca NanoSIMS 50L at The Open University. Before analysis, a large ∼700 pA Cs^+ primary beam was rastered over selected

20 × 20 m target areas during a one minute pre-sputter. After pre-sputtering, clean, crack-free apatite and glass areas were identified using real time imaging (RTI) of F and P secondary ions. Once suitable apatite and glass areas were identified, 8 × 8 μm areas were further rastered using a 110 pA beam for one minute. Secondary ions of $^{16}O^{1}H$, ^{18}O, ^{28}Si, ^{19}F, ^{31}P, and ^{35}Cl were then collected simultaneously during ∼3 minutes from the central 2 × 2 μm area of 4 × 4 μm areas using a beam current of 30 pA. An electron gun was used for charge compensation. The mass-resolving power was set to ∼6000, sufficient to resolve isobaric interferences between $^{16}O^{1}H$ and ^{17}O. During analysis the vacuum in the analysis chamber remained around 2.5×10^{-9} torr (3.4×10^{-7} Pa). The F, Cl, and OH abundances of the analyzed apatite grains were calibrated using the measured $^{19}F/^{18}O$, $^{35}Cl/^{18}O$, and $^{16}O^{1}H/^{18}O$ ratios on apatite standards with known volatile abundances (Ap.004, Ap.005, Ap.018, Ap.020; McCubbin et al., 2012). We used repeat analysis of the nominally anhydrous San Carlos olivine to quantify background corrections for F, Cl and OH abundances. We used the same procedure for glass analysis using NIST612, RLS132 (a natural obsidian from Tulancingo, Mexico) and Macusani glasses for volatile abundance calibrations (Jochum et al., 2011; MacDonald et al., 2010; Pichavant et al., 1987).

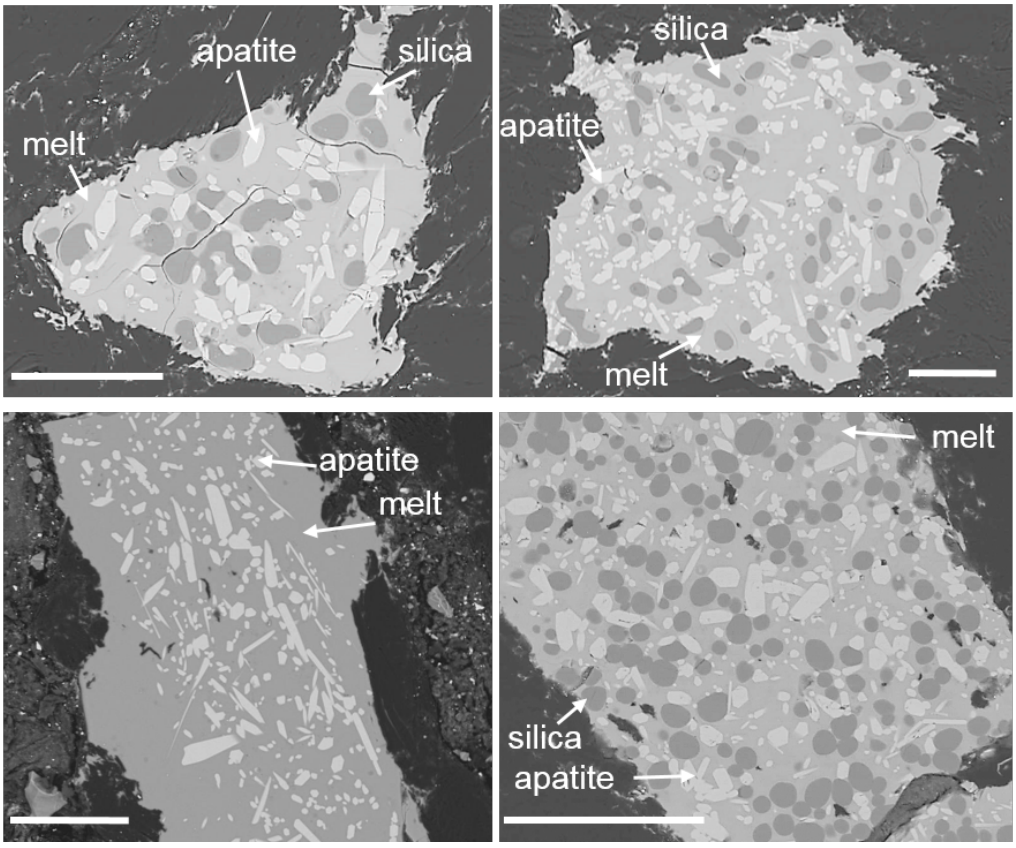

Figure 3.1: Representative back-scattered electron (BSE) images of experiments performed with the L2a and L3a compositions (see text). Number in each sample label refers to temperature in degrees Celsius. (A) L2aOH 1350; (B) L2aOH 1450; (C) L3a Cl 1450; (D) L2a 1450. In each image sample is surrounded by graphite (black), melt is light grey, apatite is lighest grey/white, and silica is dark grey.

3.3.3 Electron microporbe analysis (EPMA)

In order not to compromise volatile abundances in apatite and glass, which can be altered due to interactions with high current electron beams (e.g. Stock et al., 2014), we performed electron probe microanalysis (EPMA) after NanoSIMS analyses. After removal of the gold-coat using 0.25 μm diamond paste, the samples were cleaned and then carbon coated for EPMA analysis. Glasses and crystals were analyzed for major oxide abundances using The Open University Cameca SX 100 electron microprobe. For apatite measurements, we modified slightly the procedure given in Goldoff et al. (2012), as described by Tartèse et al. (2013a), and used an acceleration voltage of 10 kV with a beam current of 4 nA and a 2 μm spot size. EPMA analyses were calibrated against primary standards, including standardization of F using a SrF_2 crystal, and of Cl using a tugtupite crystal, and then were checked against the secondary standards Durango for apatite (Jarosewich et al., 1980; McCubbin et al., 2012) and obsidian RLS132 for glass (MacDonald et al., 2010). For glass analyses, an accelerating voltage of 20 kV and a beam current of 20 nA were used with a beam diameter of 10 μm. Standard count rates of 20 s per element were used, with a background counting time of half the peak counting time before and after peak analysis. Natural standards of feldspar (Si, Al, K), jadeite (Na), hematite (Fe), rutile (Ti), and apatite (P) were used for calibration of major elements. Note that Na should also have been measured but wasn't possible during analytical sessions.

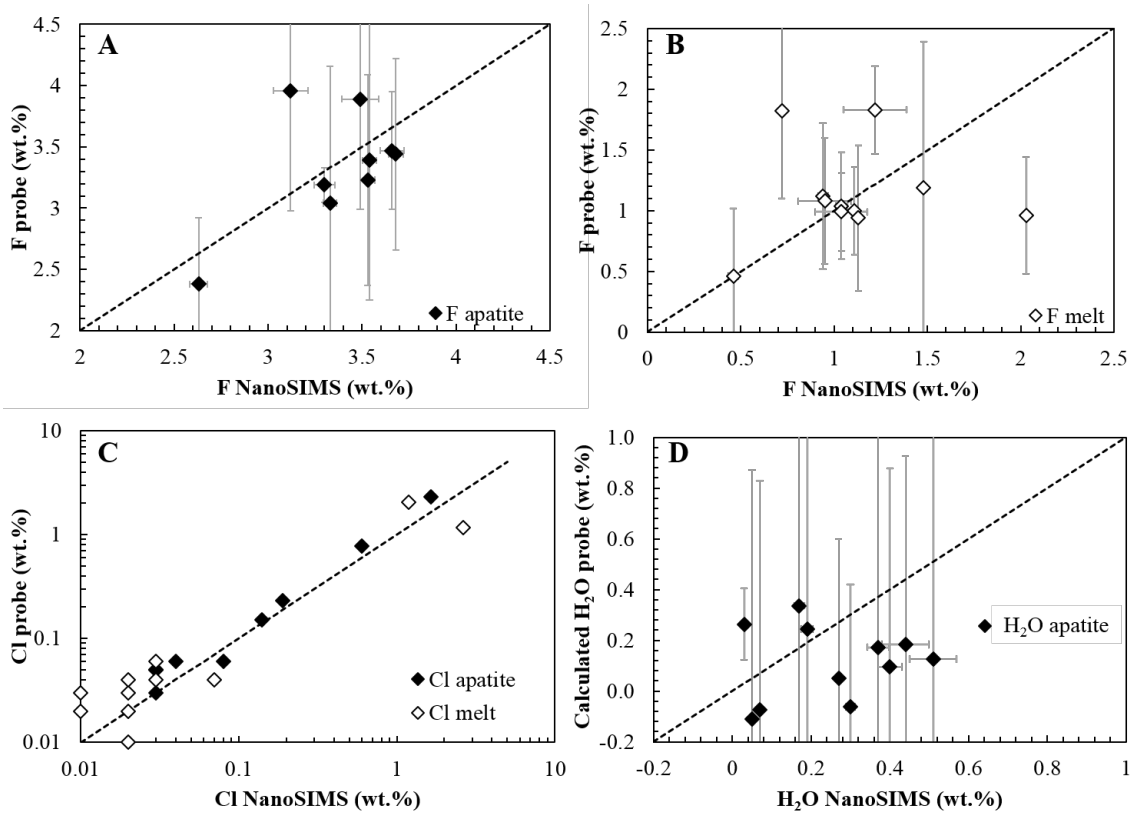

Figure 3.2: Comparison between EPMA and NanoSIMS measurements for (A) F in apatite, (B) F in melt, (C) Cl in apatite and melt, and (D) H_2O in apatite calculated by difference for EPMA. Dotted lines show 1:1 relationships as a guideline.

3.4 Results

3.4.1 Starting compositions

Experiments were run using three starting compositions, L2a, L3a, and L4a, each mixture containing the same ratio of CaF_2 to $Ca_3(PO_4)_2$. The major element composition of the different starting materials obtained from EPMA analyses is given in Table 3.1. The L2a and L3a compositions are almost identical, except for lower Na_2O and K_2O in L2a (0.37 and 0.03 wt.%, respectively) compared to L3a (0.8 and 1.8 wt.%, respectively). Additional Cl was added as NaCl to the L3a composition for Cl-bearing experiments (L3a Cl, Table 3.1). The L4a composition was prepared as an initially SiO_2-free version of L3a so that varying amounts of H_2SiO_3 + SiO_2 could later be added to conduct water-bearing experiments. The quantities of H_2SiO_3 + SiO_2 added to the L4a experiments are also given in Table 3.1. The bulk starting compositions have a dacitic composition, similar to composition of the majority of bulk mesostasis areas from which lunar apatite grows in lunar mare basalts (Chapter 2).

3.4.2 Textural descriptions

Representative BSE images of experiments are shown in Figure 3.1. In each experiment, we observed apatite and quenched silicate melt. In addition, crystalline silica formed in some experiments (Figure 3.1). In experiments run at low temperature ($\sim$1300 °C) and nominally dry conditions, apatite grains and glassy melt pools were very small, $<\sim$2 m in diameter. Such small phases are not measurable even using the NanoSIMS and these experiments are, therefore, not discussed further. Texturally, the remaining experiments are very similar, containing a primary generation of large euhedral apatite grains. In some experiments a second generation of smaller, needle-shape euhedral apatite grains was observed in the melt phase, likely formed during quenching of the experimental charges (Figure 3.1D). When present in the mineral assemblage, the silica phase is crystalline SiO_2, as indicated by Raman analysis, and forms rounded grains.

3.4.3 Apatite and melt compositions

The major element compositions of apatite crystals and co-existing melts are given in Tables 3.3 and 3.4, respectively. Low standard deviations on averaged compositions attest to the homogeneity of both apatite and melt phases, suggesting equilibrium conditions. All the melts in these experiments range between dacitic and basaltic-andesitic, with SiO_2 contents ranging between 52.8 and 66.2 wt.%, Al_2O_3 concentrations between 9.1 and 14.6 wt.%, and K_2O between 0.3 and 2.2 wt.%. In the majority of experiments melts have Na_2O contents between 1.4 and 2.5 wt.%, except for the Cl-rich experiments, in which NaCl was added, increasing the final melt Na_2O contents to 7.4 and 12.7 wt.%.

The TiO_2 contents of the melt, in all experiments, range from 2.1 to 3.5 wt.%, while the CaO contents range between 8.1 and 13.5 wt.%. The largest variation in melt concentration (apart from those with additional NaCl) is observed for FeO, which

	L2a		L3a		L3a Cl1		L3a Cl2		L4a OH1	L4a OH2	L4a OH3
SiO_2	68.61	*2.33*	66.7	*2.64*	66.7	*2.64*	66.7	*2.64*	62.5	62.5	62.5
TiO_2	2.15	*0.56*	2.44	*0.19*	2.44	*0.19*	2.44	*0.19*	2.5	2.5	2.5
Al_2O_3	8.43	*0.85*	10	*0.83*	10	*0.83*	10	*0.83*	9.5	9.5	9.5
Na_2O_3	0.37	*0.03*	0.83	*0.09*	0.83	*0.09*	0.83	*0.09*	0.8	0.8	0.8
K_2O	0.03	*0.01*	1.85	*0.09*	1.85	*0.09*	1.85	*0.09*	0.2	0.2	0.2
CaO	8.99	*0.72*	8.26	*0.73*	8.26	*0.73*	8.26	*0.73*	8	8	8
P_2O_5	3.2	*0.27*	2.96	*0.52*	2.96	*0.52*	2.96	*0.52*	3	3	3
FeO	6.2	*0.44*	5.78	*0.49*	5.78	*0.49*	5.78	*0.49*	6	6	6
Total	98		98.8		98.8		98.8		92.5	92.5	92.5
SM	77		77		69		66		32	28	19
FAp	23		23		21		20		4	3	3
NaCl	-		-		11		14		-	-	-
H_2SiO_3	-		-		-		-		23	37	55
SiO_2	-		-		-		-		41	32	23

Table 3.1: Major element composition of starting materials (in wt.%), and percentage of starting material, F_{Ap} (with F_{Ap} containing equal amounts by weight of CaF_2 and $Ca_3(PO_4)_2$), NaCl, H_2SiO_3 and SiO_2 added to seed apatite growth for each experiment. Numbers in brackets refer to standard deviation on measurements. †Nominal values for L4a.

Sample name	**Starting material**	**Starting T (C)**	**Run T (C)**	**Ramp (C/hr)**	**Run duration at final T (hr)**	**Crystal shape**	**Phases present**	**Size (m)**
L2a 1350	L2a	1550	1350	50	24	euhedral + acicular	ap + si + gl	30 × 20
L2a 1400	L2a	1550	1400	50	24	euhedral + acicular	ap + si + gl	100 × 30
L2a 1450	L2a	1550	1450	50	24	euhedral	ap + si + gl	30 × 20
L2a 1450 72	L2a	1550	1450	50	72	euhedral + acicular	ap + si + gl	50 × 20
L2a OH 1350	L2a	1550	1350	50	24	euhedral	ap + si + gl	60 × 20
L2a OH 1450	L2a	1550	1450	50	24	euhedral	ap + si + gl	60 × 20
L3a 1400	L3a	1500	1400	50	24	euhedral	ap + si + gl	50 × 20
L3a 1450	L3a	1500	1450	50	24	euhedral + acicular	ap + si + gl	50 × 20
L3a Cl 1	L3a	1500	1450	50	24	euhedral	ap + gl	70 × 20
L3a Cl 2	L3a	1500	1350	50	24	euhedral + acicular	ap + gl	20 × 10
L4a OH1	L4a	1500	1450	50	24	euhedral	ap + gl	50 × 20
L4a OH2	L4a	1500	1450	50	24	euhedral	ap + gl	50 × 20
L4a OH3	L4a	1500	1450	50	24	euhedral + acicular	ap + gl	50 × 20

Table 3.2: Experimental run conditions. All experiments run at 1 GPa. Ap. = apatite, si. = silica, gl. = glass. Crystal shape and size relate specifically to apatite grains only. Size is average of the larger generation of apatite.

	L2a 1350		L2a 1450		L2a OH 1350		L2a OH 1450		L3a 1400		L3a 1450	
Apatite												
n	*5*		*4*		*5*		*5*		*4*		*4*	
SiO_2	1.62	*0.59*	1.23	*0.46*	1.7	*0.75*	0.36	*0.31*	0.09	*0.01*	0.11	*0.04*
TiO_2	0.11	*0.01*	0.07	*0.02*	0.06	*0.11*	0.04	*0.03*	0.03	*0.02*	0.05	*0.02*
CaO	52.64	*0.04*	52.1	*0.1*	52.79	*0.1*	53.37	*0.36*	55.8	*0.17*	54.32	*0.23*
P_2O_5	41.79	*0.32*	42.23	*0.45*	40.14	*1.15*	41.89	*0.73*	42.12	*0.18*	42.65	*0.16*
FeO	0.97	*0.01*	0.93	*0.03*	0.87	*0.1*	0.74	*0.02*	0.98	*0.04*	0.96	*0.04*
MgO	0.06	*0.01*	0.06	*0.01*	0.09	*0.01*	0.09	*0.01*	0.01	*0.02*	0.02	*0.02*
F	3.04	*0.56*	3.23	*0.43*	3.39	*0.57*	3.44	*0.39*	3.96	*0.49*	3.89	*0.45*
Cl	0.05	*0.01*	0.05	*0.01*	0.03	*0.01*	0.23	*0.01*	0.06	*0.01*	0.05	*0.01*
-O=F	1.28		1.36		1.43		1.45		1.67		1.64	
-O=Cl	0.01		0.01		0.01		0.05		0.01		0.01	
Total	98.99		98.53		97.64		98.66		101.37		100.4	
Structural formulae based on 13 anions												
Si	0.5		0.4		0.6		0.1		0		0	
Ti	0		0		0		0		0		0	
Ca	4.6		4.6		4.7		4.7		4.8		4.7	
P	2.9		2.9		2.8		2.9		2.9		2.9	
Fe	0.1		0.1		0.1		0.1		0.1		0.1	
Mg	0		0		0		0		0		0	
Σ cations	8.1		8		8.2		7.8		7.7		7.7	
F	0.8		0.8		0.9		0.9		1		1	
Cl	0.007		0.007		0.004		0.032		0.008		0.007	
Σ anions	0.8		0.8		0.9		0.9		1		1	
OH	0.21		0.16		0.11		0.08		-0.01		0.01	

Table 3.3: Average apatite major element compositions including F and Cl contents, in wt%, measured by EPMA. *n* refers to the number of analyses.

	L3a Cl 1450		L3a 1350		L4a OH1		L4a OH2		L4a OH3	
Apatite										
n	*5*		*4*		*5*		*5*		*4*	
SiO_2	0.18	*0.06*	2.05	*1.23*	0.22	*0.09*	0.55	*0.34*	0.23	*0.09*
TiO_2	0.01	*0.02*	0.09	*0.04*	0.03	*0.01*	0.07	*0.02*	0.04	*0.02*
CaO	53.31	*0.24*	50.84	*0.48*	53.81	*0.12*	53.72	*0.12*	54.02	*0.18*
P_2O_2	42.27	*0.18*	40.68	*0.03*	42.38	*0.06*	42.56	*0.06*	42.31	*0.14*
FeO	0.18	*0.01*	0.02	*0*	0.87	*0.02*	0.73	*0.02*	0.38	*0.03*
MgO	0.04	*0.01*	0	*0*	0.06	*0.02*	0.07	*0.01*	0.14	*0.02*
F	3.47	*0.24*	2.38	*0.27*	3.19	*0.07*	3.35	*0.37*	3.42	*0.65*
Cl	0.77	*0.02*	2.32	*0.05*	0.05	*0.01*	0.06	*0.01*	0.15	*0.01*
-O=F	1.46		1		1.34		1.41		1.44	
-O=Cl	0.18		0.53		0.01		0.01		0.03	
Total	98.59		96.85		99.26		99.69		99.22	
Structural formulae based on 13 anions										
Si	0.1		0.7		0.1		0.2		0.1	
Ti	0		0		0		0		0	
Ca	4.7		4.5		4.7		4.7		4.7	
P	2.9		2.9		2.9		2.9		2.9	
Fe	0		0		0.1		0		0	
Mg	0		0		0		0		0	
Σ cations	7.7		8.1		7.8		7.8		7.8	
F	0.9		0.6		0.8		0.9		0.9	
Cl	0.106		0.327		0.007		0.008		0.021	
Σ anions	1		1		0.8		0.9		0.9	
OH	0		0.05		0.17		0.13		0.1	

Table 3.3 cont.

	L2a 1350		L2a 1450		L2a OH 1350		L2a OH 1450		L3a 1400		L3a 1450	
Melt												
n	*7*		*3*		*6*		*4*		*5*		*5*	
SiO_2	52.75	*1.3*	54.45	*0.97*	60.17	*0.67*	61.77	*0.47*	63.04	*1.08*	61.06	*1.43*
TiO_2	3.43	*0.11*	3.51	*0.07*	3.05	*0.02*	3.49	*0.05*	2.38	*0.02*	2.69	*0.02*
Al_2O_3	14.62	*0.17*	14.78	*0.37*	13.12	*0.31*	11.14	*0.09*	9.65	*0.37*	10.51	*0.34*
Na_2O_3	2.11	*0.06*	2.07	*0.16*	2.46	*0.18*	2.39	*0.02*	1.51	*0.02*	1.76	*0.1*
K_2O	0.3	*0.02*	0.28	*0.03*	0.32	*0.01*	0.39	*0.01*	2	*0.09*	2.19	*0.08*
CaO	13.54	*1.6*	11.59	*0.48*	10.69	*0.12*	11.22	*0.12*	9.84	*1.4*	10.2	*2.21*
P_2O_5	4.38	*1.39*	2.14	*0.37*	2.43	*0.05*	3.49	*0.05*	2.93	*1.1*	2.63	*1.72*
FeO	7.44	*0.4*	7.56	*0.37*	5.51	*0.17*	4.82	*0.17*	5.61	*0.15*	6.89	*0.14*
MgO	0.13	*0.01*	0.12	*0.48*	0.19	*0.01*	0.17	*0.01*	0.08	*0.02*	0.12	*0.01*
F	1.83	*0.09*	1.19	*0.3*	0.46	*0.14*	1.12	*0.15*	1	*0.09*	0.94	*0.15*
Cl	0.06	*0.01*	0.04	*0*	0.02	*0.02*	0.04	*0*	0.03	*0*	0.04	*0.01*
-O=F	0.77	*0.04*	0.5	*0.13*	0.19	*0.06*	0.47	*0.06*	0.42	*0.04*	0.4	*0.06*
-O=Cl	0.01	*0*	0.01	*0*	0	*0*	0.01	*0*	0.01	*0*	0.01	*0*
Total	99.81		97.22		98.22		99.56		97.64		98.63	

Table 3.4: Average major-element compositions of the melt in wt.%. F and Cl contents are those measured by EPMA. *n* refers to the number of analyses. All values in weight percent.

	L3a Cl1 1450		L3a Cl2 1350		L4a OH1		L4a OH2		L4a OH3	
Melt										
n	*8*		*10*		*5*		*6*		*5*	
SiO_2	66.23	*2.06*	59.26	*0.53*	58.72	*0.11*	63.26	*0.56*	65.11	*0.26*
TiO_2	2.3	*0.05*	2.07	*0.12*	2.98	*0.06*	3	*0.08*	2.79	*0.15*
Al_2O_3	10.18	*0.33*	9.08	*0.16*	12.6	*0.04*	12.29	*0.08*	11.73	*0.18*
Na_2O_3	7.4	*0.49*	12.66	*0.48*	2.67	*0.14*	1.95	*0.1*	1.56	*0.05*
K_2O	0.82	*0.02*	0.92	*0.01*	0.63	*0*	0.74	*0.01*	0.68	*0.01*
CaO	8.06	*1.31*	8.76	*0.36*	11.75	*0.17*	9.98	*0.21*	11.01	*0.11*
P_2O_5	4.57	*1.23*	3.47	*0.25*	4.81	*0.05*	2.61	*0.29*	2.88	*0.25*
FeO	0.11	*0.03*	2.33	*0.09*	5.39	*0.09*	4.21	*0.22*	1.96	*0.2*
MgO	0.11	*0.01*	0.1	*0.01*	0.1	*0.01*	0.1	*0*	0.33	*0.04*
F	0.96	*0.12*	1.82	*0.18*	1.04	*0.11*	0.99	*0.08*	1.08	*0.13*
Cl	1.17	*0.08*	2.06	*0.12*	0.01	*0.02*	0.03	*0.01*	0.02	*0.02*
-O=F	0.4	*0.05*	0.77	*0.08*	0.44	*0.05*	0.42	*0.03*	0.45	*0.05*
-O=Cl	0.26	*0.02*	0.46	*0.03*	0	*0*	0.01	*0*	0	*0*
Total	101.24		101.3		100.26		98.74		98.69	

Table 3.4 cont.

	L2a 1350	**L2a 1400**	**L2a 1450**	**L2a 1450 72**	**L2a OH 1350**	**L2a OH 1450**	**L3a 1400**	**L3a 1450**	**L3a Cl1 1450**	**L3a Cl2 1350**	**L4a OH1**	**L4a OH2**	**L4a OH3**
T (°C)	1350	1400	1450	1450	1350	1450	1400	1450	1450	1350	1450	1450	1450
Apatite/n	*8*	*7*	*5*	*3*	*7*	*8*	*5*	*6*	*7*	*4*	*3*	*4*	5
H_2O	0.17	0.39	0.19	0.1	0.37	0.4	0.05	0.07	0.3	0.27	0.03	0.44	0.51
2σ	*0.013*	*0.029*	*0.014*	*0.004*	*0.028*	*0.03*	*0.002*	*0.004*	*0.011*	*0.009*	*0.002*	*0.06*	*0.059*
F	3.33	3.36	3.53	3.31	3.54	3.68	3.12	3.49	3.66	2.63	3.3	-	-
2σ	*0.035*	*0.036*	*0.038*	*0.055*	*0.037*	*0.039*	*0.093*	*0.099*	*0.062*	*0.046*	*0.056*	-	-
Cl	0.03	0.03	0.03	0.17	0.03	0.19	0.04	0.03	0.6	1.65	0.03	0.08	0.14
2σ	*0.002*	*0.002*	*0.002*	*0.003*	*0.001*	*0.01*	*0.006*	*0.005*	*0.011*	*0.033*	*0.001*	*0.002*	*0.005*
$\boldsymbol{X}_{H_2O}$	0.094	0.214	0.102	0.053	0.205	0.222	0.026	0.038	0.164	0.149	0.018	0.243	0.281
$\boldsymbol{X}_F$	0.884	0.892	0.937	0.879	0.94	0.977	0.828	0.926	0.972	0.698	0.879	0.889	0.908
$\boldsymbol{X}_{Cl}$	0.004	0.005	0.004	0.025	0.004	0.028	0.006	0.004	0.088	0.242	0.004	0.012	0.022
$\boldsymbol{X}_t$	0.98	1.11	1.04	0.96	1.15	1.23	0.86	0.97	1.22	1.09	0.9	1.14	1.21
Melt/n	*7*	*6*	*6*	*3*	*5*	*5*	*5*	*5*	*6*	*4*	*3*	*3*	*4*
H_2O	0.51	0.41	0.39	0.39	0.57	0.58	0.12	0.23	0.46	0.27	0.11	0.58	0.58
2σ	*0.17*	*0.036*	*0.021*	*0.007*	*0.027*	*0.027*	*0.007*	*0.013*	*0.007*	*0.004*	*0.032*	*0.14*	*0.141*
F	1.22	0.98	1.48	1.19	0.46	0.94	1.11	1.13	2.03	0.72	1.04	1.04	0.95
2σ	*0.122*	*0.098*	*0.148*	*0.012*	*0.046*	*0.094*	*0.212*	*0.216*	*0.021*	*0.007*	*0.041*	*0.004*	*0.004*
Cl	0.03	0.019	0.03	0.08	0.01	0.07	0.02	0.02	2.62	1.19	0.02	0.01	0.02
2σ	*0.001*	*0.001*	*0.001*	*0.003*	*0*	*0.002*	*0*	*0.001*	*0.093*	*0.043*	*0.001*	*0.001*	*0.001*

Table 3.5: Average volatile contents (wt.%) in apatite and surrounding glass measured by NanoSIMS. n = number of analyses. Stoichiometry for L4a OH2, and L4a OH3 were calculated using EPMA F abundance. X_F = [F]/3.767, X_{Cl} = [Cl]/6.809, X_{H_2O} = [H_2O]/1.81.

	D						K_D					
	D_{OH}	2σ	D_F	2σ	D_{Cl}	2σ	K_D^{F-OH}	2σ	K_D^{F-Cl}	2σ	K_D^{Cl-OH}	2σ
L2a 1350	0.33	*0.042*	2.73	*0.050*	1.00	*0.002*	8.2	*0.05*	2.7	*0.05*	3	*0.004*
L2a 1400	0.95	*0.030*	3.43	*0.046*	1.58	*0.002*	3.6	*0.05*	2.2	*0.05*	1.7	*0.003*
L2a 1450	0.49	*0.014*	2.39	*0.060*	1.00	*0.002*	4.9	*0.06*	2.4	*0.06*	2.1	*0.002*
L2a 1450 72	0.26	*0.004*	2.78	*0.055*	2.13	*0.003*	10.8	*0.06*	1.3	*0.06*	8.3	*0.003*
L2a OH 1350	0.65	*0.029*	7.7	*0.039*	3.00	*0.001*	11.9	*0.04*	2.6	*0.04*	4.6	*0.002*
L2a OH 1450	0.69	*0.031*	3.91	*0.048*	2.71	*0.010*	5.7	*0.05*	1.4	*0.05*	3.9	*0.011*
L3a 1400	0.42	*0.002*	2.81	*0.138*	2.00	*0.006*	6.7	*0.14*	1.4	*0.14*	4.8	*0.006*
L3a 1450	0.3	*0.004*	3.09	*0.146*	1.50	*0.005*	10.1	*0.15*	2.1	*0.15*	4.9	*0.005*
L3a Cl1 1450	0.65	*0.011*	1.8	*0.062*	0.23	*0.020*	2.8	*0.06*	7.9	*0.06*	0.4	*0.020*
L3a Cl2 1350	1.00	*0.009*	3.65	*0.046*	1.39	*0.035*	3.7	*0.05*	2.6	*0.05*	1.4	*0.035*
L4a OH1	0.27	*0.003*	3.17	*0.058*	1.50	*0.001*	11.6	*0.06*	2.1	*0.06*	5.5	*0.001*
L4a OH2	0.76	*0.080*	3.22	*0.740*	8.00	*0.002*	4.2	*0.75*	0.4	*0.74*	10.5	*0.008*
L4a OH3	0.88	*0.079*	3.6	*1.300*	7.00	*0.005*	4.1	*1.31*	0.5	*1.30*	8.0	*0.011*

Table 3.6: Partition coefficients (D) and exchange coefficients (K_D) for experiments from this study. 2σ relates to standard error propagation from analytical values.

varies from 0.1 to 7.6 wt.%. Lower FeO contents reflect some interaction with the Pt outer capsule occurred, leading to iron loss from this experiment. MgO contents were all <0.34 wt.%, consistent with MgO not having been added to our starting materials. Apatite contains between 50.8 and 55.8 wt.% CaO, and between 40.1 and 42.6 wt.% P_2O_5. The apatite grains have minor element abundances of 0.1 to 2.1 wt.% SiO_2, <0.11 wt.% TiO_2, <0.10 wt.% MgO, and FeO contents ranging from 0.02 to 0.98 wt.%. Again, apatite with the lowest FeO contents in experiment L3a Cl2 1350 (Table 3.1) is associated with the melt with the lowest FeO content (Table 3.4) that is thought to have lost Fe. Volatile contents in this one experiment were not anomalous (see below).

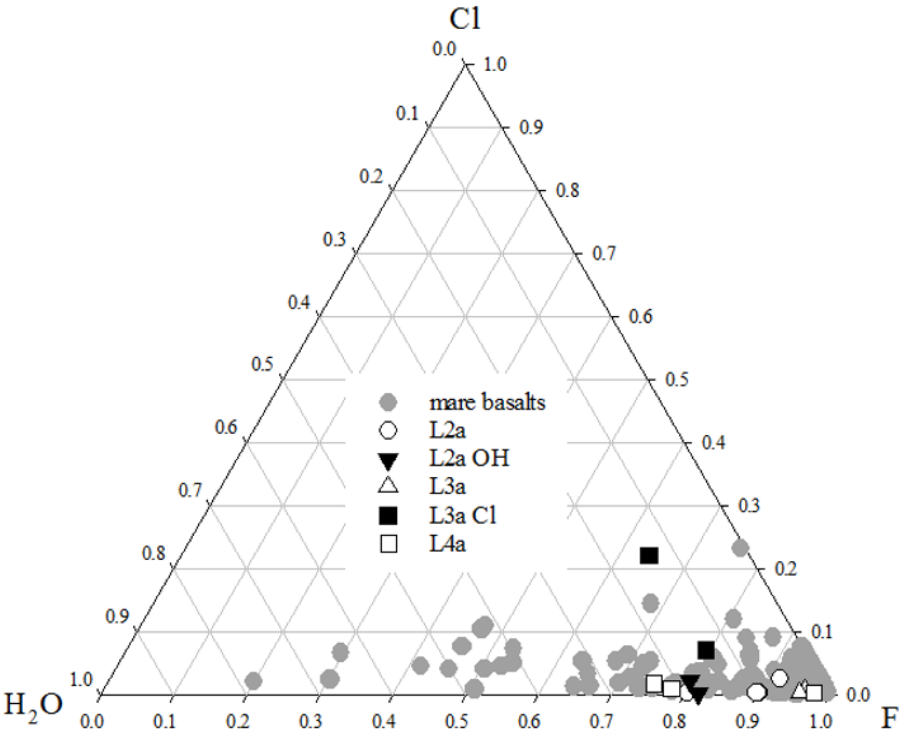

Figure 3.3: Normalized ternary plot of apatite X-site occupancy (mol.%, assuming F + Cl + OH = 100 %). Individual experiments from this study are plotted with black and white symbols that correspond to different bulk compositions as discussed in the main text. Literature data for apatite (plotted in grey for comparison) from mare basalts was taken from Barnes et al. (2016); Boyce et al. (2014); Greenwood et al. (2011); McCubbin et al. (2011, 2010a); Tartèse et al. (2013a).

3.4.4 Volatile contents of apatite and melt

Volatile abundance measurements with NanoSIMS were carried out on multiple grains and quenched melt pools within each experimental charge. Average NanoSIMS F, Cl and OH contents for apatite and glass are given in Table 3.5. In Table 3.5, hydrogen abundances are reported as equivalent amounts of H_2O in both apatite and melt, even though hydrogen could be present as H_2, OH, or H_2O species in the silicate melt (Silver and Stopler, 1985), and as OH in apatite. Figures 3.2a - c show a comparison of the F and Cl measurements by EPMA and NanoSIMS for both apatite and

melt phases. There is good agreement between the Cl contents measured in apatite by both methods (Figure 3.2c). There is also relatively good agreement between the Cl contents measured in melt phases and the F contents measured in both apatite and melt phases obtained by the two methods (Figures 3.2a - c). F abundances measured by EPMA in apatite from 2 experiments are unusually high (3.89 and 3.96 wt.%) and plot above the 1:1 line (Figure 3.2a). Although all EPMA data were obtained during the same analytical session, using the same standard calibrations, these values likely indicate an analytical problem during analysis of apatite in these two experiments. The volatile contents measured by NanoSIMS are more reproducible than those obtained by EPMA, as expressed by the lower standard deviations. Finally, Figure 3.2d illustrates that there is little agreement between H_2O concentrations in apatite calculated on the basis of Cl and F abundances measured by EPMA and stoichiometry considerations (as H_2O cannot be measured directly by EPMA), and H_2O abundances measured directly using the NanoSIMS. Two of the three experiments for which negative values were calculated for H_2O abundances in apatite based on EPMA analyses are those with the two anomalously high apatite F contents. This observation, combined with the larger standard deviations on F analyses by EPMA, suggests that our F measurements by EPMA are less precise than those obtained by NanoSIMS. We, therefore, use the apatite and melt volatile abundances determined using the NanoSIMS in the remainder of this paper, except for F abundances in apatites in experiments L4a OH2, and L4a OH3 as we were not able to obtain apatite F contents by NanoSIMS in these samples.

The volatile abundances of experimental apatites are represented in a ternary F-Cl-OH diagram in Figure 3.3. The F, Cl and H_2O abundances in apatite from our experiments range from 2.63 to 3.68 wt.%, 0.03 to 1.65 wt.% and 0.03 to 0.51 wt.%, respectively, while glasses contain 0.46 to 2.03 wt.% F, 0.01 to 2.62 wt.% Cl and 0.11 to 0.58 wt.% H_2O (Table 3.5). H_2O was present in measureable amounts in all apatite and melts including those from the L2a and L3a experiments that employed nominally dry starting materials. This indicates that truly H_2O-free high-pressure experiments are not feasible with our current experimental setup.

The total X-site occupancy (X_t) in our experimental apatite grains varies from 0.86 to 1.23 (Table 3.5). Previous apatite-melt partitioning experiments also report regular instances of apatite crystals with $X_t > 1$ (e.g. Prowatke and Klemme 2006; McCubbin et al. 2015a), and apatite with $X_t > 1$ has been recorded in natural terrestrial (Boyce and Hervig, 2008; Sarafian et al., 2014) and lunar apatite (McCubbin et al., 2010b) samples.

It is possible that this reflects analytical artefacts related to (the calibration of) volatile measurements in apatite. If this is the case, both electron microprobe and NanoSIMS measurements suffer from such issues. Electron microprobe analyses of volatiles in apatite are challenging (e.g. Stock et al., 2014, and this study for F) . We have not been able to identify any major problems with our NanoSIMS calibration curves (see Supplementary Material for Chapter 5), and have no evidence to suggest that our calibrations are inferior to others used in the past. We note that to date, only this study and that of McCubbin et al. (2015a) have measured the complete set of H_2O, Cl, and F in both apatite and co-existing melt. The use of the by difference method to fill the X-site to $X_t = 1$ may have masked these issues in many previous studies.

The complex atomic-scale OH-F-Cl mixing in apatite, derived from chemical substitutions in the cation and/or anion site (Hughes and Rakovan, 2002, 2015), could play a role in yielding $X_t < 1$. In contrast to the small F anion, the positioning of the larger OH complex and Cl anion in the apatite structure can create vacancies in the anion column (Hughes and Rakovan, 2015). Because we are unable to identify one clear reason for our findings, we have not normalized our apatite volatile measurements to $X_t = 1$, and we consider the measurements listed in Table 3.5 as the most appropriate for use in the determination of partition coefficients.

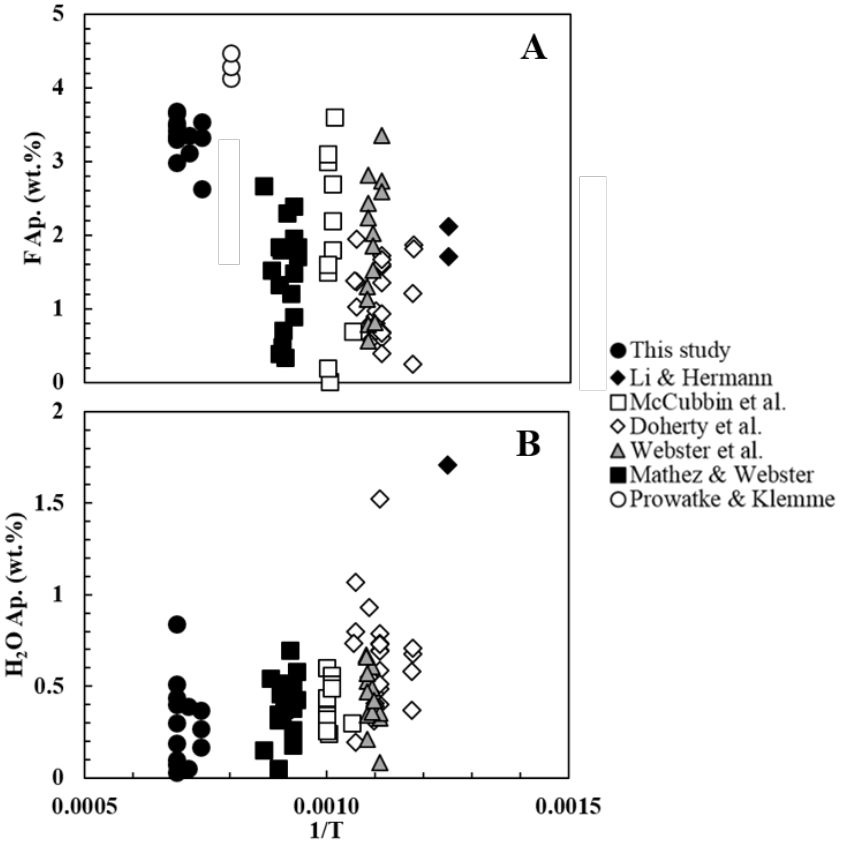

Figure 3.4: Temperature (1/T) plotted against F (A) and H_2O (B) contents in apatite from experiments in this study, Li and Hermann (2015), McCubbin et al., (2015a), Doherty et al., (2014), Webster et al., (2009), Prowatke and Klemme (2006), and Mathez and Webster (2005). Dotted circle is Prowatke and Klemme (2006) data re-calculated to stoichiometric maximum amount of F in apatite (3.767 wt.%). Note that pressure is variable between these experimental studies.

3.4.5 Apatite-melt volatile partition and exchange coefficients

Using the measured volatile contents in apatite and the surrounding glasses, we can calculate simple Nernst partition coefficients coefficients ($D = C_i^a/C_i^b$ where C_i^a and C_i^b are the concentrations of the element i in apatite and in the melt, respectively) for each experiment. These range from 1.8 to 7.7 for D_F, 0.2 to 8.0 for D_{Cl}, and 0.3 to 1.0 for D_{OH} (Table 3.6). As stated above, if it is assumed that the apatite X site

shows close to stoichiometric balance as in Equation 3.1:

$$X_{Cl}^{Ap} + X_{F}^{Ap} + X_{OH}^{Ap} = 1 \tag{3.1}$$

then exchange coefficients (K_D), most commonly associated with Fe and Mg exchange in olivine (Roeder and Emslie, 1970), could be more appropriate (Boyce et al., 2014; Li and Hermann, 2015; McCubbin et al., 2015a)). Exchange equilibrium of volatiles between apatite and melt (in this example focused on Cl and OH) can be stated as:

$$Ca_5(PO_4)_3OH(Ap) + M_{1/x}Cl(melt) = Ca_5(PO_4)_3Cl(Ap) + M_{1/x}OH(melt) \tag{3.2}$$

where $M_{1/x}Cl$ and $M_{1/x}OH$ represent melt components containing any cation with a valence (x). Using Equation 3.2 negates the poorly constrained CaO and P_2O_5 activities, allowing the apatite-melt exchange coefficients for F, Cl, and OH partitioning between apatite and melt (K_D) to be defined as:

$$K_D^{F-OH} = \frac{X_F^{Ap} X_{OH}^{melt}}{X_{OH}^{Ap} X_F^{melt}} \tag{3.3}$$

$$K_D^{Cl-OH} = \frac{X_{Cl}^{Ap} X_{OH}^{melt}}{X_{OH}^{Ap} X_{Cl}^{melt}} \tag{3.4}$$

$$K_D^{F-Cl} = \frac{X_F^{Ap} X_{Cl}^{melt}}{X_{Cl}^{Ap} X_F^{melt}} \tag{3.5}$$

where XF_{Ap} and XF_{melt} are the proportions of F in apatite and melt (where F is interchangeable for Cl and OH). These equations assume no non-ideality (activity coefficients all equal to unity). K_D values are commonly calculated using mole fractions (i.e. Ellis and Green, 1979; Li et al., 2015; Putirka et al., 2003; Roeder and Emslie, 1970), but calculations using weight fractions (Boyce et al., 2014; McCubbin et al., 2015a) give identical results as long as no assumptions are made about speciation. Li and Herman (2015), in their analysis of apatite-melt volatile partitioning, attempted to provide an improved model of the mole fraction of OH in melts, using the water speciation model of Silver and Stopler (1985). Here, we have simply assumed that all H is present as H_2O in all experiments and used simple D ratios to calculate K_D. This yields:

$$\begin{aligned} K_D^{F-OH} &= 2.8 \pm 0.060 \text{ to } 11.8 \pm 0.041 \\ K_D^{Cl-OH} &= 0.4 \pm 0.010 \text{ to } 10.5 \pm 0.080 \\ K_D^{F-Cl} &= 0.4 \pm 0.139 \text{ to } 7.8 \pm 0.024 \end{aligned}$$

The K_D values obtained in this study are shown in Table 3.6. The K_D^{F-OH} values (∼3-12) for our experiments are lower than literature values, which range from 30 to 150 (Doherty et al., 2014; McCubbin et al., 2015a). Similarly, our K_D^{Cl-OH} values (sim0.4-11) are lower than most literature data (8 to 56; Doherty et al., 2014; McCubbin et al., 2015a). The K_D^{F-Cl} values from our experiments (∼0.4 - 8, with most values <3) overlap with the majority of K_D^{F-Cl} values from the literature (3 to 7 for

McCubbin et al., 2015a; 0.4 to 15 for Doherty et al., 2014; 1 to 19 for Webster, 2009; 2 to 16 for Mathez and Webster, 2005). The two K_D^{F-Cl} values for Li and Hermann (2015) at 14.3 and 77.2 are higher than any of the experiments in this study.

3.5 Discussion

3.5.1 Apatite-melt partitioning of volatiles

Similar to previous studies, our experiments show a clear preference for partitioning of F > Cl > OH into the apatite structure. Our experiments demonstrate that apatite can incorporate significant amounts of Cl and H_2O even when the melt still contains appreciable amounts of F (Table 3.5). In general, the F contents of apatite increase with increasing temperature (Figure 3.4a) while H_2O contents in apatite appear to decrease with increasing temperature (Figure 3.4b). This suggests a temperature effect on volatile partitioning into apatite, although the scatter within each experimental suite suggests that other (compositional) effects play a major role. This precludes derivation of a quantitative model for the temperature effect on apatite-melt partitioning at this stage.

There is a strong exponential relationship between the F contents of experimental melts and the F contents of corresponding apatite (Figure 3.5a). This correlation is not observed for Cl (Figure 3.5b) or H_2O (Figure 3.5c). Our experimental data, combined with literature data, therefore, support the recent hypothesis that F partitioning into apatite is, primarily, a function of F availability in the melt (Kusebauch et al., 2015), whereas Cl and H_2O abundances in apatite are not a direct result of their availability in the melt as highlighted in previous studies (McCubbin et al. 2015a).

3.5.2 Comparison with previous models

We first compare our results with predictions made based on the recent theoretical model of Boyce et al. (2014) and the experimental model of McCubbin et al. (2015a). These authors proposed different methods to calculate the abundance of H_2O in apatite or melt based on known melt Cl and F contents, known H_2O contents of melt or apatite, and exchange coefficients K_D. Boyce et al. (2014) proposed that the H_2O content of apatite (H_2O_{Ap}) can be predicted using K_D values and the volatile content of the melt (Fm, Clm, OHm) at the time of apatite crystallization, following the equation:

$$H_2O_{Ap} = [1 + \frac{F_m}{H_2O_m}K_D^{F-OH} + \frac{Cl_m}{H_2O_m}K_D^{Cl-OH}]^{-1} \quad (3.6)$$

The model of Boyce et al. (2014) was calibrated using constant K_D values from Mathez and Webster (2005), with $K_D^{F-OH} = \sim 50$ and $K_D^{Cl-OH} = \sim 4$. Using Equation 3.6 to predict the water contents in our experimental apatite consistently underestimates the actual amount of water present in apatite in our experiments. This remains the case if K_D values are adjusted to average values from this study and that

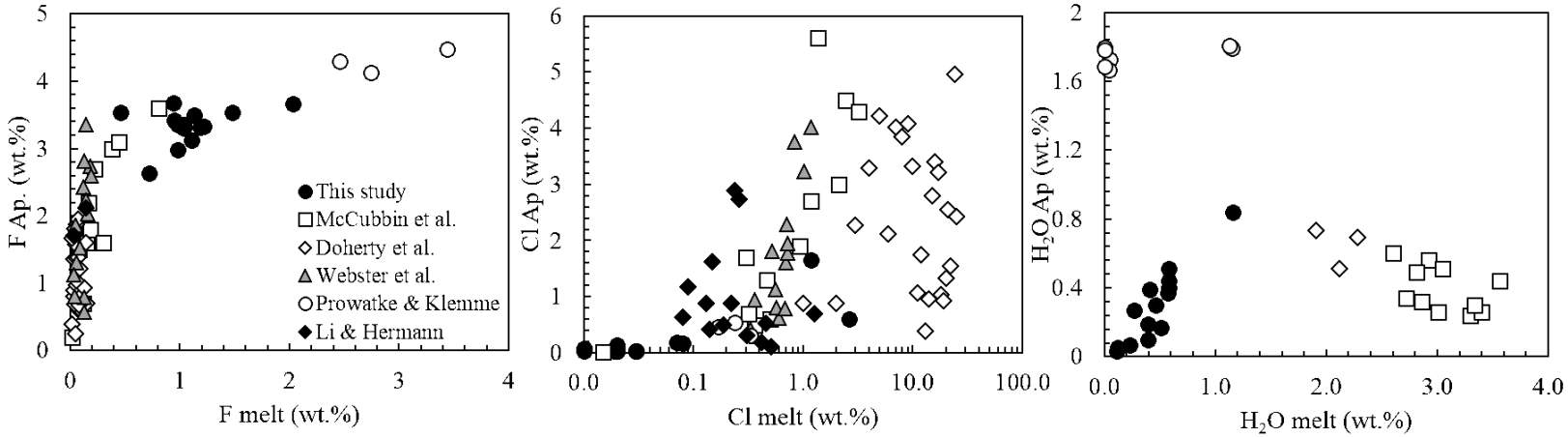

Figure 3.5: Volatile abundance data from this study, Li and Hermann (2015), McCubbin et al., (2015a), Doherty et al., (2014), Webster et al., (2009), Prowatke and Klemme (2005), and Mathez and Webster (2005). (A) F contents of apatite (F_{Ap}) plotted against F contents of the melt (F_{melt}); (B) Cl contents of apatite (Cl_{Ap}) plotted against Cl contents of the melt (Cl_{melt}); (A) H_2O contents of apatite (H_2O_{Ap}) plotted against H_2O contents of the melt (H_2O_{melt}).

of McCubbin et al. (2015a) ($K_D^{F-OH} = 75$ and $K_D^{Cl-OH} = 20$; Figure 3.6a). The Boyce et al. (2014) model assumes little to no H_2O will partition into apatite while F is still available in the melt. This assumption likely explains the poor agreement of the Boyce et al. (2014) model with our results, because several experiments from this study contain apatite with appreciable H_2O surrounded by melt with high F contents.

McCubbin et al. (2015a) proposed that H_2O contents in melts from which apatite crystallized can be calculated using the K_D values they obtained experimentally, for apatite with volatile compositions overlapping with those from their experiments, using the relationship:

$$X_{H2O}^{melt} = \frac{X_{H_20}^{Ap} X_F^{melt}}{K_D^{H_2O-F} X_F^{Ap}} \tag{3.7}$$

Using the average K_D^{OH-F} (0.014) obtained by McCubbin et al. (2015a), we calculated melt in our experiments by combining Equation 3.7 with our measured volatile abundances. Figure 3.5b shows the model of McCubbin et al. (2015a) greatly overestimates our melt H_2O contents when using the average K_D^{OH-F} value from McCubbin et al. (2015a), even though all of the apatite volatile contents from our experiments correspond to the limited F-Cl-OH parameter space for which McCubbin et al. (2015a) suggested their K_D values should be valid.

If instead the average K_D^{OH-F} (0.189) value from this study is used in Equation 3.7, better agreement is obtained for calculated melt values for our experiments. This suggests that Equation 3.7 can be used to accurately estimate melt H_2O contents, as long as appropriate K_D values along with melt F or Cl contents are known. Application of this method to lunar basaltic rocks is not straight-forward since bulk-melt F or Cl contents are difficult to constrain (given the paucity of co-existing apatite and glass pairs), combined with a limited understanding of which K_D values are relevant for individual apatite-melt pairs (as illustrated by this work and Figure 3.5b).

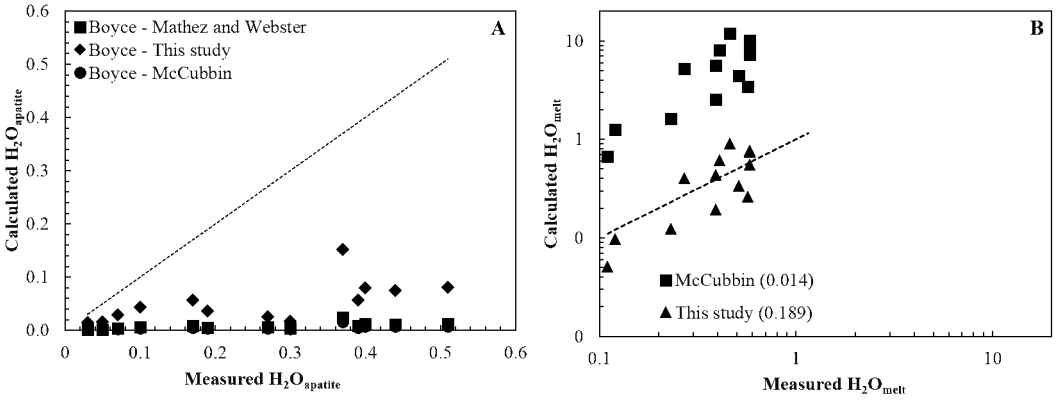

Figure 3.6: (A) Calculated apatite H_2O contents from Equation 3.6, taken from Boyce et al. (2014), for experiments in this study. Average K_D values from Mathez and Webster (2005), McCubbin et al. (2015a), and from this study were used in the calculations and are plotted for comparison. (B) Calculated H_2O melt content from Equation 3.7, taken from McCubbin et al. (2015a) for experiments in this study. Average $K_D^{H_2O-F}$ values of 0.014 from McCubbin et al. (2015a) and 0.189 from this study were used and plotted for comparison. Dotted line in both represents ideality.

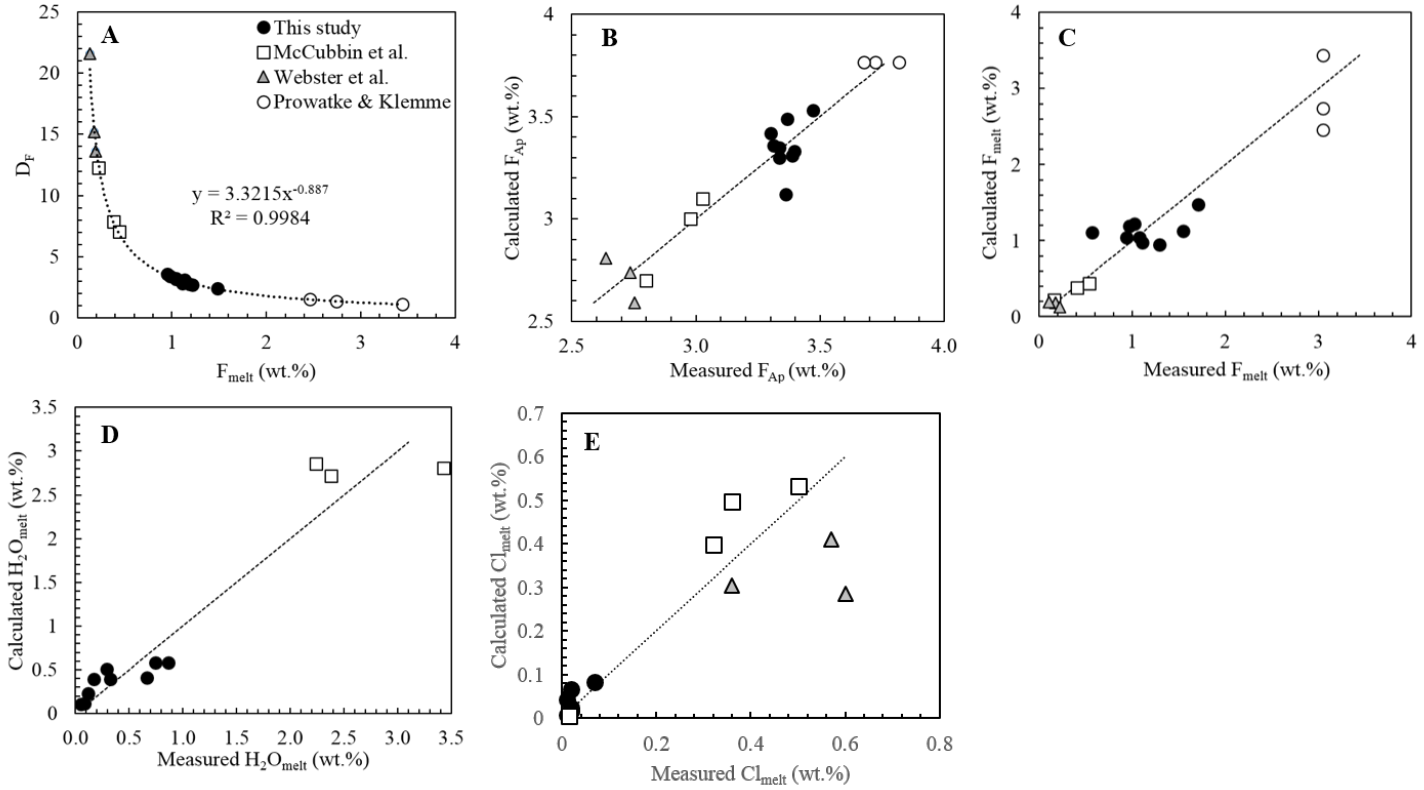

Figure 3.7: (A) D_F plotted against F_{melt} for experiments in this study, McCubbin et al. (2015a), Webster et al. (2009), and Prowatke and Klemme (2006). Only apatite with F_{Ap} >2.5 wt.% and F >> Cl (i.e. lunar relevant compositions) are plotted. The F_{Ap} contents of Prowatke and Klemme (2006) are unusually high (>4 wt.%) which may be a result of common EPMA problems analyzing F. The F_{Ap} values of these experiments have, therefore, been fixed at 3.767 wt.% (i.e. stoichiometric fluorapatite). (B) Comparison between measured F_{Ap} and calculated F_{Ap} using Equation 3.8 (C) Comparison between measured F_{melt} and calculated Fmelt using Equation 3.9 (D) Comparison between measured H_2O_{melt} and calculated H_2O_{melt} using Equation 3.12 for experiments in this study and McCubbin et al. (2015). (E) Comparison between measured Cl_{melt} and calculated Cl_{melt} using Equation 3.10. Dotted black line in (B), (C), (D), and (E) represents ideality.

3.5.3 An empirical model to predict melt volatile contents

Here, we propose a set of empirical models to estimate melt volatile contents based on our experiments. A compilation of apatite-melt F partitioning data based on the Cl-poor experiments of study (excluding the L3a Cl and L2a OH samples), experiments from McCubbin et al. (2015a), Webster et al. (2009), and Prowatke and Klemme (2006) data for apatite with F_{Ap} >2.5 wt.% and F_{Ap} > Cl_{Ap} (i.e. experiments relevant to lunar apatite) is shown in Figure 3.7a, as a function of measured melt F contents. The F_{Ap} contents of the Protwake and Klemme (2006) experiments are higher than what is stoichiometrically expected for apatite (>4 wt.%), which is likely a function of difficult EPMA measurements. The F_{Ap} values for Prowatke and Klemme (2006) where, therefore, adjusted to 3.767 wt.% in the model calibration. The experiments in these studies cover a range of temperatures, pressures, fO_2 conditions, and melt compositions, yet are fit well ($r^2 = 0.9984$) by a power law curve:

$$F_{Ap} = F_{melt} \times (3.3215 \times F_{melt}^{-0.887}) \tag{3.8}$$

Rearranging yields:

$$F_{melt} = (F_{Ap}/3.3215)^{(\frac{1}{0.113})} \tag{3.9}$$

This treatment is similar to the work of Kusebauch et al. (2015), who found a comparable trend between D_F Ap-fluid and F contents in fluids in low temperature experiments. Figure 3.7b shows that F_{Ap} of experimental samples can be calculated to within 0.2 wt.% accuracy from measured F_{melt} values, which is less than the 2 analytical uncertainty of F measured by the electron microprobe. Back-calculating F_{melt} from the measured F_{Ap} values yield accuracies of 0.03 to 0.54 wt.% for experiments in this study, in McCubbin et al. (2015a), and in Webster et al. (2009).

The experiments in our study, with the exception of L3a Cl1 and L3a Cl2, included trace amounts of Cl only and, as such, do not allow full exploration of the behavior of Cl in lunar systems to the extent performed for F above. Lunar mare basalts, however, generally contain only trace amounts of Cl as well, and so a simple model for Cl partitioning is considered acceptable at this stage. Chlorine partitioning does not show a simple relation with melt chlorine content, and we have shown in the previous section that K_D^{F-Cl} values are not constant. Instead, low-Cl and high-Cl apatite seem to be characterized by two different K_D values. Average K_D^{F-Cl} values of 1.7 (average value from our experiments for Cl_{Ap} <0.3 wt.%) and ∼7 (from McCubbin et al. 2015a for Cl_{Ap} >0.3 wt.%) can be used in combination with Equation 3.5 to calculate Cl_{melt} based on the following relationship:

$$Cl_{melt} = \frac{K_D^{F-Cl} \times (F_{melt} Cl_{Ap})}{F_{Ap}} \tag{3.10}$$

Combined with the F partitioning model of Equation 3.9, this finding suggests that Cl melt contents can be derived from measurements of the F and Cl content of apatite. It should be noted that additional work constraining Cl_{Ap}/Cl_{melt} behavior would enable refinement of this model.

Given the strong preference for F in apatite we can assume that any given OH

or Cl anion will be competing with F for a space in the X site. Incorporating F partitioning as defined in Equation 3.8 with an average K_D^{F-Cl} (as explained above) we can define below an expression for OH partitioning into apatite (note that although it is the OH anion which sites in the apatite X site for practicality we use the measured H_2O in the following expression).

$$H_2O_{melt} = (\frac{F_{Ap}}{F_{melt}} \times (\frac{K_D^{F-Cl}}{(\frac{F_{Ap}}{F_{melt}}})) \times H_2O_{Ap} \tag{3.11}$$

$$H_2O_{melt} = K_D^{F-Cl} \times H_2O_{Ap} \tag{3.12}$$

Note that only the experiments from this study and of McCubbin et al. (2015a) have SIMS measurements of both H_2O in melt and apatite for inclusion in this model calibration. Our model (Equation 3.12) predicts melt H_2O contents from apatite volatile abundance measurements only. This equation reproduces measured water contents in our experiments to within <0.3 wt.% error. For McCubbin et al. (2015a) experiments, the difference between calculated and measured H_2O melt contents is within <0.6 wt.%. It is thought that greater exploration of the Cl partitioning function in our model as well as more information on apatite growing from melts with ∼1-3 wt.% H_2O would provide greater constraints on the errors for the experiments of McCubbin et al. (2015a).

3.5.4 Volatile contents of lunar melts

Historically, volatile measurements of lunar apatite have not included F, Cl, and H_2O on the same spot and/or grain. This is because a large number of measurements have been made on the electron microprobe, where H_2O measurements arent possible while ion microprobe measurements have generally focused on H_2O and/or Cl measurements only. To provide greater clarity on the volatile contents of lunar melts and to decipher any trends between sample types a more comprehensive data set of all three volatiles in lunar apatite would be required. However, inputting available abundance data into our models provides a range of melt volatile contents of 88 to 35700 ppm H_2O, 2 to 49559 ppm F, and 33 to 53146 ppm Cl (Figure 3.8). This work highlights that lunar melts can contain considerable volatile contents, at the time of apatite formation, but that these melt contents can also be highly variable.

3.6 Implications

In this work we propose a calibrated model that can predict melt H_2O, F, and Cl contents requiring knowledge of apatite F, Cl, and H_2O abundances only. Further experiments with lower F_{Ap} and higher H_2O_{melt} contents, alongside a thorough investigation of Cl partitioning in lunar apatite, would provide greater constraint on our model. Simultaneous measurements of F, Cl, and H_2O of lunar apatite are required to make further constraints on the volatile contents of the melts from which apatite

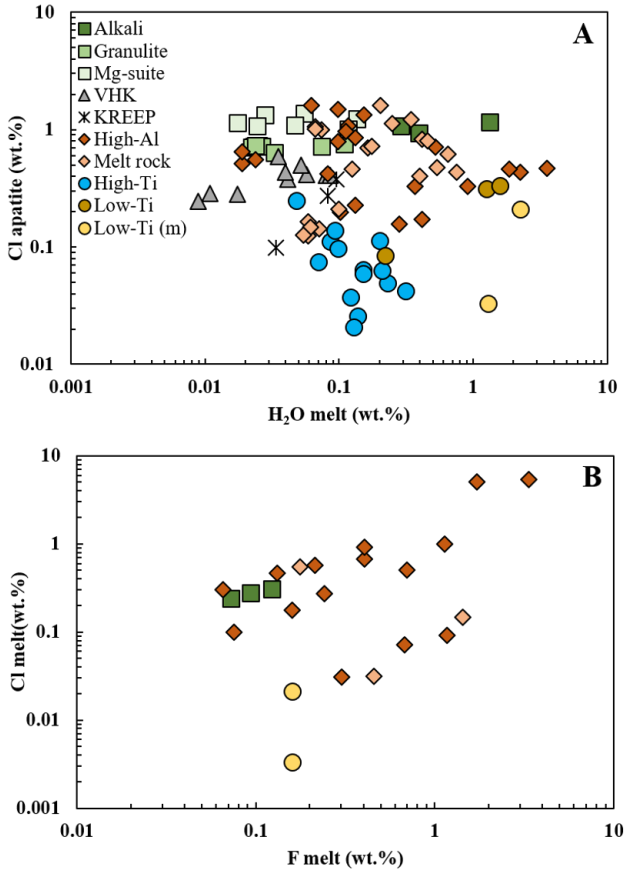

Figure 3.8: (A) Calculated H_2O_{melt} plotted against measured Clapatite and (B) calculated Cl_{melt} plotted against F_{melt} for a range of Apollo samples; where Low/High-Ti refers to Low/High-Ti mare basalts and (m) indicates meteorite sample. VHK is very high potassium and KREEP refers to KREEP-rich basaltic rocks. Data from Barnes et al. (2016); McCubbin et al. (2010a,b); Potts et al. (2015); Tartèse et al. (2013a, 2014b).

crystallized. The small database available at the moment suggests that lunar melts may have contained up to ∼3.6 wt.% dissolved H_2O, 5 wt.% F, and 5.3 wt.% Cl at the time of apatite formation.

3.7 Acknowledgements

We would like to thank Edgar Streenstra, Wouter van de Steeg, Peter Landsberg, and Feargus Abernathy for lab assistance. We would also like to thank Francis McCubbin for providing apatite standards. This work was funded by an STFC studentship awarded to NJP, a STFC research grant to MA (Grant no. ST/I001298/1) and a NWO Vici grant to WvW. NanoSIMS machine time was allocated through UKCAN (Grant no, ST/IOO1964/1 to IAF).

Chapter 4

Magmatic degassing of F and Cl under lunar conditions

ABSTRACT

Measurements of lunar volatile elemental abundances and isotopic compositions in the mineral apatite, pyroclastic glass beads, and melt inclusions are used to constrain the volatile budget of the magmas they formed from. Magmatic degassing is known to affect both absolute and relative volatile abundances and can impart isotopic fractionations. Quantifying the role of degassing is, therefore, important in models aiming at reconstructing the Moon's volatile budget. This study presents the first experimental results on volatile degassing from analogue high-Ti (for Cl) and low-Ti (for F and Cl) basaltic lunar melts, assessing the extent of lunar melt compositional effects on degassing. Water was added to some Cl degassing experiments to compare the rates of degassing in anhydrous and hydrous systems. The results from this study show that F degasses far more rapidly in low-Ti melts than previously observed. Cl degassing rates from low-Ti melt are much faster than rates from high-Ti melt. Cl degassing is much faster than F degassing in the same melt composition, consistent with previous observations from natural samples. The effect of adding water is poorly resolved –Cl degassing rates in high-Ti melt appear significantly increased when water is added, but there appears to be no effect of water addition in the low-Ti melt. The results also suggest HCl is the dominant Cl-species in the vapor with no metal chloride speciation witnessed. These experimental results (1) show how low-pressure degassing can significantly alter initial higher pressure volatile contents in lunar melts, (2) suggest that mechanisms other than metal chloride formation to fractionate Cl isotopes in lunar magmas may need to be explored, and (3) provide additional caveats to studies attempting to constrain the volatile contents of late-stage lunar magmas.

4.1 Introduction

Recent analysis of volatile (F, Cl, OH, S) elemental abundances and isotopic compositions in a wide range of lunar magmatic samples, including pyroclastic glasses (Saal et al., 2008), olivine-hosted melt inclusions (Chen et al., 2015; Hauri et al., 2011), and the mineral apatite from a variety of lithologies (McCubbin et al., 2015b, and references therein), have challenged the previously held notion of a volatile-depleted Moon (e.g. Epstein and Taylor, H. P., 1973). Sample analyses indicate much higher magmatic volatile abundances, in the interior of the Moon, than previously considered (Hauri et al., 2011; McCubbin et al., 2010a,b; Saal et al., 2008; Tartèse and Anand, 2013). To quantify the volatile contents of lunar magmatic source regions using the measured volatile elemental abundances and isotopic compositions in volcanic materials, it is paramount to constrain any processes which may have influenced magmatic volatile budgets during transport to the surface, eruption, and cooling. A major process in magmatic systems known to influence volatile contents in terrestrial rocks is degassing (e.g. Burnham, 1994; Villemant et al., 2003). There is widespread evidence for volatile degassing on the Moon; degassing has been invoked to explain core-to-rim diffusion profiles of volatiles in lunar pyroclastic glasses (e.g. Saal et al., 2008) and the formation of sublimates on the surface of these glass beads (e.g. Elkins-Tanton et al., 2003; Meyer, C. et al., 1975; Saal et al., 2008); The heavy δ^{37}Cl signature of lunar samples is thought to result from degassing during mare basalt eruption (Sharp et al., 2010) or magma ocean degassing (Barnes et al., 2016; Boyce et al., 2015), while Tartèse and Anand (2013) have suggested that the D/H ratio measured in lunar apatites could be explained by degassing of molecular H_2 during mare basalt eruption.

The majority of lunar volatile measurements are from apatite, a mineral which is ubiquitous and widespread in lunar basalts. Apatite is a late-stage mineral (McCubbin et al., 2015; Potts et al., 2016; Tartse et al., 2014) and, as such, the volatile contents recorded during apatite crystallisation likely reflect those of degassed melts (Ustunisik et al., 2011). Constraining the extent of degassing for these samples is, therefore, vital to understanding the volatile contents of the lunar interior. To date, however, little is known about volatile degassing under lunar conditions.

Reconnaissance experiments were performed by Ustunisik et al., (2011; 2015) to understand degassing in a mixed volatile system from a composition similar to high-Al mare basalt Apollo sample 14053. Their results showed more extensive degassing than previously thought based on diffusion profiles in pyroclastic glasses (Saal et al., 2008), concluding that apatites formed from degassed melts would differ greatly in their volatile contents from those forming from non-degassed melts (Ustunisik et al., 2011). Given the large range of melt compositions found on the Moon (Delano and Livi, 1981; Shearer et al., 2006) we set out to determine, experimentally, the extent of melt compositional effects on volatile degassing. Experiments were designed to determine the rate of volatile loss due to degassing at low oxygen fugacity (fO_2). Two bulk compositions were chosen for these experiments, a high-Ti melt and a low-Ti melt. Degassing of F (from the low-Ti composition) and Cl (from the low-Ti and high-Ti compositions) was explored individually, whereas mixed volatile degassing was assessed by adding water to some of the Cl degassing experiments.

4.2 Experimental Methods

4.2.1 Starting materials

Synthetic starting compositions included a high-Ti melt containing ∼9 wt% TiO_2, similar to the Apollo 17 'orange glass' composition (Delano, 1986) and low-Ti glass containing ∼3.5 wt% TiO_2 similar to sample 15427 (yellow-brown #2 from Saal et al. (2008)). Starting materials were prepared by mixing appropriate amounts of high purity (99.5 –99.99%, Alfa Aesar) powdered oxides and carbonates (MgO, Fe_2O_3, $CaCO_3$, Na_2CO_3, K_2CO_3, Al_2O_3, TiO_2, SiO_2, and $Ca_3(PO_4)_2$). MgO, Al_2O_3 and SiO_2 were initially fired overnight at 1000 °C to remove residual moisture before storage with the other oxides and the carbonates at 110 °C. The starting materials were mixed under ethanol in an agate mortar to promote homogeneity and left to air-dry overnight. The dry mixtures were then transferred to a Fe-saturated Pt crucible and decarbonated in a box furnace by gradually raising the temperature from 650 °C to 900 °C, over a period of three hours. The mixtures were then removed from the furnace, which was subsequently heated to 1580 °C. Once the furnace reached final temperature the mixtures were placed in the center of the box furnace for 60 minutes before quenching to a glass by immersing the bottom of the Pt crucible in water. After cooling, the glasses were ground to a fine powder under ethanol in an agate mortar and air-dried.

CaF_2, NaCl, or NaCl + H_2SiO_3 were subsequently added and thoroughly mixed with these starting glasses under ethanol in an agate mortar without additional melting to prevent degassing of Cl, F or H during glass production at 1 atm pressure. Resulting final starting materials were stored in powdered form at 110 °C and relate to t=0 min experiments discussed below.

4.2.2 Experimental procedures

To assess the initial F and Cl contents of our compositions prior to the degassing experiments (at time t = 0), we melted aliquots of the starting material powders at high pressure to prevent F and Cl loss. These synthesis experiments were conducted in the Depths of the Earth Quickpress at the Faculty of Earth and Life Sciences, Vrije Universiteit Amsterdam, using a 0.5 inch diameter talc-pyrex assembly (Van Kan Parker et al. 2011). For each experiment a hand-machined graphite bucket, with an inside diameter (ID) of 0.7 mm, an outside diameter (OD) of 1.7 mm and a length of ∼3 mm was filled with starting material powder under a microscope. A graphite lid of ∼1 mm thickness was made to close the bucket. The closed graphite bucket was inserted into a Pt capsule, with an ID of 1.7 mm, an OD of 2 mm, and a length of ∼8 –9 mm. The Pt capsule was closed at one end with a triple crimp, flattened and welded shut. After insertion of the graphite bucket in the Pt capsule the other extremity was also crimped and welded shut and placed in an alumina inner tube. The Pt-graphite capsule imposes an (fO_2) close to the C-CO equilibrium of ∼IW+2 (Medard et al., 2008), ensuring (fO_2) was low during these experiments.

A W_5Re_95 –W_26Re_74 (type C) thermocouple was inserted axially into the talc-pyrex assembly using four-bore high purity alumina tubing to measure T throughout the high-pressure experiment. The sample was placed in the hotspot of the assembly,

2 mm from the thermocouple tip end, shown to be 10 °C from the thermocouple reading in these types of assemblies (Watson et al., 2002). The runs were performed at a pressure of 1 GPa using a hot piston-in technique (McDade et al., 2002). Samples were heated to 1500 °C at 100 °C/minute. The pressure was initially kept low, at ∼300 psi, until a temperature of approximately 700 °C was reached. P was then gradually raised to ∼715 psi (equivalent to the target sample pressure of 1 GPa) during further heating. The samples dwelled at temperature for ten minutes before being quenched. The runs were quenched by turning off the power to the furnace, while P was kept stable. The Pt capsules were subsequently embedded in epoxy, and cut to expose the volatile-bearing glasses synthesized during the high-pressure experiments. The composition of these glasses constituted the t = 0 measurements of the degassing experiments.

To quantify the rates of F and Cl degassing, time series experiments were carried out at 1500 °C using run times of 4, 40, and 240 minutes for F, and 4 and 6 minutes for Cl. The experiments were run in the CO-CO_2 gas-mixing furnace facility at the Faculty of Earth and Life Sciences, Vrije Universiteit Amsterdam. Samples were inserted into Re buckets (Alfa Aesar, 0.025 mm thick, 99.97 % purity Re foil). The buckets were left open to optimize gas exchange between the sample and the furnace atmosphere. A mixture of CO (97.9 %) and CO_2 (2.1 %) gas continually flowed into the furnace to provide Moon-relevant reducing conditions at an fO_2 of two log units below the iron-wustite buffer (IW-2). Sample buckets were suspended from Pt wire attached to the end of a 4-bore Al_2O_3 ceramic tube and contained the initial starting material. After the gas mixture had equilibrated in the hot spot of the furnace, indicated by an yttrium-stabilized ZrO_2-solid-electrolyte sensor (Ceramic Oxide Fabricators Pty. Ltd, Victoria, Australia), the sample was lowered into the hot spot through a gas-tight sliding mechanism. After the experiments, samples were removed from the furnace and cooled in air.

4.2.3 Analytical methods

The low-Ti + F starting materials and degassed run products were analyzed by a JEOL JXA-853OF Hyperprobe Field Emission Electron probe at Utrecht University GeoLab. A defocused beam with a current of 15 nA and an accelerating voltage of 15 kV was used for analyses with 10 μm spot sizes. A selection of natural standards was used for calibration of Al (corundum), Cr (Cr-metal), Si, Ca (diopside), Mg (forsterite), Fe (haematite), Na (jadeite), K ($KTiPO_5$), Ti (rutile), Mn (tephroite), F (fluorite), and Cl (marialite). The high-Ti + Cl and low-Ti + Cl starting materials and run products were analyzed using The Open University Cameca SX 100 electron microprobe. An accelerating voltage of 20 kV and a beam current of 20 nA were used with a defocused beam diameter of 10 μm. Standard count rates of 20 s per element were used, with a background counting time of half the peak counting time before and after peak analysis. Natural standards of feldspar (Si, Al, K), jadeite (Na), hematite (Fe), rutile (Ti), and apatite (P) were used for calibration of major elements while F and Cl were standardized with a SrF_2 crystal and a tugtupite crystal, respectively.

4.3 Results

The low-Ti + F high-pressure and degassing experiments yielded homogenous, crystal-free glasses. Some metallic residue from the Re capsule was present on the surface but back-scattered electron (BSE) images confirmed this Re was implanted into the surface by smearing during polishing (Figure 4.1). The low-Ti + Cl and high-Ti + Cl experiments produced homogenous, phase-free, glasses as well (Figures 4.2 and 4.3). The low-Ti + Cl + H and high-Ti + Cl + H experiments displayed quench, skeletal-olivine, textures in both high-pressure and degassing runs (Figures 4.2c and 4.3c), a likely result of the additional H in the system. In these experiments some silica grains also seem to have formed either during the experiments or during quench. Clean areas of unquenched glass were chosen for analysis. As the quench laths and silica are F- and Cl-free, the total sample F and Cl contents could be lower than reported in the H-bearing experiments (i.e. loss due to degassing could be higher than reported).

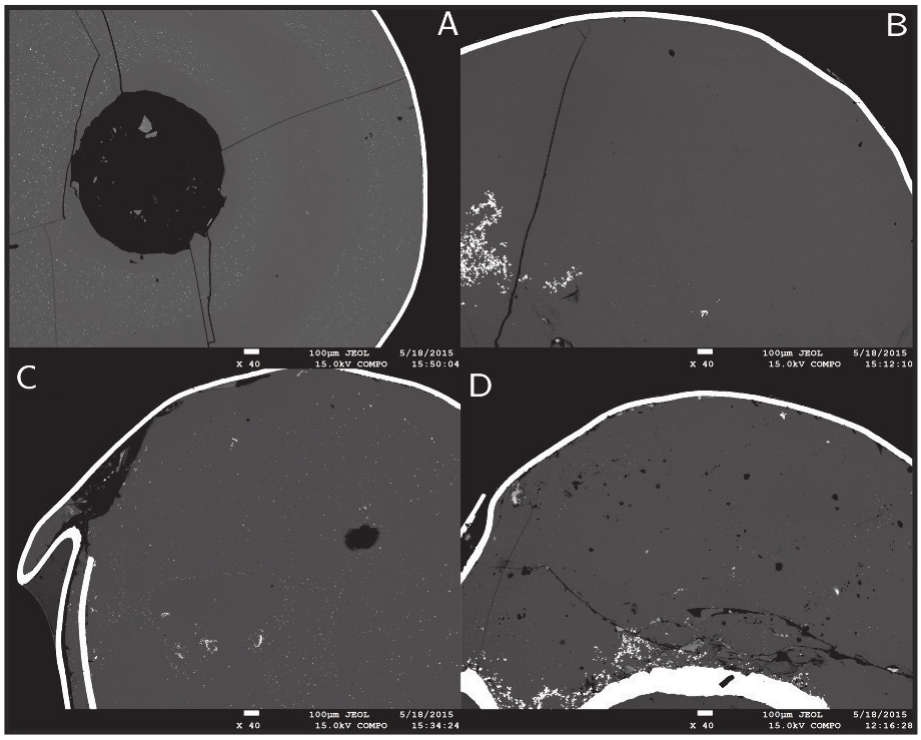

Figure 4.1: BSE images of low-Ti + F degassing experiments. (A) 4 minute run durtion. (B) Close up image of A. (C) 40 minute run duration. (D) 4 hours run duration. The bright strip in the images is the Re capsule. The smaller white blebs inside the experiments correspond to Re smeared onto the sample surface during polishing.

4.3.1 Low Ti + F experiments

Table 4.2 shows the results of the starting material synthesis (t = 0 min) and the degassing experiments for the low-Ti + F composition. At t = 0 min a Cl contamination of 334 ppm was found. The level of Cl was reduced to below the ∼100 ppm EPMA detection limit in the other samples. The FeO content in the t = 0 min experiment is lower than in degassing experiments, suggesting some Fe alloying with

the outer Pt capsule occurred. Significant FeO loss is not seen in the t = 4 and t = 6 minute experiments, but is clear after degassing for 240 mins. This is likely an effect of Fe diffusion into the surrounding Re capsule (Figure 4.4). The Na_2O contents began as 1 wt.% and decreased to 0.4 wt.% at t = 4 min. There was no subsequent loss after 4 minutes. There is not enough information to decipher whether Na_2O reached maximum degassing within the first 4 minutes or if the t = 0 min experiment is anomalous for this element.

There is a clear systematic loss of F from t = 0 min with initial contents of 2606 ppm F to t = 240 min when 99 % of F is lost, with only 26 ppm remaining . The final F content of 26 ppm is very close to the detection limit of the EPMA and, therefore, it is likely that total F content loss ranges from 96 to 100 % at 240 minutes. The largest proportion of F (63 %) was lost during the first 4 minutes of the experiment. At t = 40 min, 269 ppm F remains in the melt, a total percentage loss of 90 % (Table 4.2; Figure 4.5).

The reported F loss here is greater than previously noted in the literature. In Ustunisik et al. (2011) ∼60 % F degassed after 6 hours and 38 % F was lost after 10 minutes in Ustunisik et al. (2015). The synthetic low-Ti composition used here differs from that of Ustunisik et al. (2011) where a synthetic melt, similar to Apollo basalt 14053, was utilized.

This difference may be responsible for the differences in F degassing seen between the two studies. Alternatively, the addition of H_2O, Cl, and S as well as F in the Ustunisik et al. (2011) study, compared to only F in the experiments could have affected degassing rates. No S was added to any experiments here and no background contamination of S is thought to be present in these samples. The experimental powders were stored in a 110 °C oven to minimize H_2O contamination. Although direct measurement of H_2O was not performed, it is thought that only minor amounts of H were available in these F-bearing experiments based on our previous nominally water-free experiments partition experiments using the same set up (Chapter 3). We note, however, that the absence of significant H should have led to lower rates of F degassing in our experiments, as the gas species HF is thought to dominate the vapor phase (Spilliaert et al., 2006). It, therefore, remains unclear what causes the difference in degassing rates of F between our work and the Utsunisik et al. (2011; 2015) studies.

	Low- Ti Glass			High Ti Glass			Ustunisik et al.		
	Target	Glass	1σ	Target	Glass	1σ	Target	Glass	1σ
SiO_2	42.7	39.5	0.25	38.8	36.7	0.22	45.86	46.04	0.29
TiO_2	3.6	3.63	0.05	9.3	9.7	0.07	2.9	2.77	0.02
Al_2O_3	8.1	6.97	0.05	7.6	7.8	0.04	12.48	12.74	0.07
FeO	22.2	23.75	0.27	22.9	20.7	0.33	16.89	16.83	0.17
MgO	13.6	11.54	0.11	11.6	11.1	0.1	8.93	9.23	0.08
CaO	8.3	7.25	0.03	8.6	8.3	0.14	11.02	10.39	0.06
Na_2O	0.3	0.44	0.02	0.4	0.4	0.02	0.44	0.43	0.01
K_2O	0.06	0.02	0.01	0	0	0	0.1	0.11	0.01
MnO	0.3	0.26	0.01	0.3	0.3	0.02	-	-	-
Cr_2O_3	0.7	0.27	0.01	0.7	0.3	0.01	-	-	-
P_2O_5	-	-	-	-	-	-	0.11	0.13	0.01
F*	0	0	0	0	11.2	0	5000	5352	193
Cl*	0	117.33	33.09	0	159	0	5000	4787	49
Total	99.9	93.6	0.21	100.1	95.3	0.12	100	100	

Table 4.1: Target compositions and mean composition of initial starting material. Low-Ti target composition from Saal et al., (2008) and High-Ti target composition from Delano et al., (1986). *ppm)

	0 min	1σ	4 min	1σ	40 min	1σ	4 hrs	1σ
n	*9*		*15*		*15*		*20*	
SiO_2	44.55	0.57	41.09	0.64	42.58	0.10	47.17	0.17
TiO_2	3.54	0.09	3.71	0.08	3.90	0.05	4.32	0.05
Al_2O_3	9.01	0.14	7.21	0.03	7.45	0.05	8.24	0.07
FeO	17.14	0.53	25.23	0.47	22.74	0.20	15.12	0.13
MgO	12.48	0.18	12.19	0.13	12.61	0.09	13.83	0.08
CaO	7.88	0.17	8.05	0.08	8.29	0.04	8.94	0.04
Na_2O	0.95	0.06	0.37	0.02	0.35	0.03	0.39	0.03
K_2O	0.06	0.01	0.00	0.00	0.00	0.00	0.01	0.01
MnO	0.21	0.02	0.25	0.02	0.28	0.03	0.28	0.03
Cr_2O_3	0.24	0.02	0.30	0.02	0.31	0.02	0.34	0.02
F*	2606	430	967	350	269	260	26	62
Cl*	334	266	b.d.	-	b.d.	-	b.d.	-
Total	96.4	1.31	98.5	0.31	98.5	0.21	98.7	0.21

Table 4.2: Low-Ti + F experiment compositions (wt.%) after 0, 4, 40 minutes, and 4 hours. *ppm

Table 4.3: Low-Ti + Cl experiment compositions (wt.%) after 0, 4, and 6 minutes. *ppm

							+H	
	0 min	1σ	4 min	1σ	6 min	1σ	4 min	1σ
n	*10*		*9*		*6*		*8*	
SiO_2	41.7	0.42	41.4	0.26	36.6	0.14	41.5	0.12
TiO_2	3.7	0.09	3.6	0.12	3.5	0.33	3.6	0.10
Al_2O_3	7.1	0.09	6.9	0.07	7.0	1.20	7.0	0.03
FeO	24.0	0.33	24.3	0.78	22.6	0.36	23.6	0.12
MgO	12.0	0.53	12.3	0.07	20.5	3.08	11.9	0.08
CaO	7.3	0.08	7.4	0.07	7.0	0.94	7.1	0.04
Na_2O	1.3	0.29	0.9	0.10	0.5	0.09	0.9	0.08
K_2O	0.0	0.01	0.0	0.0	0.0	0.01	0.0	0.0
MnO	0.2	0.01	0.2	0.01	0.2	0.01	0.2	0.01
Cl*	8182	1144	890	181	63	77.67	660	383
Total	98.28	0.45	97.15	0.75	97.90	0.68	95.82	0.15

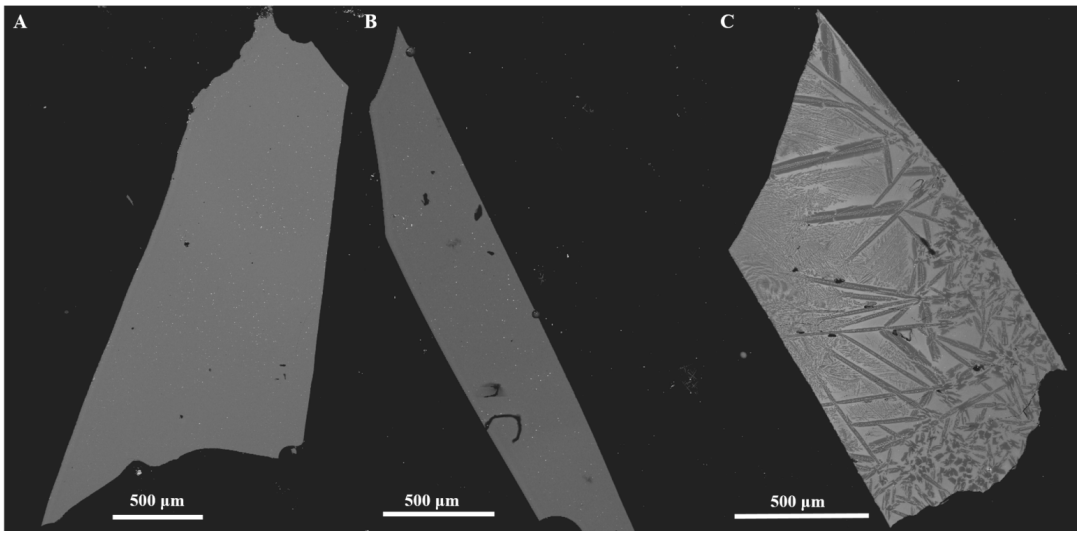

Figure 4.2: BSE images of low-Ti + Cl degassing experiments (A) 4 minute run duration (B) 6 minute run duration, and (C) 4 minute run duration including H in the starting material.

4.3.2 Low Ti + Cl experiments

Data for the low Ti + Cl experiments (Table 4.3; Figure 4.6) show that at least 99 % Cl is degassed from the melt between t = 0 min and t = 6 min. The reported 63 ppm Cl at t = 6 min is just below the detection limit of the probe and could possibly be background noise. The initial Cl content of 8182 ppm is reduced to 890 ppm, a loss of 89 %, after t = 4 min.

The observed rate of Cl degassing here is again greater than that reported in the literature at 84 to 89 % at 6 hours (Ustunisik et al., 2011) and 66 % to 95 % loss at 10 minutes and 6 hours, respectively (Ustunisik et al., 2015). These literature experiments, as discussed for the low Ti + F experiments above, presumably have higher

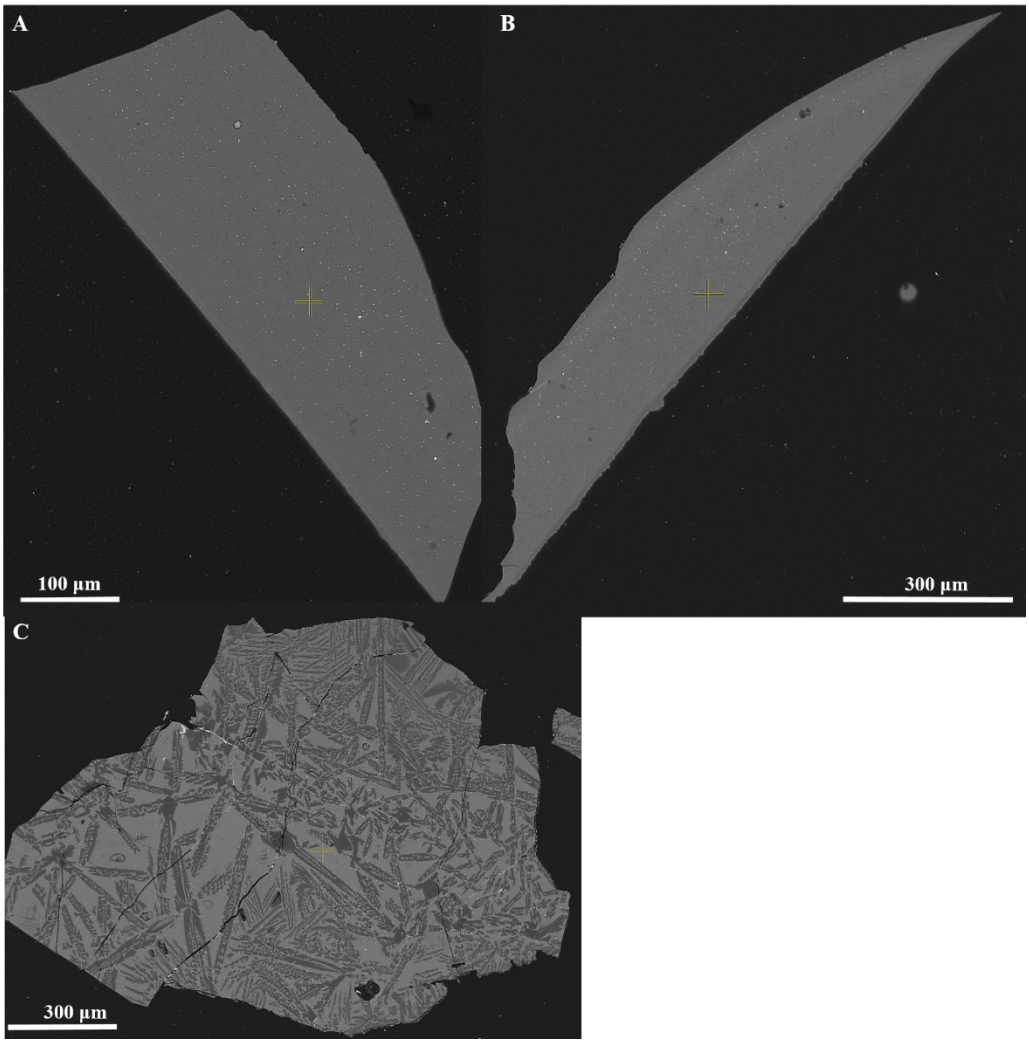

Figure 4.3: BSE images of high-Ti + Cl degassing experiments (A) 4 minute run duration (B) 6 minute run duration, and (C) 4 minute run duration including H in the starting material.

H_2O contents in addition to using different bulk silicate compositions. Although H_2O was not quantitatively measured in these experiments, the same precautions to run 'dry' experiments were taken with the Cl powders as with the F powders with only background H contamination present in the system. No F was measured in these experiments.

No significant iron loss is observed in these experiments, the lowest FeO contents are only 0.2 wt.% ± 0.36 lower at t = 6 min compared to the initial glass and other experiments. This reduction is most likely to be a result of minor diffusion into Re. There is a general decrease in Na_2O contents from 1.3 wt.% at t = 0 min to 0.9 wt.% at t = 4 min and finally to 0.5 wt.% at t = 6 min. This overall 0.8 wt.% loss of Na_2O is slightly larger than the 0.6 wt.% loss seen in F-bearing experiments, suggesting some NaCl may have been present in the vapor phase although not enough to dominate Cl loss. The dominant Cl-bearing compound in the vapor phase is, therefore, likely to be HCl. Interestingly, even though the Ustunisik et al. (2011;2015) experiments contained greater amount of H_2O a higher amount of Cl loss is observed here, suggesting Cl degassing is not a direct function of H availability. There is an unexpected decrease

in the amount of SiO_2 combined with a clear increase in MgO observed in the t = 6 min experiment. Perhaps this is due to crystallization of a silicate phase, but no such phase was observed in our back scatter electron images. This is not thought to influence Cl degassing.

Table 4.4: High-Ti + Cl experiment compositions (wt.%) after 0, 4, and 6 minutes. *ppm

							+H		
	0 min	1σ	4 min	1σ	6 min	1σ	0 min	4 min	1σ
n	*10*		*9*		*6*			*8*	
SiO_2	40.0	0.7	38.9	0.26	38.1	0.3	31.3	30.0	2.0
TiO_2	7.6	0.8	9.8	0.2	9.6	0.1	13.2	14.3	1.2
Al_2O_3	14.7	2.2	7.7	0.1	7.8	0.1	11.4	11.7	0.3
FeO	15.0	1.5	21.0	0.5	21.3	0.3	19.3	21.9	2.6
MgO	8.0	0.8	11.7	0.1	11.6	0.1	10.4	6.3	0.3
CaO	6.1	0.5	8.6	0.1	8.5	0.1	12.3	13.1	1.2
Na_2O	5.8	0.7	0.8	0.1	0.9	0.1	0.7	0.9	0.1
MnO	0.2	0.0	0.3	0.0	0.3	0.0	0.2	0.3	0.0
Cl*	4536	751	2431	708	2765	364	3030	626	319
Total	98.1	0.5	99.0	0.4	98.3	0.3	99.4	98.6	1.1

4.3.3 Low Ti + Cl + H experiments

The introduction of H_2O to the low Ti + Cl material resulted in quenched glass material in the PC experiments and the degassing series. Representative glass material was analyzed where possible, but these areas were too small in the t = 0 min experiment for EPMA. Based on the amount of NaCl added to the starting mixture, it can be assumed that initial Cl contents were ∼6060 ppm. This would yield 89 % Cl loss by t = 4 min which contained 660 ppm Cl (Figure 4.6). This is identical to the degassing rate of the 'dry' experiments.

4.3.4 High Ti + Cl experiments

At t = 0 min the Cl concentration in the high-Ti + Cl system was 4536 ppm, which is reduced to 2430 ppm by t = 4 min - a loss of 40 %. By t = 6 min there is a total Cl loss of 44 % with 2765 ppm Cl remaining (Table 4.4; Figure 4.6). The proportion of Cl loss in the high-Ti melt is less than half of the 89 % seen in the low-Ti melt at t = 4 min. The total 44 % Cl loss observed in this system is lower than the ∼ 60 % Cl loss reported by Ustunisik et al. (2011) at 6 minutes compared to 6 hours. Overall this strongly suggests that bulk silicate composition has a clear effect on Cl degassing from lunar melts.

There is no FeO loss between the initial high-Ti melt and that of the t = 4 and 6 min experiments. The initial FeO in the t = 0 min experiment is lower (15 wt.%) than observed in the degassing experiments, again suggesting that some FeO may have been lost to the Pt capsule during this experiment. The MgO and Al_2O_3 contents in the t = 0 min experiment are also anomalous compared to the degassing experiments.

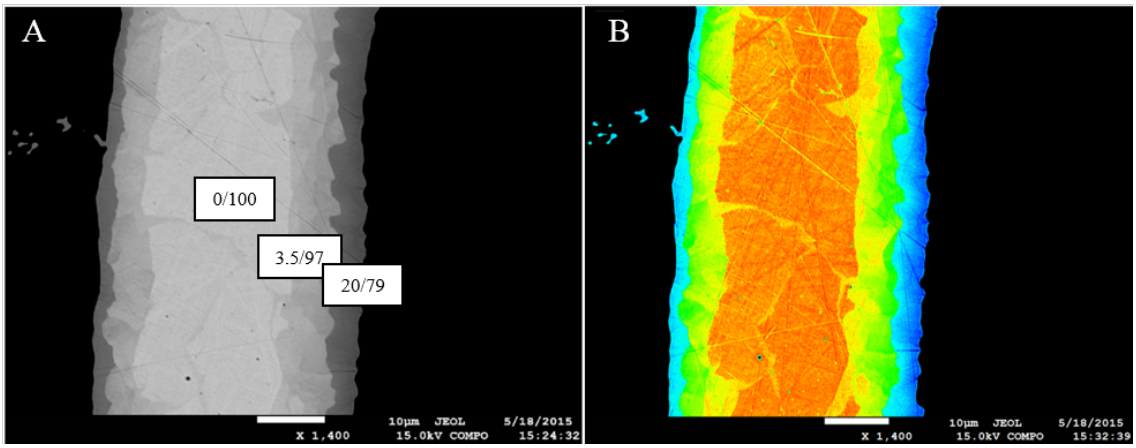

Figure 4.4: (A) BSE and (B) false-color BSE images of Re capsule and surrounding melt from low-Ti + Cl experiment run for 40 minutes. Numbers in boxes refer to EDS wt.% of Re_2O_7 and FeO showing Fe diffusion from the melt into the Re capsule at contact with glass.

There is a greater proportion of Na_2O loss seen in these samples compared to the low-Ti experiments with overall 5 wt.% Na_2O loss. Given the lower Cl loss from these melts it seems unlikely that NaCl is the main complex in the vapor phase.

4.3.5 High Ti + Cl + H experiments

The addition of H_2O into the high-Ti + Cl system increased the proportion of Cl lost up to 79 % loss at t = 4 min. The 626 ppm remaining Cl in the high-Ti + Cl + H system is lower than seen in any of the experiments without additional H_2O. The presence of Cl-free quench minerals means that the actual percentage of Cl degassed could be even higher. In this system the proportion of Cl degassed is similar to that of the low Ti + Cl experiments, indicating that in the high-Ti system the presence of H_2O increases the rate of Cl degassing. The difference in FeO and MgO contents between the t = 0 min and t = 4 min experiments is likely an effect of quenching which took place in these experiments.

4.4 Bulk composition effects

The Cl degassing rate varies significantly as a function of composition. Cl losses as a function of time differ significantly between the low-Ti and high-Ti compositions and the 14053-type melt of Ustunisik et al. (2011;2015). It could be argued that if the high-Ti experiments reached 6 hours they would exhibit similar amounts of Cl loss to those of Ustunisik et al. (2011;2015). This seems unlikely, however, given the degassing trend trajectory, especially given that Cl loss was reported as 4 % per hour in the Ustunisik et al. (2015) experiments. The experiments here and those of Ustunisik et al. (2011) were run at 1-atm while those of Ustunisik et al. (2015) were run at 1/3 bar. Additionally, the experiments of Ustunisik et al. (2011;2015) were run in sealed silica glass tubes compared to our open gas-flux experiments, where you would expect more efficient gas escape. Experimental temperatures differed between these studies. In this study, temperatures were higher (∼1460 °C) than that of the 14053-type melt

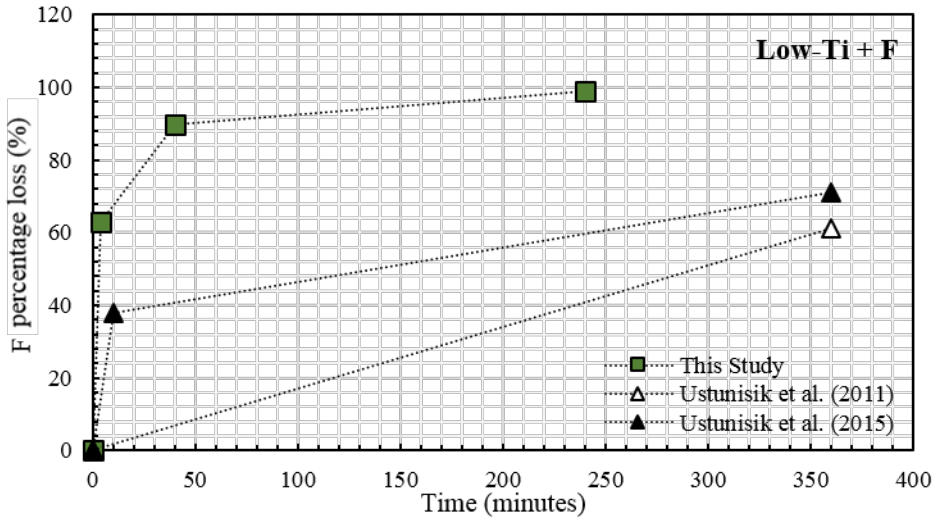

Figure 4.5: Proportion of F lost plotted against time for low-Ti + F experiments (this study), compared to experiments conducted in 14053-like melt by Ustunisik et al. (2011) and Ustunisik et al. (2015).

(∼1250 °C) which affects volatile loss but cannot explain the differences in our study, which occurred at constant temperature. The differences in volatile degassing between the samples indicates that some aspect of bulk composition is influencing degassing rates, however, the current database is not extensive enough to assess what exactly is driving this difference.

As well as bulk composition, the experiments here and those of Ustunisik et al. (2011; 2015) differ in fO_2. Experiments here were run under more reducing conditions (IW-2) compared to the FMQ conditions of Ustunisik et al. (2011; 2015), which has important implications for H speciation. In the experiments of Ustunisik et al. (2011; 2015) OH- is the primary diffusing species (Zhang and Stolper, 1991), while at IW-2 the reduced species H_2 is likely the dominant H-bearing volatile phase degassed. In a silica glass, H_2 diffuses three orders of magnitude faster than H_2O (Zhang and Ni, 2010). It can, therefore, be assumed that any H_2O present in these experiments was lost to the vapor phase quicker than in the experiments of Ustunisik et al. (2011; 2015). It has been suggested that in water-free environments metal chlorides are the dominant chloride species (Sharp et al., 2013, 2010), and if there were any trends in metal loss accompanying Cl degassing this would support that claim. Given that H_2O is less soluble in the melt than Cl, and >90 % Cl was lost after 6 minutes it would be expected that by this time H_2O would have been completely degassed from the melts and metal chloride species began to form. Table 4.5 shows the calculated Fe and Mn loss if $FeCl_2$ (and indeed FeF_2), or $MnCl_2/MnF_2$, were the primary degassed species. The calculated amount of FeO lost varies from ∼0.6 wt.% for high-Ti melts, ∼1.3 wt.% for low-Ti + F, and ∼2.4 wt.% for low-Ti + Cl. For the high-Ti melt the amount of Fe lost is within the analytical uncertainty. If $FeCl_2$ or FeF_2 were the dominating species for Cl loss, however, Fe contents in low-Ti + Cl/F melts are expected to be lower than those measured. The calculated Mn lost as $MnCl_2$ or MnF_2 would result in melts completely depleted in Mn which is not observed here. The results here do not display

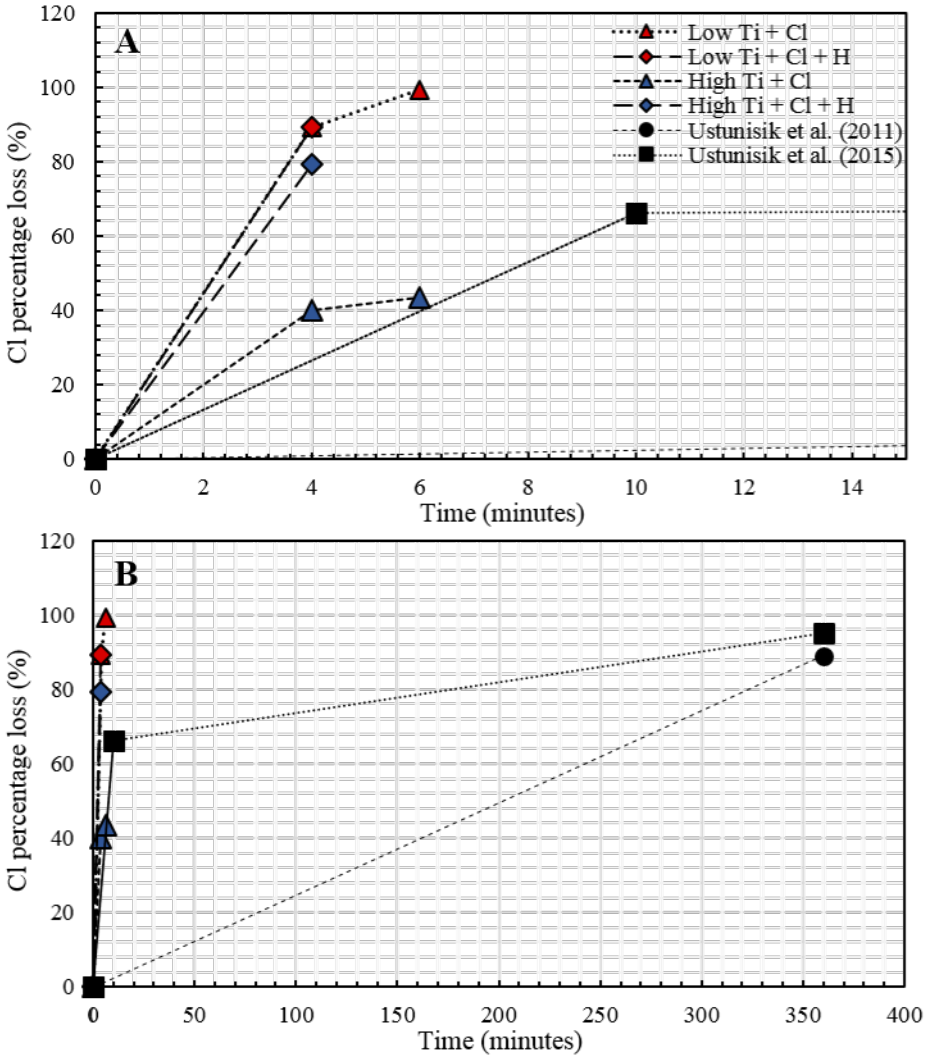

Figure 4.6: (A) Proportion of Cl lost plotted against time for low-Ti + Cl and high-Ti + Cl experiments (this study), as well as low-Ti + Cl + H and high-Ti + Cl + H experiments (this study). Experiment at 10 minutes from Ustunisik et al. (2015), conducted in 14053-like melt, is plotted for comparison. (B) The experiments from the literature study run at 360 minutes have 89 % (Ustunisik et al., 2011) and 95 % (Ustunisik et al., 2015) Cl loss.

	Fe lost	Fe remain	Fe actual	Mn lost	Mn remain	Mn actual
Low-Ti + F 4 m	1.0	16.2	25.2	0.9	>0	0.2
Low-Ti + F 40 m	1.4	15.8	22.7	1.4	>0	0.3
Low-Ti + F 240 m	1.5	15.6	15.1	1.5	>0	0.3
Low-Ti + Cl 4 m	2.3	21.7	24.3	2.3	>0	0.3
Low-Ti + Cl 6 m	2.5	21.5	22.6	2.5	>0	0.2
Low-Ti + Cl + H 4 m	2.4	21.6	23.6	2.3	>0	0.2
High-Ti + F 4 m	0.7	16.2	25.2	0.7	>0	0.2
High-Ti + F 6 m	0.6	16.2	25.2	0.5	>0	0.3
High-Ti + Cl + H 4 m	0.8	16.2	25.2	0.7	>0	0.3

Table 4.5: Calculated amount of Fe lost as FeF_2 or $FeCl_2$ assuming all F/Cl is lost as FeX_2 and the amount of Mn lost as MnF_2 or $MnCl_2$ assuming all F/Cl is lost as MnX_2. Values in wt.%

strong support for metal chloride formation as the primary Cl-species. Instead HCl is thought to be the dominant chloride species, as seen with other studies on volatile degassing under lunar conditions (Colson, 1992; Fegley, 1991).

The difference in Cl degassing between low-Ti and high-Ti melts may result from a difference in melt structure and/or solubility. The major cation composition of the two melts is similar apart from TiO_2 which is not known to create a complex with Cl, but which can affect melt physical properties such as viscosity (Rai et al., 2013). A significant increase in Cl solubility is seen with decreasing H_2O (Rebbert and Webster, 1998), however, as the Ustunisik et al. (2015) experiments have greater H_2O content more Cl should be lost to the vapor phase than in our drier low-Ti/high-Ti experiments, contrary to what is observed.

4.5 Implications for lunar melts

This study presents the first experimental results for degassing of F and Cl in both low-Ti and high-Ti melt systems. Degassing as a mechanism to alter volatile contents in lunar melts has been invoked in numerous studies (Barnes et al., 2016; Boyce et al., 2015; Hauri et al., 2011; Saal et al., 2008; Sharp et al., 2010; Tartse and Anand, 2013), yet understanding how and how fast volatiles degas under lunar conditions has been largely unexplored. This study provides preliminary results, for typical lunar basaltic melts and conditions, where H is thought to be relatively low in abundance. These results show how degassing can significantly alter high-pressure volatile contents and how rates of F degassing could be higher than previously thought. This has important implications for studies which back-calculate volatile contents. Using a single rate of F degassing for lunar melts regardless of composition or water content may not be appropriate. It is also not known if there is any influence on bulk composition as observed for Cl and so care should be taken for any study wishing to explore F contents in lunar basaltic melts.

The difference in Cl degassing rates between low/high-Ti and 14053-type melts shows how that bulk composition is an important factor in volatile loss. We note that little evidence was shown in these experiments for $FeCl_2$ or $MnCl_2$ loss (Table 4.2)

suggesting that HCl is the dominant chloride species. This is an important consideration as degassing either on a whole-Moon scale or within localized basaltic melts, has been invoked to explain the unusually heavy δ^{37}Cl isotopic signature on the Moon plus its large range in isotopic values. If the majority of Cl is lost from a system as HCl then it is difficult to reconcile how degassing could create such large variations in δ^{37}Cl but not in δD. Additional data on how Cl isotopes fractionate are required to understand the unusual values observed in lunar samples.

Chapter 5

Chlorine isotopic signatures of Apollo 14 rocks: Evidence for widespread vapor-phase metasomatism on the lunar nearside ∼4 billion years ago.

Nicola J. Potts[1,2,3*], Jessica J. Barnes[1,4*] Romain Tartése[1,5], Ian A. Franchi[1], Mahesh Anand[1,6]

[1]Planetary & Space Science, The Open University, Walton Hall, Milton Keynes, MK7 6AA, UK
[2]Faculty of Earth & Life Sciences, Vrije Universiteit Amsterdam, 1081 HV Amsterdam, NL
[3]School of GeoSciences, Kings Buildings, University of Edinburgh, Edinburgh, EH9 3JW, UK
[4]Lunar and Planetary Institute, USRA, 3600 Bay Area Boulevard, Houston, TX 77058, USA
[5]Institut de Minralogie, de Physique des Matriaux et de Cosmochimie, Musum National dHistoire Naturelle, Sorbonne Universits, CNRS, UPMC & IRD, 75005 Paris, France
[6]Department of Earth Sciences, The Natural History Museum, London, SW7 5BD, UK

This chapter has been prepared for submission to *Geochimica et Cosmochimica*.

ABSTRACT

Compared to most other planetary materials in the Solar System some lunar rocks display heavy δ^{37}Cl signatures. Loss of Cl in a H << Cl environment has been invoked to explain the heavy δ^{37}Cl signatures observed in lunar samples, either during magmatic eruption onto the lunar surface or during large scale degassing of the lunar magma ocean. To explore the conditions under which Cl isotope fractionation occurred in lunar magmas, five Apollo 14 basaltic samples were selected (14053,19, 14072,13, 14073,9, 14310,171 and basaltic clast 14321,1482) for in situ analysis of Cl isotope compositions using secondary ion mass spectrometry (SIMS). Cl isotopes were measured within the mineral apatite, with measured δ^{37}Cl values ranging from $+14.6 \pm 1.6$ ‰to $+40.0 \pm 2.9$ ‰. These values encompassing the range previously obtained for lunar rocks, and include some of the heaviest Cl isotope compositions measured in lunar samples to date. The observed trends between increasing rare earth element contents and δ^{37}Cl values support the hypothesis of a lunar urKREEP component characterised by a heavy δ^{37}Cl composition. The wide inter- and intra-sample variability of δ^{37}Cl values cannot be easily explained by KREEP assimilation, however, suggesting that other processes were also involved in producing the Cl isotope signatures that we observe. A variety of equilibrium and kinetic processes are explored to try and explain the range in Cl isotope compositions measured here. The favored hypothesis is late-stage interaction with a volatile-rich gas phase, originating from devolatilization of lunar surface regolith rocks ∼3.9 billion years ago. This period coincides with vapor-induced metasomastism recorded in other lunar samples collected at the Apollo 16 and 17 landing sites, pointing to the possibility of widespread volatile-induced metasomatic events on the lunar nearside at that time.

5.1 Introduction

Rejuvenated interest in lunar samples has led to increasing discoveries of similar isotopic signatures between the Earth and the Moon, including calcium (Dauphas et al., 2015; Valdes et al., 2014), chromium (Lugmair and Shukolyukov, 1998), iron (Beard and Johnson, 1999), potassium (Humayun and Clayton, 1995), stable strontium isotopes (Charlier et al., 2012), silicon (Armytage et al., 2011, 2012; Zambardi et al., 2013), titanium (Zhang et al., 2012), and zirconium (Schönbächler et al., 2003). These isotopic similarities have been used to provide new constraints on lunar formation models, most prominently that the Moon may have formed by reconsolidation of materials largely derived from the proto-Earths mantle, after a giant impact event (Canup, 2012; Canup et al., 2015; Ćuk and Stewart, 2012; Rubie et al., 2015). Differences in copper (Herzog et al., 2009), hydrogen (Barnes et al., 2013; Saal et al., 2013), and zinc (Paniello et al., 2012) isotopes between the silicate Earth and lunar samples have been explained by isotope fractionation as a consequence of volcanic degassing (Hauri et al., 2015), and are not thought to reflect primary differences between Earth and Moon. An additional isotopic system which varies considerably between the Earth and the Moon is chlorine (Barnes et al., 2016; Boyce et al., 2015; Sharp et al., 2010a; Tartèse et al., 2014a; Treiman et al., 2014); suggesting that substantial fractionation of Cl isotopes occurred during and/or after the formation of the Moon. Understanding the processes that may have contributed to the fractionation of Cl isotopes in lunar magmas and rocks can, therefore, provide new insights into the history and evolution of volatiles (including Cl, F, H_2O) in the Moon.

5.1.1 Chlorine isotope fractionation in lunar environments

Two competing mechanisms are believed to fractionate Cl isotopes in terrestrial systems. The lighter isotope ^{35}Cl is preferentially vaporized (Graham's Law) in volcanic gases, for example, while the heavier isotope ^{37}Cl, which has a relatively high bond strength, becomes incorporated into $HCl_{(g)}$ (Schauble et al., 2004) in systems where H >> Cl (Sharp et al., 2010b). All primitive terrestrial basalts measured to date have $\delta^{37}Cl$ values clustering $\sim 0 \pm 2$ ‰, suggesting that these two fractionation mechanisms cancel each other out in terrestrial systems (Bonifacie et al., 2008; Sharp and Draper, 2013; Sharp et al., 2007). To explain the elevated $\delta^{37}Cl$ values of lunar samples, Sharp et al. (2010b) favored the hypothesis in which lunar basaltic melts were characterized by H << Cl, leading to dominant degassing of Cl as metal chlorides (e.g., NaCl, $FeCl_2$, etc.) instead of $HCl_{(g)}$. This process preferentially incorporated the lighter isotope ^{35}Cl and resulted in degassed melts enriched in ^{37}Cl (Sharp et al., 2010b). This view is obviously simplified as, for example, $HCl_{(g)}$ is thought to be the dominant H-degassing species (Fegley, 1991) in low H, reducing environments and, therefore, some ^{37}Cl must also be lost via degassing.

In a recent study, Boyce et al. (2015) reported paired H and Cl measurements (abundances and isotopic compositions) for lunar apatite in a range of mare basalts, and proposed that if the hypothesis of Sharp et al. (2010b) is correct then (1) $\delta^{37}Cl$ should be inversely proportional to Cl abundance; (2) elevated $\delta^{37}Cl$ should not be observed in apatite with abundant H; (3) elevated $\delta^{37}Cl$ should be correlated with

enrichments in D/H. Boyce et al. (2015) observed that samples with the higher δ^{37}Cl values were among the most Cl-rich, with some samples displaying a positive correlation between isotopes and abundances. This suggests that whatever mechanisms cause the extreme fractionation of chlorine isotopes must have been capable of producing a reservoir that is rich in Cl and is characterized by elevated δ^{37}Cl values (Boyce et al., 2015). This seems to preclude ^{37}Cl enrichment by preferential outgassing of ^{35}Cl from magmas (at least as the sole mechanism). Additionally, one of the samples, analysed by Boyce et al. (2015), with the highest apatite H_2O contents, ∼2500 ppm, also contains apatite with elevated δ^{37}Cl values ∼+17 ‰, indicating that Cl isotopes can be fractionated to very heavy δ^{37}Cl values in a melt containing significant dissolved H. Finally, Boyce et al. (2015) did not observe any correlation between apatite D/H and δ^{37}Cl values, which would be expected if volatile degassing was the main driver for Cl isotope fractionation, since magmas should also have had the opportunity to degas H (Sharp et al., 2010a, 2007; Ustunisik et al., 2011). The study carried out by Boyce et al. (2015), therefore, appears to preclude the hypothesis proposed by Sharp et al. (2010b) that high δ^{37}Cl values in lunar samples result from magmatic degassing of Cl, in the form of metal chlorides, during ascent and emplacement of low-H basaltic melts.

Boyce et al. (2015) did observe positive correlations between apatite δ^{37}Cl values and some bulk rock trace element characteristics, such as La/Lu ratios and Th contents, which are indicative of involvement of a KREEP (potassium (K), rare earth elements (REE), phosphorous (P)) component (Warren and Wasson, 1979). Such correlations suggest that heavy Cl isotope signatures are characteristic of the Moon as a whole, and Boyce et al. (2015) attributed this large scale Cl isotope fractionation to the degassing of metal chlorides from the molten lunar magma ocean (LMO). In their scenario, the elevated δ^{37}Cl values measured in apatite, within mare basalts, would have been acquired during assimilation of a KREEP-component.

The strong link between elevated δ^{37}Cl values and urKREEP is also supported by the work of Barnes et al. (2016). In their study Barnes et al. (2016) analysed Cl isotopes in apatite from a large range of samples (high- and low-Ti mare basalts, a KREEP-rich basalt, a very high K basalt, as well as Mg- suite plutonic rocks) and observed a similar trend between KREEP-related trace element characteristics and δ^{37}Cl values. One of the samples from this study was the Mg-suite norite 78235, a plutonic rock that was likely not affected by volatile degassing (Barnes et al., 2014), which yielded elevated apatite δ^{37}Cl values of ∼+31.1 ± 1.4 ‰(Barnes et al., 2016). Given that the Mg-suite volatiles were thought to originate from a KREEP component (e.g. McCubbin et al., 2015), this is further evidence for the elevated δ^{37}Cl signature of lunar KREEP material. Barnes et al. (2016) also suggested that KREEP-poor samples, which have lower δ^{37}Cl values compared to KREEP-rich samples, may indicate that the lunar mantle is characterized by terrestrial-like δ^{37}Cl values. Furthermore, Barnes et al. (2016) suggested that the ∼34 to ∼43 km of lunar crustal material (Wieczorek et al., 2013) was sufficiently thick to prevent loss of Cl via degassing, especially given the high solubility of Cl in basaltic melts (Webster et al., 2009) and the likely presence of an early lunar atmosphere. Instead, they propose that during the final stages of LMO solidification (>95 %) crust-breaching impact events exposed KREEP-rich melts to low pressure environments, which promoted the loss of metal chlorides and induced Cl isotope fractionation (Barnes et al., 2016).

Finally, one of the heaviest lunar δ^{37}Cl values, ∼+32 ‰, has been measured

in apatite from the granulite sample 79215, yet, this signature is not thought to be from any process described above (Treiman et al., 2014). This sample is characterized by an elevated P content (∼200 CI chondrite P contents) but by low K or REE contents (∼10 CI; e.g., P/Sm = ∼20). The δD values measured in apatite in this sample, corrected for spallation production of D, are between +350 ‰and +700 ‰(Treiman et al., 2014), which is within the range of values reported for lunar mare basalts (Barnes et al., 2013; Tartèse et al., 2013a). Treiman et al. (2014) suggested that P and the halogens in 79215 were largely added during vapor-phase metasomatism likely originating from impact-induced devolatilization of a KREEP-rich target. Vapor-phase metasomatism is favored given that lunar conditions are too reduced for abundant H_2O or CO_3^{2-} to be present and the lack of supporting evidence for fluid metasomatism (Treiman et al., 2014). REE abundances in this vapor would have been reduced due to vapor-mineral (e.g., merrillite, oxides) interactions. Finally, this residual vapor, rich in P and halogens, interacted with the protolith of 79215 to facilitate the crystallization of apatite with elevated δ^{37}Cl.

Detailed understanding of the individual petrological histories of the rocks investigated in Cl isotope studies is, therefore, critical to deciphering the mechanism(s) of Cl isotope fractionation in lunar melts. In order to investigate the potential processes that contributed to the elevated δ^{37}Cl values observed in lunar apatite, five Apollo 14 samples were studied: high-Al basalts 14053 and 14072, a basaltic clast from breccia 14321, and impact melt rocks 14073 and 14310. The abundance and large size (typically > 50 μm in the longest dimension) of apatite grains in these samples permitted thorough inter-sample variations to be identified, as well as multiple analyses of individual grains, which allowed an assessment of any intra-grain variations.

5.2 Apollo 14

The Apollo 14 mission landed on the Fra Mauro Formation, which is part of the ejecta blanket formed from the excavation of the Imbrium basin (Nemchin et al., 2009). Mare Imbrium is the largest basin-affiliated mare deposit on the Moon (assuming that the Procellarum KREEP Terrane is not an impact feature), and was expected to have excavated original lunar crust material during the Imbrium basin-forming event. It remains unclear, however, which Apollo 14 samples represent true Imbrium ejecta and which are locally derived (Hiesinger and Head, 2006). The consistent dates obtained by ^{40}Ar/^{39}Ar dating on whole rocks and fines (Alexander and Davis, 1974; Turner et al., 1971, 1972) and Rb-Sr dating (Compston et al., 1972a,b; Papanastassiou and Wasserburg, 1971b) of ∼3.87 Ga old were interpreted as representing the timing of the formation of the Imbrium basin (Stöffler and Ryder, 2001; Wilhelms et al., 1987). Recent, high-precision, U-Pb dating on phosphate and zircon in Apollo 14 impact melt breccias has provided an improved estimate for the formation of the Imbrium basin at ∼3.93 Ga (Snape et al., 2016, and references therein). Zircon grains from Apollo 14 lunar breccias, however, have yielded U-Pb dates ranging from ∼4.0 to ∼4.4 Ga, with distinct date peaks at ∼4.35 and ∼4.20 Ga (Meyer et al., 1996; Nemchin et al., 2008), suggesting that a significantly older pre-Imbrium history is recorded by the breccias. The temperature and shock effects associated with the development of the Fra Mauro

	Ages		Geochemical	Features
	$^{40}Ar/^{39}Ar$	Rb-Sr	Group	Crystallization
14053	3.92 ± 0.08[a]	3.96 ± 0.04[b]	C	open
14072	4.04 ± 0.05[c]	3.99 ± 0.09[d]	A –C*	unknown
14053	3.92 ± 0.08[a]	3.96 ± 0.04[b]	B	open
14053	3.88 ± 0.05[f]	3.88 ± 0.04[b]	melt rock	closed
		3.94 ± 0.03[g]		
14053	3.88 ± 0.05[f]	3.84 ± 0.04[h]	melt rock	closed

Table 5.1: Ages for Apollo 14 samples studied here and their geochemical grouping. All ages are in Ga. Data from (a) Husain et al. (1971), York et al. (1972) (b) Papanastassiou and Wasserburg (1971) (c) York et al. (1972) (d) Compston et al. (1972b) (e) Dasch et al. (1987) (f) Turner et al. (1972) (g) Mark et al. (1974) (h) Tatsumoto et al. (1972). *Intermediate between Group A and C.

Formation were, therefore, sufficient to reset $^{40}Ar/^{39}Ar$ and Rb-Sr dates but not to reset the zircon U-Pb systems in all samples (Nemchin et al., 2010).

Some basalts from this region remain the only Apollo samples to record >∼4 Ga volcanism on the Moon (Neal and Kramer, 2006). Basaltic clasts from Fra Mauro indicate a period of 400 million years of volcanism, from ∼4.3 to ∼3.9 Ga (Compston et al., 1972a,b; McKay et al., 1979; Papanastassiou and Wasserburg, 1971b), predating the main period of mare volcanism (Snyder et al., 2000). Volcanics from the Fra Mauro region may, therefore, provide insights into the evolution of the Moon from solidification of the crust, at around ∼4.5 to ∼4.3 Ga (Elkins-Tanton et al., 2011), to the beginning of the main period of mare volcanism which commenced around ∼3.85 Ga (Shearer et al., 2006). Crystallization and/or impact-resetting ages for all the Apollo 14 samples studied here are given in Table 5.1, and range between ∼4.1 Ga and ∼3.8 Ga (Compston et al., 1972a; Dasch et al., 1987; Husain et al., 1971; Mark et al., 1974; Papanastassiou and Wasserburg, 1971b; Tatsumoto et al., 1972; Turner et al., 1972; York et al., 1972).

In addition to their old age, the Apollo 14 basalts are also geochemically distinct, in that they are relatively enriched in Al_2O_3 (11 16 wt.%), leading to their classification as high-Al rocks (Neal and Kramer, 2006; Ridley, 1975). Two petrologic models have been proposed for the formation of these high-Al samples: (1) pristine volcanic rocks, that formed solely through endogenous lunar processes and (2) impact generated melts referred to as melt-rocks (Hui et al., 2011).

Based on incompatible trace element (ITE) abundances and crystallisation ages, the Apollo 14 high-Al basalts have been separated into three distinct groups: Group A (∼4.3 Ga), Group B (∼4.1 Ga), and Group C (∼3.9 Ga) (Neal and Kramer, 2006). Samples within these groups are thought to be related via a closed-system crystal fractionation model for Group A, and an open-system evolution model, involving assimilation of a KREEP component and/or granitic melts, for Groups B and C (Hui et al., 2011; Neal and Kramer, 2006; Neal et al., 1988, 1989a,b). The main geochemical features of the samples studied here are summarised in Table 5.1. The melt-rock samples, 14073 and 14310, are crystallization products of impact-melted lunar regolith and/or feldspathic crust (Schonfeld and Meyer, Charles, 1972), and could have inher-

ited their high-Al contents from melting anorthosite-rich targets (Hui et al., 2011). In such a model, plagioclase would have been one of the first liquidus phases in these melts, explaining the high modal abundance of plagioclase (∼70 %) observed in these melt-rocks (Gancarz et al., 1971). In contrast, for the endogenous, pristine, basalts (14053, 14072, and 14321,1483), the high-Al content is not related to any contribution from the melting of anorthosite-rich rocks and it is more likely that elevated Al contents were directly inherited from the mantle source regions of these basalts (Hui et al., 2011; Neal and Kramer, 2006). These different formation mechanisms have been used to explain the compositional differences between the Apollo 14 pristine basalts and melt-rock samples.

5.3 Analytical techniques

Before secondary ion mass spectrometry (SIMS) measurements, each polished thin-section was carbon-coated and studied using a scanning electron microscope (SEM) at the Open University, following the protocol described in Tartèse et al. (2013a). The SEM was used to locate apatite crystals suitable for ion probe analyses and their surrounding petrography. The carbon coat was then removed and the samples were cleaned with isopropanol and stored in a vacuum oven at ∼55 ℃ for a minimum of 48 hours. Subsequently, samples were coated with ∼30 nm of gold using an EMITECH K575X peltier cooled gold sputter coater. After coating, the samples were immediately loaded into the Cameca NanoSIMS 50L at The Open University. Apatite was located following initial pre-sputtering for several minutes of large (>10 × 10 μm areas), then areas ∼8 μm × 8 μm, containing the target apatite minerals, were pre-sputtered by rastering a ∼40 pA Cs+ beam with an accelerating voltage of 16 kV for ∼2 minutes, in order to clean the target surface. For analysis, the 40 pA probe was then rastered over ∼4 μm × 4 μm areas for ∼4 minutes. No electronic gating was used so as to reduce the analysis time without compromising the precision of isotope measurements. An electron flood gun was used for charge compensation. During analysis the vacuum in the analysis chamber remained around $\sim 5 \times 10^{-9}$ Torr. The NanoSIMS was tuned to achieve a mass resolving power of around >8000, and the negative secondary ions of $^{16}O^{1}H$, ^{18}O, 35Cl, ^{37}Cl, and $^{40}Ca^{19}F$ were collected simultaneously on electron multipliers. ^{19}F ions were also monitored, but only for ∼66s each analysis because of the high count rates.

The abundances of Cl and H_2O were calibrated using the published Cl and H_2O contents of Ap005 and Ap004 reference apatite crystals (McCubbin et al., 2012) and the measured $^{16}O^{1}H/^{18}O$ and $^{35}Cl/^{18}O$ ratios. The standards used were mounted in epoxy resin. Reported uncertainties for abundances incorporate the 2σ uncertainty of the calibration slope and analytical uncertainties associated with individual measurements. Ap004 was used to correct the measured $^{37}Cl/^{35}Cl$ ratios of unknown samples for instrumental mass fractionation (IMF). The Cl isotope composition is reported using standard delta notation with respect to $^{37}Cl/^{35}Cl$ of standard mean ocean chloride. Isotope measurements are reported with associated 2σ uncertainties, which include the reproducibility of the $^{37}Cl/^{35}Cl$ measurements on appropriate standard(s) and the internal precision of each analysis (∼±2 ‰). Background measurements of

H_2O were collected from nominally anhydrous minerals within sample sections (∼100 ppm) which was subtracted from the measured results.

5.4 Results

In the following section, textural descriptions and δ^{37}Cl values, with corresponding Cl and H_2O abundances, are described for each sample. High-resolution BSE images showing the petrographic setting of apatite analysed in this study are shown in Figures 1 to 5. The results of NanoSIMS analyses of apatite for both Cl isotopic compositions and H_2O and Cl abundances are listed in Table 5.2, in addition F abundances for apatite in some samples are listed in Table 5.3.

5.4.1 14053,19

In sample 14053,19, eight analyses were carried out in eight apatite crystals occurring in four separate areas (Figure 5.1A-D). Apatite crystals in this sample are all associated with mesostasis regions. Here, mesostasis regions were identified by the breakdown of fayalite into Fe metal (often described as spongy Fe in the literature (Taylor et al., 2004)) and silica-rich glass, as well as the presence of a diverse range of phases with relatively small grain sizes (<20 μm in the longest dimension; Chapter 2). All of the apatite grains measured here were subhedral to anhedral, >10 μm in the longest dimension, and were found in contact with quenched K-rich glass. The majority of apatite grains in this section were also found in contact with plagioclase, except Ap#4a and Ap#4b (Figure 5.1B). The volatile abundances of apatite in this section overlap with those of Mg- and alkali- suite rocks (Figure 5.6), which are fluorapatites with greater amounts of Cl than H_2O. The δ^{37}Cl values of apatite in 14053,19 range from +15.6 ± 2.2 ‰to +34.3 ± 2.9 ‰. H_2O abundances of apatite in this sample range from 89 ± 4 ppm to 1662 ± 80 ppm (Figure 7A). The Cl concentrations of apatite in this sample range from 1569 ± 2 ppm to 16054 ± 17 ppm (Figure 5.7B). Apatite 4b (Figure 5.1B) shows the highest δ^{37}Cl value (+34.3 ± 2.9 ‰) whilst having the lowest H_2O content (89 ± 4 ppm) and highest Cl content (16054 ± 17 ppm) of any apatite measured from this sample. In contrast, Ap#1 (Figure 5.1A) has the lowest δ^{37}Cl value (+15.6 ± 2.2 ‰) measured from this sample and has the highest H_2O content (1662 ± 80 ppm) and lowest Cl content (1569 ± 2 ppm). Both apatite crystals Ap#4b and Ap#1 are found within mesostasis regions although there is significantly more fayalite reduction surrounding Ap#4b than Ap#1a (Figures 5.1B and 5.1A, respectively). Overall, there is strong correlations between increasing δ^{37}Cl value and (a) decreasing H_2O abundance and (b) increasing Cl abundance for apatite in 14053,19 (Figure 5.7A-B). There is little intra-region variation, in terms of δ^{37}Cl, in this section except for Area #1 in which the two analyses yielded a difference of ∼12 ‰. The two heaviest values (>+32 ‰) in this section are from two apatite grains within the same region (area 4, Figure 5.1B), which displays the highest proportion of reduction-related texture. These apatite also display resorbed edges compared to apatites within areas 1 (Figure 5.1A) and 5 (5.1C) which are characterized by δ^{37}Cl

Sample	δ^{37}Cl (‰)	2σ	Cl (ppm)	2σ	H_2O (ppm)	2σ
Sample 14053,19						
14053 A1 Ap#1	15.6	2.2	1569	2	1662	80
14053 A1 Ap#2	27.1	2.1	1967	2	601	29
14053 A4 Ap#4b	32.5	2.9	13332	14	218	11
14053 A4 Ap#4a	34.3	2.9	16054	17	89	4.3
14053 A5 Ap#5a	22.6	3.1	3292	4	526	25
14053 A5 Ap#5b	27.9	3.0	7109	8	743	36
14053 A8 Ap#8a	24.0	3.1	2251	3	779	38
14053 A8 Ap#8b	20.8	3.1	3263	4	1292	62
Sample 14072,13						
14072 A3 Ap#1	16.3	2.9	14759	15	140	7
14072 A3 Ap#1	19.7	3.0	8589	10	189	9
14072 A4 Ap#1	20.0	3.0	4167	5	117	6
14072 A6 Ap#1	40.0	2.9	10737	12	167	8
14072 A7 Ap#3	28.8	2.9	9580	11	160	8
Sample 14321,1482						
14321,1482 A3 Ap#1a	28.6	1.1	5117	9	27	1
14321,1482 A3 Ap#1b	24.2	1.1	5549	10	34	1
14321,1482 A4 Ap#1a	25.4	1.0	7897	14	140	5
14321,1482 A5 Ap#2a	20.1	0.9	6414	10	27	1
Sample 14073,9						
14073 A11 Ap#1	27.5	2.6	1241	2	346	17
14073 A11 Ap#2	23.7	2.3	1421	2	419	20
14073 A11 Ap#3	24.1	2.2	1648	2	346	17
14073 A11 Ap#4	21.0	2.2	1479	2	360	17
14073 A11 Ap#5	22.5	2.3	1254	2	317	15
14073 A12 Ap#a	16.5	2.2	4317	5	1081	52
14073 A12 Ap#b	27.7	2.0	4713	5	766	37
14073 A12 Ap#c	22.8	2.1	4021	5	572	28
14073 A12 Ap#d	16.5	3.1	580	1	893	43
14073 A17 Ap#a	22.3	2.0	6157	7	929	45
14073 A17 Ap#b	24.4	1.9	16149	18	291	14
14073 A18 Ap#a	34.3	2.4	2097	3	588	28
14073 A19 Ap#a	36.9	2.1	12146	13	493	24
14073 A19 Ap#b	25.8	1.9	8311	9	598	29
14073 A19 Ap#c	25.7	1.9	8033	8	649	31
Sample 14310,171						
14310 A1 Ap#1	14.6	1.6	6962	12	234	8
14310 A1 Ap#2	15.1	1.7	4597	8	179	6
14310 A2 Ap#1a	14.6	1.6	11256	19	354	11
14310 A2 Ap#1b	22.8	2.0	9992	18	105	4
14310 A2 Ap#1c	25.3	2.0	10654	19	95	3
14310 A2 Ap#1d	18.6	2.0	10121	19	95	3
14310 A5 Ap#1	18.2	2.1	7238	13	251	8

Table 5.2: Measured Cl isotopic values (‰), Cl (ppm), and background corrected H_2O (ppm) abundances of apatite in the Apollo 14 samples analyzed in this study

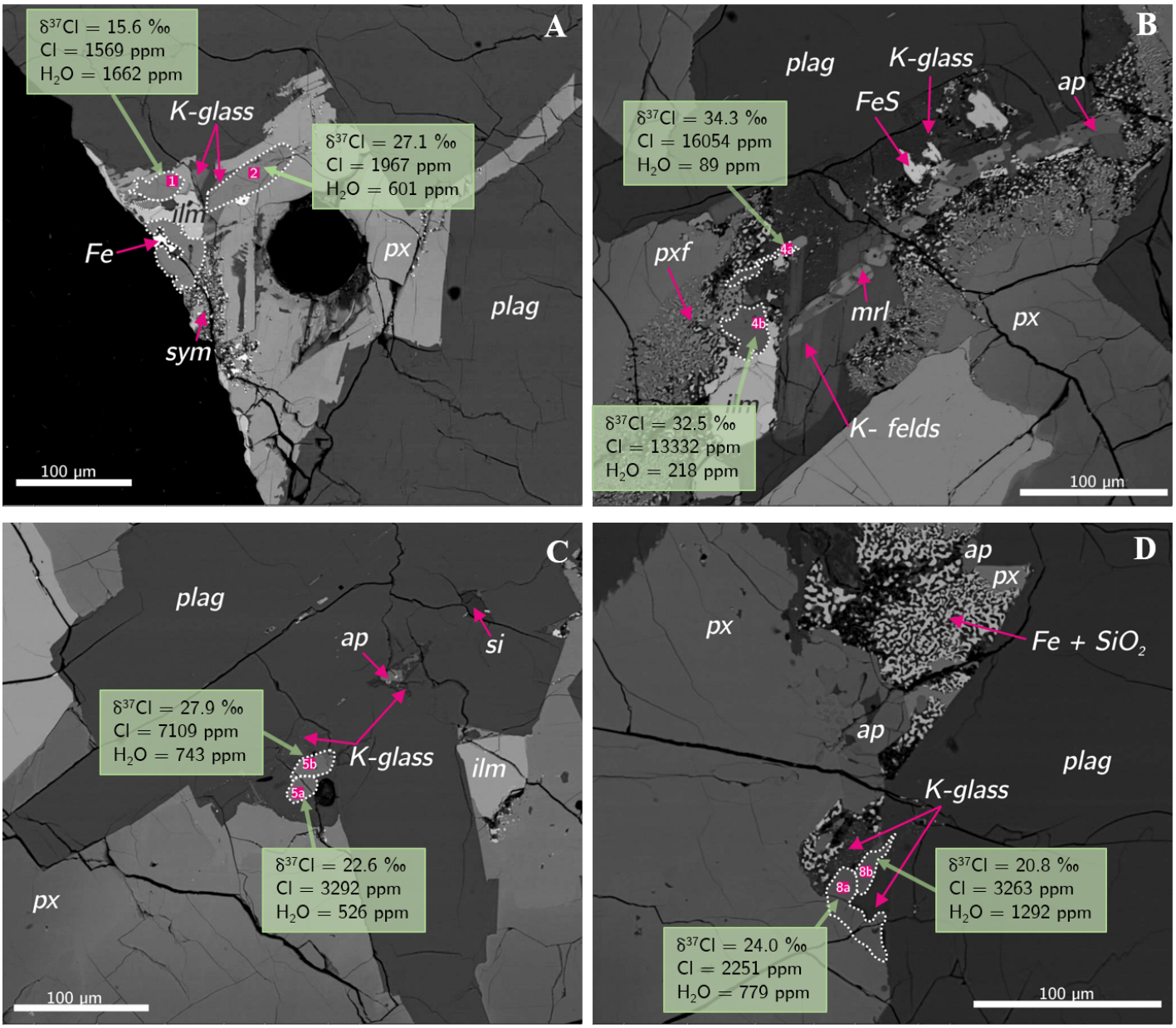

Figure 5.1: BSE images of apatite grains analyzed in 14053,19 and surrounding mineralogy. (A) Area 1, (B) Area 4, (C) Area 5, (D) Area 8. Apatite grains analysed in this study are outlined with dashed lines. Analysis points labelled with pink boxes and number corresponding to analysis. Nomenclature of mineral abbreviations as follows: plag = plagioclase, px = pyroxene, ilm = ilmentite, sym = symplectite texture, mrl = merrillite, si = silica, ap = apatite, K-glass = K-rich glass.

values around +23 to +28 ‰(except Ap#1 in Figure 5.1A). Apatite within area 8 also appear to have resorbed edges (Figure 5.1D), and have δ^{37}Cl values of between +21 and +24 ‰. The more euhedral apatite grains within areas 1 and 5 have higher H_2O contents (>500 ppm) compared to H_2O abundances measured in the andehral apatite grains within area 4 (<200 ppm). The highest H_2O contents (>700 ppm), however, are found in, sunhedral, apatite grains in area 8. The highest Cl contents have been measured in the, subhedral, grains found in area 4.

5.4.2 14072,13

In sample 14072,13, five analyses were carried out in five distinct apatite crystals occurring in four different areas (Figures 5.2A-E where Band C are part of one larger area). All apatite crystals were found within mesostasis regions that were texturally similar to those in 14053,19, although those in 14072,13 generally contained a larger fraction (>30 modal %) of spongy Fe. Large (>20 μm) euhedral to sub-euhedral apatite yielded δ^{37}Cl values ranging from +16.3 ± 2.9 ‰to +40.0 ± 2.9 ‰, with Cl and H_2O abundances ranging from 4167 ± 5 to 14759 ± 15 ppm and 117 ± 6 to 189 ± 9 ppm, respectively (Figures 5.7A –B). The volatile abundances of apatites in this thin-section overlap with those of Mg- and alkali-suite rocks (Figure 5.6). Unlike sample 14053,19, there is no clear correlation between apatite Cl or H_2O abundance and the associated δ^{37}Cl values in 14072,13 (Fig 8), which may be related to the limited number of analyses. All of the apatite grains in this section are in contact with spongy Fe and K-rich glass, while the mesostasis pockets are contained within plagioclase. The lower δ^{37}Cl values of around +16 to +20 ‰have been measured in euhedral apatite grains (Figures 5.2B-C), while the heaviest δ^{37}Clvalues (+28.8 ± 2.9 ‰and +40.0 ± 2.9 ‰) are associated with anhedral crystals (Figure 5.2D –E). This relationship is broadly consistent to what we observed in sample 14053,19.

5.4.3 14321,1482

In sample 14321,1482, four analyses were carried out in three apatite crystals occurring in three different areas (Figure 5.3A-C). Apatite crystals in 14321,1482 are euhedral to subhedral, >∼10 μm in the longest dimension, and were located in mesostasis regions, which contain spongey Fe in Areas 3 and 5 (Figures 5.3A and 5.3C), fayalite, silica, and K-rich glass (Figures 5.3A –C). The apatite δ^{37}Cl values range from +20.1 ± 0.9 ‰to +28.6 ± 1.1 ‰and are associated with fairly homogeneous Cl abundances of ∼5000-8000 ppm and very low H_2O contents <150 ppm (Figures 5.7A-B). The limited number of analyses in 14321,1482 are consistent with the Cl abundance and chlorine isotope measurements made of most of the apatite grains from 14053 and 14072. The lowest δ^{37}Cl value in this sample is from Area 5 (Figure 5.3C) which is the most anhedral apatite grain in this section. This grain also has altered edges and is in direct contact with spongey Fe. The other apatite grains within this section have δ^{37}Cl values between +24 and +28 ‰are all euhedral.

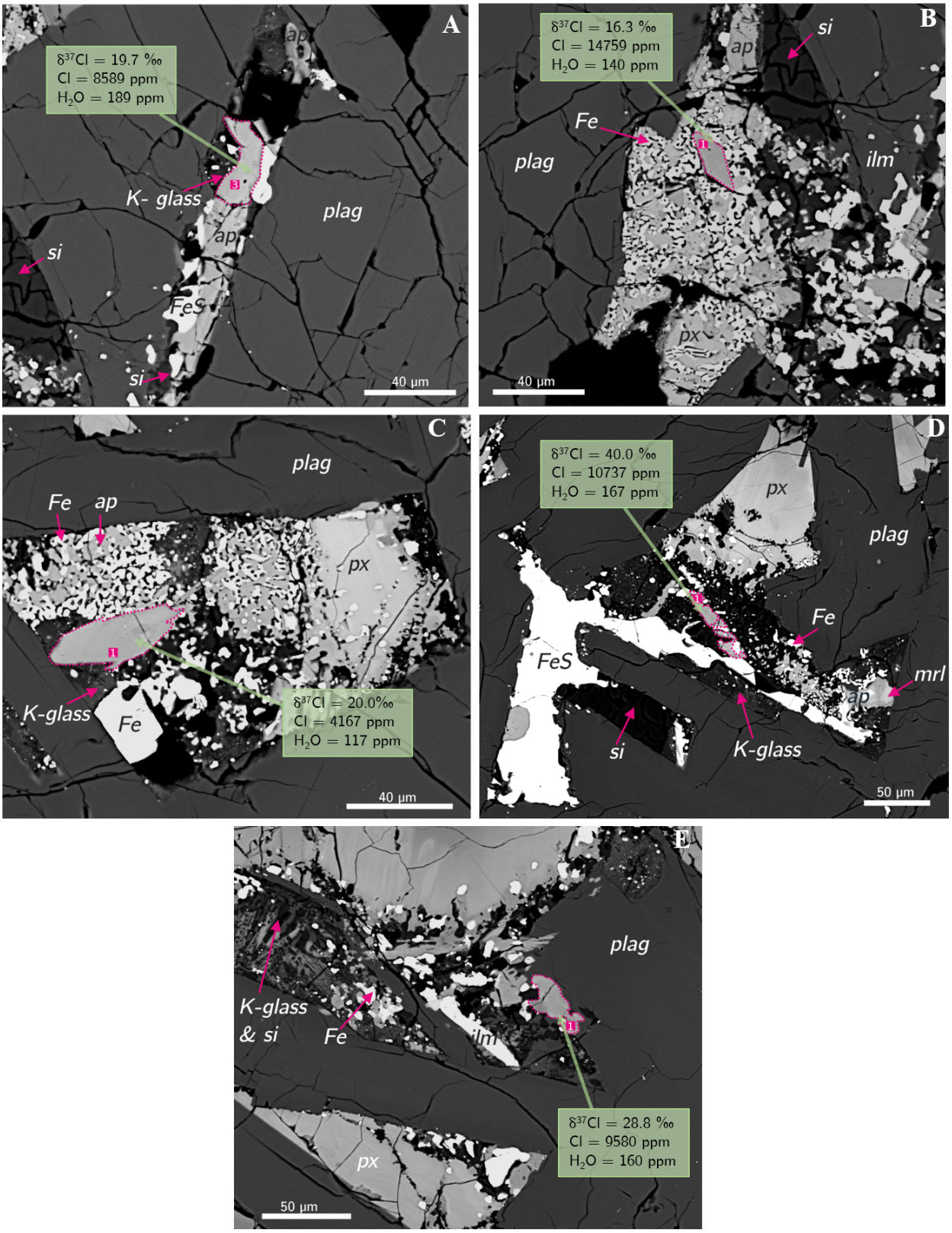

Figure 5.2: BSE images of apatites analyzed in 14072,13 and surrounding mineralogy. (A) Area 7, (B) Area 3, (C) Area 3, (D) Area 4, (E) Area 6. Nomenclature same as in Figure 5.1.

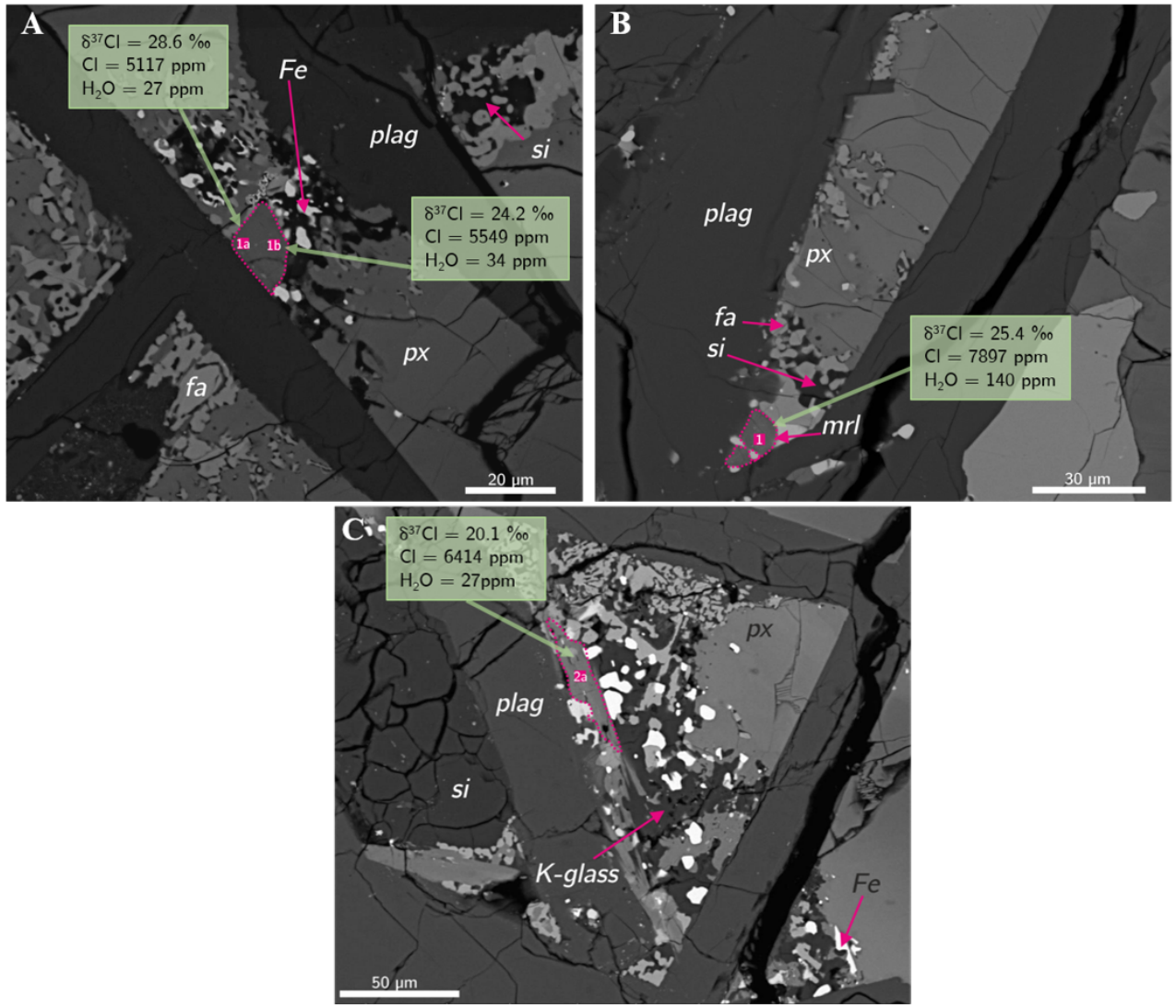

Figure 5.3: BSE images of apatites analysed in 14321,1482 and surrounding mineralogy. (A) Area 3, (B) Area 4, (C) Area 5. Nomenclature same as in Figure 5.1.

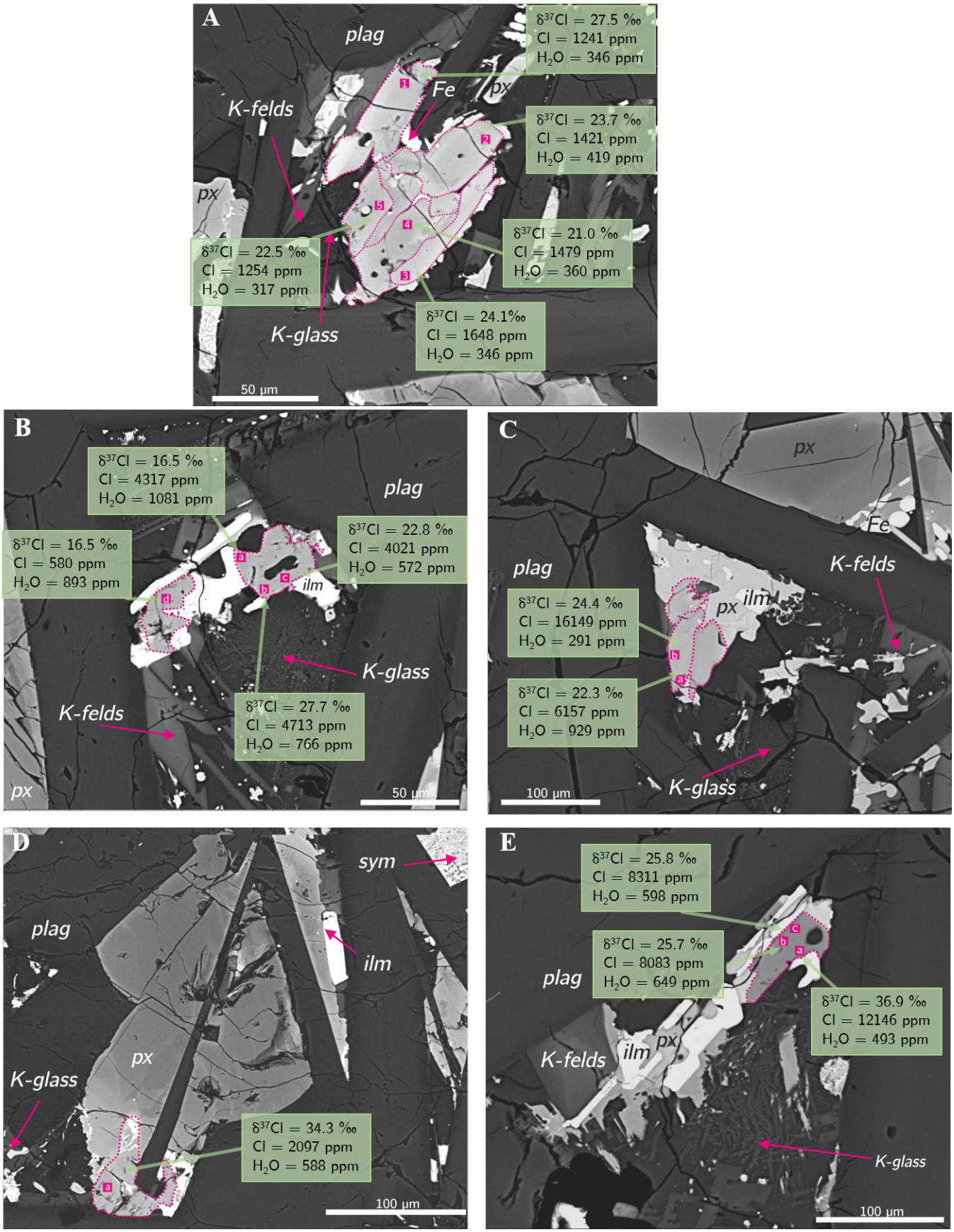

Figure 5.4: BSE images of apatites analysed in 14073,9 and surrounding mineralogy. (A) Area 11, (B) Area 12, (C) Area 17, (D) Area 18, (E) Area 19. Nomenclature same as in Figure 5.1.

5.4.4 14073,9

In sample 14073,9, fifteen analyses were carried out in nine apatite crystals occurring in five different areas (Figure 5.4A –E). All apatite grains in this sample were located in mesostasis regions, identified by the presence of K-rich glass. The mesostasis regions in 14073, however, are texturally and compositionally different to those in 14053 and 14072, as they do not display spongy Fe, but instead contain interstitial K-rich glass associated with K-feldspar (e.g., Figures 5.4B and 5.4E). The apatite grains analyzed here are subhedral, up to 50 μm in the longest dimension, and are all in contact with K-rich glass, with some containing melt inclusions (e.g., Figures 5.4B and 5.4E). The analyzed apatite grains are H_2O-poor and Cl-rich compared to typical mare basalts (Figure 5.6). The δ^{37}Cl values of apatite from sample 14073,9 display a large range from +16.5 ± 2.2 ‰to +36.9 ± 2.1 ‰, most of the analyses clustering between ∼+21 and +28 ‰(Figure 5.7A –B). The Cl and H_2O abundances of these apatite range from 580 ± 1 ppm to 16149 ± 18 ppm and 291 ± 14 ppm to 1081 ± 52 ppm, respectively. Generally, the higher δ^{37}Cl values correspond to low to moderate H_2O contents, while there is no real correlation between δ^{37}Cl values and Cl abundances. In some mesostasis areas, such as area 11 (a cluster of apatite crystals) in which 5 analyses were carried out (Figure 5.4A), apatite crystals are fairly homogeneous in terms of abundances of H_2O (317 ± 15 ppm to 419 ± 20 ppm) and Cl (1241 ± 2 ppm to 1648 ± 2 ppm) and Cl isotopic composition (+21.0 ± 2.2 ‰to 27.5 ± 2.6 ‰). In other areas, the intra-region variations of δ^{37}Cl are high, ranging from +16.5 ± 2.2 ‰to +27.7 ± 2.0 ‰within a single apatite grain (Ap#12; Figure 5.4B) in area 12, and between +25.7 ± 1.9 ‰and +36.9 ± 2.1 ‰in a single grain analyzed in area 19 (Figure 5.4E).

5.4.5 14310,171

Seven analyses were made across four apatite crystals in three areas (Figures 5.5A –C) in thin section 14310,171. Generally apatite was found in mesostasis regions in this sample, although these areas noticeably lack the large amount of K-rich glass observed in other Apollo 14 mesostasis regions, particularly 14073,9. The apatite grains in 14310,171 were euhedral to subhedral, and varied in size from >∼30 μmin the longest dimension to ∼10 m in the longest dimension. Apatite is associated with pyroxene, plagioclase, K-feldspar, and some ilmenite (Figure 5.5A & C). The δ^{37}Cl values for apatite in this sample range from +14.6 ± 1.6 ‰to +25.3 ± 2.0 ‰, and apatite Cl and H_2O abundances range from 4597 ± 8 ppm to 11256 ± 19 ppm and 95 ± 3 to 354 ± 11 ppm, respectively. Similarly to apatite in sample 14073,9, elevated δ^{37}Cl values tend to be associated with lower H_2O abundances (Figure 5.8A). In this sample, the higher δ^{37}Cl values also tend to be associated with higher Cl abundances (Figure 5.8B). As in sample 14073,9, the degree of intra-region heterogeneity in δ^{37}Cl values varies across the sample, particularly in area 4 (Figure 5.5C). The euhedral apatite grains in this section have the lower δ^{37}Cl values <+18 ‰, while the heavier Cl isotope values are associated with a smaller (<10 μm) subhedral apatite grain, apart from those in area 1.

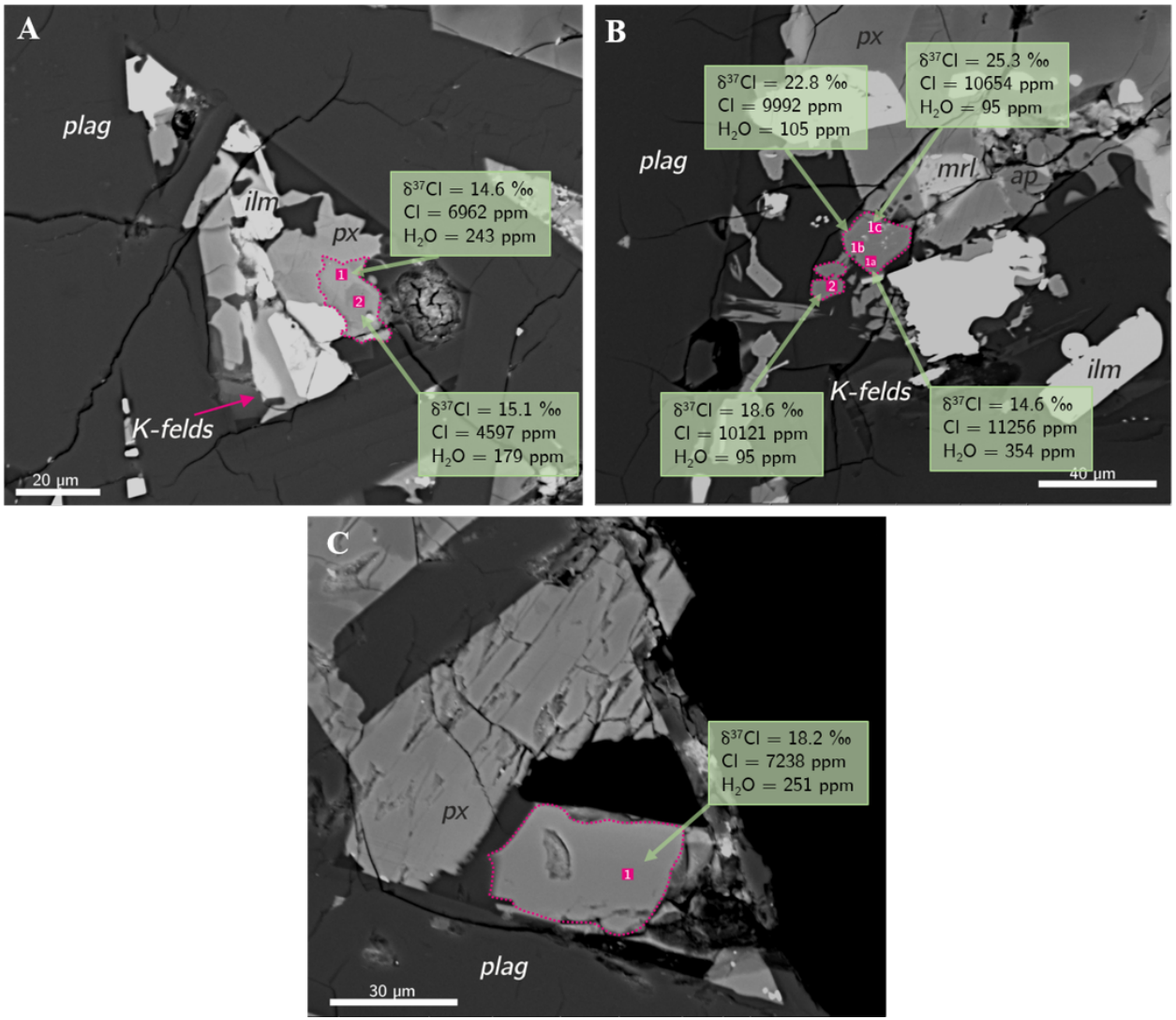

Figure 5.5: BSE images of apatites analysed in 14310,171 and surrounding mineralogy. (A) Area 1, (B) Area 2, (C) Area 4. Nomenclature same as in Figure 5.1.

Sample	F (wt.%)	2σ
14073 A11 Ap#1b	3.04	0.03
14073 A18 Ap#1	3.46	0.04
14073 A19 Ap#1a	2.73	0.03
14072 A3 Ap#2	3.53	0.04
14072 A3 Ap#3	3.81	0.04
14072 A4 Ap#1	3.37	0.04
14072 A6 Ap#1	2.79	0.03
14072 A7 Ap#1	3.00	0.03
14053 A1 Ap#1	3.38	0.04
14053 A1 Ap#2	3.18	0.03
14053 A4 Ap#1a	2.64	0.03
14053 A4 Ap#1b	2.44	0.03
14053 A5 Ap#1	3.19	0.03
14053 A5 Ap#2	3.00	0.03

Table 5.3: F (wt.%) measured by NanoSIMS in apatites in the Apollo 14 samples analyzed in this study.

5.5 Discussion

This study has provided a comprehensive dataset on the chlorine isotopic compositions of apatite from Apollo 14 samples, including both igneous high-Al basalts and impact melt-rocks. This study also significantly increases the pre-existing data set for the Cl isotope compositions of lunar samples. As shown in Figure 5.7, the δ^{37}Cl values measured in apatite in the studied samples all fall within a broad range of δ^{37}Cl between around +15 and +35 ‰, and are consistent with the upper end of the range of δ^{37}Cl values measured in high- and low-Ti mare basalts and with those obtained on KREEP-rich samples (Barnes et al., 2016; Boyce et al., 2015; Sharp et al., 2010a; Tartèse et al., 2014a; Treiman et al., 2014). The heaviest δ^{37}Cl values around +35 to +40 ‰measured in apatite in samples 14053, 14072 and 14073 are comparable to the heaviest δ^{37}Cl values reported for lunar samples previously, which were generally measured in apatite from KREEP-rich samples representing the lunar crust ($\sim$+25 to $\sim$+36 ‰; Treiman et al., 2014; Barnes et al., 2016). The unique petrogeneses of the Apollo 14 samples studied here provides an opportunity to evaluate the potential mechanisms for Cl isotope fractionation under lunar magmatic conditions.

5.5.1 Volatile abundances in Apollo 14 apatite

All of the apatite analyzed here are fluorine rich, with compositions congregating around the fluorine apex of the apatite X-site ternary (Figure 5.6). Volatile compositions of apatite in samples 14072, 14310, and 14321 plot almost exclusively along the F-Cl binary, in the field typically occupied by apatite from samples from the lunar highlands, while apatite compositions for 14053 and 14073 have a greater H_2O compo-

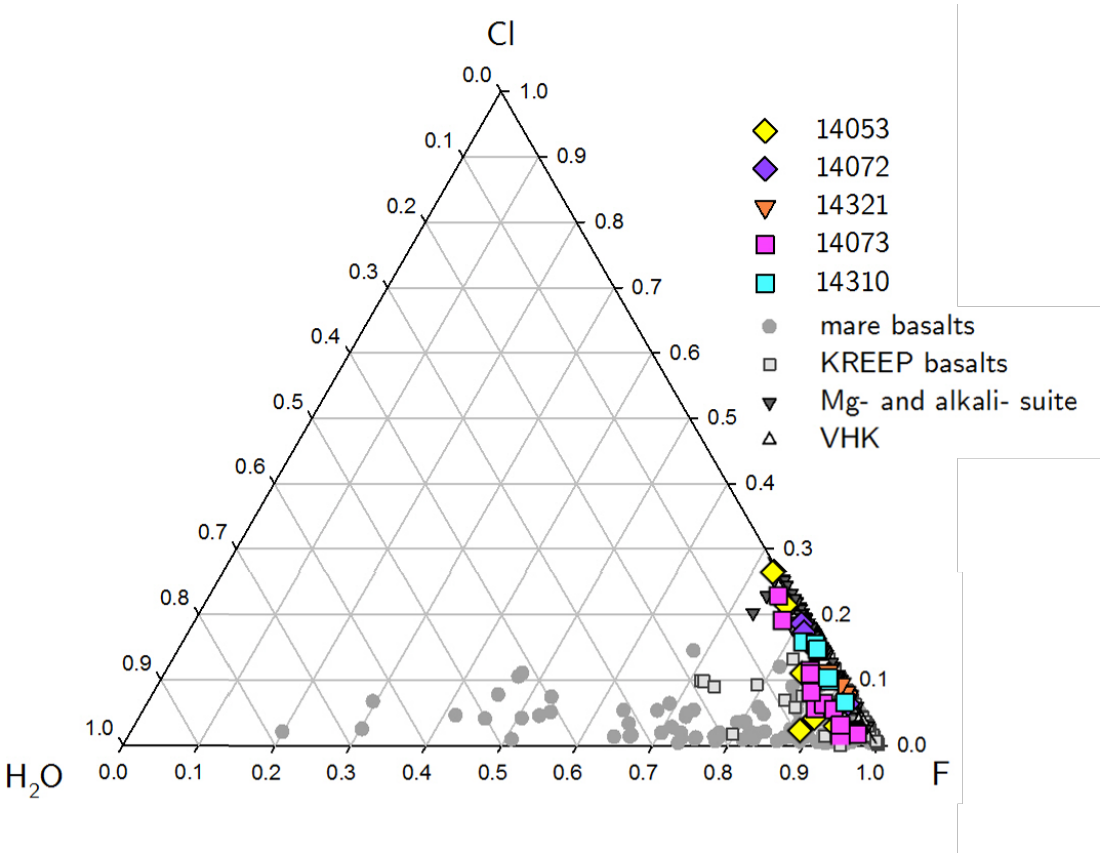

Figure 5.6: Ternary diagram of apatite X-site occupancy (mol %), assuming that X-site is completely filled with F + Cl + H_2O. Fields for mare basalts (pink), KREEP basalts (blue), and Mg –and alkali –suite rocks (orange) represented by dashed boxes.

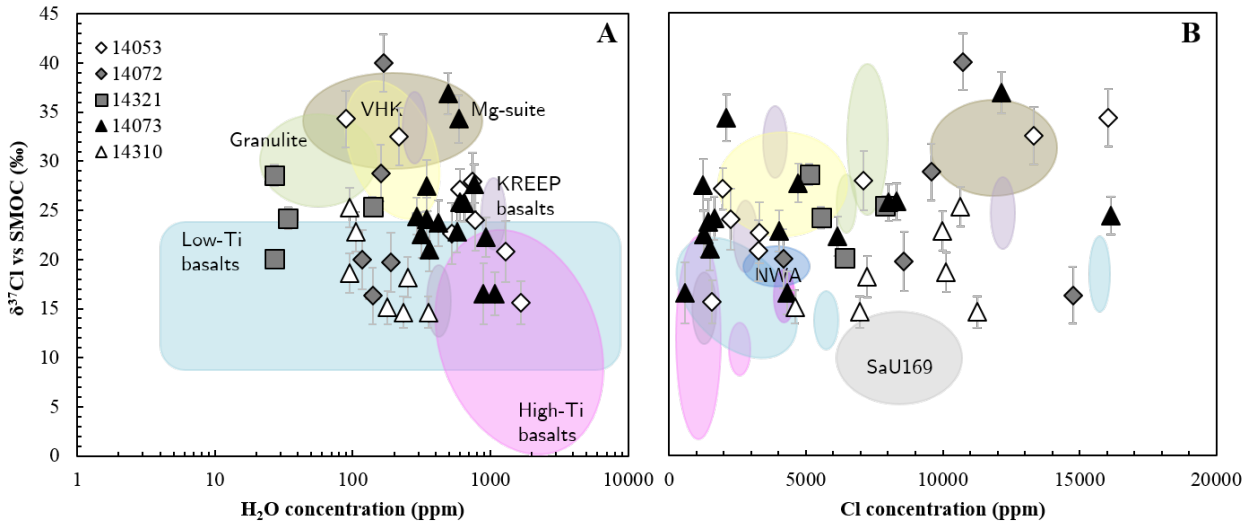

Figure 5.7: All available δ^{37}Cl data plotted against (A) H_2O (ppm), and (B) Cl (ppm). Literature data from Barnes et al. (2016); Boyce et al. (2015); Sharp et al. (2010a); Tartèse et al. (2014a); Treiman et al. (2014). NWA refers to KREEP-clast in NWA4472 from Tartèse et al. (2014a).

nent, and are consistent with apatite compositions in KREEP basalts and H_2O-poor apatite in mare basalts Barnes et al. (2013, 2014); Boyce et al. (2010); Greenwood et al. (2011); McCubbin et al. (2011, 2010a,b, 2015b); Robinson et al. (2016); Tartèse et al. (2013a, 2014a,c).

The range of water content measured within apatite in high-Al basalt 14053 (∼90-1660 ppm H2O) is similar to the range obtained in previous studies, from around 200 ppm up to ∼2400 ppm H_2O (Boyce et al., 2010; Greenwood et al., 2011; McCubbin et al., 2010a; Pernet-Fisher et al., 2014). Similarly, previously measured apatite Cl contents of ∼0.17 to 0.47 wt.% in 14053 (Boyce et al., 2010; McCubbin et al., 2010a) are consistent with the low end of the range of apatite Cl abundances we measured (∼0.16 to 1.6 wt.%).

Determining the volatile contents of the melt from which apatite crystallized, based on the measured volatile contents of apatite, is not trivial given that F, Cl, and OH (reported here as H_2O) share the crystallographic X-site within the apatite crystal lattice, and as such they are essential structural components, meaning that simple Nernst partitioning behaviour cannot be applied to volatile partitioning into apatite (Boyce et al., 2014; McCubbin et al., 2015a). Using the model for back-calculating melt H_2O contents, derived in Chapter 2, estimates for 14053 range from 0.09 to 0.21 wt.% melt H_2O while 14072 is estimated to have lower amounts of water in the melt at 0.02 to 0.08 wt.%. Melt H_2O contents for 14073 are similar to 14053 at 0.10 to 0.27 wt.%. In the case of 14053 and 14073 there is considerable water present at the time of apatite formation

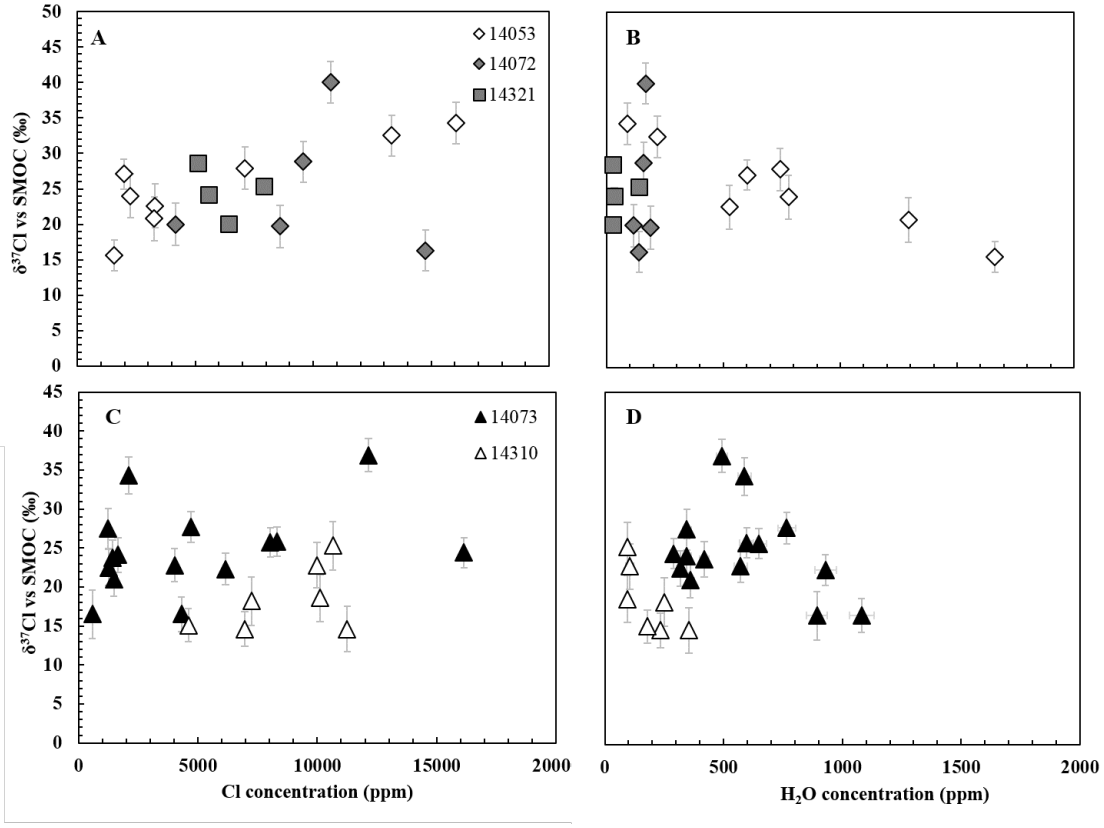

Figure 5.8: δ^{37}Cl data for volcanic samples (see text) 14053, 14072, 14321, and 14321,1482 plotted against (A) Cl and (B) H_2O abundances, and for impact melt samples (see text) 14073 and 14310 plotted against (C) Cl concentration (D) H_2O abundances.

5.5.2 Linking assimilation of KREEP to the Cl isotope composition of magmatic apatite

Magmatic degassing of chlorine, in the form of metal chlorides, from the LMO has been invoked to explain the elevated chlorine isotopic compositions of lunar samples (Boyce et al., 2015; Barnes et al., 2016). Both hypotheses result in an enrichment of ^{37}Cl in the KREEP-rich residual melts of the LMO, and are supported by the positive correlations observed between bulk-rock incompatible trace element contents (REE, Th) and apatite δ^{37}Cl values (Figure 5.9). Our analyses of apatite in five Apollo 14 samples generally support the existence of a KREEP-component characterized by an elevated δ^{37}Cl value (Figure 5.9). Petrologically, the high-Al pristine basalts 14053, 14072 and 14321,1482 are all believed to have assimilated an evolved KREEP-rich component even though they are not *sensu stricto* KREEP-basalts (Hui et al., 2011; Neal et al., 1988; Neal and Kramer, 2006). The impact melt samples 14073 and 14310 also contain a significant KREEP component (El Goresey et al., 1971; McKay et al., 1979) but are thought to have formed via the melting of feldspathic regolith or anorthosite material (Hui et al., 2011; Schonfeld and Meyer, 1972). The Apollo 14 samples, therefore, add supporting evidence for a heavy δ^{37}Cl KREEP component in the Moon. The large range of δ^{37}Cl values at the sample-scale, however, also suggests that additional processes may have contributed to altering apatite δ^{37}Cl values.

5.5.3 The role of volatile degassing from magmatic melts

Chlorine is incompatible in the major silicate minerals that crystallize from basaltic melts (e.g. Webster et al., 2009). When Cl reaches saturation it will partition into the vapor phase, and will degas from basalts (Boyce and Hervig, 2008; Patiño Douce and Roden, 2006; Shinohara, 2009; Ustunisik et al., 2011, 2015; Webster et al., 1999). Sharp et al. (2010b) suggested that under anhydrous lunar magmatic conditions the bonding potentials of both isotopes (^{35}Cl and ^{37}Cl) are similar. The kinetic loss of ^{35}Cl is, therefore, not cancelled out by ^{37}Cl bond incorporation (e.g. HCl(g)). The melt is then enriched in ^{37}Cl and, therefore, explains the heavy δ^{37}Cl values acquired by late-crystallising apatite. Theoretical modelling of Cl isotope fractionation during degassing of metal chloride species indicates that a δ^{37}Cl increase of up to 20 ‰is expected for 95 % Cl loss as $FeCl_2$ (Sharp et al., 2010a; Ustunisik et al., 2015) which could, therefore, explain the range in δ^{37}Cl values exhibited by apatite from most mare basalt samples (Barnes et al., 2016; Boyce et al., 2015; Sharp et al., 2010a; Tartése et al., 2014a). It is important to note that the H << Cl conditions required in the Sharp et al. (2010a) model does not necessarily imply that lunar melts were dry, but it does require H << Cl at the time of Cl degassing.

Based on their experimental study of volatile degassing from lunar magmas, Ustunisik et al. (2015) argue that the first apatite to crystallize from a melt undergoing volatile degassing should contain a few tens of mol.% of Cl and OH, and that apatite compositions would progressively move towards becoming more F-rich as degassing progresses. Apatite compositions from samples 14053 and 14073 exhibit the opposite relationship compared to that expected for apatite crystallizing from a melt experienc-

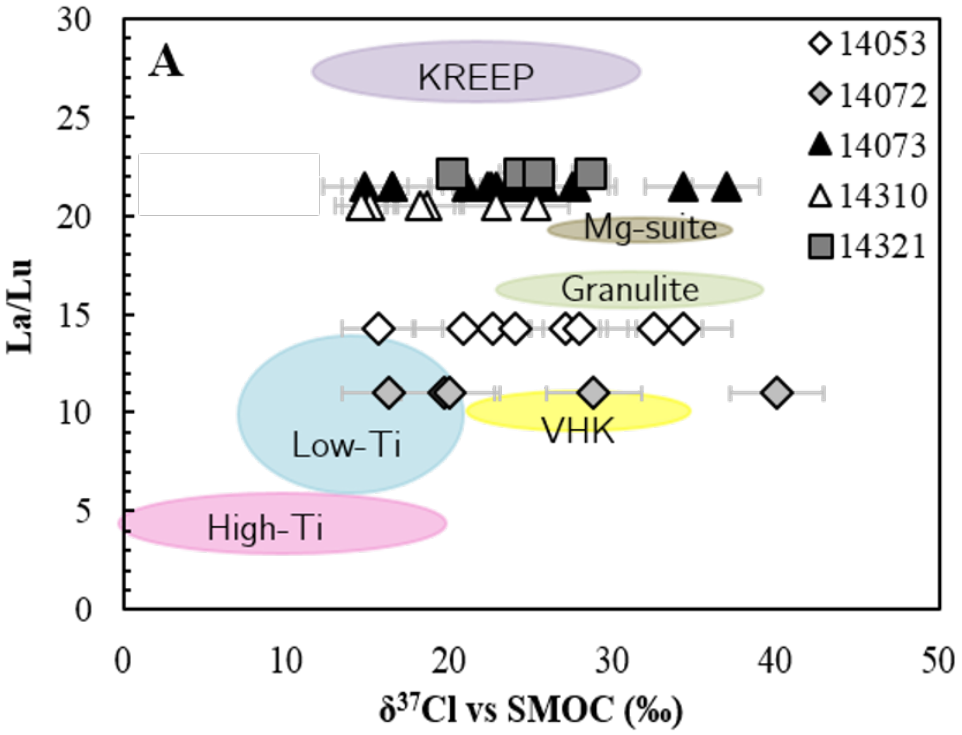

Figure 5.9: All available δ^{37}Cl data for Apollo samples plotted against bulk rock La/Lu. La and Lu abundances averaged from data taken from Lunar Sample Compendium. Literature data Barnes et al. (2016); Boyce et al. (2015); Sharp et al. (2010a); Tartèse et al. (2014a); Treiman et al. (2014).

ing volatile degassing (Ustunisik et al., 2015), with higher F/Cl ratios accompanying high OH contents (XOH; Figure 5.10). Apatite compositions in the other three samples do not show any relationship between F/Cl ratios and XOH (Figure 5.10A). Overall this suggests that apatite in the studied samples did not crystallize from melts undergoing volatile degassing, and that processes other than degassing were responsible for the broad trend of decreasing δ^{37}Cl with increasing F/Cl ratio displayed by apatite in the studied samples (Figure 5.10B).

5.5.4 Preferential incorporation of Cl into apatite

A potential caveat when considering apatite Cl isotope values is the preferential uptake of ^{37}Cl over ^{35}Cl into the apatite crystal structure, especially given the positive trend between Cl abundance and δ^{37}Cl observed here. Under equilibrium conditions, *ab initio* modelling reports a stronger concentration of ^{37}Cl in substances bonded with +2 cations (i.e. $FeCl_2$, $MnCl_2$) compared to those bonded with only +1 cation such as NaCl (Schauble et al., 2003). At room temperature, this leads to a fractionation of ∼2 –3 ‰in silicates (where Cl atoms have +2 cation nearest neighbours) compared to the co-existing brine (Schauble et al., 2003). This is supported by the heavier δ^{37}Cl values observed in terrestrial hydrothermal silicates and mid-ocean ridge basalts (Magenheim et al., 1995). In apatite, Cl forms a central bond with three Ca atoms (Hughes and Rakovan, 2002), and should preferentially uptake ^{37}Cl at room temperature assuming apatite behaves similar to silicates. The partition function ratio of ^{37}Cl –^{35}Cl, however, is greatly reduced with increasing temperature (Schauble et al., 2003), and would presumably tend towards 0 at temperatures applicable to lunar apatite formation. In addition, subtle variations of δ^{37}Cl by 2 –3 ‰are within the precision currently available for individual Cl isotope measurements in apatite.

5.5.5 Diffusion-controlled isotope fractionation

The majority of apatite grains in the samples are found in contact with glass, which may encourage kinetic isotope fractionation. If there was a chemical potential gradient in the apatite-glass system (in terms of Cl abundance), grain-boundary diffusion of Cl ions may occur along the phase interface (Zhang and Ni, 2010). There is no evidence to suggest that Cl diffusion from melt to apatite would lead to isotope fractionation, given the low preferential uptake of ^{35}Cl (into apatite) expected, and would create a maximum <∼2 ‰lighter Cl isotope signature (Schauble et al., 2003). If, during cooling, ^{35}Cl diffused from apatite to melt then isotopic zonation alongside light Cl isotopic ratios in the melt would be expected. There is no experimental evidence to support isotope fractionation in this way, however, a significant gradient would be required to drive high levels of isotope fractionation from Cl diffusion out of apatite. If this mechanism had occurred then correlation between larger grain sizes and isotope fractionation would be expected, although given the 2D nature of thin sections total diffusion distance cannot be measured to provide further constraint on this.

In the absence of a chemical potential gradient, if there is a δ^{37}Cl difference between apatite and the glass, then self-diffusion may occur (Lesher, 2010), which is

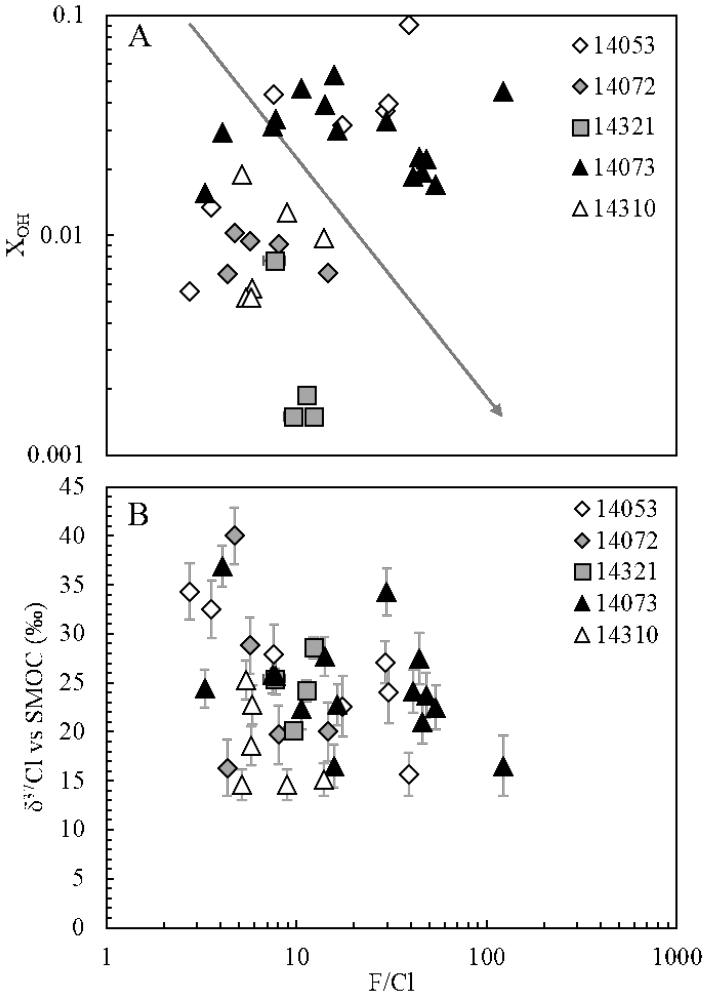

Figure 5.10: Plot of F/Cl (mol %) ratio against OH (mol %) for samples studied here. The model by Ustunisik et al. (2015), which suggests that degassed magmas would crystallise apatite with higher F/Cl ratios and very low OH contents, is indicated by the black arrow on the plot (which represents the ideal from this data set). For F contents not measured were calculated by difference assuming that the apatite X-site is filled with only F, Cl, and OH.

referred to here as diffusion-controlled fractionation. We know that diffusion-controlled isotopic fractionation can lead to large cation fractionations (∼20 ‰) in silicate melts at high temperatures (∼1450 °C; Watkins et al., 2011); however, scarce data exist for Cl isotope fractionations under these conditions. Experiments conducted at low temperature in aqueous environments have shown that δ^{37}Cl variations of up to 2 ‰could be produced by diffusion-controlled fractionation (Eggenkamp and Coleman, 2009). Not surprisingly, experiments conducted at higher temperatures >∼550 °C yielded lower Cl isotope fractionations (Herzog and Klemm, 1958). This suggests that diffusion-controlled isotope fractionation would produce, at best, <2 ‰variation of δ^{37}Cl values. Any potential effect of diffusion-controlled fractionation if it occurred is, therefore, likely to be masked by analytical uncertainty. In any case, such a process cannot explain the large isotope variations (>10 ‰) observed in these samples.

5.5.6 Vapor-phase interactions

To date, the only experimental study in which large Cl isotope fractionations (9 ‰) have been observed in terrestrial-like systems was related to volcanic fumaroles (Sharp et al., 2010a). These experiments produced δ^{37}Cl signatures overlapping with δ^{37}Cl values, around 9 to 12 ‰, measured in high-temperature fumaroles on Earth (Barnes et al., 2009), where near-surface isotope fractionation is thought to have occurred (Sharp et al., 2010a). In this scenario, heavy δ^{37}Cl signatures originate from the distillation of $H^{35}Cl$ from steam. According to Sharp et al. (2010a), this requires a large crater lake or hydrothermal system that creates disequilibria in the fumarole, leading to a two-way H_2O system (Sharp et al., 2010a). Localized fumarolic activity has been hypothesized for the Moon (Krähenbühl et al., 1973; Nunes and Tatsumoto, 1973), which might call upon a similar mechanism to that of Sharp et al. (2010a) to explain the elevated δ^{37}Cl values measured.

Near-surface fractionation of Cl isotopes via Cl evaporation (Huang et al., 1999) has been suggested as a potential mechanism to induce such fractionation in terrestrial systems (Gola et al., 2005), which is supported by modelling work (Richet et al., 1977), and thought to be responsible for elevated signatures in lunar granulite 79215 (Treiman et al., 2014).

It is, therefore, conceivable that a volatile-rich vapor, enriched in ^{37}Cl, interacted with the late-stage Apollo 14 melts, similar to what has been proposed by Treiman et al. (2014) to account for elevated apatite δ^{37}Cl values in granulite 79215. Such a process would create a heterogeneous increase/decrease of apatite δ^{37}Cl values and Cl contents depending on the timing and degree of interaction. It has been argued that subsolidus interaction with solar-wind hydrogen in basalts 14053 and 14072 during a high temperature metasomatic event induced important mineralogical changes, particularly in mesostasis areas (Taylor et al., 2004). These authors showed that apatite in contact with intensely reduced fayalite underwent secondary changes, notably characterized by higher La_2O_3 and Ce_3O_3 contents compared to unaltered apatite in these rocks. Metasomatism of Apollo 14 basalts prior to late-stage melt crystallization involving a Cl-rich phase derived from heating a KREEP-rich ^{37}Cl—enriched lithology could be a viable mechanism to explain part of the δ^{37}Cl variations observed at the sample scale (e.g., Treiman et al., 2014). Indeed, such a process could have enriched

apatite grains in Cl without really affecting its H_2O budget (if the metasomatic agent was low in H for example), and, at the same time, increased apatite δ^{37}Cl values. Also, no strong correlation between apatite Cl and H_3O abundances and δ^{37}Cl values is expected in this scenario since measured abundances would be variable depending on the initial apatite volatile contents. Such a process could also create variations of apatite volatile abundances and isotopic compositions from grain to grain and from mesostasis area to mesostasis area in a single sample depending on the apatite size or the local permeability, for example. In the case of granulite 79215, Treiman et al. (2014) suggested that the addition of P and halogens due to vapor-phase metasomatism triggered growth of large apatite crystals characterized by homogeneous, elevated, δ^{37}Cl values. In the studied Apollo 14 samples, the large variations of δ^{37}Cl values at the sample scale suggest that apatite grains formed before any metasomatism, during crystallization of the basalts and the impact melt samples, and were later altered during the metasomatic event(s).

5.5.7 Global fumarole activity >3.8 Ga on the Moon

It has been suggested that lunar ejecta blankets, such as the Fra Mauro unit, can initiate non-volcanic fumarole activity (McKay et al., 1972). Vapors released during crystallization within hot zones (∼1000 °C) percolate up through colder zones where non-condensable gases (i.e. Cl) may escape through the ejecta blanket forming fumaroles (Shearer et al., 2014). This process has also been identified within 'rusty-rock' 66095 (Shearer et al., 2014) and is similar to the mechanism proposed to explain crystallization of large apatite with elevated δ^{37}Cl values in granulite 79215 (Treiman et al., 2014). These two samples have yielded $^{40}Ar/^{39}Ar$ dates around 3.8 —3.9 Ga, similar to the Apollo 14 samples studied here (Table 5.1). Altogether, these samples hint at the widespread occurrence of vapor-related metasomatism during a period when the impact flux on the lunar surface may have been particularly high (Gomes et al., 2005; Morbidelli et al., 2012; Tera et al., 1974). As samples 66095 and 79215 are from landing sites on the Western limb of the nearside, this work extends the geographical reach of vapor-rich mestasomatism on the lunar surface to include the Apollo 14 site on the mid-eastern section of the nearside; hinting at large-scale volatile release during this period.

5.6 Conclusions

Understanding processes that have affected the volatile contents and their isotopic compositions in lunar samples is important for constraining the volatile budget of the lunar interior. The Apollo 14 samples studied here have provided an opportunity to explore the various processes that can fractionate Cl isotopes in lunar magmatic and surface environments. Overall the data that we present supports the hypothesis that the KREEP component in the Moon may be characterised by an elevated δ^{37}Cl signature. The wide-range in δ^{37}Cl values in the Apollo 14 samples investigated, however, suggests that secondary processes may have altered the values inherited from

a KREEP source. The mechanism we ultimately favor, to explain the vast intra- and inter-sample variability in δ^{37}Cl isotope values measured, is variable interaction of late-stage melts with a volatile-rich vapor-phase. The presence of vapor-induced metasomatism in these samples points to wide-spread fumarolic activity on the near-side of the Moon $\sim$ 4 Ga.

5.7 Acknowledgements

We thank NASA CAPTEM for the allocation of Apollo samples. STFC are thanked for a PhD studentship to N.J.P and a research grant to M.A. and I.A.F. (grant number ST/I001298/1). NanoSIMS access was through UKCAN funded through STFC grant ST/1001964/1.

Chapter 6

Summary and further work

6.1 Summary

The work presented in this thesis provides new insight regarding the use of apatite to constrain the volatile content of the lunar interior. Although water (throughout this summary, water refers to the various oxidized forms of H, mostly hydroxyls, unless otherwise mentioned) and other volatiles (F, Cl, S) have been measured in lunar glasses (Saal et al., 2008, 2013), olivine-hosted melt inclusions (Chen et al., 2015; Hauri et al., 2011), and anorthosites (Hui et al., 2013), the majority of *in situ* volatile analysis have been made in the mineral apatite (McCubbin et al., 2015b, and references therein). Lunar highland samples (Barnes et al., 2014, 2016; Greenwood et al., 2011; Treiman et al., 2014), mare basalts (Barnes et al., 2013; Boyce et al., 2010, 2015; McCubbin et al., 2011, 2010a,b; Sharp et al., 2010b; Tartèse et al., 2013a), high-Al basalts (Boyce et al., 2010; Greenwood et al., 2011), KREEP-rich basalts (Barnes et al., 2016; Boyce et al., 2015; Sharp et al., 2010b; Tartèse et al., 2014a), plutonic rocks (Barnes et al., 2014; McCubbin et al., 2010a; Robinson and Taylor, 2014), and lunar meteorites (McCubbin et al., 2010b; Tartèse et al., 2014a) are all represented in apatite-volatile measurements. It is, therefore, vital to assess if and how these volatile measurements can be used to infer initial bulk-melt volatile values.

Apatite forms from bulk basaltic melts, which are partial melts of the lunar mantle, at around ∼85 % (Tartèse et al., 2014b) to ∼95 % (McCubbin et al., 2011) melt solidification. In general, apatite is associated with late-stage melt pockets referred to as mesostasis regions (Pernet-Fisher et al., 2014; Potts et al., 2016). The melts pockets represent the last dregs of melt, after major silicate crystallization, with conditions very different to those during bulk-melt solidification. Although phosphate saturation and partitioning into apatite are known to be composition dependent, recent studies on apatite-melt volatile partitioning have been performed in bulk basaltic compositions. Here, detailed petrographic and mineralogical characterisation of mesostasis regions in mare basalts were completed to provide, for the first time, an accurate and relevant composition for experimental studies on apatite-melt volatile partitioning in lunar environments. This work is presented in Chapter 2 of this thesis, and highlights how the majority of mesostasis regions do not fit on fractional crystallization trends, resulting in unique evolution between different regions within individual samples. Despite the broad range in chemical compositions displayed in mare basalt mesostasis regions a dacitic composition was found to be an average, representative, evolved melt

composition from which apatite crystalizes in bulk lunar basaltic melts.

A synthetic mixture of the composition derived from Chapter 2 was utilized for the apatite-melt volatile partitioning experiments reported in Chapter 3. These experiments covered a range of temperatures and volatile contents to provide insight into the behaviour of volatiles during apatite growth. In addition to the lunar relevant bulk-composition, fluorapatite was synthesized so that varying amounts of Cl and OH could be added to the apatite X-site. This produced apatite compositions that overlap with those found in lunar samples. This experimental work led to the derivation of three empirical models to back-calculate melt volatile (F, Cl, H_2O) compositions at the time of apatite formation. Applying this model to lunar apatites, where data was available, estimates of lunar melt volatile contents range from 88 to 35700 ppm H_2O, 2 to 49559 ppm F, and 33 to 53146 ppm Cl. Future studies combining analysis all F, Cl, and H_2O in a range of Apollo samples would provide greater constraint on any trends within this data.

A further complication to the apatite-volatile story is degassing. It is likely that some amount of degassing has occurred in basaltic melts by the time of apatite formation (Sharp et al., 2010b; Tartèse and Anand, 2013; Ustunisik et al., 2011, 2015). Experiments, presented in Chapter 4 of this thesis, showed significantly higher rates of degassing than previously reported in the literature (Ustunisik et al., 2011, 2015). In our experiments >90 % Cl and >60 % F was lost within the first four minutes of degassing contrary to the <30 % Cl and <40 % F lost in literature studies (Ustunisik et al., 2011, 2015). The difference in degassing rates observed may result from differences in bulk-compositions, fO_2, or bulk-volatile contents. It is, therefore, likely that mesostasis regions within individual pockets would undergo different amounts of degassing. This means that a global model for volatile degassing in lunar basaltic melts would be ineffective, with individual degassing models required for each late-stage melt pocket instead.

In Chapter 5 of this thesis chlorine isotopes and volatile abundances were measured in apatite grains from a range of high-Al Apollo 14 samples including basaltic rocks, a basaltic clast, and impact melt-rocks. The work here contributes significantly to the current Cl isotope dataset and explores various mechanisms which could fractionate Cl isotopes in lunar environments. The Cl isotope measurements made in this sample suite show a general support for the current hypothesis of heavier Cl isotope signatures being KREEP-derived (Boyce et al., 2015), yet, unlike other samples show a wide-range of isotopic values. Also, general trends between increasing δ^{37}Cl and Cl abundance, alongside decreasing H_2O are shown in some of these apatite analysis. The favoured hypothesis for this spread in values is vapour-induced metasomatism altering apatite volatile contents and isotopic signatures similar to the work of Treiman et al. (2014). Thus an extra complication to utilizing apatite volatile contents is the potential for vapour-induced volatile changes within apatite.

Additional samples from the lunar farside would aide in understanding whether the widespread vapor release identified in Chapter 5 is a global phenomenon, or if this is isolated to the lunar nearside. If this activity was concentrated on the lunar nearside, a dichotomy in lunar volatile contents could be expected. Although further measurements of Apollo apatites are required, the main outcome of this thesis highlights that the basaltic melts are not devoid of volatiles. A considerable amount

of volatile material is present during the last stages of melt solidification. However, highlighting whether this value is inherited from surface interactions or deep mantle sources remains to be seen.

6.2 Suggestions for further work

The work completed as part of this PhD thesis has highlighted the complex nature of understanding lunar volatiles, and highlights how there is clearly a lot of work to do in constraining the volatile inventory of the lunar interior.

Additional experiments on apatite-melt volatile partitioning are paramount to enhancing the model developed as part of this work. As shown in Chapter 3, these experiments must be run in compositions relevant to lunar melts and should be similar, if not the same, as proposed in Chapter 2. Additional experiments should be run with F <2.5 wt.$ F and >1 wt.% H_2O to extend the calibration range of this model. Furthermore, experiments run at varying Cl contents would provide a better fit parameter for the Cl expression in this model.

Crystal chemistry investigations into how F, Cl, and OH exchange within the apatite anion column would also be extremely useful, to allow further constraints on and understanding of volatile partitioning.

Simultaneous measurements of H_2O, F, and Cl within lunar apatite are essential to provide constraints on the water contents of late-stage melts.

If apatite is to be used to understand bulk-basaltic melt volatile contents then additional data on volatile degassing is also required. The variations in volatile degassing rates observed in the experiments are troublesome to those who wish to utilise apatite as a hygrometer. Further experiments, constraining volatile degassing varying total volatile contents, using different bulk compositions, relevant to lunar melts, and run at relevant oxygen fugacities are essential.

Chlorine isotope measurements of degassed experimental glasses would also provide key insight into the amount of isotopic fractionation expected under lunar conditions, which would feed into the current hypothesis on chlorine isotope fractionation in the Moon.

Detailed petrography of not only lunar apatites, but also the mesostasis regions within apatite is found, should be an essential component to any apatite-volatile study.

Therefore, if apatite is to be utilized as a tool for understanding lunar volatile contents then, at a minimum, the following must be addressed:

- Amount of degassing prior to, and during, apatite growth.
- Reliable test to confirm no vapour induced change to initial apatite volatile contents.

Appendix A

Instrumental Methods

A.1 Scanning Electron Microscopy (SEM)

The scanning electron microscope (SEM) was used to take high resolution images of experimental sample runs and apatite grains in Apollo thin sections. The SEM images the interaction products of collisions between an incident electron beam and the sample surface. A thermal emission source is used to create electrons above the sample, which are then focused onto the sample via a series of electromagnetic lenses (See Figure A.1). An electron beam, with a diameter on the few micron scale, is rastered across a sample to create images. There are two types of imagery that can be recorded depending on which interaction products are measured: Backscattered electrons (BSE) or Secondary Electrons (SE).

The interaction between the electron beam and sample surface produces scattered electrons which have a high energy (10 - 30 keV) that allows them to escape from a sample depth of $\sim$5 μm. This back scattering of electrons is strongly dependant on the atomic number of the elements within a sample which creates the image contrast observed in BSE imaging. BSE imaging, therefore, allows compositions variations between minerals/elements to be observed at a relatively low resolution.

SE imaging, however, is reliant on the interaction between the primary beam with the outer electrons of the sample. This creates scattering of low energy elections ($<$ 50 eV) is highly dependant on the topography of the surface which allows any surface topography/morphology to be observed.

Additionally, chemical identification of phases can be performed on the SEM with an attached energy dispersive X-ray spectrometer (EDS). This EDS system is similar to that of the EPMA, except that the SEM uses a solid state detector which differentiates based on X-ray energies as opposed to diffracting crystals used in EPMA analysis. This greatly reduces the detection limits of the SEM, however, is more than powerful enough to identify phases (i.e. apatite) and distinguish between phases (i.e. apatite from merrillite).

A.2 Electron Probe Microanalysis (EPMA)

The EPMA is a quantitative technique to provide chemical compositions of phases in Apollo sections and experimental charges. While SIMS was used to give

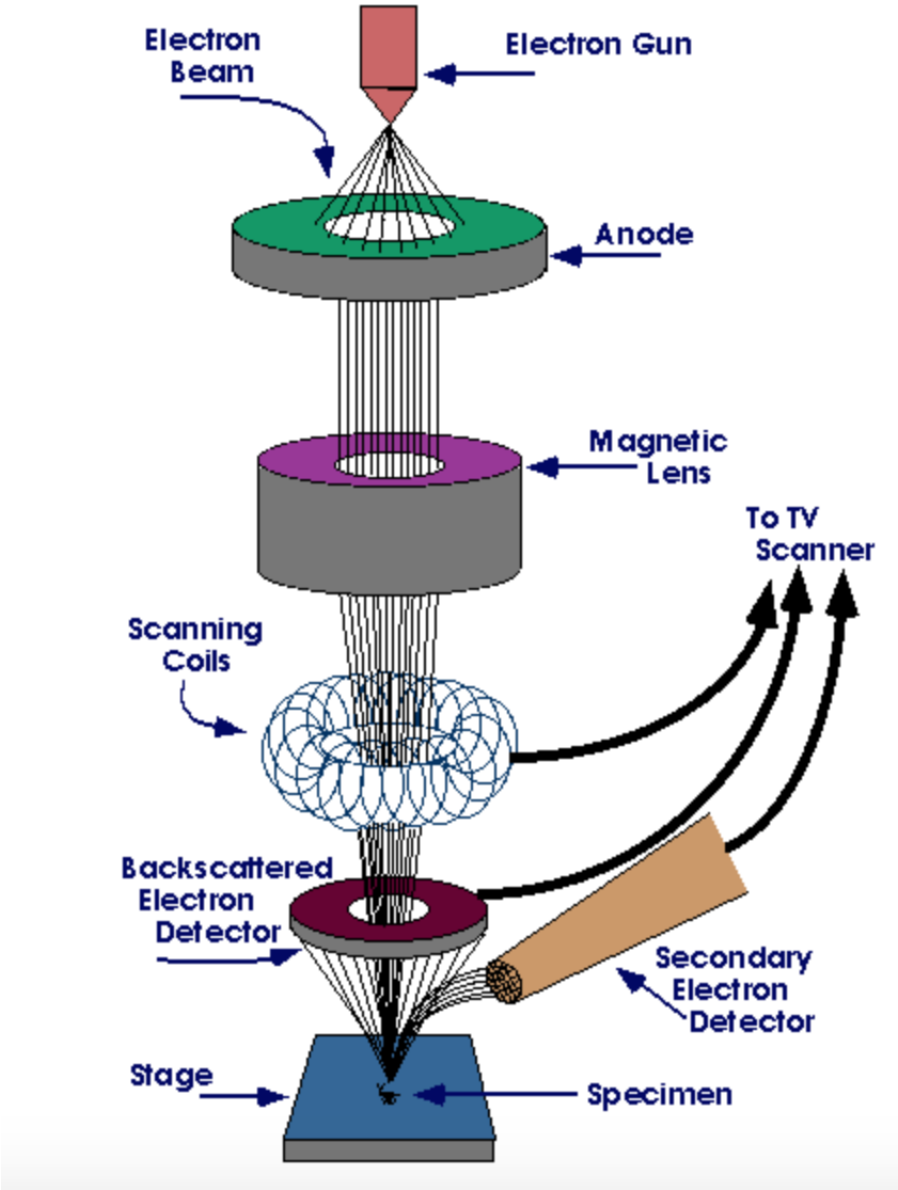

Figure A.1: Schematic diagram of Cameca SX 100 Electron Probe Micro-Analyser

high-precision volatile analysis, EPMA is a cheaper, easier, technique to obtain bulk-chemistry on a given spot within a phase. An overview on the EPMA instrument is shown in Figure A.2.

During EPMA a focused electron beam (∼5 - 30 keV) is bombarded on a sample surface, within a ∼1 - 30 μm spot. The X-ray photons emitted from various elemental species within the sample are collected at spectrometers. The wavelengths of these X-rays is unique to a given element allowing for sample composiiton to be recorded via Wavelength Dispersive Spectroscopy (WDS). WDS spectrometers rely on Bragg's law and various moveable, shaped monocrystals as monochromators. This allows for non-destructive, quantitative, analysis on the ppm level.

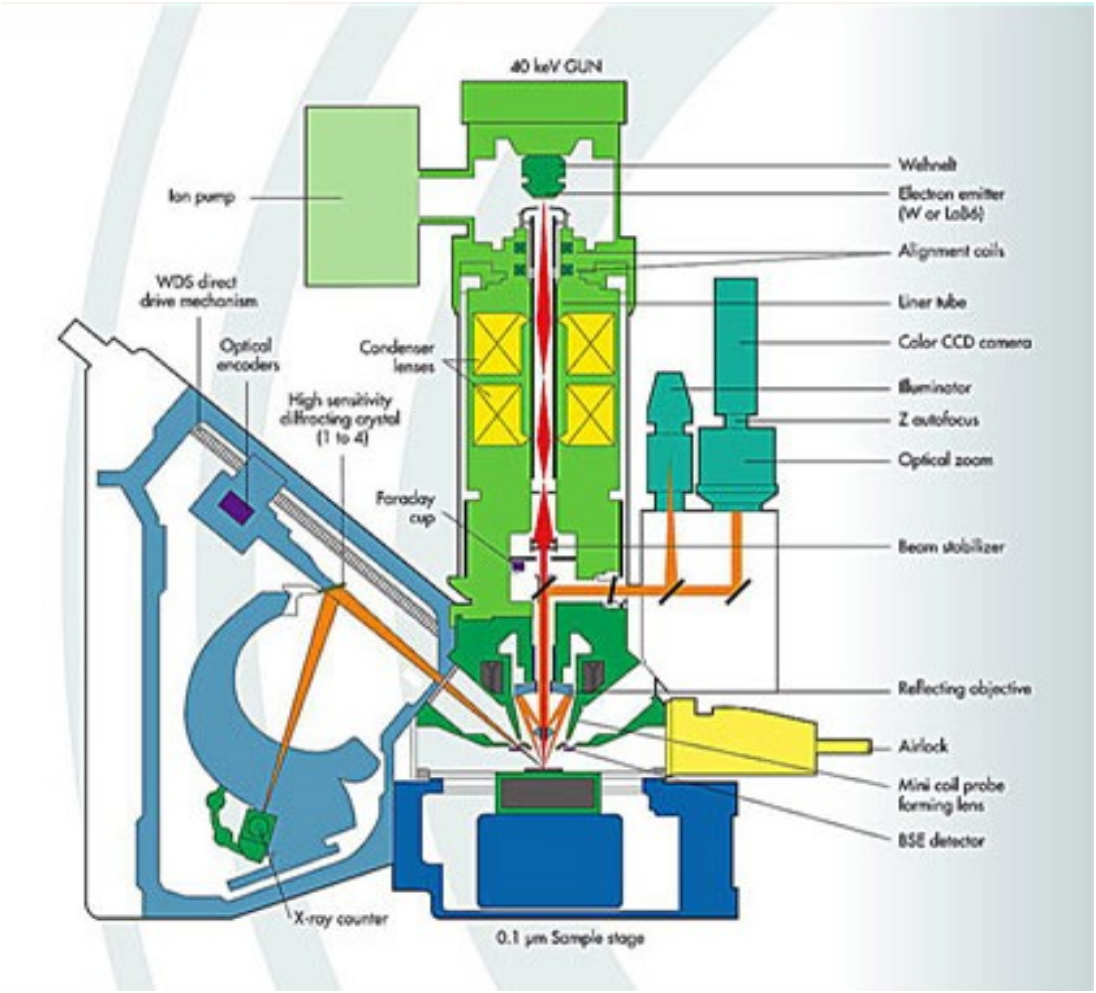

Figure A.2: Schematic diagram of Cameca SX 100 Electron Probe Micro-Analyser

A.3 Secondary Ion Mass Spectrometry (SIMS)

Secondary ion mass spectrometry (SIMS) permits *in situ* analysis of abundances and isotopes from a range of materials. One incarnation of the SIMS instrument is the ion microprobe or ion probe which allows *in situ* analysis on the micrometer or sub-micrometer scale. The CAMECA NanoSIMS 50L ion probe provides, simultaneous,

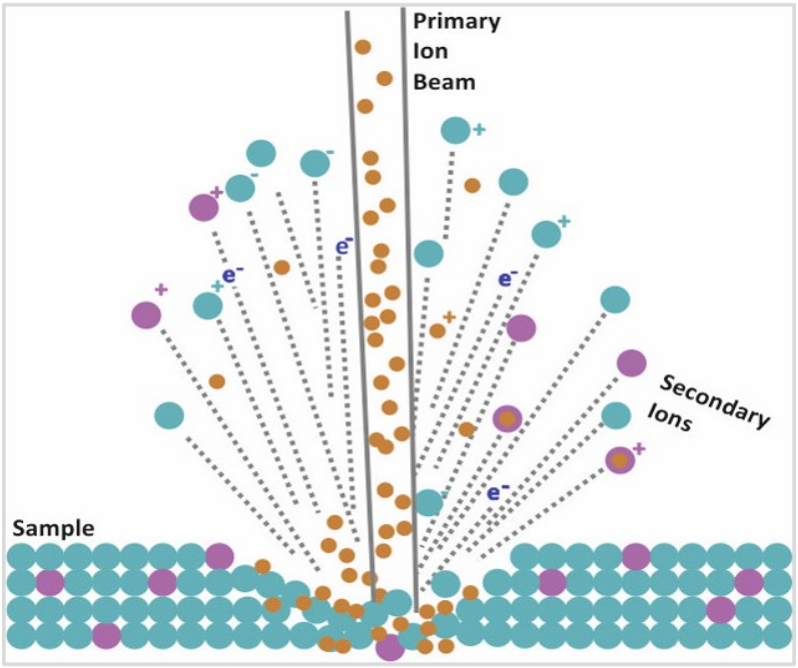

Figure A.3: Schematic diagram of NanoSIMS beam of Cs^+ ions bombarding sample surface to produce secondary ions which are then directed to electron multipliers for measurements.

high spatial resolution (50 nm), high sensitivity analysis (ppb for some elements), and high mass resolution ($M/\Delta M = 5000$). An overview of the CAMECA NanoSIMS 50L is given in Figure A.7.

The physical principle of NanoSIMS is illustrated in Figure A.3. The description of the NanoSIMS is adapted from Hoppe et al. (2013). A solid, sample, surface is bombarded with a primary beam of ions (in this instance Cs^+) which have energies in the range of several keV. As a primary ion hits the surface a collision cascade is triggered. This allows for a process called 'sputtering' to occur, where atoms and small molecules of the upper layers of the sample ($\sim$5 - 20 nm) are released into the vacuum. The majority of these atoms are neutral and, therefore, can't be analysed but a small fraction of the sputtered particles ($\sim 10^{-5}$ to 10^{-2}) are ionised in the process. The number of ionised particles is highly dependant on the species and matrix of the sample. These ionised particles are referred to as 'secondary ions', and it is these ions that are physically separated and counted in the mass spectrometer. The NanoSIMS is unique to a SIMS instrument in that it has a magnetic section mass spectrometer which allows for secondary ions with different mass-to-charge ratios to be physically separated by the Lorentz force while passing through a magnetic field. This magnetic field is laid out perpendicular to the velocity vector of the secondary ions (Hoppe et al., 2013).

An electrostatic field transfers the secondary ions (which have relatively low kinetic energies, eV range) to a mass spectrometer. High transmission, i.e. low loss of secondary ions between the sample surface and the detectors, combined with high mass resolution achievable with the NanoSIMS which is required for high precision isotope measurements.

One of the caveats to NanoSIMS measurements is the trade off between very small beam spot sizes (optimum for studying small (>50 μm) apatite grains in this study) and low primary beam currents. The low primary beam current means that the number of secondary ions produced is relatively low (compared to a conventional SIMS instrument) making high analytical precision more difficult to obtain.

In all quantitative SIMS measurements, complications include isobaric interferences, matrix effects, and instrumental mass fractionation (IMF) along with problems related to ion detection and sample preparation. The magnetic sector in the NanoSIMS provides high mass resolutions that are sufficient to resolve interferences for the low atomic number elements. Although matrix effects can lead to extreme fractionation of major, minor, or trace elements as the ionisation yield of elements can change dramatically with sample matrix. Small differences in ionisation can also lead to IMF. Well characterised standards, within similar matrix material, provides a resolution to these problems.

All analysis in this thesis occurred on electron multipliers, although a Faraday cup detector is also available on the NanoSIMS. Electron multipliers convert arriving ions into electrical pulses, that are then amplified and registered. They also have a large, dynamic range which permits measurements of ion counts between <1 and 10^6 cps.

From the source, the primary ion beam is demagnetised by three electrostatic lenses (L0, L1, and L2; Figure A.7). The primary beam is then turned 79°when entering an electrostatic spherical sector (SS30). To guide the beam onto the target it passes through an octopole to correct astigmatism before being deflected by the P1 plates which allow for it to hit the sample surface at a perpendicular angle. The angular distribution of the beam is trimmed by an aperture of varying sizes (D1), the D1 lens also acts as a field aperture for the secondary ions. The beam is then focused to its final spot size by the EOP lens. Rastering of the primary beam occurs by three sets of scanning plates (B1, B2, and B3) displacing the beam horizontally across the sample surface.

The normal incidence of the primary beam is a unique feature of the NanoSIMS and allows for the ion optical elements to be placed closer to the sample than in normal SIMS instruments. This is because the coaxial extraction of secondary ions allows for the same ion optical system as the primary beam to be used (EOW, EOP, EOS, L4). In a conventional SIMS instrument the beam hits at an oblique angle with the optics about a cm away from the sample surface, instead of at the μm scale. The ability to do real-time imaging of the sample via an optical microscope is lost because of the short distance between optics and sample on the NanoSIMS.

Several lenses (EOW, EOS, L4) and two slit lenses (LF2, LF3) transfer secondary ions to a double-focusing mass spectrometer by focusing these ions into a beam. This beam, which has a rectangular cross-section, enters the mass spectrometer through the entrance slit (ES) which has two external coils to compensate for mass fractionation. Primary and secondary ions are separated from each other by a set of deflection plates (P1), while another set of deflection plates trim and center the secondary beam. The secondary beam is further trimmed by an aperature slit (AS) of variable widths, thus limiting its angular dispersion. Second-order angular aberrations are further reduced by a hexapole. At this stage the secondary beam enters SS100, an electrostatic spherical analyser, which dispenses the secondary ions according to energy. Angular and

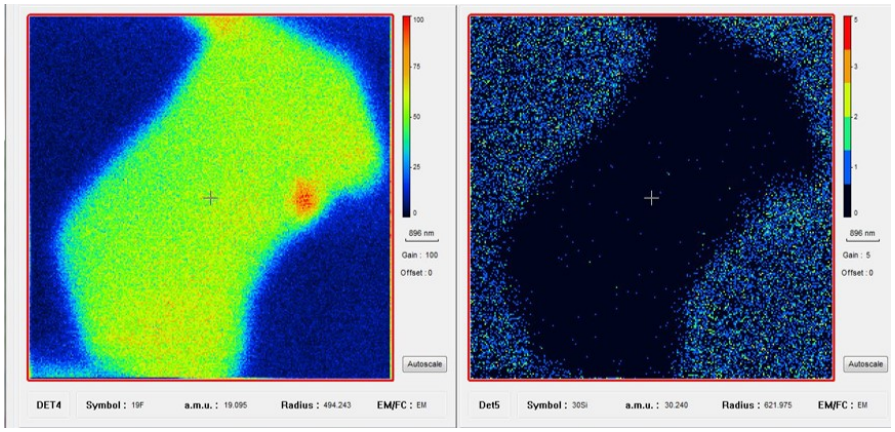

Figure A.4: Real Time Image (RTI) of secondary ^{19}F (left) and ^{30}Si (right). Light blue - orange pixels represent high number of counts and outline apatite grains within experimental sample

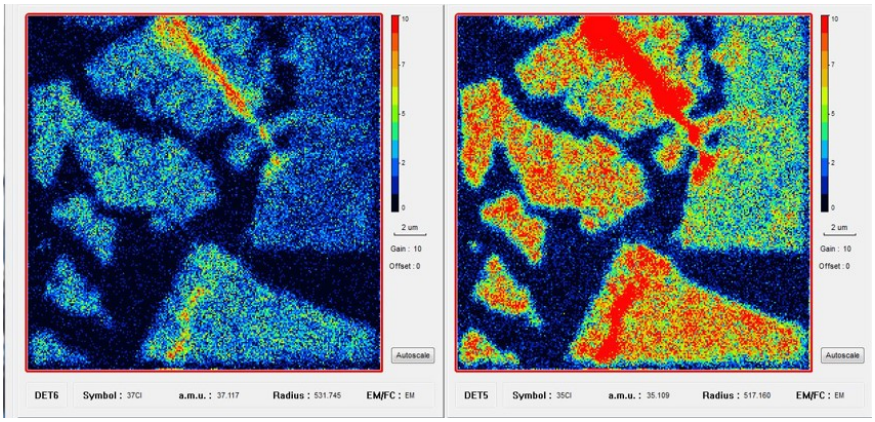

Figure A.5: RTI of secondary ^{37}Cl (left) and ^{35}Cl (right). Light blue - orange pixels represent high number of counts and outline apatite grains within Apollo 14 section.

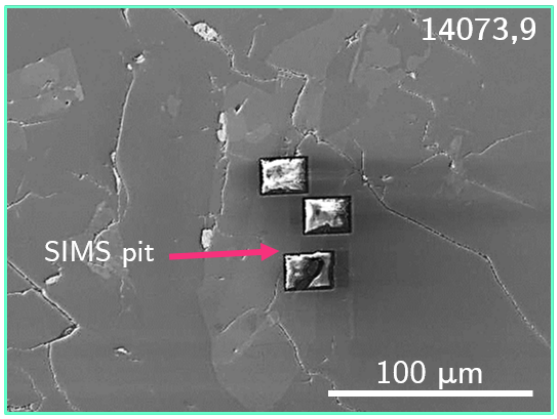

Figure A.6: Secondary electron image of NanoSIMS sputter pits on Apollo sample 14073,9. The SIMS pits are the 20 × 20 μm raster and analysis are taken within an inner 4 × 4 μm.

energy focusing occurs from two slit lenses (LF4 and LF5) and a quadruple lens (Q) before the secondary beam enters the magnet where the detectors are located. Mass separation occurs in a laminated magnet.

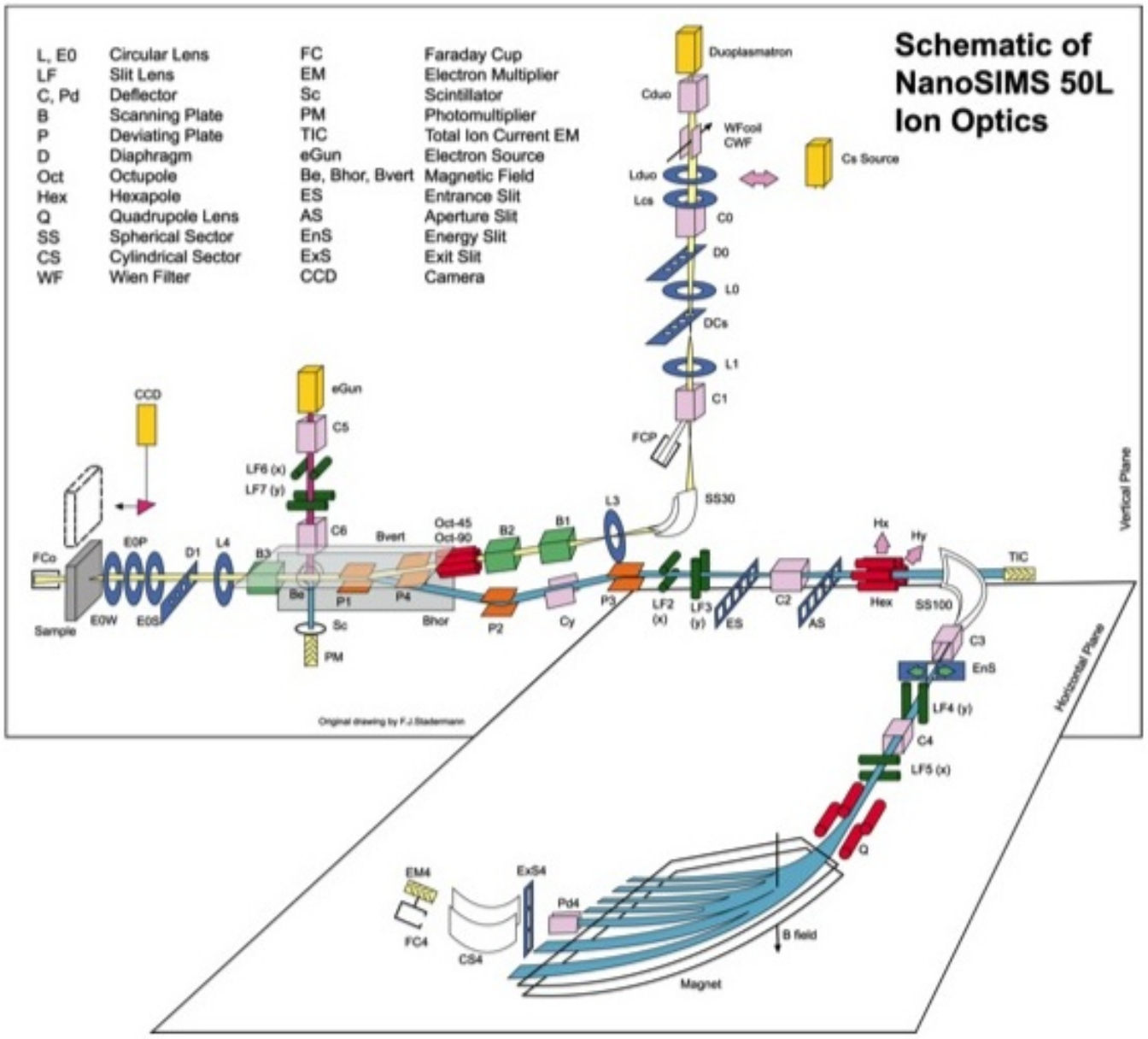

Figure A.7: Schematic diagram of Cameca NanoSIMS 50L ion microprobe.

Appendix B

Supplementary Material for Chapter 2

B.1 Additional diagrams

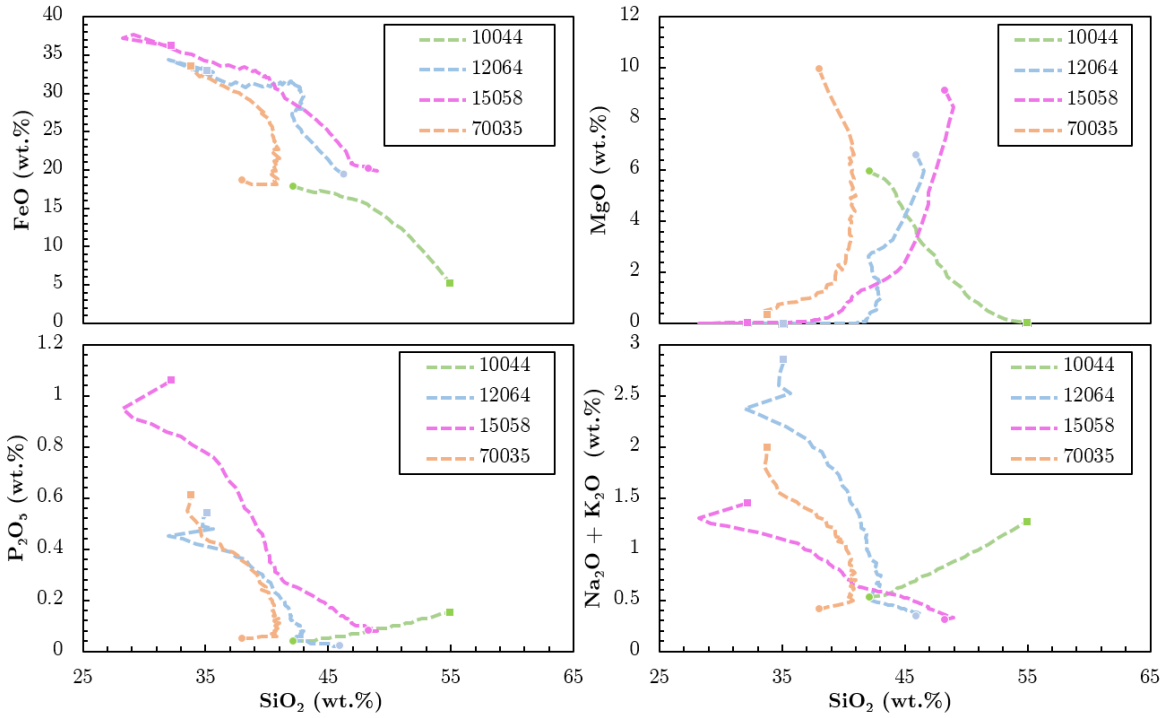

Figure B.1: Harker diagrams of SPICEs modeling data. Circles indicate starting points while squares indicate finishing points.

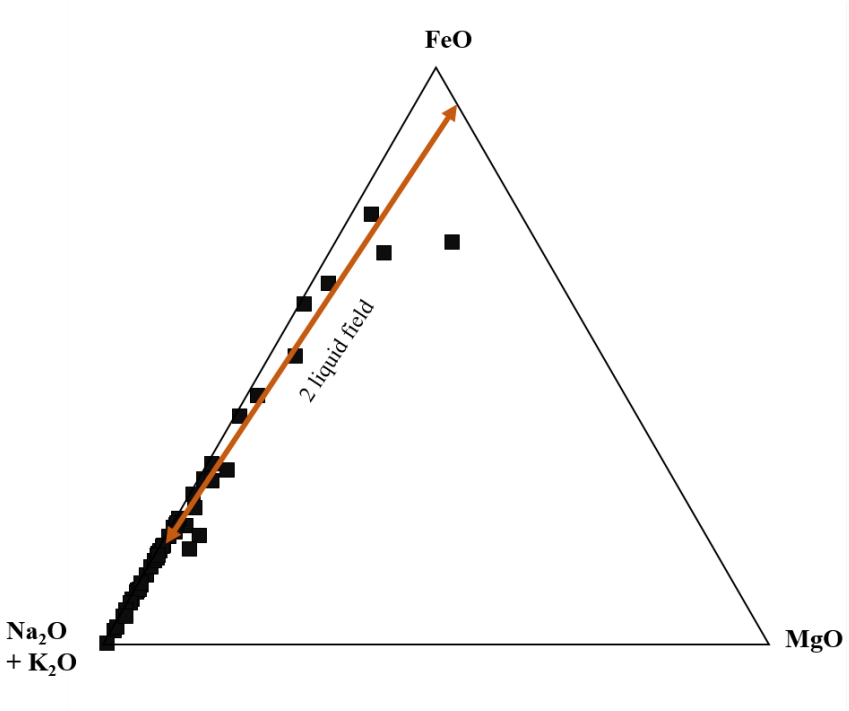

Figure B.2: AFM diagram of glasses within Apollo sections measured here. The 2-liquid line represents immiscibility between a silica and Fe-rich liquid showing how SLI is a dominant process in late-stage liquids.

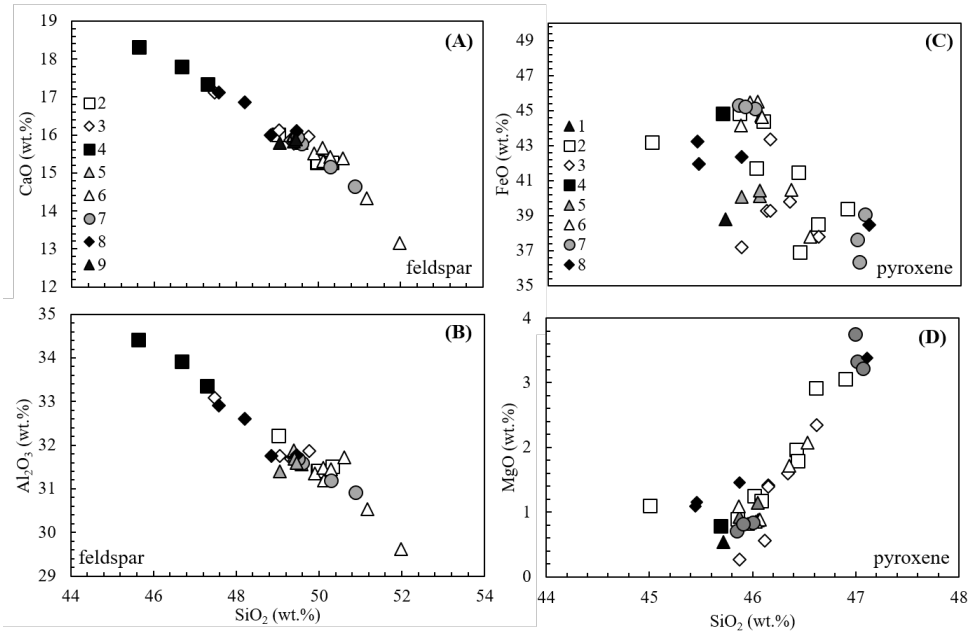

Figure B.3: Variations of feldspar and pyroxene chemical composition from mesostasis regions in sample 10044. Feldspar SiO_2 contents plotted against (A) CaO and (B) Al_2O_3 and pyroxene SiO_2 contents plotted against (C) FeO and (D) MgO.

B.2 Apatite solubility modeling

In addition to modelling bulk compositions of mesostasis regions previous studies of phosphate solubility were explored to find optimum SiO_2 and CaO contents for apatite growth. Phosphate saturation has been shown to be dependent on a variety of parameters, including temperature and liquid composition (Harrison and Bruce, 1984; Watson, 1979). In the Harrison-Watson model of phosphate growth, SiO_2 was shown to be an important control on how much P_2O_5 is required for crystallization (Harrison and Watson, 1984). Bea et al. (1992) suggest that CaO content may also play a role in affecting phosphate saturation in granitic systems. Tollari et al. (2006) showed an anticorrelation of P_2O_5 and SiO_2 similar to Harrison and Watson (1984) which is independent of fO_2 and temperature. They were also able to expand on previous work on CaO content (Bea et al., 1992) and show how CaO and P_2O_5 concentrations are correlated in the melt. These experimentally derived equations are plotted to constrain SiO_2 and CaO concentrations required for apatite growth.

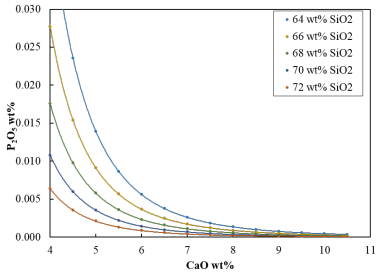

Figure B.4: Apatite solubility as a function of CaO at 1000 °C.

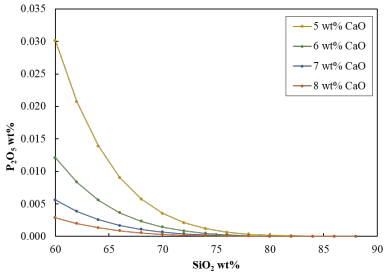

Figure B.5: Apatite solubility as a function of SiO_2 at 1000 °C.

Phosphate saturation as a function of SiO_2 and CaO concentrations (Figure) indicate that at 0.01 wt.% P_2O_5, 4 wt.% CaO is required for phosphate growth, if the SiO_2 content is 70 wt.%. As SiO_2 concentrations decrease then the amount of CaO required increases. At lower SiO_2 concentrations (<70 wt.%) more CaO (>6 wt.%) is required for 0.01 wt.% phosphate growth. CaO contents from modal abundances of mesostasis regions indicates ∼6 wt.% is present in the melt, requiring SiO_2 contents of 63 wt.% or more for 0.01 wt.% P_2O_5 based on this model. Reducing SiO_2 concentrations increases the amount of P_2O_5 required to reach phosphate saturation while increasing CaO decreases the amount.

B.3 Whole rock data for samples in this study

	Engel and Engel (1970)	Wänke et al. (1970)	Wakita et al. (1970)	Beaty and Albee (1978)	Rhodes and Blanchard (1980)	Agrell et al. (1970)	Dymek et al. (1975)	Average	StDev
SiO_2	42.01	43	52	42.21	42.89	42.46	41.61	**43.7**	**3.7**
TiO_2	8.81	10.5	9.84	10.25	8.47	9.18	10.05	**9.6**	**0.8**
Al_2O_3	11.67	11.9	8.7	10.35	10.49	10.21	11.1	**10.6**	**1.1**
FeO	17.98	17.1	20.4	17.88	18.46	17.6	17.73	**18.2**	**1.1**
MnO	0.24	0.6	0.3	0.27	0.28	0.28	0.27	**0.3**	**0.1**
MgO	6.25	6.47	6.8	5.95	5.98	5.96	5.58	**6.1**	**0.4**
CaO	12.18	7.13	11.7	12.08	12.4	12.25	12.33	**11.4**	**1.9**
Na_2O	0.48	0.48	0.37	0.5	0.38	0.48	0.51	**0.5**	**0.1**
K_2O	0.11	0.1	0.11	0.03	0.11	0.11	0.16	**0.1**	**0.0**
P_2O_5	0.08	0	0	0.04	0.12	0.04	0.07	**0.1**	**0.0**
Total	99.81	97.28	110.22	99.56	99.58	98.57	99.41	**100.6**	**4.3**

Table B.1: Whole rock bulk compositions for 10044. Taken from Lunar Sample Compendium.

	Kushiro and Haramura (1971)	Scoon (1971)	LSPET (1970)	Average	StDev
SiO_2	46.19	46.41	40	**44.2**	**3.6**
TiO_2	3.83	4.14	4.9	**4.3**	**0.6**
Al_2O_3	10.96	10.5	12	**11.2**	**0.8**
FeO	19.83	19.95	22	**20.6**	**1.2**
MnO	0.26	0.27	0.32	**0.3**	**0.0**
MgO	6.6	6.38	8	**7.0**	**0.9**
CaO	11.84	11.71	12	**11.9**	**0.1**
Na_2O	0.27	0.3	0.42	**0.3**	**0.1**
K_2O	0.07	0.07	0.084	**0.1**	**0.0**
P_2O_5	0.02	0.04	0	**0.0**	**0.0**
Total	99.87	99.77	99.724	**99.8**	**0.1**

Table B.2: Whole rock bulk compositions for 12064. Taken from Lunar Sample Compendium

	Rhodes and Hubbard (1973)	Willis et al. (1972)	Average	StDev
SiO_2	47.81	48.47	**48.1**	**0.5**
TiO_2	1.77	1.6	**1.7**	**0.1**
Al_2O_3	8.87	8.9	**8.9**	**0.0**
FeO	19.97	19.75	**19.9**	**0.2**
MnO	0.28	0.274	**0.3**	**0.0**
MgO	9.01	9.56	**9.3**	**0.4**
CaO	10.32	10.23	**10.3**	**0.1**
Na_2O	0.28	0.28	**0.3**	**0.0**
K_2O	0.03	0.038	**0.0**	**0.0**
P_2O_5	0.08	0.049	**0.1**	**0.0**
Total	98.42	99.151	**98.8**	**0.5**

Table B.3: Whole rock bulk compositions for 15058. Taken from Lunar Sample Compendium.

	Rhodes et al. (1976)
SiO_2	37.8
TiO_2	13
Al_2O_3	8.85
FeO	18.5
MnO	0.28
MgO	9.89
CaO	10.1
Na_2O	0.35
K_2O	0.06
P_2O_5	0.05
Total	98.88

Table B.4: Whole rock bulk compositions for 70035. Taken from Lunar Sample Compendium.

B.4 Apatite compositions for samples in this study

B.5 EPMA data used for modal abundances

10044								
Analysis	Ap1#1	Ap1#2	Ap3#1	Ap5#1	Ap5#2	Ap5#3	Ap6d#1	Ap6c#1
P_2O_5	38.46	39.16	35.9	37.79	37.74	39.01	36.15	37.57
SiO_2	1.15	0.87	2.38	1.47	1.66	0.98	3.26	1.57
SO_2	0	0	0	0	0	0.01	0.18	0
CaO	52.93	53.11	50.79	52.57	51.88	53.22	51.77	51.63
FeO	0.64	0.46	0.89	0.8	0.76	0.85	2.29	1.11
MgO	0.06	0.06	0.04	0.06	0.05	0.06	0.05	0.05
MnO	0.04	0.04	0.07	0.04	0.05	0.05	0.03	0.04
Na_2O	0	0	0	0	0	0	0	0
Ce_2O_3	0.32	0.3	0.75	0.42	0.48	0.27	0.46	0.51
Y_2O_3	1.06	0.8	2.05	1.33	1.48	0.92	1.22	1.4
F	3.38	3.38	3.46	3.77	3.62	3.39	2.86	3.71
Cl	0.04	0.08	0.08	0.06	0.03	0.08	0.05	0.04
Total	98.08	98.26	96.41	98.29	97.75	98.84	98.31	97.62
Structural formulae based on 13 anions								
P	2.86	2.9	2.75	2.83	2.83	2.88	2.69	2.83
Si	0.1	0.08	0.22	0.13	0.15	0.09	0.29	0.14
S	0	0	0	0	0	0	0.01	0
Ca	4.99	4.98	4.93	4.99	4.93	4.98	4.88	4.93
Fe	0.05	0.03	0.07	0.06	0.06	0.06	0.17	0.08
Mg	0.01	0.01	0.01	0.01	0.01	0.01	0.01	0.01
Mn	0	0	0.01	0	0	0	0	0
Na	0	0	0	0	0	0	0	0
Ce	0.01	0.01	0.02	0.01	0.02	0.01	0.01	0.02
Y	0.05	0.04	0.1	0.06	0.07	0.04	0.06	0.07
F	0.94	0.93	0.99	1.05	1.01	0.93	0.8	1.04
Cl	0.01	0.01	0.01	0.01	0	0.01	0.01	0.01
OH	0.05	0.05	0	0	0	0.05	0.2	0
Total	8.07	8.05	8.1	8.09	8.06	8.07	8.13	8.07
P Site	2.96	2.98	2.97	2.96	2.98	2.97	2.99	2.97
Ca Site	5.11	5.07	5.13	5.13	5.08	5.1	5.13	5.1

Table B.5: Apatite compositions from sample 10044. Taken from Tartèse et al. (2013a)

	12064							
	Ap10#1	Ap10#3	Ap11#1	Ap12#1	Ap12#2	Ap12#3	Ap13#1	Ap13#2
P_2O_5	41.99	41.81	40.53	42.22	40.23	41.55	40.12	41.07
SiO_2	0.49	0.47	0.83	0.54	1.12	0.75	3.65	0.62
SO_2								
CaO	54.44	54.03	54.66	54.1	52.71	53.83	51.57	53.63
FeO	1.05	0.6	0.92	0.8	1.47	0.86	0.93	0.91
MgO	0	0.02	0	0	0	0	0	0.02
MnO								
Na_2O	0	0	0	0	0	0	0	0
Ce_2O_3								
Y_2O_3								
F	2.58	2.84	2.36	2.43	1.94	2.76	2.69	2.67
Cl	0.13	0.09	0.09	0.09	0.51	0.08	0.08	0.13
Total	100.67	99.87	99.39	100.19	97.97	99.83	99.03	99.07
Structural formulae based on 13 anions								
P	2.98	2.99	2.92	3	2.93	2.97	2.86	2.97
Si	0.04	0.04	0.07	0.05	0.1	0.06	0.31	0.05
S	-	-	-	-	-	-	-	-
Ca	4.9	4.9	4.99	4.86	4.87	4.88	4.66	4.91
Fe	0.07	0.04	0.07	0.06	0.11	0.06	0.07	0.07
Mg	0	0	0	0	0	0	0	0
Mn	-	-	-	-	-	-	-	-
Na	0	0	0	0	0	0	0	0
Ce	-	-	-	-	-	-	-	-
Y	-	-	-	-	-	-	-	-
F	0.68	0.76	0.63	0.64	0.53	0.74	0.72	0.72
Cl	0.02	0.01	0.01	0.01	0.07	0.01	0.01	0.02
OH	0.3	0.23	0.35	0.34	0.4	0.25	0.27	0.26
Total	7.99	7.97	8.05	7.96	8	7.98	7.9	8
P Site	3.02	3.03	2.99	3.04	3.03	3.04	3.17	3.02
Ca Site	4.97	4.94	5.06	4.92	4.98	4.94	4.73	4.98

Table B.6: Apatite compositions from sample 10044. Taken from Tartèse et al. (2013a)

	15058	
	Ap3#1	Ap3#2
P_2O_5	39.83	40.25
SiO_2	0.66	0.66
SO_2	0.03	0
CaO	54.04	54.02
FeO	0.7	0.65
MgO	0.06	0.06
MnO	0.03	0.03
Na_2O	0	0
Ce_2O_3	0.24	0.26
Y_2O_3	0.19	0.2
F	3.83	2.95
Cl	0.3	0.25
Total	99.9	99.33
Structural formulae based on 13 anions		
P	2.91	2.93
Si	0.06	0.06
S	0	0
Ca	5.01	4.98
Fe	0.05	0.05
Mg	0.01	0.01
Mn	0	0
Na	0	0
Ce	0.01	0.01
Y	0.01	0.01
F	1.05	0.8
Cl	0.04	0.04
OH	0	0.16
Total	8.06	8.04
P Site	2.97	2.99
Ca Site	5.09	5.06

Table B.7: Apatite compositions from sample 10044. Taken from Tartèse et al. (2013a)

	MS2_a	MS2_g	MS2_kk	MS2_ll	MS3_a	MS3_h	MS3_j	MS3_m
P_2O_5	0.01	0.02	0.03	0.02	0.04	0.00	0.02	0.00
SiO_2	49.02	49.97	50.33	49.98	49.05	47.47	49.32	49.40
TiO_2	0.06	0.06	0.10	0.05	0.05	0.10	0.09	0.06
Al_22O_3	32.22	31.42	31.52	31.41	31.76	33.09	31.69	31.66
MgO	0.10	0.04	0.05	0.04	0.11	0.20	0.17	0.15
CaO	16.00	15.27	15.27	15.29	16.13	17.12	15.87	15.77
MnO	0.00	0.02	0.00	0.02	0.02	0.01	0.02	0.02
FeO	0.75	0.87	0.93	0.97	0.66	0.45	0.61	0.75
Na_2O	1.94	2.09	2.04	2.07	1.94	1.60	2.01	2.03
K_2O	0.14	0.40	0.44	0.48	0.19	0.05	0.12	0.18
Total	100.23	100.16	100.71	100.32	99.95	100.10	99.90	100.01
P	0.00	0.00	0.00	0.00	0.00	0.00	0.00	0.00
Si	2.24	2.28	2.29	2.28	2.25	2.18	2.26	2.26
Ti	0.00	0.00	0.00	0.00	0.00	0.00	0.00	0.00
Al	1.74	1.69	1.69	1.69	1.72	1.79	1.71	1.71
Mg	0.01	0.00	0.00	0.00	0.01	0.01	0.01	0.01
Ca	0.78	0.75	0.74	0.75	0.79	0.84	0.78	0.77
Mn	0.00	0.00	0.00	0.00	0.00	0.00	0.00	0.00
Fe	0.03	0.03	0.04	0.04	0.03	0.02	0.02	0.03
Na	0.17	0.19	0.18	0.18	0.17	0.14	0.18	0.18
K	0.01	0.02	0.03	0.03	0.01	0.00	0.01	0.01
Total	4.98	4.97	4.97	4.97	4.98	4.99	4.97	4.98
An	0.81	0.78	0.78	0.78	0.81	0.85	0.81	0.80
Ab	0.18	0.19	0.19	0.19	0.18	0.14	0.19	0.19
Or	0.01	0.02	0.03	0.03	0.01	0.00	0.01	0.01
Total	1.0	1.0	1.0	1.0	1.0	1.0	1.0	1.0

Table B.8: EPMA data for feldspar in 10044

	MS1_y	MS2_ddd	MS2_f	MS2_ff	MS2_k	MS2_oo	MS2_w	MS2_x	MS2_zz	MS3_b	MS3_f	MS3_k
P_2O_5	0.03	0.01	0.02	0.01	1.01	0.04	0.02	0.02	0.00	0.00	0.00	0.02
SiO_2	45.72	45.85	46.90	46.61	45.00	46.02	46.42	46.08	46.44	45.88	46.12	46.62
TiO_2	1.23	0.44	0.71	0.86	0.62	0.96	0.45	0.51	0.93	1.06	0.81	1.04
Al_2O_3	0.94	0.38	0.63	0.78	0.52	0.76	0.64	0.54	0.89	1.13	0.85	0.92
MgO	0.54	0.90	3.06	2.92	1.10	1.25	1.96	1.18	1.80	0.27	0.56	2.34
CaO	11.50	5.51	7.72	8.59	6.91	7.97	7.34	5.96	11.69	12.79	10.60	10.12
MnO	0.52	0.75	0.68	0.61	0.62	0.60	0.65	0.63	0.49	0.51	0.57	0.61
FeO	38.77	44.84	39.40	38.49	43.18	41.70	41.48	44.39	36.92	37.19	39.26	37.78
Na_2O	0.04	0.03	0.04	0.07	0.02	0.00	0.02	0.00	0.03	0.06	0.03	0.02
K_2O	0.00	0.00	0.00	0.00	0.00	0.00	0.00	0.00	0.00	0.00	0.00	0.00
Total	99.27	98.70	99.15	98.95	98.99	99.30	98.98	99.29	99.18	98.89	98.78	99.47
P	0.00	0.00	0.00	0.00	0.04	0.00	0.00	0.00	0.00	0.00	0.00	0.00
Si	1.95	1.99	1.98	1.97	1.93	1.96	1.98	1.98	1.96	1.95	1.97	1.96
Ti	0.04	0.01	0.02	0.03	0.02	0.03	0.01	0.02	0.03	0.03	0.03	0.03
Al	0.05	0.02	0.03	0.04	0.03	0.04	0.03	0.03	0.04	0.06	0.04	0.05
Mg	0.03	0.06	0.19	0.18	0.07	0.08	0.12	0.08	0.11	0.02	0.04	0.15
Ca	0.52	0.26	0.35	0.39	0.32	0.36	0.34	0.27	0.53	0.58	0.48	0.45
Mn	0.02	0.03	0.02	0.02	0.02	0.02	0.02	0.02	0.02	0.02	0.02	0.02
Fe	1.38	1.63	1.39	1.36	1.55	1.49	1.48	1.59	1.30	1.32	1.40	1.33
Na	0.00	0.00	0.00	0.01	0.00	0.00	0.00	0.00	0.00	0.01	0.00	0.00
K	0.00	0.00	0.00	0.00	0.00	0.00	0.00	0.00	0.00	0.00	0.00	0.00
Total	3.99	3.99	3.99	3.99	3.98	3.99	3.99	3.99	3.99	3.99	3.98	3.99
En	0.02	0.03	0.10	0.10	0.04	0.04	0.06	0.04	0.06	0.01	0.02	0.08
Fs	0.71	0.84	0.72	0.70	0.80	0.77	0.76	0.82	0.67	0.69	0.73	0.69
Wo	0.27	0.13	0.18	0.20	0.16	0.19	0.17	0.14	0.27	0.30	0.25	0.24
Total	1.0	1.0	1.0	1.0	1.0	1.0	1.0	1.0	1.0	1.0	1.0	1.0

Table B.9: EPMA data for pyroxenes in 10044

	MS3_n	MS3_r	MS3_z	MS4_c	MS5_l	MS5_w	MS5_x	MS6_aa	MS6_bb	MS6_ff	MS6_gg	MS6_hh
P_2O_5	0.02	0.04	0.00	0.01	0.02	0.00	0.00	0.02	0.03	0.01	0.03	0.17
SiO_2	46.15	46.34	46.15	45.69	46.05	45.87	46.05	46.06	46.07	46.03	45.96	45.87
TiO_2	0.91	0.90	0.69	0.54	0.91	0.89	0.90	0.46	0.38	0.38	0.39	0.58
Al_2O_3	0.86	0.92	0.54	0.39	0.86	0.86	0.87	0.41	0.40	0.40	0.38	0.46
MgO	1.41	1.59	1.40	0.79	0.87	0.93	1.14	0.88	0.89	0.85	0.82	1.09
CaO	9.89	9.34	6.49	5.93	9.75	9.72	9.22	5.77	5.61	5.41	5.41	5.97
MnO	0.61	0.54	0.69	0.79	0.56	0.54	0.58	0.83	0.75	0.77	0.79	0.77
FeO	39.25	39.77	43.34	44.82	40.11	40.08	40.41	44.73	44.63	45.51	45.48	44.16
Na_2O	0.03	0.00	0.00	0.01	0.04	0.00	0.01	0.00	0.01	0.00	0.00	0.03
K_2O	0.00	0.00	0.00	0.00	0.00	0.00	0.00	0.00	0.00	0.00	0.00	0.00
Total	99.15	99.44	99.30	98.95	99.16	98.89	99.18	99.14	98.77	99.35	99.25	99.08
P	0.00	0.00	0.00	0.00	0.00	0.00	0.00	0.00	0.00	0.00	0.00	0.01
Si	1.96	1.96	1.98	1.98	1.96	1.96	1.96	1.99	1.99	1.99	1.98	1.97
Ti	0.03	0.03	0.02	0.02	0.03	0.03	0.03	0.02	0.01	0.01	0.01	0.02
Al	0.04	0.05	0.03	0.02	0.04	0.04	0.04	0.02	0.02	0.02	0.02	0.02
Mg	0.09	0.10	0.09	0.05	0.06	0.06	0.07	0.06	0.06	0.05	0.05	0.07
Ca	0.45	0.42	0.30	0.28	0.44	0.45	0.42	0.27	0.26	0.25	0.25	0.28
Mn	0.02	0.02	0.02	0.03	0.02	0.02	0.02	0.03	0.03	0.03	0.03	0.03
Fe	1.39	1.41	1.55	1.62	1.43	1.43	1.44	1.61	1.61	1.64	1.64	1.59
Na	0.00	0.00	0.00	0.00	0.00	0.00	0.00	0.00	0.00	0.00	0.00	0.00
K	0.00	0.00	0.00	0.00	0.00	0.00	0.00	0.00	0.00	0.00	0.00	0.00
Total	3.99	3.99	3.99	3.99	3.99	3.99	3.99	3.99	3.98	3.99	3.99	3.99
En	0.05	0.05	0.05	0.03	0.03	0.03	0.04	0.03	0.03	0.03	0.03	0.04
Fs	0.72	0.73	0.80	0.83	0.74	0.74	0.74	0.83	0.84	0.84	0.84	0.82
Wo	0.23	0.22	0.15	0.14	0.23	0.23	0.22	0.14	0.13	0.13	0.13	0.14
Total	1.0	1.0	1.0	1.0	1.0	1.0	1.0	1.0	1.0	1.0	1.0	1.0

EPMA data for pyroxene in 10044 (cont.)

	MS6_ii	MS6_n	MS7_a	MS7_i	MS7_j	MS7_k	MS7_l	MS7_m	MS8_h	MS8_k	MS8_l	MS8_q
P_2O_5	0.02	0.00	0.02	0.01	0.01	0.04	0.01	0.02	0.01	0.01	0.00	0.02
SiO_2	46.54	46.36	46.00	47.02	47.07	45.85	46.99	45.91	45.87	45.44	45.46	47.11
TiO_2	0.78	0.68	0.44	0.84	0.65	0.43	0.75	0.45	0.80	1.61	1.20	0.99
Al_2O_3	0.87	0.71	0.41	0.98	0.63	0.44	0.76	0.41	0.82	1.15	1.27	0.94
MgO	2.07	1.72	0.84	3.33	3.23	0.71	3.75	0.82	1.46	1.09	1.16	3.39
CaO	10.43	8.69	5.51	10.21	8.04	5.23	8.70	5.50	7.04	6.35	7.46	8.51
MnO	0.63	0.60	0.74	0.63	0.63	0.88	0.66	0.68	0.70	0.60	0.69	0.62
FeO	37.78	40.46	45.11	36.34	39.07	45.32	37.62	45.22	42.34	43.22	41.94	38.48
Na_2O	0.01	0.04	0.00	0.02	0.01	0.00	0.02	0.00	0.00	0.04	0.02	0.01
K_2O	0.00	0.00	0.00	0.00	0.00	0.00	0.00	0.00	0.00	0.00	0.00	0.00
Total	99.13	99.27	99.06	99.37	99.33	98.89	99.26	99.02	99.03	99.52	99.18	100.07
P	0.00	0.00	0.00	0.00	0.00	0.00	0.00	0.00	0.00	0.00	0.00	0.00
Si	1.96	1.97	1.99	1.96	1.98	1.99	1.97	1.98	1.96	1.94	1.94	1.96
Ti	0.02	0.02	0.01	0.03	0.02	0.01	0.02	0.01	0.03	0.05	0.04	0.03
Al	0.04	0.04	0.02	0.05	0.03	0.02	0.04	0.02	0.04	0.06	0.06	0.05
Mg	0.13	0.11	0.05	0.21	0.20	0.05	0.23	0.05	0.09	0.07	0.07	0.21
Ca	0.47	0.40	0.25	0.46	0.36	0.24	0.39	0.25	0.32	0.29	0.34	0.38
Mn	0.02	0.02	0.03	0.02	0.02	0.03	0.02	0.03	0.03	0.02	0.02	0.02
Fe	1.33	1.44	1.63	1.27	1.37	1.64	1.32	1.64	1.52	1.54	1.50	1.34
Na	0.00	0.00	0.00	0.00	0.00	0.00	0.00	0.00	0.00	0.00	0.00	0.00
K	0.00	0.00	0.00	0.00	0.00	0.00	0.00	0.00	0.00	0.00	0.00	0.00
Total	3.99	3.99	3.99	3.99	3.99	3.99	3.99	3.99	3.99	3.98	3.99	3.99
En	0.07	0.06	0.03	0.11	0.10	0.02	0.12	0.03	0.05	0.04	0.04	0.11
Fs	0.69	0.74	0.84	0.66	0.71	0.85	0.68	0.84	0.78	0.81	0.78	0.69
Wo	0.24	0.20	0.13	0.24	0.19	0.13	0.20	0.13	0.17	0.15	0.18	0.20
Total	1.0	1.0	1.0	1.0	1.0	1.0	1.0	1.0	1.0	1.0	1.0	1.0

EPMA data for pyroxene in 10044 (cont.)

	MS6_b	MS8_n
P_2O_5	0.00	0.01
SiO_2	0.02	0.03
TiO_2	52.41	52.26
Al_2O_3	0.07	0.09
MgO	0.15	0.27
CaO	0.01	0.00
MnO	0.40	0.41
FeO	45.71	45.47
Na_2O	0.00	0.00
K_2O	0.00	0.00
Total	98.77	98.53
P	0.00	0.00
Si	0.00	0.00
Ti	1.00	1.00
Al	0.00	0.00
Mg	0.01	0.01
Ca	0.00	0.00
Mn	0.01	0.01
Fe	0.97	0.97
Na	0.00	0.00
K	0.00	0.00
Total	1.99	2.00

Table B.10: EPMA data for ilmenite in 10044

	meso1	MS1_aa	MS1_v	MS1_w	MS1_x	MS3_e	MS3_o	MS3_t	MS3_u	MS3_v	MS4_g	MS4_h
P_2O_5	0.00	0.00	0.03	0.00	0.00	0.00	0.01	0.00	0.00	0.01	0.00	0.00
SiO_2	98.73	99.40	98.98	99.85	100.34	99.38	99.85	99.52	99.21	99.86	99.24	99.58
TiO_2	0.17	0.33	0.30	0.34	0.28	0.19	0.24	0.34	0.11	0.16	0.28	0.27
Al_2O_3	0.63	0.68	0.60	0.71	0.62	0.80	0.63	0.87	0.63	0.50	0.60	0.63
MgO	0.00	0.00	0.00	0.00	0.00	0.00	0.01	0.00	0.00	0.00	0.00	0.00
CaO	0.06	0.12	0.11	0.17	0.13	0.09	0.11	0.17	0.06	0.06	0.11	0.12
MnO	0.00	0.00	0.00	0.01	0.00	0.00	0.00	0.03	0.00	0.00	0.00	0.00
FeO	0.07	0.19	0.10	0.45	0.27	0.14	0.08	0.04	0.03	0.14	0.04	0.07
Na_2O	0.10	0.28	0.20	0.21	0.22	0.18	0.25	0.26	0.15	0.11	0.21	0.27
K_2O	0.29	0.02	0.01	0.01	0.04	0.35	0.00	0.01	0.26	0.20	0.01	0.01
Total	100.05	101.02	100.34	101.73	101.90	101.13	101.18	101.24	100.44	101.03	100.50	100.95
P	0.00	0.00	0.00	0.00	0.00	0.00	0.00	0.00	0.00	0.00	0.00	0.00
Si	0.99	0.99	0.99	0.99	0.99	0.99	0.99	0.99	0.99	0.99	0.99	0.99
Ti	0.00	0.00	0.00	0.00	0.00	0.00	0.00	0.00	0.00	0.00	0.00	0.00
Al	0.01	0.01	0.01	0.01	0.01	0.01	0.01	0.01	0.01	0.01	0.01	0.01
Mg	0.00	0.00	0.00	0.00	0.00	0.00	0.00	0.00	0.00	0.00	0.00	0.00
Ca	0.00	0.00	0.00	0.00	0.00	0.00	0.00	0.00	0.00	0.00	0.00	0.00
Mn	0.00	0.00	0.00	0.00	0.00	0.00	0.00	0.00	0.00	0.00	0.00	0.00
Fe	0.00	0.00	0.00	0.00	0.00	0.00	0.00	0.00	0.00	0.00	0.00	0.00
Na	0.00	0.01	0.00	0.00	0.00	0.00	0.00	0.00	0.00	0.00	0.00	0.01
K	0.00	0.00	0.00	0.00	0.00	0.00	0.00	0.00	0.00	0.00	0.00	0.00
Total	1.01	1.01	1.01	1.01	1.01	1.01	1.01	1.01	1.01	1.01	1.01	1.01

Table B.11: EPMA data for silica in 10044

	MS4_i	MS4_n	MS5_e	MS5_f	MS5_g	MS5_h	MS5_j	MS5_k	MS5_s	MS8_s	MS8_u	MS9_b	MS9_d
P_2O_5	0.00	0.00	0.00	0.02	0.00	0.00	0.00	0.00	0.00	0.00	0.00	0.00	0.02
SiO_2	99.96	98.72	99.60	99.50	98.67	98.60	99.70	99.47	98.56	98.62	99.28	98.71	98.75
TiO_2	0.24	0.34	0.28	0.29	0.31	0.40	0.19	0.21	0.20	0.21	0.26	0.16	0.18
Al_2O_3	0.51	0.94	0.81	0.75	0.90	0.88	0.90	0.80	0.95	0.75	0.66	0.62	0.63
MgO	0.00	0.01	0.00	0.00	0.00	0.00	0.00	0.00	0.00	0.00	0.00	0.00	0.00
CaO	0.13	0.19	0.15	0.15	0.06	0.06	0.08	0.06	0.05	0.05	0.08	0.07	0.13
MnO	0.00	0.00	0.00	0.01	0.00	0.01	0.01	0.00	0.00	0.00	0.01	0.00	0.00
FeO	0.11	0.05	0.05	0.06	0.04	0.06	0.23	0.15	0.27	0.11	0.09	0.05	0.26
Na_2O	0.19	0.30	0.29	0.28	0.15	0.12	0.23	0.21	0.21	0.14	0.20	0.18	0.16
K_2O	0.01	0.02	0.01	0.01	0.44	0.45	0.32	0.32	0.49	0.35	0.21	0.21	0.15
Total	101.15	100.55	101.20	101.06	100.57	100.58	101.67	101.22	100.73	100.22	100.78	100.00	100.30
P	0.00	0.00	0.00	0.00	0.00	0.00	0.00	0.00	0.00	0.00	0.00	0.00	0.00
Si	0.99	0.99	0.99	0.99	0.99	0.99	0.99	0.99	0.99	0.99	0.99	0.99	0.99
Ti	0.00	0.00	0.00	0.00	0.00	0.00	0.00	0.00	0.00	0.00	0.00	0.00	0.00
Al	0.01	0.01	0.01	0.01	0.01	0.01	0.01	0.01	0.01	0.01	0.01	0.01	0.01
Mg	0.00	0.00	0.00	0.00	0.00	0.00	0.00	0.00	0.00	0.00	0.00	0.00	0.00
Ca	0.00	0.00	0.00	0.00	0.00	0.00	0.00	0.00	0.00	0.00	0.00	0.00	0.00
Mn	0.00	0.00	0.00	0.00	0.00	0.00	0.00	0.00	0.00	0.00	0.00	0.00	0.00
Fe	0.00	0.00	0.00	0.00	0.00	0.00	0.00	0.00	0.00	0.00	0.00	0.00	0.00
Na	0.00	0.01	0.01	0.01	0.00	0.00	0.00	0.00	0.00	0.00	0.00	0.00	0.00
K	0.00	0.00	0.00	0.00	0.01	0.01	0.00	0.00	0.01	0.00	0.00	0.00	0.00
Total	1.01	1.01	1.01	1.01	1.01	1.01	1.01	1.01	1.01	1.01	1.01	1.01	1.01

EPMA data for silica in 10044 (cont.)

	MS2_h	MS2_pp	MS2_qq	MS2_y	MS3_w	MS7_d	Si1	Si4
P_2O_5	0.05	0.11	0.05	0.06	0.05	0.06	0.06	0.09
SiO_2	78.02	77.21	75.77	76.23	78.11	75.08	75.34	78.56
TiO_2	0.37	0.41	0.29	0.23	0.41	0.32	0.26	0.34
Al_2O_3	11.28	11.48	12.48	11.69	11.81	12.34	11.54	10.24
MgO	0.00	0.00	0.00	0.01	0.00	0.01	0.01	0.00
CaO	0.53	0.88	1.17	1.07	1.47	0.50	1.55	0.93
MnO	0.00	0.00	0.00	0.02	0.00	0.01	0.00	0.00
FeO	0.97	1.31	0.74	1.13	0.61	1.17	0.82	0.62
Na_2O	0.73	0.30	0.42	0.41	0.38	0.24	0.49	0.34
K_2O	7.88	8.23	8.56	7.96	7.76	9.93	7.93	7.84
Total	99.83	99.93	99.49	98.80	100.60	99.66	98.17	99.08
P	0.00	0.00	0.00	0.00	0.00	0.00	0.00	0.00
Si	3.40	3.37	3.33	3.37	3.37	3.32	3.36	3.44
Ti	0.01	0.01	0.01	0.01	0.01	0.01	0.01	0.01
Al	0.58	0.59	0.65	0.61	0.60	0.64	0.61	0.53
Mg	0.00	0.00	0.00	0.00	0.00	0.00	0.00	0.00
Ca	0.02	0.04	0.06	0.05	0.07	0.02	0.07	0.04
Mn	0.00	0.00	0.00	0.00	0.00	0.00	0.00	0.00
Fe	0.04	0.05	0.03	0.04	0.02	0.04	0.03	0.02
Na	0.06	0.02	0.04	0.03	0.03	0.02	0.04	0.03
K	0.44	0.46	0.48	0.45	0.43	0.56	0.45	0.44
Total	4.55	4.55	4.59	4.56	4.54	4.63	4.57	4.51

Table B.12: EPMA data for K-glass in 10044

	MS5_q
P_2O_5	0.08
SiO_2	29.55
TiO_2	0.12
Al_2O_2	0.00
MgO	0.55
CaO	0.38
MnO	0.87
FeO	66.47
Na_2O	0.06
K_2O	0.00
Total	98.07
P	0.00
Si	1.01
Ti	0.00
Al	0.00
Mg	0.03
Ca	0.01
Mn	0.03
Fe	1.90
Na	0.00
K	0.00
Total	2.99

Table B.13: EPMA data for fayalite in 10044

	MS10_g	MS10_o	MS10_y	MS11_a	MS11_b	MS11_c	MS11_f	MS11_g	MS11_h	MS12_k	MS13_a	MS13_g
P_2O_5	0.00	0.00	0.01	0.01	0.01	0.03	0.00	0.00	0.04	0.06	0.00	0.00
SiO_2	46.21	46.56	47.41	47.58	46.88	46.55	46.59	47.04	48.05	48.62	46.82	46.59
TiO_2	0.04	0.02	0.01	0.00	0.00	0.02	0.03	0.05	0.04	0.07	0.09	0.06
Al_2O_3	33.42	33.34	32.62	32.52	32.94	33.43	33.41	33.11	32.27	31.84	33.33	33.47
MgO	0.10	0.08	0.03	0.03	0.04	0.06	0.08	0.04	0.02	0.03	0.13	0.28
CaO	17.93	17.48	17.10	16.78	17.18	17.81	17.72	17.50	16.86	16.10	17.73	18.05
MnO	0.01	0.00	0.00	0.01	0.02	0.00	0.02	0.00	0.00	0.00	0.03	0.00
FeO	0.74	0.81	0.99	0.96	0.87	0.76	0.83	0.83	0.97	0.93	0.83	0.57
Na_2O	1.00	1.10	1.13	1.15	1.06	0.99	0.96	0.99	1.10	1.20	1.03	0.93
K_2O	0.07	0.10	0.31	0.48	0.22	0.13	0.11	0.19	0.41	0.78	0.07	0.03
Total	99.53	99.50	99.61	99.52	99.20	99.78	99.75	99.75	99.77	99.62	100.05	99.97
P	0.00	0.00	0.00	0.00	0.00	0.00	0.00	0.00	0.00	0.00	0.00	0.00
Si	2.14	2.16	2.19	2.20	2.18	2.15	2.15	2.17	2.22	2.24	2.16	2.15
Ti	0.00	0.00	0.00	0.00	0.00	0.00	0.00	0.00	0.00	0.00	0.00	0.00
Al	1.83	1.82	1.78	1.77	1.80	1.82	1.82	1.80	1.75	1.73	1.81	1.82
Mg	0.01	0.01	0.00	0.00	0.00	0.00	0.01	0.00	0.00	0.00	0.01	0.02
Ca	0.89	0.87	0.85	0.83	0.85	0.88	0.88	0.87	0.83	0.80	0.88	0.89
Mn	0.00	0.00	0.00	0.00	0.00	0.00	0.00	0.00	0.00	0.00	0.00	0.00
Fe	0.03	0.03	0.04	0.04	0.03	0.03	0.03	0.03	0.04	0.04	0.03	0.02
Na	0.09	0.10	0.10	0.10	0.10	0.09	0.09	0.09	0.10	0.11	0.09	0.08
K	0.00	0.01	0.02	0.03	0.01	0.01	0.01	0.01	0.02	0.05	0.00	0.00
Total	4.99	4.99	4.98	4.98	4.98	4.98	4.98	4.98	4.97	4.96	4.98	4.98
An	0.90	0.89	0.88	0.86	0.89	0.90	0.90	0.90	0.87	0.84	0.90	0.91
Ab	0.09	0.10	0.11	0.11	0.10	0.09	0.09	0.09	0.10	0.11	0.09	0.08
Or	0.00	0.01	0.02	0.03	0.01	0.01	0.01	0.01	0.03	0.05	0.00	0.00
Total	1.0	1.0	1.0	1.0	1.0	1.0	1.0	1.0	1.0	1.0	1.0	1.0

Table B.14: EPMA data for feldspar in 12064

	MS10_d	MS10_m	MS10_n	MS11_d	MS11_e	MS11_i	MS11_k	MS12_c	MS12_d	MS12_h	MS12_i
P_2O_5	0.03	0.00	0.02	0.01	0.02	0.02	0.02	0.03	0.01	0.01	0.01
SiO_2	46.43	45.91	47.01	47.34	45.77	46.03	47.00	45.94	46.08	45.86	46.55
TiO_2	1.09	1.00	0.96	1.08	0.99	0.94	0.37	0.82	0.86	1.01	0.80
Al_2O_3	0.89	0.87	0.95	1.07	0.87	0.93	0.31	0.95	0.93	1.23	0.85
MgO	1.29	1.55	4.77	4.65	1.56	1.36	1.00	1.20	1.28	1.12	1.35
CaO	15.69	9.15	9.72	12.43	9.22	12.42	5.81	9.59	9.76	10.74	12.50
MnO	0.44	0.46	0.47	0.45	0.50	0.38	0.60	0.39	0.42	0.38	0.32
FeO	32.82	39.74	34.73	31.72	39.92	36.62	44.91	39.81	39.16	38.42	36.52
Na_2O	0.00	0.02	0.00	0.00	0.02	0.01	0.00	0.01	0.00	0.01	0.03
K_2O	0.00	0.00	0.00	0.00	0.00	0.00	0.00	0.00	0.00	0.00	0.00
Total	98.68	98.70	98.62	98.74	98.86	98.71	100.01	98.73	98.51	98.79	98.92
P	0.00	0.00	0.00	0.00	0.00	0.00	0.00	0.00	0.00	0.00	0.00
Si	1.95	1.96	1.96	1.95	1.95	1.95	2.00	1.96	1.97	1.95	1.97
Ti	0.03	0.03	0.03	0.03	0.03	0.03	0.01	0.03	0.03	0.03	0.03
Al	0.04	0.04	0.05	0.05	0.04	0.05	0.02	0.05	0.05	0.06	0.04
Mg	0.08	0.10	0.30	0.29	0.10	0.09	0.06	0.08	0.08	0.07	0.08
Ca	0.71	0.42	0.43	0.55	0.42	0.56	0.27	0.44	0.45	0.49	0.57
Mn	0.02	0.02	0.02	0.02	0.02	0.01	0.02	0.01	0.02	0.01	0.01
Fe	1.15	1.42	1.21	1.09	1.42	1.30	1.60	1.42	1.40	1.37	1.29
Na	0.00	0.00	0.00	0.00	0.00	0.00	0.00	0.00	0.00	0.00	0.00
K	0.00	0.00	0.00	0.00	0.00	0.00	0.00	0.00	0.00	0.00	0.00
Total	3.99	3.99	3.99	3.99	3.99	3.99	3.98	3.99	3.98	3.99	3.99
En	0.04	0.05	0.15	0.15	0.05	0.04	0.03	0.04	0.04	0.04	0.04
Fs	0.59	0.73	0.62	0.57	0.73	0.67	0.83	0.73	0.73	0.71	0.66
Wo	0.36	0.22	0.22	0.28	0.22	0.29	0.14	0.23	0.23	0.25	0.29
Total	1.0	1.0	1.0	1.0	1.0	1.0	1.0	1.0	1.0	1.0	1.0

Table B.15: EPMA data for pyroxene in 12064

	MS13_b	MS13_c	MS13_e	MS13_j	MS13_m	MS13_p
P_2O_5	0.05	0.01	0.02	0.02	0.00	0.03
SiO_2	45.75	45.87	45.70	45.68	46.83	46.01
TiO_2	0.38	0.92	0.89	0.79	0.91	0.93
Al_2O_3	0.28	0.95	0.94	0.83	1.02	1.08
MgO	0.88	1.21	1.27	1.22	3.62	1.17
CaO	5.08	9.92	9.02	9.69	10.27	11.48
MnO	0.63	0.46	0.48	0.42	0.48	0.44
FeO	45.66	39.61	40.24	39.87	35.80	37.80
Na_2O	0.00	0.03	0.00	0.00	0.00	0.00
K_2O	0.00	0.00	0.00	0.00	0.00	0.00
Total	98.69	98.98	98.54	98.52	98.93	98.94
P	0.00	0.00	0.00	0.00	0.00	0.00
Si	1.99	1.95	1.96	1.96	1.96	1.95
Ti	0.01	0.03	0.03	0.03	0.03	0.03
Al	0.01	0.05	0.05	0.04	0.05	0.05
Mg	0.06	0.08	0.08	0.08	0.23	0.07
Ca	0.24	0.45	0.41	0.45	0.46	0.52
Mn	0.02	0.02	0.02	0.02	0.02	0.02
Fe	1.66	1.41	1.44	1.43	1.25	1.34
Na	0.00	0.00	0.00	0.00	0.00	0.00
K	0.00	0.00	0.00	0.00	0.00	0.00
Total	3.99	3.99	3.99	3.99	3.99	3.99
En	0.03	0.04	0.04	0.04	0.12	0.04
Fs	0.85	0.73	0.74	0.73	0.65	0.69
Wo	0.12	0.23	0.21	0.23	0.24	0.27
Total	1.0	1.0	1.0	1.0	1.0	1.0

EPMA data for pyroxene in 12064 (cont.)

	MS10_q	MS10_r
P_2O_5	0.00	0.01
SiO_2	0.03	0.02
TiO_2	51.51	51.27
Al_2O_3	0.08	0.04
MgO	0.16	0.16
CaO	0.14	0.01
MnO	0.31	0.30
FeO	45.06	45.46
Na_2O	0.00	0.02
K_2O	0.00	0.00
Total	97.28	97.28
P	0.00	0.00
Si	0.00	0.00
Ti	1.00	1.00
Al	0.00	0.00
Mg	0.01	0.01
Ca	0.00	0.00
Mn	0.01	0.01
Fe	0.97	0.98
Na	0.00	0.00
K	0.00	0.00
Total	2.00	2.00

Table B.16: EPMA data for ilmenite in 12064

	MS10_cc	MS10_dd	MS10_jj	MS10_qq	MS10_rr	MS10_ww	MS13_o
P_2O_5	0.03	0.00	0.00	0.00	0.00	0.00	0.00
SiO_2	99.45	99.60	96.74	99.20	99.39	99.17	99.33
TiO_2	0.19	0.24	0.26	0.19	0.18	0.20	0.24
Al_2O_3	0.30	0.37	0.78	0.39	0.39	0.44	0.47
MgO	0.00	0.00	0.00	0.00	0.00	0.00	0.00
CaO	0.03	0.02	0.30	0.04	0.03	0.03	0.04
MnO	0.00	0.01	0.00	0.01	0.00	0.00	0.01
FeO	0.18	0.03	0.45	0.10	0.08	0.08	0.46
Na_2O	0.02	0.07	0.16	0.05	0.04	0.04	0.03
K_2O	0.20	0.25	0.01	0.27	0.26	0.30	0.31
Total	100.39	100.58	98.70	100.24	100.37	100.24	100.90
P	0.00	0.00	0.00	0.00	0.00	0.00	0.00
Si	0.99	0.99	0.99	0.99	0.99	0.99	0.99
Ti	0.00	0.00	0.00	0.00	0.00	0.00	0.00
Al	0.00	0.00	0.01	0.00	0.00	0.01	0.01
Mg	0.00	0.00	0.00	0.00	0.00	0.00	0.00
Ca	0.00	0.00	0.00	0.00	0.00	0.00	0.00
Mn	0.00	0.00	0.00	0.00	0.00	0.00	0.00
Fe	0.00	0.00	0.00	0.00	0.00	0.00	0.00
Na	0.00	0.00	0.00	0.00	0.00	0.00	0.00
K	0.00	0.00	0.00	0.00	0.00	0.00	0.00
Total	1.00	1.00	1.01	1.01	1.00	1.01	1.01

Table B.17: EPMA data for silica in 12064

	MS10_gg
P_2O_5	0.05
SiO_2	74.86
TiO_2	0.50
Al_2O_3	11.78
MgO	0.00
CaO	1.55
MnO	0.02
FeO	2.27
Na_2O	0.27
K_2O	7.90
Total	99.20
P	0.00
Si	3.32
Ti	0.02
Al	0.62
Mg	0.00
Ca	0.07
Mn	0.00
Fe	0.08
Na	0.02
K	0.45
Total	4.59
An	0.14
Ab	0.04
Or	0.82
Total	1.0

Table B.18: EPMA data for K-glass in 12064

	MS11_l	MS10_uu
P_2O_5	0.08	0.11
SiO_2	29.42	29.47
TiO_2	0.11	0.11
Al_2O_5	0.00	0.00
MgO	0.86	0.80
CaO	0.38	1.07
MnO	0.72	0.71
FeO	66.83	66.11
Na_2O	0.00	0.05
K_2O	0.00	0.00
Total	98.40	98.42
P	0.00	0.00
Si	1.00	1.00
Ti	0.00	0.00
Al	0.00	0.00
Mg	0.04	0.04
Ca	0.01	0.04
Mn	0.02	0.02
Fe	1.91	1.88
Na	0.00	0.00
K	0.00	0.00
Total	2.99	2.99

Table B.19: EPMA data for fayalite in 12064

	MS20_o	MS20_w	MS20_y	MS21_a	MS21_b	MS21_f	MS21_g
P_2O_5	0.02	0.03	0.00	0.02	0.01	0.00	0.00
SiO_2	49.12	45.30	48.22	47.61	47.52	45.54	47.78
TiO_2	0.05	0.03	0.05	0.06	0.05	0.05	0.05
Al_2O_3	31.04	34.12	31.91	32.16	32.01	33.94	32.00
MgO	0.03	0.22	0.35	0.30	0.30	0.16	0.15
CaO	15.93	18.59	17.18	17.13	17.05	18.37	16.85
MnO	0.00	0.02	0.00	0.01	0.00	0.01	0.02
FeO	1.03	0.46	0.77	0.75	0.76	0.53	0.76
Na_2O	1.42	0.81	1.41	1.42	1.42	0.94	1.47
K_2O	0.64	0.02	0.05	0.05	0.06	0.03	0.23
Total	99.27	99.60	99.94	99.50	99.19	99.58	99.31
P	0.00	0.00	0.00	0.00	0.00	0.00	0.00
Si	2.27	2.10	2.22	2.20	2.20	2.11	2.21
Ti	0.00	0.00	0.00	0.00	0.00	0.00	0.00
Al	1.69	1.87	1.73	1.75	1.75	1.86	1.75
Mg	0.00	0.02	0.02	0.02	0.02	0.01	0.01
Ca	0.79	0.92	0.85	0.85	0.85	0.91	0.84
Mn	0.00	0.00	0.00	0.00	0.00	0.00	0.00
Fe	0.04	0.02	0.03	0.03	0.03	0.02	0.03
Na	0.13	0.07	0.13	0.13	0.13	0.08	0.13
K	0.04	0.00	0.00	0.00	0.00	0.00	0.01
Total	4.96	5.00	4.98	4.98	4.98	5.00	4.98
An	0.83	0.93	0.87	0.87	0.87	0.91	0.85
Ab	0.13	0.07	0.13	0.13	0.13	0.08	0.13
Or	0.04	0.00	0.00	0.00	0.00	0.00	0.01
Total	1.0	1.0	1.0	1.0	1.0	1.0	1.0

Table B.20: EPMA data for feldspar in 15058

	MS20_x	MS21_z	MS21_c
P_2O_5	0.00	0.04	0.00
SiO_2	49.15	48.09	47.36
TiO_2	0.79	1.20	1.09
Al_2O_3	1.16	1.30	1.14
MgO	10.92	8.30	4.84
CaO	9.99	13.27	13.44
MnO	0.39	0.36	0.40
FeO	25.97	25.81	30.32
Na_2O	0.02	0.11	0.01
K_2O	0.00	0.00	0.00
Total	98.38	98.48	98.60
P	0.00	0.00	0.00
Si	1.96	1.94	1.95
Ti	0.02	0.04	0.03
Al	0.05	0.06	0.06
Mg	0.65	0.50	0.30
Ca	0.43	0.57	0.59
Mn	0.01	0.01	0.01
Fe	0.87	0.87	1.04
Na	0.00	0.01	0.00
Total	3.99	4.00	3.99
En	0.33	0.26	0.15
Fs	0.45	0.45	0.54
Wo	0.22	0.30	0.31
Total	1.0	1.0	1.0

Table B.21: EPMA data for pyroxene in 15058

	MS20_c	MS20_j	MS20_r	MS20_v	MS21_h	MS21_i
P_2O_5	0.00	0.00	0.01	0.00	0.02	0.01
SiO_2	98.75	98.57	98.68	98.73	98.95	98.51
TiO_2	0.22	0.19	0.24	0.21	0.30	0.18
Al_2O_3	0.97	0.48	0.46	0.46	0.44	0.57
MgO	0.00	0.00	0.00	0.00	0.00	0.00
CaO	0.25	0.04	0.05	0.07	0.10	0.11
MnO	0.02	0.01	0.00	0.00	0.00	0.00
FeO	0.04	0.08	0.08	0.20	0.03	0.17
Na_2O	0.10	0.11	0.10	0.09	0.17	0.10
K_2O	0.31	0.23	0.16	0.17	0.01	0.25
Total	100.66	99.72	99.78	99.92	100.02	99.90
P	0.00	0.00	0.00	0.00	0.00	0.00
Si	0.99	0.99	0.99	0.99	0.99	0.99
Ti	0.00	0.00	0.00	0.00	0.00	0.00
Al	0.01	0.01	0.01	0.01	0.01	0.01
Mg	0.00	0.00	0.00	0.00	0.00	0.00
Ca	0.00	0.00	0.00	0.00	0.00	0.00
Mn	0.00	0.00	0.00	0.00	0.00	0.00
Fe	0.00	0.00	0.00	0.00	0.00	0.00
Na	0.00	0.00	0.00	0.00	0.00	0.00
K	0.00	0.00	0.00	0.00	0.00	0.00
Total	1.01	1.01	1.01	1.01	1.00	1.01

Table B.22: EPMA data for silica in 15058

	MS21_j	MS21_m	MS21_n	MS21_r	MS21_s	MS21_w	MS21_y
P_2O_5	0.00	0.00	0.01	0.03	0.00	0.02	0.00
SiO_2	98.52	97.50	97.48	97.87	98.10	97.70	98.47
TiO_2	0.34	0.33	0.36	0.32	0.27	0.33	0.29
Al_2O_3	0.73	0.71	0.45	0.49	0.49	0.68	0.52
MgO	0.00	0.00	0.00	0.00	0.00	0.00	0.00
CaO	0.20	0.14	0.11	0.09	0.11	0.12	0.14
MnO	0.01	0.00	0.01	0.00	0.00	0.00	0.00
FeO	0.10	0.17	0.60	0.13	0.19	0.11	0.23
Na_2O	0.19	0.22	0.15	0.14	0.17	0.20	0.21
K_2O	0.01	0.00	0.01	0.00	0.01	0.01	0.00
Total	100.10	99.08	99.17	99.06	99.35	99.16	99.86
P	0.00	0.00	0.00	0.00	0.00	0.00	0.00
Si	0.99	0.99	0.99	0.99	0.99	0.99	0.99
Ti	0.00	0.00	0.00	0.00	0.00	0.00	0.00
Al	0.01	0.01	0.01	0.01	0.01	0.01	0.01
Mg	0.00	0.00	0.00	0.00	0.00	0.00	0.00
Ca	0.00	0.00	0.00	0.00	0.00	0.00	0.00
Mn	0.00	0.00	0.00	0.00	0.00	0.00	0.00
Fe	0.00	0.00	0.01	0.00	0.00	0.00	0.00
Na	0.00	0.00	0.00	0.00	0.00	0.00	0.00
K	0.00	0.00	0.00	0.00	0.00	0.00	0.00
Total	1.01	1.01	1.01	1.00	1.01	1.01	1.01

EPMA data for silica in 15058 (cont.)

	G2
P_2O_5	0.04
SiO_2	76.61
TiO_2	
Al_2O_3	12.20
MgO	0.00
CaO	0.14
MnO	0.00
FeO	0.19
Na_2O	0.15
K_2O	8.13
Total	100.10
P	0.00
Si	3.40
Ti	0.00
Al	0.64
Mg	0.00
Ca	0.01
Mn	0.00
Fe	0.01
Na	0.01
K	0.46
Total	4.52
An	0.01
Ab	0.03
Or	0.96
Total	1.0

Table B.23: EPMA data for K-glass in 15058

	MS30_g	MS30_h	MS30_l	MS31_b	MS31_h	MS31_l	MS31_m	MS32_a	MS32_i	MS32_j	MS32_m
P_2O_5	0.02	0.00	0.02	0.04	0.05	0.01	0.03	0.03	0.00	0.03	0.02
SiO_2	47.14	46.98	50.05	49.59	50.42	49.45	48.86	49.08	50.04	49.74	50.49
TiO_2	0.10	0.08	0.11	0.28	0.08	0.05	0.07	0.12	0.09	0.06	0.08
Al_2O_3	32.95	32.91	30.67	29.80	30.67	31.73	31.72	31.48	30.34	30.59	30.25
MgO	0.23	0.23	0.17	0.14	0.13	0.18	0.23	0.20	0.15	0.16	0.20
CaO	17.35	17.35	15.17	15.17	14.76	15.69	16.35	15.91	15.22	15.23	15.12
MnO	0.02	0.02	0.00	0.00	0.03	0.00	0.02	0.00	0.01	0.01	0.00
FeO	0.47	0.41	0.69	0.97	0.96	0.69	0.59	0.52	0.62	0.58	0.60
Na_2O	1.38	1.60	2.13	2.29	2.29	2.09	1.80	2.00	2.25	2.20	2.22
K_2O	0.09	0.07	0.41	0.26	0.51	0.18	0.11	0.17	0.30	0.35	0.24
Total	99.75	99.63	99.41	98.54	99.89	100.07	99.77	99.51	99.02	98.94	99.20
P	0.00	0.00	0.00	0.00	0.00	0.00	0.00	0.00	0.00	0.00	0.00
Si	2.17	2.17	2.30	2.31	2.31	2.26	2.24	2.26	2.31	2.30	2.32
Ti	0.00	0.00	0.00	0.01	0.00	0.00	0.00	0.00	0.00	0.00	0.00
Al	1.79	1.79	1.66	1.63	1.66	1.71	1.72	1.71	1.65	1.67	1.64
Mg	0.02	0.02	0.01	0.01	0.01	0.01	0.02	0.01	0.01	0.01	0.01
Ca	0.86	0.86	0.75	0.76	0.72	0.77	0.80	0.78	0.75	0.75	0.75
Mn	0.00	0.00	0.00	0.00	0.00	0.00	0.00	0.00	0.00	0.00	0.00
Fe	0.02	0.02	0.03	0.04	0.04	0.03	0.02	0.02	0.02	0.02	0.02
Na	0.12	0.14	0.19	0.21	0.20	0.19	0.16	0.18	0.20	0.20	0.20
K	0.01	0.00	0.02	0.02	0.03	0.01	0.01	0.01	0.02	0.02	0.01
Total	4.99	5.00	4.97	4.98	4.97	4.98	4.98	4.98	4.97	4.97	4.96
An	0.87	0.85	0.78	0.77	0.76	0.80	0.83	0.81	0.77	0.78	0.78
Ab	0.13	0.14	0.20	0.21	0.21	0.19	0.17	0.18	0.21	0.20	0.21
Or	0.01	0.00	0.02	0.02	0.03	0.01	0.01	0.01	0.02	0.02	0.01
Total	1.0	1.0	1.0	1.0	1.0	1.0	1.0	1.0	1.0	1.0	1.0

Table B.24: EPMA data for feldspar in 70035

	MS32_n	MS33_e	MS33_g	MS33_m	MS33_r	MS33_t	MS33_u	MS33_y	MS34_a	MS34_b	MS34_j
P_2O_5	0.02	0.04	0.05	0.22	0.10	0.01	0.00	0.00	0.01	0.02	0.02
SiO_2	48.33	50.33	50.69	50.09	48.24	50.23	50.46	46.04	48.45	47.45	50.27
TiO_2	0.08	0.04	0.15	0.41	0.21	0.11	0.08	0.12	0.10	0.04	0.07
Al_2O_3	31.55	30.44	29.89	29.13	31.17	30.14	30.44	33.67	31.62	32.34	30.25
MgO	0.18	0.17	0.21	0.38	0.22	0.21	0.21	0.23	0.22	0.23	0.18
CaO	15.92	14.50	14.54	14.29	15.45	14.95	14.94	17.91	16.00	16.66	14.73
MnO	0.02	0.02	0.02	0.03	0.02	0.00	0.03	0.00	0.02	0.02	0.01
FeO	0.52	0.59	0.65	1.66	0.83	0.56	0.63	0.45	0.44	0.40	0.67
Na_2O	1.91	2.37	2.48	2.29	1.93	2.19	2.21	1.22	1.88	1.68	2.22
K_2O	0.14	0.54	0.35	0.38	0.35	0.32	0.27	0.05	0.13	0.09	0.24
Total	98.66	99.03	99.03	98.86	98.51	98.72	99.27	99.70	98.85	98.94	98.65
P	0.00	0.00	0.00	0.01	0.00	0.00	0.00	0.00	0.00	0.00	0.00
Si	2.24	2.32	2.34	2.32	2.25	2.32	2.32	2.13	2.24	2.20	2.32
Ti	0.00	0.00	0.01	0.01	0.01	0.00	0.00	0.00	0.00	0.00	0.00
Al	1.73	1.65	1.62	1.59	1.71	1.64	1.65	1.84	1.73	1.77	1.65
Mg	0.01	0.01	0.01	0.03	0.01	0.01	0.01	0.02	0.01	0.02	0.01
Ca	0.79	0.72	0.72	0.71	0.77	0.74	0.74	0.89	0.79	0.83	0.73
Mn	0.00	0.00	0.00	0.00	0.00	0.00	0.00	0.00	0.00	0.00	0.00
Fe	0.02	0.02	0.03	0.06	0.03	0.02	0.02	0.02	0.02	0.02	0.03
Na	0.17	0.21	0.22	0.21	0.17	0.20	0.20	0.11	0.17	0.15	0.20
K	0.01	0.03	0.02	0.02	0.02	0.02	0.02	0.00	0.01	0.01	0.01
Total	4.98	4.97	4.97	4.97	4.98	4.96	4.96	5.00	4.98	4.99	4.96
An	0.81	0.75	0.75	0.76	0.80	0.77	0.78	0.89	0.82	0.84	0.77
Ab	0.18	0.22	0.23	0.22	0.18	0.21	0.21	0.11	0.17	0.15	0.21
Or	0.01	0.03	0.02	0.02	0.02	0.02	0.02	0.00	0.01	0.01	0.01
Total	1.0	1.0	1.0	1.0	1.0	1.0	1.0	1.0	1.0	1.0	1.0

EPMA data for feldspar in 70035 (cont.)

	MS30_a	MS30_b	MS30_o	MS31_a	MS31_i	MS33_d	MS33_j	MS33_v	MS34_c	MS34_l
P_2O_5	0.02	0.04	0.00	0.02	0.02	0.01	0.02	0.02	0.00	0.03
SiO_2	49.77	49.62	49.64	49.83	51.05	50.17	50.37	50.41	51.13	49.53
TiO_2	1.84	1.75	1.58	1.77	0.69	1.51	1.56	1.77	1.11	1.12
Al_2O_3	2.28	2.27	1.83	2.10	0.80	1.77	1.70	2.10	1.27	1.56
MgO	13.54	13.54	12.90	13.26	16.87	14.64	13.57	13.68	18.35	9.85
CaO	17.48	16.24	14.43	17.09	5.96	14.63	12.50	17.35	6.67	13.86
MnO	0.24	0.31	0.36	0.27	0.39	0.34	0.35	0.23	0.35	0.39
FeO	13.38	14.94	18.12	14.44	23.13	15.63	19.33	13.57	19.83	22.40
Na_2O	0.07	0.08	0.06	0.09	0.08	0.10	0.04	0.08	0.00	0.12
K_2O	0.00	0.01	0.00	0.00	0.00	0.00	0.00	0.00	0.00	0.00
Total	98.61	98.80	98.92	98.87	98.97	98.78	99.43	99.20	98.72	98.86
P	0.00	0.00	0.00	0.00	0.00	0.00	0.00	0.00	0.00	0.00
Si	1.90	1.90	1.92	1.91	1.97	1.92	1.93	1.92	1.95	1.95
Ti	0.05	0.05	0.05	0.05	0.02	0.04	0.05	0.05	0.03	0.03
Al	0.10	0.10	0.08	0.09	0.04	0.08	0.08	0.09	0.06	0.07
Mg	0.77	0.77	0.74	0.76	0.97	0.84	0.78	0.78	1.04	0.58
Ca	0.72	0.67	0.60	0.70	0.25	0.60	0.51	0.71	0.27	0.59
Mn	0.01	0.01	0.01	0.01	0.01	0.01	0.01	0.01	0.01	0.01
Fe	0.43	0.48	0.59	0.46	0.74	0.50	0.62	0.43	0.63	0.74
Na	0.01	0.01	0.00	0.01	0.01	0.01	0.00	0.01	0.00	0.01
K	0.00	0.00	0.00	0.00	0.00	0.00	0.00	0.00	0.00	0.00
Total	3.99	4.00	3.99	3.99	4.00	4.00	3.98	3.99	3.99	3.98
En	0.40	0.40	0.39	0.39	0.49	0.43	0.41	0.41	0.54	0.30
Fs	0.22	0.25	0.30	0.24	0.38	0.26	0.32	0.23	0.32	0.39
Wo	0.37	0.35	0.31	0.37	0.13	0.31	0.27	0.37	0.14	0.31
Total	1.0	1.0	1.0	1.0	1.0	1.0	1.0	1.0	1.0	1.0

Table B.25: EPMA data for pyroxene in 70058

	MS30_j	MS32_d	MS32_c
P_2O_5	0.00	0.01	0.00
SiO_2	0.00	0.01	0.06
TiO_2	53.43	53.45	53.45
Al_2O_3	0.02	0.03	0.04
MgO	2.56	2.24	2.33
CaO	0.00	0.01	0.05
MnO	0.38	0.39	0.36
FeO	41.65	41.97	41.86
Na_2O	0.00	0.00	0.05
K_2O	0.00	0.00	0.00
Total	98.04	98.10	98.19
P	0.00	0.00	0.00
Si	0.00	0.00	0.00
Ti	1.01	1.01	1.01
Al	0.00	0.00	0.00
Mg	0.10	0.08	0.09
Ca	0.00	0.00	0.00
Mn	0.01	0.01	0.01
Fe	0.88	0.88	0.88
Na	0.00	0.00	0.00
K	0.00	0.00	0.00
Total	1.99	1.99	1.99

Table B.26: EPMA data for ilmenite in 70058

	MS30_c	MS30_m	MS32_b	MS32_k	MS32_l	MS33_f	MS33_h	MS33_l	MS33_s	MS34_h	MS34_i	MS34_k
P_2O_5	0.00	0.01	0.03	0.00	0.04	0.00	0.03	0.00	0.00	0.00	0.01	0.00
SiO_2	98.04	98.60	97.36	98.15	98.69	97.88	97.24	98.15	97.15	97.68	97.26	97.98
TiO_2	0.34	0.38	0.34	0.27	0.32	0.52	0.38	0.51	0.41	0.33	0.34	0.30
Al_2O_3	0.71	0.83	1.02	0.80	0.63	1.02	0.92	1.05	1.17	0.86	0.97	0.73
MgO	0.00	0.00	0.00	0.00	0.01	0.00	0.01	0.00	0.00	0.01	0.00	0.00
CaO	0.14	0.20	0.26	0.08	0.14	0.29	0.21	0.24	0.36	0.11	0.22	0.08
MnO	0.00	0.00	0.00	0.01	0.00	0.00	0.00	0.01	0.01	0.00	0.01	0.00
FeO	0.18	0.20	0.11	0.08	0.24	0.26	0.29	0.18	0.12	0.21	0.03	0.10
Na_2O	0.20	0.29	0.29	0.16	0.21	0.32	0.34	0.37	0.30	0.17	0.32	0.19
K_2O	0.09	0.03	0.00	0.33	0.17	0.01	0.01	0.02	0.01	0.29	0.01	0.28
Total	99.69	100.55	99.42	99.89	100.45	100.30	99.43	100.53	99.52	99.65	99.17	99.65
P	0.00	0.00	0.00	0.00	0.00	0.00	0.00	0.00	0.00	0.00	0.00	0.00
Si	0.99	0.99	0.98	0.99	0.99	0.98	0.98	0.98	0.98	0.99	0.99	0.99
Ti	0.00	0.00	0.00	0.00	0.00	0.00	0.00	0.00	0.00	0.00	0.00	0.00
Al	0.01	0.01	0.01	0.01	0.01	0.01	0.01	0.01	0.01	0.01	0.01	0.01
Mg	0.00	0.00	0.00	0.00	0.00	0.00	0.00	0.00	0.00	0.00	0.00	0.00
Ca	0.00	0.00	0.00	0.00	0.00	0.00	0.00	0.00	0.00	0.00	0.00	0.00
Mn	0.00	0.00	0.00	0.00	0.00	0.00	0.00	0.00	0.00	0.00	0.00	0.00
Fe	0.00	0.00	0.00	0.00	0.00	0.00	0.00	0.00	0.00	0.00	0.00	0.00
Na	0.00	0.01	0.01	0.00	0.00	0.01	0.01	0.01	0.01	0.00	0.01	0.00
K	0.00	0.00	0.00	0.00	0.00	0.00	0.00	0.00	0.00	0.00	0.00	0.00
Total	1.01	1.01	1.01	1.01	1.01	1.01	1.01	1.01	1.01	1.01	1.01	1.01

Table B.27: EPMA data for silica in 70035

	MS32_h	G1	G2
P_2O_5	0.29		
SiO_2	74.47	76.83	76.89
TiO_2	0.76		
Al_2O_3	11.44	11.64	11.47
MgO	0.12	1.29	1.30
CaO	1.72	0.02	0.01
MnO	0.02	0.02	0.01
FeO	1.43	0.62	0.59
Na_2O	0.78	0.90	0.98
K_2O	6.24	6.53	6.28
Total	97.25	98.65	97.83
P	0.01	0.00	0.00
Si	3.33	3.38	3.39
Ti	0.03	0.00	0.00
Al	0.60	0.60	0.60
Mg	0.01	0.08	0.09
Ca	0.08	0.00	0.00
Mn	0.00	0.00	0.00
Fe	0.05	0.02	0.02
Na	0.07	0.08	0.08
K	0.36	0.37	0.35
Total	4.54	4.54	4.53

Table B.28: EPMA data for K-glass in 70035

Appendix C

Supplementary Material for Chapter 3

C.1 NanoSIMS calibrations

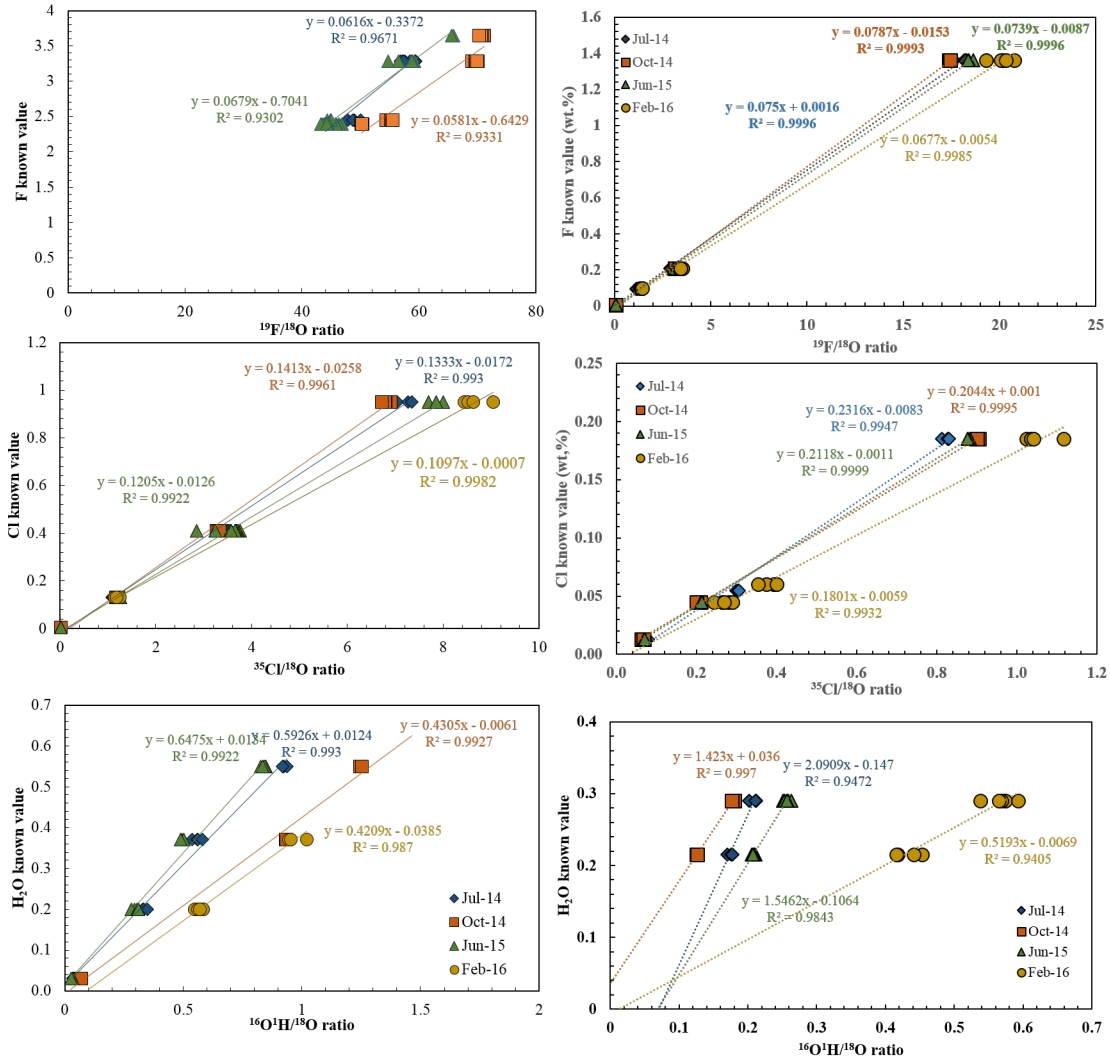

Figure C.1: Calibration curves for apatite and glass NanoSIMS measurements.

C.2 BSE images of all experimental runs

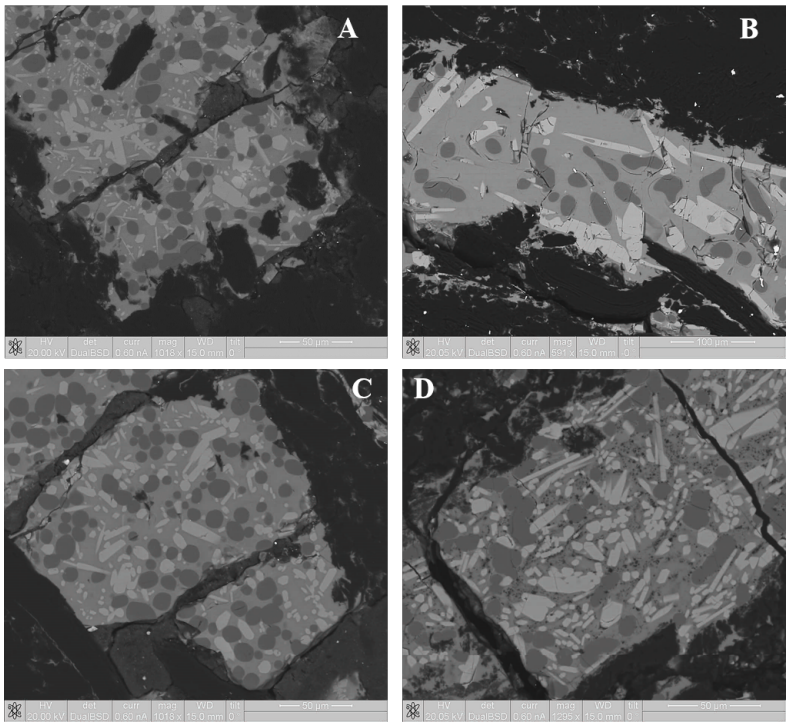

Figure C.2: (A) L2a 1350, (B) L2a 1400, (C) L2a 1450, (D) L2a 1450 72

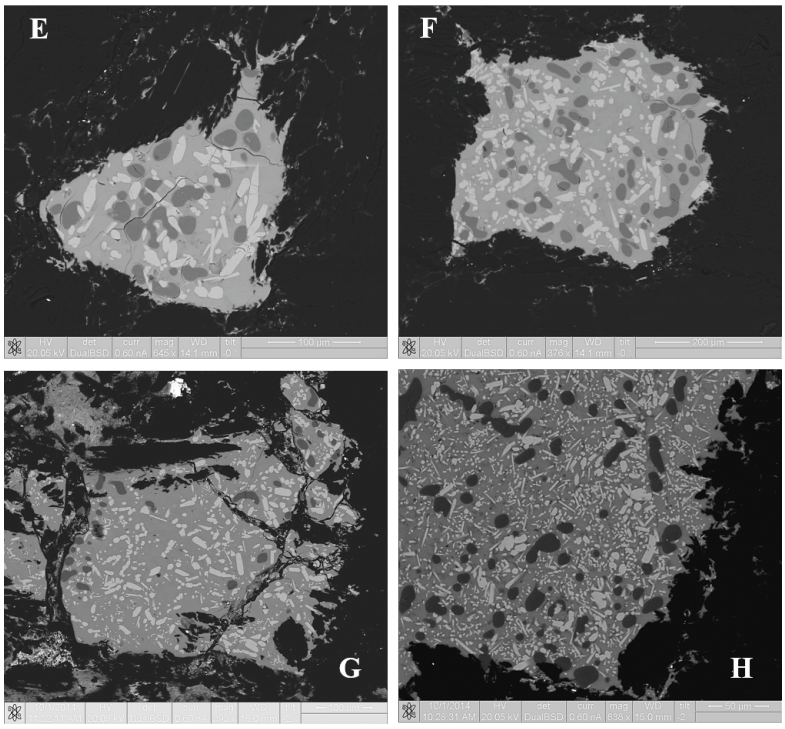

Figure C.3: (E) L2a OH 1350, (F) L2a OH 1450, (G) L3a 1400, (H) L3a 1450

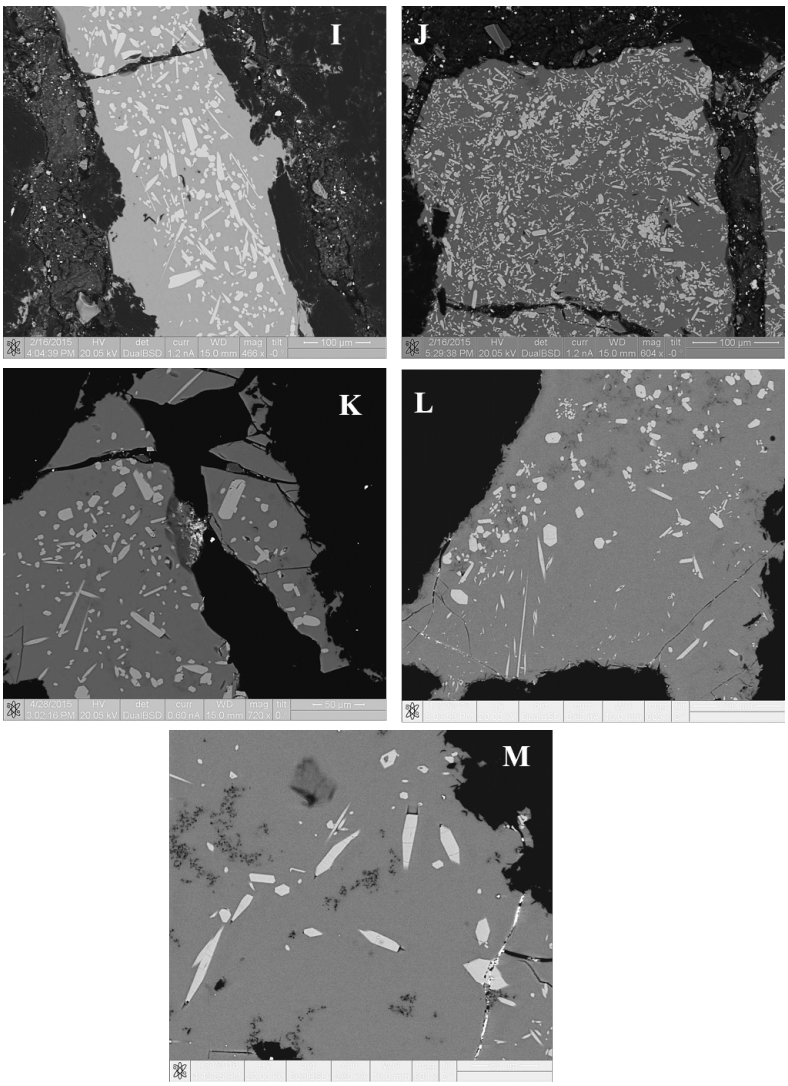

Figure C.4: (I) L3a Cl1 1450, (J) L3a Cl2 1350, (K) L4a OH1, (L) L4a OH2, (M) L4a OH3

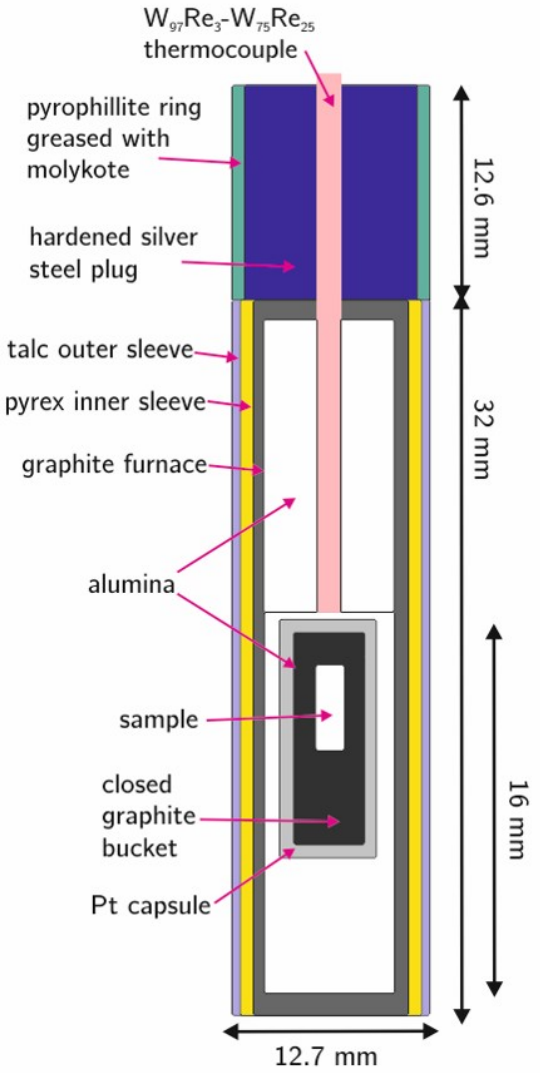

Figure C.5: Talc-pyrex assembly used in piston-cylinder experiments

C.3 Experimental Assembly

Appendix D

Supplementary Material for Chapter 5

D.1 Sample petrogenesis

The Apollo 14 Preliminary Examination Team reported that the majority of rocks from this mission were breccias with unconsolidated soil samples (LSPET, 1971). The only crystalline rocks, collected during this mission, >50 g were 14310 and 14053. Subsequently, 14073 and 14310 were found to be pairs of 14310 and 14053, respectively. 14310 and 14073 later became type specimens for "melt rocks" Taylor et al. (2004), while 14053 and 14072 are basaltic rocks. Further basaltic specimens have been identified in clasts of Apollo 14 breccias including those of 14321 (Neal and Kramer, 2006).

D.1.1 14053,19

Sample 14053 was a 251.3 g rock, collected at Station C2 (photographs AS14-64-9130 to AS14-64-9133). The sample was taken from taken a weathered boulder, ∼130 m south of the rim of Cone crater (LSPET, 1971). The area in which the sample was collected appears to be a continuous eject blanket of Cone crater, which is moderately covered by large rounded boulders and smaller more angular to rounded blocks. Small irregular craters, < 10 cm, are common in the sample locale.

Original investigations reported sample 14053 as a basalt (Quaide and Wrigley, 1972; Wilshire and Jackson, 1972), then as a mare basalt (Hubbard et al., 1972; Simonds et al., 1977). It was also been suggested this sample is a clast from a larger breccia boulder (Swann et al., 1977), given the rarity of crystalline rocks in the Apollo 14 collection. The Al_2O_3 concentration in 14053 is more like that of KREEP basalts (>12 %) but it has lower REE values and an intermediate K/U ratio that expected (Hubbard et al., 1972).

14053 is inhomogeneous in hand specimen, on a 1 –2 cm scale, with areas of concentrated olivine and pyroxene (LSPET, 1971). It is a holocrystalline, fine-grained, equigranular sample consisting dominantly of augite and plagioclase with minor ilmenite, chromite-ulvospinel, and tridymite (Carlson and Walton, 1978). There is also a mesostasis containing fayalite, troilite, K-Ba-rich glass, K-feldspar, apatite, merrillite, cristobalite, and badeleyite (Taylor et al., 2004). The inhomogeneous nature

of this rock means reports of feldspar modal abundance ranges from 30 % to 60 % (Carlson and Walton, 1978). Average plagioclase compositions, from a variety of thin sections, have found to range from $An_{91.3}$ (n = 3; Wenk et al., 1972) to An_{85-93} (n = 1) to An_{89-94} (n = 1; Czank et al., 1972). The absence of zircon in the sample places an upper limit on the oxygen fugacity during 14053's formation, which combined with the presence of schreibersite, baddeleyite and fayalite breakdown texture, indicates this sample (and other Apollo 14 crystalline rocks) formed under more reducing conditions than other Apollo rocks (El Goresey et al., 1971).

Dates for this sample from Rb-Sr (Papanastassiou and Wasserburg, 1971b)and $^{40}Ar/^{39}Ar$ (Husain et al., 1971; York et al., 1972) put its formation at 3.96 ± 0.04 b.y. and 3.92 ± 0.08 b.y. respectively. The exposure age for sample 14053,34, based on $^{38}Ar/^{37}Ar$ thermal release patterns is 21 ± 5 m.y. (Husain et al., 1971).

Initial crystallization of pyroxenes, from 14052, involved slow cooling from a near-surface magma at ∼1200 °C (Finger et al., 1972). This is shown by exsolution lamellae and cation disordering in Ca-poor pigeonite cores (Finger et al., 1972; Ghose et al., 1972). Cation distribution in pigeonites, from 14053, indicates rapid quenching from >1000 °C (Finger et al., 1972; Ghose et al., 1972; Schürmann and Hafner, 1972). This difference is reconciled by cooling to >840 °C followed by a short period of reheating leading to rapid cooling (Finger et al., 1972; Ghose et al., 1972). This short period of reheating has been attributed to impact events at Fra Mauro with successive cooling by conduction/radiation to surrounding cold regolith (Finger et al., 1972; Ghose et al., 1972; Schürmann and Hafner, 1972). Schürmann and Hafner (1972) suggest 14053 was a fist-sized rock projected from the Imbrium Basin impact. The lack of oxygen isotope re-equilibration <960 °C means that there was no pre-Imbrium metamorphism affecting this rock, supporting the above hypothesis (Clayton et al., 1972). Although the expose age of 14053 corresponds with the formation of Cone Crater (Turner et al., 1971)the mechanics of this craters formation are not great enough to reheat this rock (Schürmann and Hafner, 1972).

The subsequent reheating of 14053 is thought to be responsible for extreme subsolidus hydrogen reduction in the exterior regions of this rock, with limited permeability preventing the interior regions from being reduced to the same degree (Taylor et al., 2004). During reheating solar-wind hydrogen become implanted on the exterior of this rock, reacting with fayalite and spinel minerals in the mesostasis, making 14053 the most reduced lunar rock examined to date (Taylor et al., 2004). The reduction-breakdown texture of fayalite to Fe-metal and silica is unique to this sample and its smaller pair 14072, providing evidence for extreme reduction in these samples, and is represented by the reaction:

$$Fe_2SiO_2 + 2H_2 = 2Fe^{\circ} + SiO_2 + 2H_2O \uparrow \tag{D.1}$$

D.1.2 14072,13

Sample 14072 was a 45.06 g rock, collected at Station C (photograph AS14-64-9126) 100 m SE of Cone Crater. The rock was found exposed at the surface, beside the MET tracks, along with other fragments (14086 –14071) which resembled one another at first sight. The 21 m.y. exposure age of this sample coincides with the age of Cone Crater (York et al., 1972).

Original investigations reported 14072 as a ophitic to subophitic basalt (Wilshire and Jackson, 1972) with similarities drawn with Apollo 12 basalts (Taylor et al., 1972) based on REE concentrations (Helmke et al., 1972). 14072 is texturally and mineralogically homogenous in hand-specimen and consists of fine to medium grained plagioclase laths (∼30 %), subhedral to anhedral pyroxene (∼65 %), anhedral olivine (∼1 %), and a mesostasis (∼3 %) consisting of opaques, metallic Fe, ilmenite, apatite, and cristobalite (Carlson and Walton, 1978). Initial similarities were drawn between 14072 and 14053 (El Goresy et al., 1972) given the highly reduced sections of both rocks identified by a spongey Fe texture and similar mineral chemistry. The REE chemistry of 14072, however, is unique to the other Apollo 14 basalts with this rock not fitting within the traditional Apollo 14 high-Al groupings (Neal and Kramer, 2006).

Dates for this sample from Rb-Sr (Compston et al., 1972b) and $^{40}Ar/^{39}Ar$ (York et al., 1972) put its formation at 3.99 ± 0.09 b.y. and 4.04 ± 0.05 b.y. respectively. The exposure age based on $^{38}Ar/^{37}Ar$ thermal release patterns is 21 ± 5 m.y. (York et al., 1972).

D.1.3 14073,9

Sample 14073 was a 10.35 g pebble, collected in the soil mechanics trench at Triplet Crater (photograph AS14-68-9487). Triplet crater is situated between the Apollo 14 landing site and Cone crater. This sample was collected from a side of the trench which collapsed and so it was uncertain whether or not it was actually buried LSPET (1971). An exposure age of 113 m.y. (Turner et al., 1972), however, requires the sample was at (or near) the lunar surface for at least this amount of time before collection.

Original investigations reported 14073 as a basalt (Gancarz et al., 1971; LSPET, 1971) then as a KREEP-basalt due to its high REE content (El Goresy et al., 1972). High Ni and Ir contents combined with Fe-Ni-P-S melt globules in this sample indicate its not of pristine igneous origin (Kushiro et al., 1972; Ridley et al., 1972), leading to its classification as an melt rock (Schonfeld and Meyer, Charles, 1972).

14073 is a subophitic, intergranular to intersertal, igneous rock. It consists of euhedral plagioclase laths (∼ 50 %) with intersertal anhedral pyroxenes (∼25 % clinopyroxene; ∼20 % orthopyroxene) with minor ilmenite (∼2 %), and a late-stage mesostasis of apatite, merrillite, fayalite, and K-Ba-rich glass (LSPET 1971). Here, it is studied in polished thin section 14073,9 with mineral modal abundances and textures broadly consistent in what is reported for 14073,8 by Gancarz et al. (1971). The texture of 14073,9 is nearly identical to that of 14310, although no orthopyroxene is reported in the latter. Plagioclase compositions for 14073 vary from An_{95} (core) to An_{65} (rim; Hui et al., 2011) which is consistent with those seen for 14310 (An_{94-58}; Wenk et al., 1972).

Apollo 14 soils have similar chemical compositions to 14073, except for ∼10-15 % higher Al_2O_2, CaO, Na_2O and ∼20-30 % TiO_2, FeO and ∼50 % lower Co abundances in 14073 relative to the soils. The REE abundances in 14073 are significantly higher than those of Apollo 11, 12, and Luna 16 igneous rocks and ∼90 % of those in Apollo 14 (Gancarz et al., 1971). Compared to typical KREEP values, however, the REE abundances of 14073 are lower than expected (McKay et al., 1979). The similar

chemical composition between 14073 and 14310 (Helmke et al., 1972; LSPET, 1971; Wasserburg et al., 1972) was used to suggest a common lava flow for the two. Similarities in trace element abundances between 14310, soil, and breccia have, however, been used as further evidence this rock is an impact melt rock (Morgan et al., 1972).

Dates for this sample from Rb-Sr (Papanastassiou and Wasserburg, 1971b)and $^{40}Ar/^{39}Ar$ (Turner et al., 1972) agree on a formation age of 3.88 ± 0.04 b.y. and 3.88 ± 0.05 b.y. respectively. Rb-Sr ages for 14310 range from 3.94 ± 0.03 b.y. (Mark et al., 1974) to 3.84 ± 0.04 (Tatsumoto et al., 1972). $^{40}Ar/^{39}Ar$ ages for 14310 are within error of that of 14073 (e.g. Turner et al., 1972). If 14073 and 14310 are impact melt rocks, then these ages would provide the best estimates for the Imbrium impact.

D.1.4 14310,171

Sample 14310 was a 3.4 kg rock collected at Station G during the second EVA. No lunar-surface photographs were made of 14310's collection. The rock was described in the field as a blocky-melt rock and heavily pitted on two sides which are also subrounded. Feldspar-lined vugs (0.5 –2mm in diameter) cover ∼1 % of the surface of 14310 suggesting volatile escape during its formation. In larger cavities the feldspar was found to have a honeycomb texture (Carlson and Walton, 1978).

Similar to 14073, 14310 was originally to be a type sample of KREEP basalts, this plus its large size led this sample being the subject of many studies (Gancarz et al., 1971; Hollister et al., 1972; Longhi et al., 1972; O'Hara, 1972). The composition of 14310, however, was found to be strikingly similar to soil sample 14163 (Gancarz et al., 1972)with high proportion of siderophile elements and Fe-Ni-P-S melt globules. This indicated 14310 is not of pristine igneous origin (Kushiro et al., 1972; Ridley et al., 1972), leading to its classification as an melt rock (Schonfeld and Meyer, Charles, 1972). Melt-rocks are non-endogenous, igneous, rocks which contain a mixture of lithic, mineral, and glass phases picked up from melting of lunar regolith (Taylor et al., 2004).

14310 is a fine-grained subophitic to fine-grained intergranular rock. It consists of interstitial to subophitic pigeonite (∼31 %) with plagioclase laths (∼68 %), and mesostasis of ilmenite, metallic iron, K-glass, and apatite (∼1 %). One thin section, 14310, 564, contains a breccia clast enclosed in crystalline material; a relict of pre-impact material (LSPET, 1971). The texture of 14310 has been reported as being identical to that of 14073, however, the plagioclase contents in 14310 are less variable (An_{90} Carlson and Walton, 1978).

Multiple studies have dated 14310 with good agreement of 3.84 ± 0.04 to 3.94 ± 0.04 b.y. from Rb-Sr (Compston et al., 1972a; Papanastassiou and Wasserburg, 1971b; Rama Murthy et al., 1972) and 3.88 ± 0.06 to 3.91 ± 0.05 b.y from $^{40}Ar/^{39}Ar$ dating (Stettler et al., 1973; Turner et al., 1971; York et al., 1972). These ages are identical to that of 14073 again providing the best estimates for the Imbrium impact.

D.1.5 14321,1482

Sample 14321 was a football-sized, 9 kg, rock collected at Station C1 (photograph AS14-64-9128 to AS14-64-9129) near the hummocky ejecta blanket of Cone Crater. The sample was described in the field as blocky, with a moderate covering of glass-lined zap pits on all surfaces and irregular fracturing along one side. The predominantly dark clasts set in a lighter matrix of this polymict breccia is apparently typical of the dominant rock type in the Cone Crater ejecta (LSPET, 1971). 14321, colloquially known as Big Bertha, is the largest rock collected during the Apollo 14 mission and, as such, has been the focus of a great many studies; Initial investigations of 14321 were reported in a series of papers from the 1970s (Duncan et al., 1975; Grieve et al., 1975; Morgan et al., 1972) where the lithic fragments were grouped according to composition and degree of metamorphism. The majority of clasts are generally interpreted as parts of the Fra Mauro Formation, excavated by the Imbrium impact (Duncan et al., 1975; Swann et al., 1977; Wilshire and Jackson, 1972), while the final emplacement of 14321 was a result of the minor Cone Crater impact event (Duncan et al., 1975).

The polymict nature of this sample allowed a relative time sequence to be deciphered from the four generations of microbreccia, including two distinct episodes of thermal metamorphism (Duncan et al., 1975). The first thermal metamorphic episode led to recrystallization textures within some lithic units while the latter episode was less severe. Duncan et al. (1975) derived a partial schematic history for 14321 consisting of:

- Serinitatis impact ejecta blanket deposited over Imbrium area.
- KREEP basalt erupted followed by Apollo 14-type basaltic eruption.
- Early brecciation resulting from impacts on south Imbrium region.
- Fra Mauro ejecta formed from Imbrium impact.
- Extrusion of 14321-type basalt and additional Apollo 14-type basalts on the Fra Mauro Formation and adjacent areas.
- Impacting events led to final formation of 14321.
- Cone Crater impact excavates 14321.

Clasts, in sample 14321, of low-Ti high Al basalts were of interest to this study namely 1482 and 1483. These clasts are part of Group 1B (as described by Duncan et al., 1975) in which original igneous textures has been preserved with minor recrystallization. The petrography of these clasts are described in the literature (Fagan et al., 2013; Hui et al., 2011; Neal and Kramer, 2006) as holocrystalline with intersertal to subophitic textures, consisting of euhedral to subhedral olivine, pyroxene, and plagioclase. High-Al basaltic clasts in 14321 are dated at 4.12 $\pm$ 0.08 b.y. (Dasch et al., 1987).

Appendix E

Robotic traverse and sample return strategies for a lunar farside mission to the Schrödinger basin

Nicola J. Potts[1,2], Amber L. Gullikson[3], Natalie M. Curran[4], Jasmeet K. Dhaliwal[5], Mark K. Leader[6], Rushal N. Rege[7], David A. Kring[8]

[1]Department of Physical Sciences, The Open University, Milton Keynes,UK
[2]Faculty of Earth & Life Sciences, Vrije Universiteit Amsterdam, NL
[3]Department of Geology, Northern Arizona University, Arizona USA
[4]School of Earth, & Environmental Sciences, University of Manchester, Manchester, UK
[5]Scripps Institute for Oceanography, UC San Diego, California, USA
[6]Cockrell School of Engineering, University of Texas, Austin, USA
[7]School of Engineering and Applied Sciences, Columbia University, New York, USA
[8]Centre for Lunar Science and Exploration, Lunar and Planetary Institute, Texas, USA

The work in this chapter was completed as part of a summer internship at the Lunar and Planetary Institute, Houston, Texas (2013). This chapter has been published as Potts et al. (2015) *Advances in Space Sciences*. **55**, 1241-1254.

ABSTRACT

Most of the highest priority objectives for lunar science and exploration (e.g., NRC, 2007) require sample return. Studies of the best places to conduct that work have identified Schrödinger basin as a geologically rich area, able to address a significant number of these scientific concepts. In this study traverses were designed for a robotic mission within previously identified crewed landing sites in Schrödinger basin. Traverse routes and sampling locations were identified using LROC imagery and LOLA topography data, combined with a theoretical rover travel and operations model. The findings of this investigation highlight the need to consider increased rover capabilities. A significant number of samples that can address many of the NRC (2007) scientific goals can be returned in a robotic mission during one period of lunar illumination (∼14 Earth days) using specifications from previous lunar rovers.

E.1 Introduction

Following the NASA Vision for Space Exploration (VSE, 2004), the US National Research Council (NRC) identified eight scientific concepts (Table E.1) containing thirty-five prioritized goals (Table E.2) for future human and robotic exploration of the Moon (NRC, 2007). These objectives are broadly consistent with those identified throughout the international community (e.g. Crawford et al., 2012), with the majority requiring sample return from the Moon. From 2008 to 2012, a series of studies determined the most suitable locations on the Moon where each of the scientific concepts, and their sub-goals, could be investigated (Flahaut et al., 2012; Kring and Durada, 2012; O'Sullivan et al., 2011). These studies highlighted Schrödinger basin as a geologically-rich location where the majority of the NRC (2007) goals could be addressed (Tables E.1 and E.2).

As Schrödinger basin is an attractive scientific target, potential landing sites and traverses have been designed for crewed missions with different assumptions about rover capabilities (Bunte et al., 2011; O'Sullivan et al., 2011). At this time, however, there is no infrastructure in place for landing crew on the Moons surface. Subsequently, a human-assisted robotic sample return mission has been proposed (Burns et al., 2013), in which crew on NASAs Orion spacecraft would tele-operate a rover on the lunar surface from the Earth-Moon L2 Lagrange point.

In this work, two of the Schrödinger landing sites from O'Sullivan et al. (2011) are re-investigated to determine if they are suitable for a robotic lander and rover mission with sample return capability. Traverses within the two sites are developed, using remote sensing datasets, to maximize scientific return in relation to the NRC (2007) goals. A concept of operations (ConOps) is used to provide realistic rover time constraints for the mission, which lasts no more than one period of lunar illumination (∼14 Earth days).

Table E.1: The 8 NRC (2007) science concepts listed in order of importance. Goals in bold font can be addressed at Schrödinger (concept 4 could also be addressed)

1	**The bombardment history of the inner Solar System is uniquely revealed on the Moon**
2	**The structure and composition of the lunar interior provide fundamental information on the evolution of a differentiated planetary body**
3	**Key planetary processes are manifested in the diversity of lunar crustal rocks**
4	The lunar poles are special environments that may bear witness to the volatile flux over the latter part of Solar System history
5	**Lunar volcanism provides a window into the thermal and compositional evolution of the Moon**
6	**The Moon is an accessible laboratory for studying the impact process on planetary scales**
7	**The Moon is a natural laboratory for regolith processes and weathering on anhydrous airless bodies**
8	Processes involved with the atmosphere and dust environment of the Moon are accessible for scientific study while the environment remains in a pristine state

Table E.2: The 10 highest science priorities within the 8 NRC (2007) concepts. Goals in bold font can be addressed at Schrodinger with the traverses presented here. 4a and 2b could also potentially be addressed.)

Rank	Goal	
1	**1a**	**Test the cataclysm hypothesis by determining the spacing in time of the creation of the lunar basins**
2	**1b**	**Anchor the early EarthMoon impact flux curve by determining the age of the oldest lunar basin (South Pole-Aitken basin)**
3	1c	Establish a precise absolute chronology
4	4a	Determine the compositional state (elemental, isotopic, mineralogical) and compositional distribution (lateral and depth) of the volatile component in lunar polar regions
5	**3a**	**Determine the extent and composition of the primary feldspathic crust, KREEP layer, and other products of planetary differentiation**
6	**2a**	**Determine the thickness of the lunar crust (upper and lower) and characterize its lateral variability on regional and global scales**
7	2b	Characterize the chemical/physical stratification in the mantle, particularly the nature of the putative 500-km discontinuity and the composition of the lower mantle
8	8a	Determine the global density, composition, and time variability of the fragile lunar atmosphere before it is perturbed by further human activity
9	2c	Determine the size, composition, and state of the Moons core
10	**3b**	**Inventory the variety, age, distribution, and origin of lunar rock types**

E.2 Schrödinger basin

Schrödinger, situated on the lunar farside (75°S, 132.5°E), is the best preserved basin of its size, with a rim-to-rim diameter of ∼320 km. The basin floor, at its deepest points, is -4.5 km beneath the crater rim. A peak ring, roughly half the diameter of the crater rim (∼150 km diameter), rises 1 to 2.5 km above the basin floor. Schrödinger is the second youngest basin on the Moon and located within the oldest and largest lunar basin, South Pole-Aitken. A sample return mission to Schrödinger, therefore, has the potential to recover samples of both basins and, thus, bracket the basin-forming epoch. This would simultaneously provide samples to test the lunar cataclysm hypothesis and determine the age of the oldest lunar basin the two highest NRC (2007) science priorities (NRC Goals 1a and 1b; Table E.2). Sampling peak ring lithologies (lower crust and, potentially, mantle) and adjacent clast-bearing impact breccia would provide the material needed to test the lunar magma ocean hypothesis and crustal evolution (NRC Goals 2 and 3); while also characterizing regolith in a previously unsampled region of the Moon (NRC Goal 7). Two types of volcanism (mare basalts and pyroclastic glasses) within the basin provide unique opportunities to explore the magmatic evolution of the Moon (NRC Goal 5). As a large impact structure, sampling of Schrödinger would also provide insight into cratering processes (NRC Goal 6), especially the formation of large craters. Finally, there is potential for volatiles to be sampled from permanently shadowed regions within the basin (NRC Goal 4). Figure E.1 locates the two sites in which traverses were constructed, referred to as North and East these are comparable to sites A and C, respectively, from O'Sullivan et al. (2011).

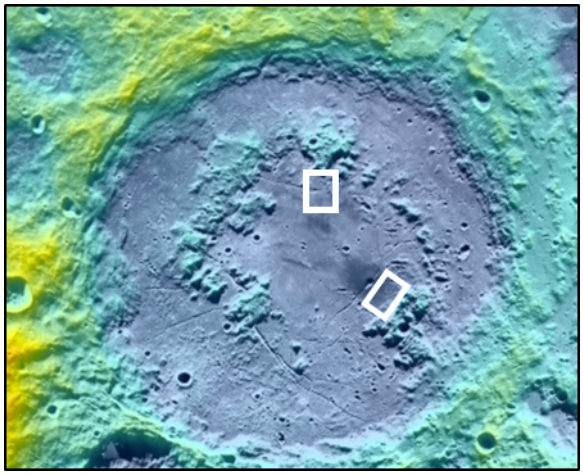

Figure E.1: Schrödinger basin with location of traverse sites marked with white boxes. Top box corresponds to site referred to here as North site; bottom box corresponds to site referred to here as East site.

E.3 Datasets and methods

A number of data sets were combined using ArcGIS to construct traverses for two sites within Schrödinger. A Digital Elevation Map (DEM) of Schrödinger was created by combining a Wide Angle Camera (WAC) image of Schrödinger, taken from the Lunar Reconnaissance Orbiter Camera (LROC), with Lunar Orbiter Laser Altimeter (LOLA) data. The DEM had a spatial resolution of 30 m per pixel and was used to calculate terrain slopes and, therefore, suitable routes for a rover. Narrow Angle Camera (NAC) images of the sites, taken from LROC, were overlaid on the DEM and WAC basemap. NAC images have far greater resolution than WAC images (0.5 m per pixel compared to 100 m per pixel). This allows rock outcrops and individual boulders to be identified on a meter-scale. Geological maps of Schrödinger (Kramer et al., 2013; Mest, 2011; Shankar et al., 2013; Shoemaker et al., 1994) were integrated with spectral reflectance data (with a spatial resolution of 280 m per pixel) from the Moon-Mineralogy Mapper (M^3; Kramer et al., 2013; Pieters et al., 2009) to produce traverse routes that maximized scientific sample return.

Three traverse options were constructed at each site: an optimum traverse and two descope options. The optimum traverse maximizes the mission period ($\sim$14 Earth days) and scientific return in terms of the NRC (2007) goals. The descope options have shorter traverses (referred to here as medium and short) and contain fewer sampling opportunities. Landing sites were chosen based on surface morphology within a 200 m landing ellipse (as per Apollo; Spudis and Pieters, 1991) where the slope was 0 –2°.

E.4 Rover capabilities and operations

E.4.1 Rover specifications

The engineering constraints of the rover are central to determining key aspects of the mission i.e., traverse routes, sampling time, and overall duration. In this work total mission length is one period of lunar illumination ($\sim$14 Earth days), as a solar-

powered rover is considered. For a rover to operate during subsequent period(s) of illumination, rover design must include the capability to survive the ∼100 K lunar night.

Based on specifications of previous lunar rovers (the robotic Lunokhod 1 and 2 rovers and the astronauts Lunar Roving Vehicles) and a theoretical rover-wheel study (Ding et al., 2011), rover velocity as a function of slope angle was solved using the following equation:

$$v = \frac{Pr}{F_N(lsin\alpha + e)} \tag{E.1}$$

In this model power input (P) and the radius of the rovers wheels (r) over the normal force on the wheel by the soil (F_N), drawbar pull (l), normal force (e), and the gradient of the slope (α) control rover velocity (v). This equation was derived from those in Ding et al. (2011) for equilibrium conditions on rover wheels and that of Berkelman (1995) for sink as a function of soil mechanics. The derivation of this equation can be found in Leader et al. (2014). Mechanical properties of the lunar soil were taken from Carrier (2006).

Several parameters that affect rover mobility were explored. These included speed as a function of slope with different wheel radii (Figure E.2A), rover masses (Figure E.2B), power (Figure E.2C) and wheel base length (Figure E.2D). Based on previous parameter studies and experience with the Lunokhod rovers, the following values were assumed for the traverse study: a total mass of 600 kg (where the centre of mass is midway between the front and rear wheels and 0.5 m above the ground), a constant power supply to the wheels of 200 W, and a four-wheel configuration with a wheelbase length of 2.20 m, where each wheel has a radius of 0.3 m and a width of 0.25 m. The maximum slope the rover can traverse is 16° with a baseline velocity of 1.7 km/hr. Figure E.3 illustrates how rover velocity is affected by slope. As expected, an increase in slope decreases rover velocity while a significantly lighter rover could travel faster and find slopes easier to navigate (Figure E.2B).

E.4.2 Conceptual Operations (ConOps)

ConOps are the operations a rover will perform at stations of interest and when starting up/packing down on the lunar surface. Given the lack of precedent for a robotic rover sample return missions, ConOps presented here are based on available experimental and theoretical data for a rover designed to analyse lunar soil (Seeni et al., 2008, 2010). Times given for rover traverses account for the following ConOps: 18 hours start-up time, 10 hours of rover pack down at the lunar lander and 23 hours at each station (Table E.3). The rover is operating 24 hrs/day, implying rotating teams on Earth if the rover is managed from mission control (as with the Lunokods; Jaffe and Choate, 1974) or rotating teams in space and on Earth if the rover is managed from both an orbiting platform (e.g. the Orion spacecraft; Burns et al., 2013) and mission control. In this mission scenario, analysis on the lunar surface will be minimal, but sufficient enough to confirm the composition of the rock types being sampled using an Alpha Particle X-Ray Spectrometer (APXS). Each APXS analysis will take 4 hours with an additional 0.5 hours to position the instrument (Table E.3). The majority of time spent at each station will be used to image station/sample locations, providing

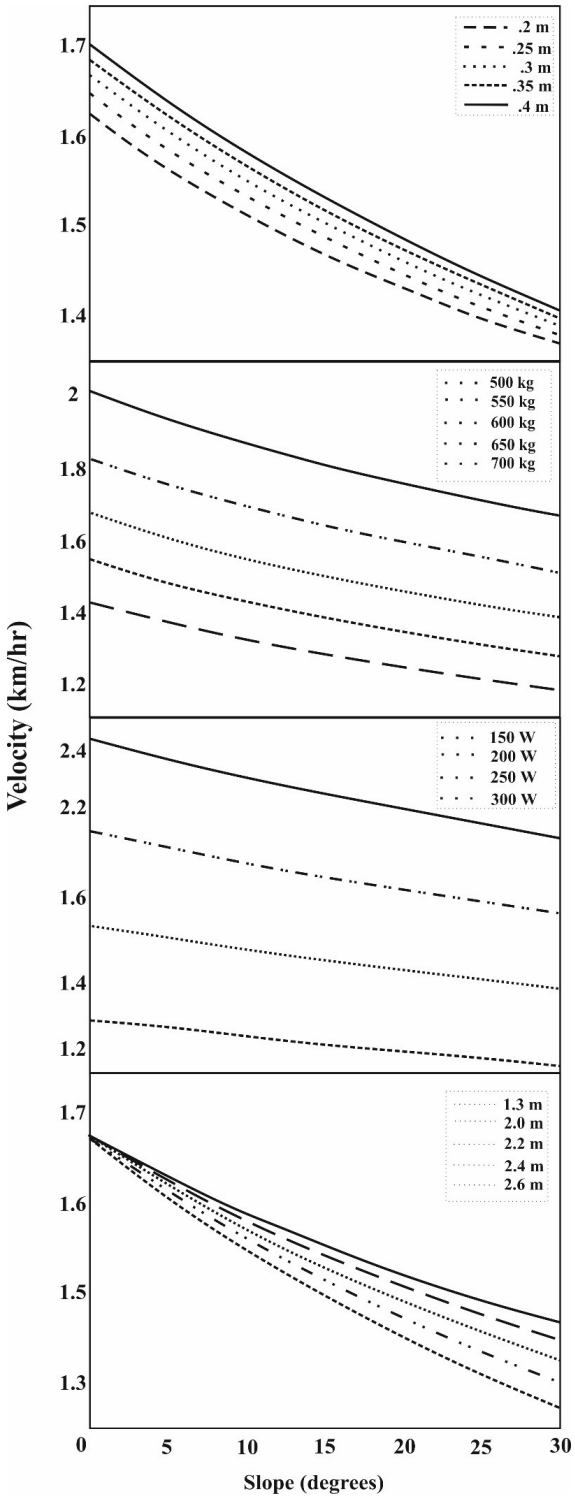

Figure E.2: Rover velocity as a function of slope, with varying (A) wheel radii (B) rover mass, (C) power (D) wheel base length

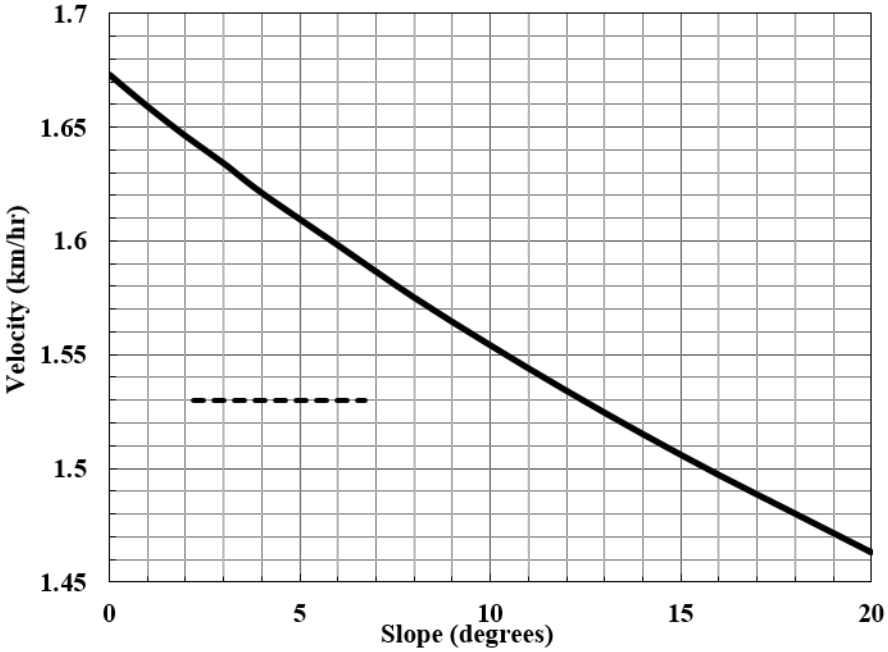

Figure E.3: Rover velocity as a function of slope for the parameters used in traverses here, with the following parameters; 200 W, 630 kg, r = 0.3 m, L = 2.2 m, h = 0.5 m. The dashed line corresponds to the average slopes of the traverses in this study.

geologic context for collected samples. Robotic sampling can be done with a claw (similar to that on TALON rovers used on Earth) and/or a scoop. A trade study of sampling techniques is something, however, that needs to be examined in a second-generation study. The sample mass that can be returned to Earth will be governed by the capabilities of an ascent vehicle. From a science perspective, however, ideal sample masses can be constrained based on a CAPTEM sample return study (Shearer et al., 2007). For the long traverse at the East site (Section E.6.1) for example, four hand specimen basalts from the peak ring material (stations 1 to 4), two rake samples from the pyroclastic material (stations 5 and 7), and unsieved regolith material from the inter-peak ring material (station 6) would require a minimum of 40 kg of material. This assumes only one sample is collected per station.

It should be noted that ConOps in this study do not account for repetition of any activity at a station. Activities such as APXS analysis may have to be performed multiple times at some stations; repeat analyses would increase time spent at each station by at least 4.5 hours (Table E.3). The traverses presented in this work can be completed in 9.1 days or less (see Section E.6); some redundancy time is, therefore, available (given the 14 period of lunar illumination) if additional analyses are required. Durations for traverses, however, are based on NAC images (0.5 m/px), and so, smaller rocks not visible at this resolution may require the rover to make slight adjustments (increasing distance/time) to the traverse. All traverse paths are closed to allow the rover to return samples to the ascent vehicle.

The traverses here assume constant communication coverage. A communication satellite orbiting the Earth-Moon L2 position could provide communication relay over the entire 14-day-long lunar day (Lupisella and Bobskill, 2012). If a crewed Orion vehicle provided the communication relay and was also the vehicle tasked to return

the samples to Earth, requiring time for rendezvous between an accent vehicle and Orion, then surface operations would be limited to 10 days assuming a 31-day-long Orion mission architecture (Hopkins, 2013).

E.5 Solar irradiance

Rover constraints require the mission to coincide with a period of lunar illumination (∼14 Earth days). Solar irradiance (sunlight power on surface) data covering both site localities (-72.55445°N, 131.041°E to -72.108°N, 148.4384°E) were taken from the Lunar Mapping and Modeling Portal (LMMP; www.lmmp.nasa.gov.). Illumination and irradiance were examined from January 2018 to December 2021, which encompasses the Exploration Mission 2 launch date for Orion. LMMP utilizes LOLA topography data combined with lunar ephemeris to provide the highest resolution grids of lunar polar topography thus far (Mazarico et al., 2011). When combined with local topography, variations in the amount of sunlight available across the lunar surface can be extracted. Within the LMMP portal a mesh size of 1 m with 39% Earth shine and terrain reflection were used for selecting solar irradiance data.

The optimal periods of solar irradiance are the months from July to September, which have a ∼15% longer than average period of lunar illumination. The period of August 2021 was identified as an optimum date for this mission in terms of solar irradiance, illumination, and potential Orion mission dates.

Tracking variations in sun angle over one year periods indicates some regions within Schrödinger may be in complete shadow one year, but have adequate illumination the next. This is evident behind local topographic highs, such as the peak ring at the North site, which was not always illuminated during the four year period of interest. The base of the peak ring at the East site, however, did not have any areas that were shadowed during periods of lunar illumination. Traverse routes in this region are, therefore, less restricted in date than those at the North site.

As solar irradiance within Schrödinger varies by a factor of three depending on the time of year, not every 14-day-long illumination period provides the same solar power on the surface. The position of the Earth-Moon system in its orbit around the sun governs this change. This does not preclude missions in the first half of the year, but they may require larger solar panels or a more power-efficient rover.

E.6 Traverses

E.6.1 East site

The East site is located within the peak ring of Schrödinger and roughly corresponds to Site C in O'Sullivan et al. (2011). The landing site is located at 75.50°S, 141.37°E, between a pyroclastic vent and the south-eastern portion of the peak ring. Access to those units, plus intervening impact breccia can provide samples needed to determine the age of the Schrödinger impact event, and therefore, the end of the lunar cataclysm (NRC Goal 1). Additionally, locations at this site will provide information on: basin-forming processes (NRC Goal 6); the petrologic structure of the lunar interior (NRC Goals 2 and 3); the thermal and compositional evolution of the Moon (NRC

Table E.3: ConOps used for traverse times. Science Site Activities repeated for individual stations and time is in Earth hours. (See text for description).

Begin surface mission	Time (hours)
Download remaining descent imagery	1
HAZCAM' image prior to ramp deployment	1
Deploy landing ramps	1
HAZCAM' image of deployed ramps for verification	1
Rover robotic arm (RA) launch lock release	0.5
Perform payload health verification test	2
Deploy RA to imaging positions	1
Take imager panorama	3
Release rover mechanical connection to lander	0.5
Perform mobility assessment	1
Switch over to rover primary battery	0.5
Health verification test of all rover subsystems	1
Release rover electrical connection to lander	0.5
Rover deploy to lunar surface	2
Image lander from lunar surface	2
Drive short distance from lander (with Nav imaging)	1
Perform surface mobility assessment (slipage)	1
Radiation sensor ON (Leave on entire mission)	∼336
Science Site 1 activities	
Take short panorama using imager and RA	8
Position rover if necessary for in-situ target	0.5
Position robotic arm on surface	0.5
Position neutron sensor down	0.5
Neutron sensor analysis	6
Position APXS down	0.5
APXS analysis	4
Take image of sample area	1
Collect sample	3
Sample transfer to bag and storage	1
Drive to Science Site 2 (with Nav imaging)	various
Begin surface end	
Connect rover sample storage to ascent vehicle	2
Transfer samples to ascent vehicle	5
Drive short distance from lander (with Nav imaging)	1
Image ascent vehicle from lunar surface	2
Radiation sensor OFF	∼336

Table E.4: Coordinates for the landing sites and stations for each traverse (optimum,medium, and short) at the North and East sites.

	Latitude	Longitude
North site optimum traverse		
Landing site	-73.359	134.4712
Station 1	-72.359	134.4712
Station 2	-73.1776	134.8586
Station 3	-72.9500	134.6216
Station 4	-72.8967	134.5090
Station 5	-73.1910	134.5013
North site medium traverse		
Landing site	-72.583	133.424
Station 1	-72.583	133.424
Station 2	-72.6435	133.5333
Station 3	-72.6354	133.5965
Station 4	-72.6215	133.5476
Station 5	-72.6232	133.4784
North site short traverse		
Landing Site	-73.289	131.141
Station 1	-73.289	131.141
Station 2	-73.3963	131.3133
Station 3	-73.3867	131.3220
East site optimum traverse		
Landing site	-75.476	141.378
Station 1	-75.4995	142.0664
Station 2	-75.4058	142.1311
Station 3	-75.3725	142.1666
Station 4	-75.2664	148.2822
Station 5	-75.158	141.9584
Station 6	-75.3105	141.9292
Station 7	-75.5002	141.3767
East site medium traverse		
Landing site	-75.476	141.378
Station 1	-75.4995	142.0664
Station 2	-75.4058	142.1311
Station 3	-75.3725	142.1666
Station 4	-75.2664	148.2822
Station 5	-75.3105	141.9292
Station 6	-75.5002	141.3767
East site short traverse		
Landing site	-75.195	142.011
Station 1		
Station 2	-75.3725	142.1666
Station 3	-75.2664	148.2822
Station 4	-75.158	141.9584
Station 5	-75.195	142.011

Goals 3 and 5); and regolith processes and weathering (NRC Goal 7). The pyroclastic deposit in this site was identified by Bunte et al. (2011) as an ideal location for a sortie mission due to its *in situ* resource utilization potential.

E.6.2 Optimum traverse

The optimum traverse for this site (Figure E.4) can address Goals 1, 2, 5, 6 and 7 of the NRC (2007) report. The traverse route is 28.8 km and accommodates seven stations. Taking into consideration ConOps and variation in slope this traverse would take a minimum of 9.1 days to complete. Stations 1 to 4 (Figure E.6.1A - D) are located along the base of the peak ring. Using M^3 data, three types of crustal lithologies were identified along the peak ring in this region: anorthosite, an orthopyroxene-bearing lithology, and an olivine-bearing lithology (potentially mantle material; Figure E.6). Samples here will aid in understanding crust formation and planetary differentiation (NRC Goals 2 and 3).

Station 1 (Figures E.6.1 and E.6A) is located within an area of the peak ring that has a spectral absorption signature indicative of an anorthositic-type lithology. Stations 2 and 3 (Figures E.6.1 and E.6B - C) are within an orthopyroxene-bearing unit thought to be norite. Station 3 (Figure E.6C) is of particular interest due to the proximity of the boundary between the orthopyroxene-bearing lower crustal lithology and an olivine-bearing lower crustal or possibly upper mantle lithology. Station 4 (Figure E.6D) is located within the olivine-bearing unit, presumed to be troctolite or dunite. A number of outcrops are found high up on the peak ring outside the traverse capabilities of the rover (slopes exceed 16°); boulders at the base of the peak ring can, however, be sampled. Tracks identified by NAC imagery show these boulders have travelled down the peak ring from the inaccessible outcrops (Figure E.5). The rover can, therefore, sample rocks from the higher outcrops at the base of the peak ring.

Station 5 (Figure E.6.1, E.6E) is located on the rim of a deep fracture, thought to be associated with the pyroclastic vent. M^3 data suggests that the rocks exposed on the rim of this fracture are an orthopyroxene-bearing unit, possibly noritic. If this outcrop is noritic in composition, then sampling this crustal unit will provide further insight into the structure of the lunar interior and the diverse compositions of lunar crustal rocks (NRC Goal 3).

Station 6 (Figure E.6.1, E.6F) is located in the inter-peak ring floor material. This is an impact-melt breccia that consists of both peak ring material and Schrödinger impact melt (Kramer et al., 2013; O'Sullivan et al., 2011). Sampling breccia that is comprised of Schrödinger impact-melt will provide an absolute age for the Schrödinger impact event.

Station 7 (Figure E.6.1) is located at the landing site, within the pyroclastic material. Shoemaker et al. (1994) suggest a Copernican (>0.8 Ga) age for this unit, which would represent one of the youngest lunar volcanic events. Studies using recent data, however, estimate the pyroclastic material to be late Imbrian (∼3.8 –3.2 Ga) to Eratosthenian (∼3.2 –1.1 Ga) in age (Mest, 2011). Sampling in this area will provide insight into the thermal and compositional evolution of the lunar interior (NRC Goal 5). This pyroclastic vent was also one of the *in situ* resource utilization (ISRU) sites studied during the Exploration Systems Mission Directorate phase of the Lunar Reconnaissance Orbiter (LRO) mission and, thus, is a target with important human

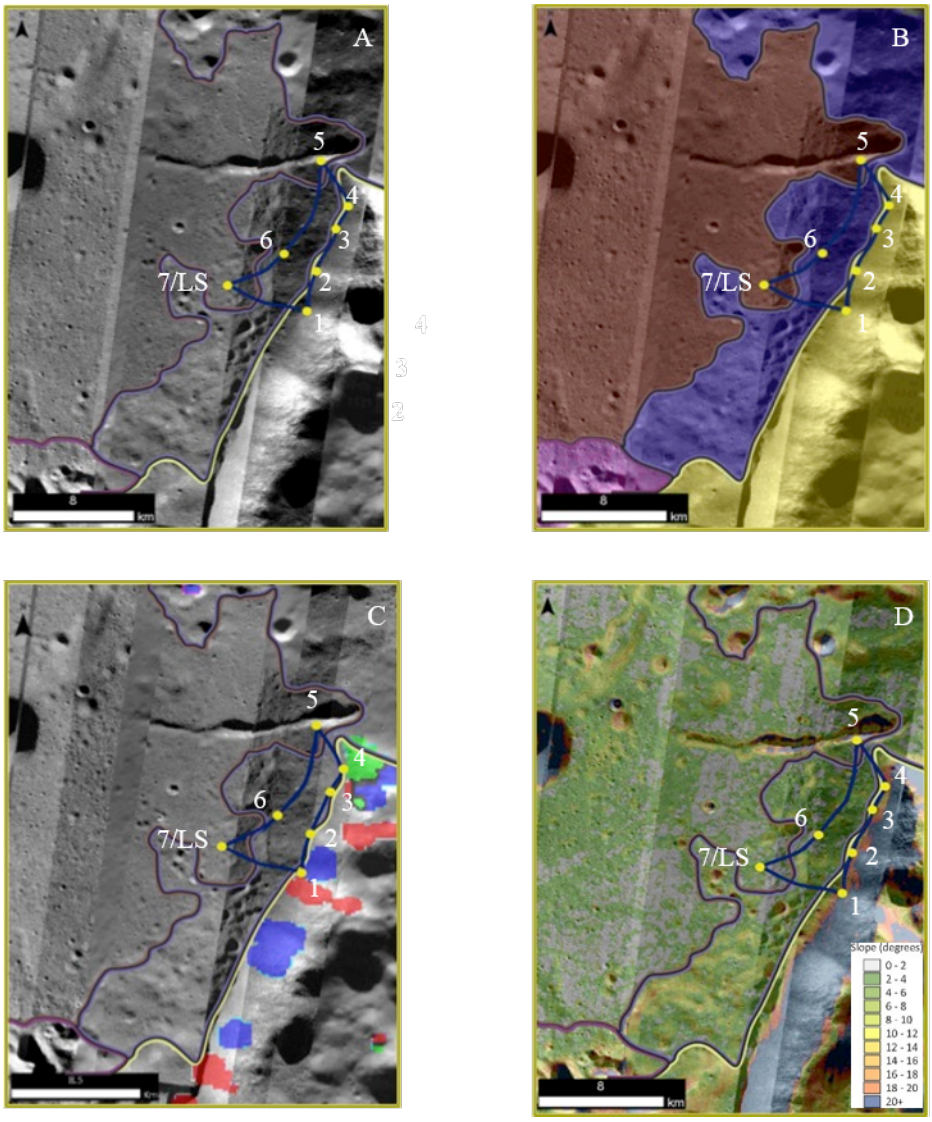

Figure E.4: East site optimum traverse. Maps generated in ArcGIS using LRO NAC images; M123697929L/R, M123647929R/L, and M12347929L. (A) WAC image, overlain with multiple NAC images. LS = landing site, numbers represent stations. (B) Geologic map (Kramer et al., 2013) overlain with NAC imagery. Brown = pyroclastic material, yellow = peak ring material, purple = inter-peak ring material. (C) M^3 data (Kramer et al., 2013). Blue = anorthositic lithology, red = orthopyroxene-bearing lithology, green = olivine-bearing lithology. (D) Slope map.

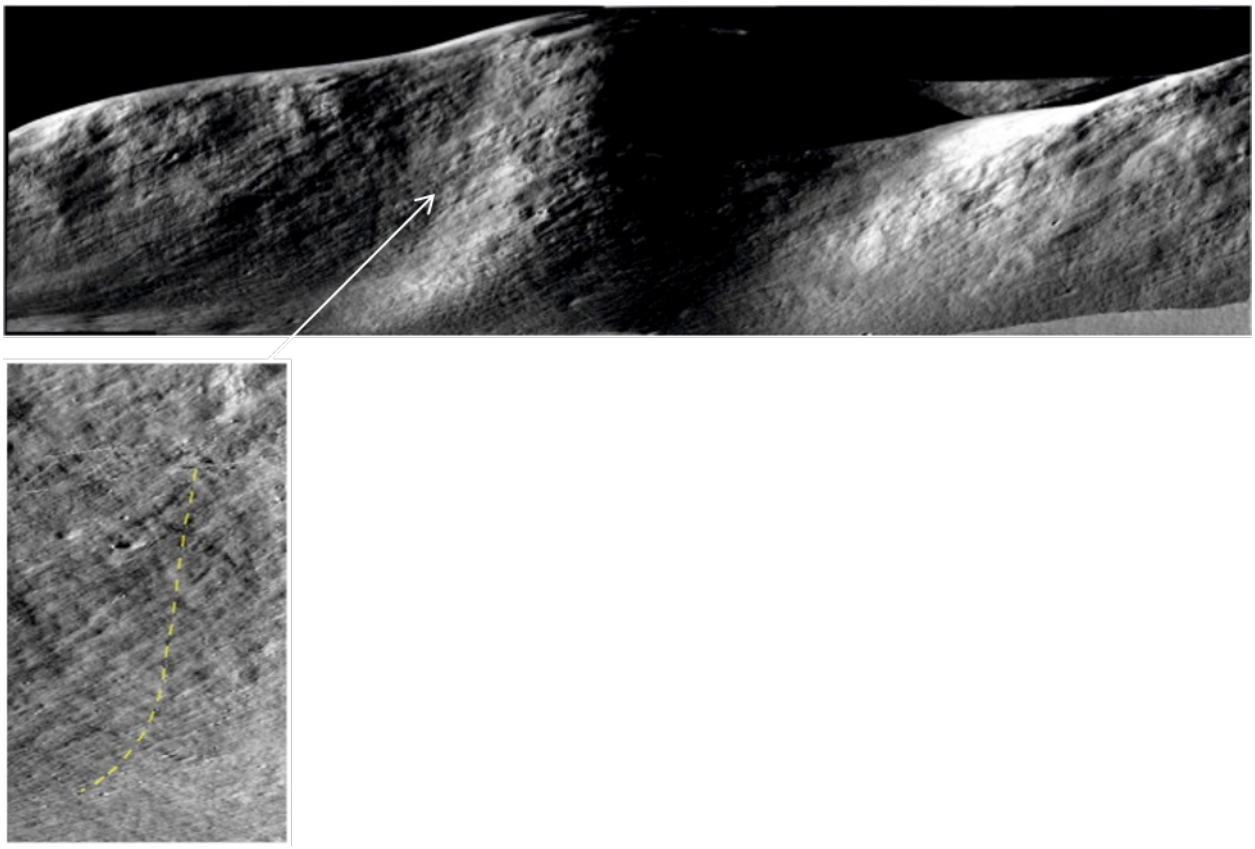

Figure E.5: (A) Oblique view of the peak ring within the East site; stations 24 are located along the base of this area. Image was generated using LRO NAC images overlain on LOLA topography data using ArcScene (B) Detail of NAC image M123647929R shows a boulder track preserved in the regolith. Boulder originated higher up in the slope from a rock exposure; length of the boulder track is 1.5 km, with an 8 m boulder emplaced at the base of the slope.

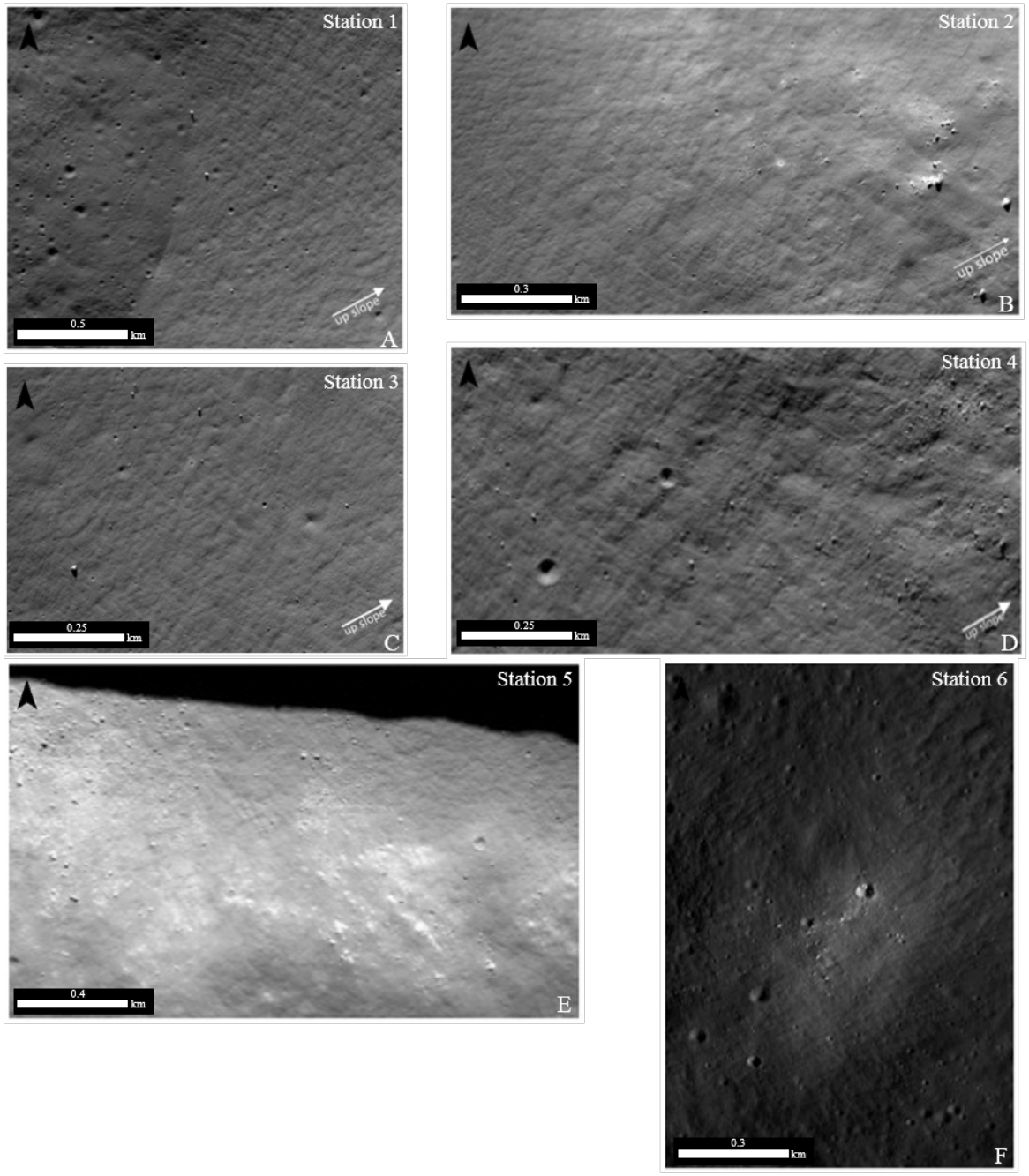

Figure E.6: NAC images of stations from East site optimum traverse. (A) Station 1 (detail of M123647929L); boulders here are 10 m in diameter. (B) Station 2 (detail of M123647929R); located at the base of this slope with rock exposures higher up. (C) Station 3 (detail of M123647929R); boulder shown here is 10 m in diameter. (D) Station 4 (detail of M123647929R); boulder track shown here has a length of 600 m. (E) Station 5 (detail of M123647929L). (F) Station 6 (detail of M123647929L); diameter of crater is 30 m.

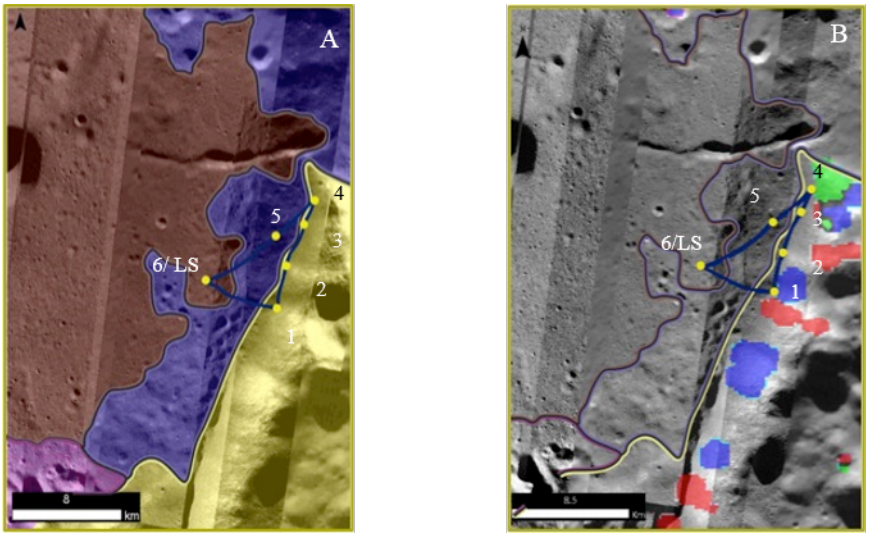

Figure E.7: East site medium traverse. Maps generated in ArcGIS using LRO NAC images M123697929L/R, M123647929R/L, and M12347929L. (A)Geologic map (Kramer et al., 2013) overlain with NAC imagery. Brown = pyroclastic material, yellow = peak ring material, purple = inter-peak ring material. (B) M^3 data (Kramer et al., 2013). Blue = anorthositic lithology, red = orthopyroxene-bearing lithology, green = olivine-bearing lithology.

exploration potential.

E.6.3 Medium traverse

The medium distance traverse (Figure E.7) offers a descope from the optimal traverse, with a length of 22.5 km therefore taking 7.9 days to complete. This traverse will use the same landing site as the optimum traverse and visit the same first four stations, thereby sampling three different types of crustal and possibly mantle lithologies. Sampling on the rim of the deep fracture, was eliminated from the traverse, decreasing the diversity of crustal samples that could be collected. Station 5 is located in the inter-peak ring floor material, where impact-melt breccia will be collected (NRC Goal 1). Station 6, also the landing site, will sample pyroclastic material which will address NRC (2007) Goals 2 and 5.

E.6.4 Short traverse

A final, short distance, descope option is proposed for this site. This traverse is 10.8 km and can be completed in 6.5 days. The landing site for this traverse is located just south of the deep fracture, near the boundary between the pyroclastic and inter-peak ring floor material and will sample impact-melt breccia (Figure E.8). Station 1 is located in the inter-peak ring floor material. Stations 2 –3 are located along the peak ring, though with a shortened traverse it is not possible to sample all the different types of crustal lithologies that are available in this area. Station 2 is within the orthopyroxene-bearing unit, near the contact with the olivine-bearing unit. Station 3 is located in the olivine-bearing unit. In this traverse there are fewer stations along the peak ring; sampling of an anorthositic lithology has been eliminated. Sampling both the orthopyroxene-bearing and olivine-bearing lithologies can provide an in depth look

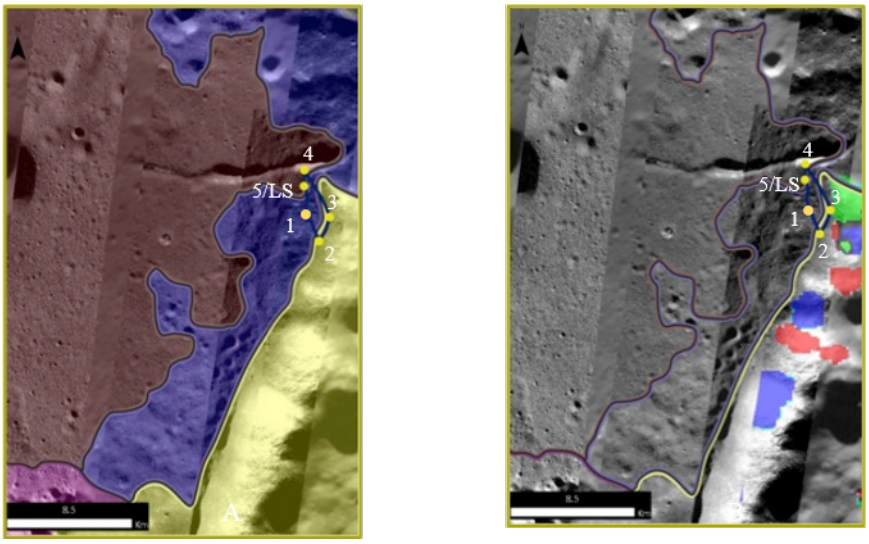

Figure E.8: East site short traverse. Maps generated in ArcGIS using LRO NAC images; M123697929L/R, M123647929R/L, and M12347929L. (A) Geologic map (Kramer et al., 2013) overlain with NAC imagery Brown = pyroclastic material, yellow = peak ring material, purple = inter-peak ring material. (B) M^3 data (Kramer et al., 2013); blue = anorthositic lithology, red = orthopyroxene-bearing lithology, green = olivine-bearing lithology.

into the differentiation and interior structure of the Moon (NRC Goal 2). Station 4 is located on the rim of the deep fracture, sampling an orthopyroxene-bearing unit associated with the pyroclastic vent. Station 5, also the landing site, is located within the pyroclastic material.

E.6.5 North site

The North site is located within the peak ring of Schödinger and corresponding approximately to Site A in O'Sullivan et al. (2011). There are two proposed landing sites located at -73.359°S, 134.4712°E and -72.583°S, 133.424°E in a mare-type unit and an impact melt sheet, respectively. Access to these units can provide the samples needed to; determine the age of the Schrödinger impact event and help bracket the lunar cataclysm (NRC Goal 1), provide information on basin-forming processes (NRC Goal 6), improve our knowledge of the petrologic structure of the lunar interior, and probe the thermal and compositional evolution of the Moon (NRC Goals 3 and 5). Sampling of regolith (NRC Goal 7) will also aid in understanding surface modification processes on an airless body (Lucey et al., 2006).

E.6.6 Optimum traverse

The optimum traverse is 37 km long and accommodates five stations for sampling (Figure E.9, E.10). NRC (2007) Goals 1, 2, 3, 5, 6, 7 and potentially 4 can be addressed in this area. Taking into consideration the ConOps and variation in slope, it would take 7.5 days to complete this traverse. The slope of the traverse does not exceed 14.1° at any given point and has an average slope of 3.7°.

Station 1, also the landing site (LS; Figure E.9), is located in a mare deposit. Crater counting from Mest (2011) and Shoemaker et al. (1994) suggest this unit has

an age of ∼3.8 –∼3.2 Ga. The lower age bracket of this unit being poorly represented in the current lunar sample collection (Hiesinger et al., 2000). It is expected that the regolith in this area will be dominated by underlying basaltic material, similar to the Apollo 11 landing site (Korotev and Gillis, 2001). The mare samples here would provide the first ground-truth samples derived from the farside lunar mantle and, consequently, provide a unique opportunity to explore the lunar interior (NRC Goal 5) from a farside perspective.

Station 2 (Figure E.9, E.10A) is located in the smooth inner peak plains. M^3 data for this area shows glass-rich spectra indicative of impact melt (Kramer et al., 2013). If samples of impact melt are collected and returned to Earth, then the age of the Schrödinger impact event could be determined, thereby helping to constrain the end of the basin-forming epoch and test the lunar cataclysm hypothesis (NRC Goal 1).

Station 3 (Figure E.9, E.10B) is located in the inter-peak ring floor material and samples a young crater, ∼80 m in diameter. This unit is interpreted as breccia comprised of Schrödinger melt material deeply excavated material, sampling of which would be relevant for NRC (2007) Goals 1 and 6.

Station 4 (Figure E.9, E.10C) is located at the base of the peak ring near the boundary between peak ring and inter-peak ring floor material. The peak ring material was uplifted from the base of the crust (e.g. 20 to 30 km Kring and Durada, 2012) and potentially the upper mantle (Kramer et al., 2013). A variety of crustal rocks can be collected from the base of the uplifted peak ring, providing insight into the variability of deep crustal material (NRC Goal 3).

Station 5 (Figure E.9, E.10D) is located on the edge of a ∼50 km long fracture that is up to ∼400 m deep in some areas; at this station the fracture is 40 m deep. M^3 data for the fracture suggest an orthopyroxene-bearing lithology (investigate NRC Goal 3), which could be potentially collected from the ridge using a tether attached to the rover (Abad-Manterola et al., 2009). This fracture is permanently shadowed in certain regions creating the potential to sample surface volatiles with a slight adjustment to this traverse (NRC Goal 4).

E.6.7 Medium traverse

Constructing descoped traverses in this area was challenging due to the distances between different units of interest. For example the peak ring and mare units, in this area, are a minimum of 20 km apart. The medium length traverse is located to the north-west of the optimum traverse. The focus of this traverse is to return samples that can be used to determine the age of the Schrödinger impact event (NRC Goal 1) and investigate the diversity in crustal rocks uplifted in the peak ring (NRC Goal 2 and 3); sampling stations within the mare unit are, consequently, omitted (NRC Goal 5).

The traverse is 12.7 km long and accommodates five stations, taking 6.5 days to complete (Figure 11). The average slope of the traverse is 7.1° with a maximum slope, located near the base of the peak ring, of 15.7°. Station 1, which is also the landing site, is located in the inner peak ring material where impact melt and breccia can be sampled (NRC Goal 1). Stations 2 and 3 are located at the bottom of the peak ring, aiming to sample crustal material (NRC Goal 3). The final two stations (4 and 5) are

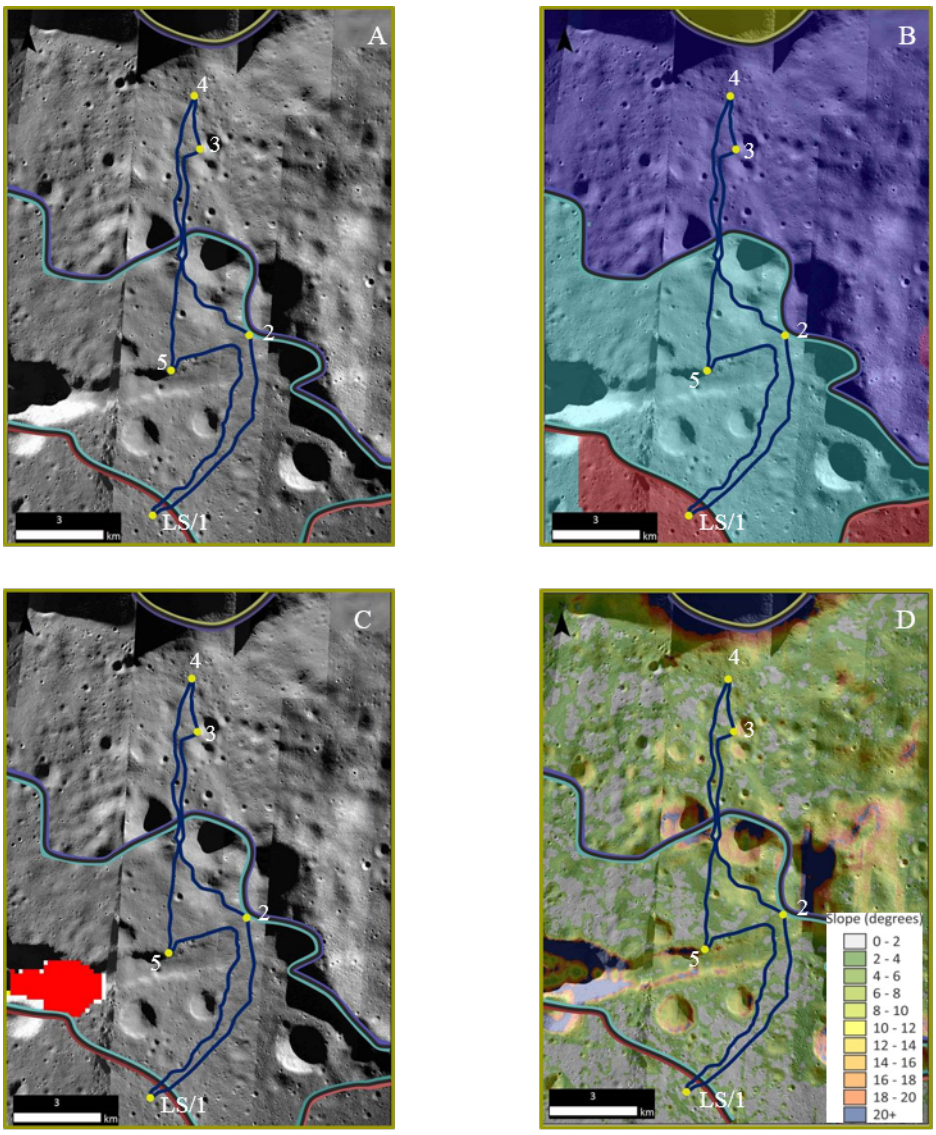

Figure E.9: North site, optimum traverse: Maps generated in ArcGIS using LRO NAC images: M113260100RE/LE, M113067665LE/RE, M1110902117LE/RE, M126051080LE/RE, and M113060880RE/LE. (A) WAC image, overlain with multiple NAC images. LS = landing site, numbers represent stations. (B) Geological map (Kramer et al., 2013) overlain with NAC imagery. Red = mare material, blue = smooth inner-peak ring floor material, purple = inter-peak ring floor material. (C) M^3 data (Kramer et al., 2013): red = orthopyroxene-bearing lithology. D) Slope map.

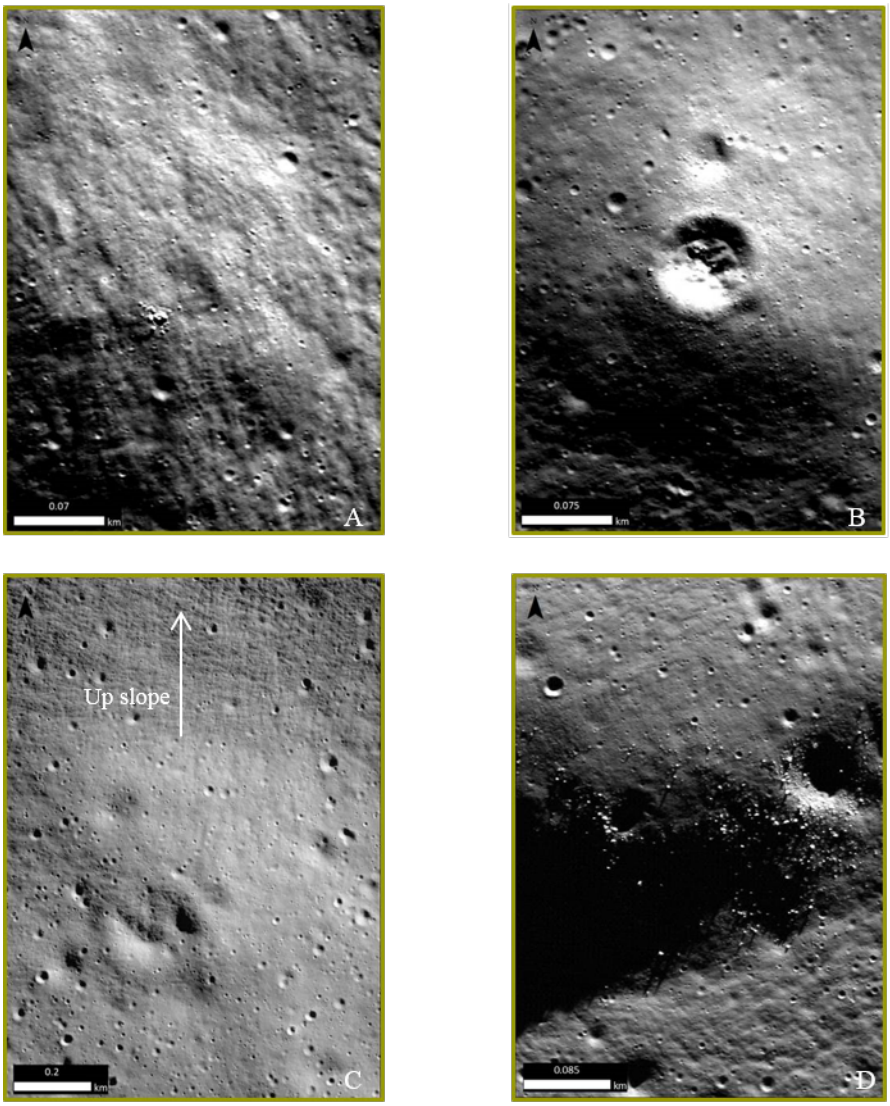

Figure E.10: NAC images of stations from North site optimum traverse. (A) M110704557LE, (B) M113067665LE, (C) M113067665LE, and (D) M113067665LE.

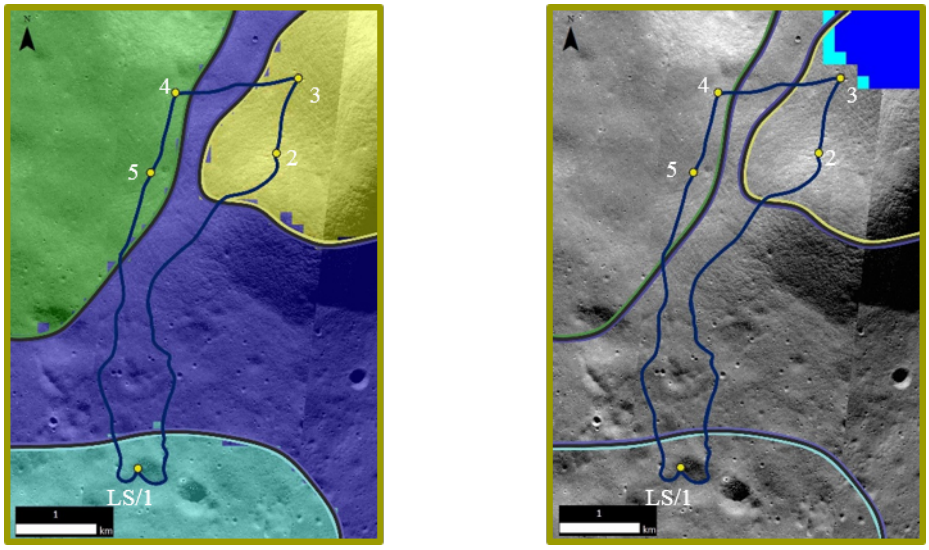

Figure E.11: North site, Medium distance traverse. Images produce in ArcGIS using LRO NAC images: M118979214RE/LE, M1117983708RE/LE, and M1117976605RE/LE. (A) Geological map (Kramer et al., 2013) overlain with NAC imagery. Green = impact crater material, yellow = peak ring material, purple = inter-peak ring material, blue = smooth inner peak material. (B) M^3 data (Kramer et al., 2013) blue = anorthositic unit.

located within a unit described as impact crater material (Kramer et al., 2013) and will address NRC (2007) Goals 1 and 6 by sampling impact melt material and regolith material.

E.6.8 Short traverse

A short distance traverse, descoped from the optimum traverse, is 3.2 km and accommodates three stations (Figure E.12). This traverse would take 4.2 days to complete, with an average slope of 2.2°, and a maximum slope of 6.5°. Stations 1 and 2 are the same as those in the optimum traverse, sampling the mare lithology and impact melt (NRC Goals 1, 2, 5). Station 3 samples the deep fracture (equivalent to Station 5 of the optimum traverse: NRC Goal 3). Sampling sites in the peak ring material are not possible in this traverse (NRC Goal 2 and 3).

E.7 Conclusion

Previous studies have shown Schrödinger basin to be an exceptional location to address the majority of science concepts identified by the NRC (2007) report. In this study traverse routes for a robotic mission with sample return capabilities were constructed at two locations within Schrödinger. The traverses illustrate the diverse nature of samples that can be collected in a solar-powered robotic mission to Schrödinger. The most significant constraint on time was found to be the ConOps and not rover speed. Further investigations into increasing rover capabilities are therefore required to optimize the mission scenario.

The medium/short traverses are those with reduced distance and/or number of stations. These represent descope options that may be preferable in terms of

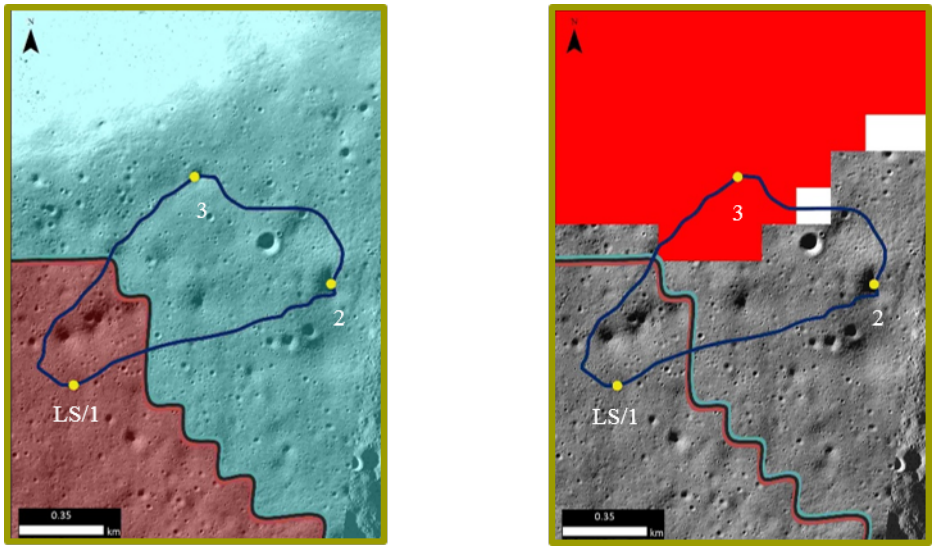

Figure E.12: North site, Short distance traverse. Images produce in ArcGIS using LRO NAC images: M1113260100RE/LE and M113067665RE/LE. (A) Geological map (Kramer et al., 2013) overlain with NAC imagery. Red = mare material, blue = smooth inner peak material. (B) M^3 data (Kramer et al., 2013) red = orthopyroxene-bearing lithology.

time/money but reduce the variety of samples which can be collected. The rover velocity used here is easily achievable, given the precedent of the Soviet Union Lunokhods in the 1970s, with the expectation it could be exceeded. A rover on the Moon can be operated in real time (∼2.6 s, two-way communications delay to Earth or a ∼0.4 s relay to L2; Burns et al., 2013), along traverses pre-designed from high resolution images which aid in pre-empting hazards, providing another argument for increasing rover velocity. Increased rover capabilities make the optimum traverses, and therefore greater scientific output, increasingly viable.

Incorporating these traverses into a mission utilizing Orion would allow the rover to be tele-operated from the Earth-Moon L2 position, virtually removing any time delay. A rover mission, without time delay, would increase flexibility and rover speed (e.g. travel velocity, analysis time) within a mission scenario, having the ability to react almost instantly. Combining a robotic lander and rover mission to be tele-operated by Orion would, therefore, produce the highest amount of scientific output from a mission not including humans on the lunar surface.

E.8 Acknowledgements

This work was carried out through the 2013 Lunar Exploration Summer Intern Program hosted by the Lunar and Planetary Institute (LPI) and funded through LPI and NLSI (NASA Lunar Science Institute). We thank the staff at LPI for their help throughout the internship and the LMMP team for their guidance and support. We especially thank George Chang for his help with LMMP data and Ross Potter for helpful comments on this manuscript. We are also grateful to Ian Crawford and an anonymous reviewer for their thoughtful and insightful comments.

Bibliography

Agrell, S. O., J. H. Scoon, I. D. Muir, J. V. P. Long, J. D. McConnell, and A. Peckett
1970. Observations on the chemistry, mineralogy and petrology of some Apollo 11 lunar samples. *Geochimica et Cosmochimica Acta Supplement*, 1:93 – 128.

Alexander, E. and P. K. Davis
1974. 40Ar-39Ar ages and trace element contents of Apollo 14 breccias; an interlaboratory cross-calibration of 40Ar-39Ar standards. *Geochimica et Cosmochimica Acta*, 38(6):911–928.

Anand, M., R. Tartèse, and J. J. Barnes
2014. Understanding the origin and evolution of water in the Moon through lunar sample studies. *Philosophical Transactions of the Royal Society A: Mathematical, Physical and Engineering Sciences*, 372(August):2–32.

Anand, M., L. A. Taylor, K. C. Misra, I. Demidova, Svetlana, and M. A. Nazarov
2003. KREEPy lunar meteorite Dhofar 287A: A new lunar mare basalt. *Meteoritics & Planetary Science*, 38(4):485–499.

Anderson, A. T., A. V. Crewe, J. R. Goldsmith, P. B. Moore, J. C. Newton, E. J. Olsen, J. V. Smith, and P. J. Wyllie
1970. Petrologic history of moon suggested by petrography, mineralogy, and crystallography. *Science (New York, N.Y.)*, 167(3918):587–90.

Armytage, R., R. Georg, P. Savage, H. Williams, and A. Halliday
2011. Silicon isotopes in meteorites and planetary core formation. *Geochimica et Cosmochimica Acta*, 75(13):3662–3676.

Armytage, R., R. Georg, H. Williams, and A. Halliday
2012. Silicon isotopes in lunar rocks: Implications for the Moon's formation and the early history of the Earth. *Geochimica et Cosmochimica Acta*, 77:504–514.

Barnes, J., I. Franchi, M. Anand, R. Tartèse, N. Starkey, M. Koike, Y. Sano, and S. Russell
2013. Accurate and precise measurements of the D/H ratio and hydroxyl content in lunar apatites using NanoSIMS. *Chemical Geology*, 337-338:48–55.

Barnes, J., R. Tartese, M. Anand, F. M. M. Mccubbin, I. A. A. Franchi, N. A. Starkey, and S. S. Russell
2015. Volatiles in the lunar crust - An evaluation of the role of metasomatism. In *46th Lunar and Planetary Science Conference*, P. 1352.

Barnes, J. D., Z. D. Sharp, T. P. Fischer, D. R. Hilton, and M. J. Carr
2009. Chlorine isotope variations along the Central American volcanic front and back arc. *Geochemistry, Geophysics, Geosystems*, 10(11):1–17.

Barnes, J. J., R. Tartèse, M. Anand, F. M. McCubbin, I. A. Franchi, N. A. Starkey, and S. S. Russell
2014. The origin of water in the primitive Moon as revealed by the lunar highlands samples. *Earth and Planetary Science Letters*, 390:244–252.

Barnes, J. J., R. Tartèse, M. Anand, F. M. McCubbin, C. R. Neal, and I. A. Franchi
2016. Early degassing of lunar urKREEP by crust-breaching impact(s). *Earth and Planetary Science Letters*, 447:84–94.

Bea, F., G. Fershtater, and L. Corretgé
1992. The geochemistry of phosphorus in granite rocks and the effect of aluminium. *Lithos*, 29(1-2):43–56.

Beard, B. L. and C. M. Johnson
1999. High precision iron isotope measurements of terrestrial and lunar materials. *Geochimica et Cosmochimica Acta*, 63(11-12):1653–1660.

Beaty, D. W. and A. L. Albee
1978. Comparative petrology and possible genetic relations among the Apollo 11 basalts. In *In: Lunar and Planetary Science ConferenceLunar and Planetary Science Conference*, volume 9, Pp. 359–463.

Berkelman, P.
1995. Design of a day/night rover. Technical report, Robotics Institute, Carnegie Mellon University.

Birck, J. L., S. Fourcade, and C. J. Allegre
1975. 87Rb-86Sr age of rocks from the Apollo 15 landing site and significance of internal isochrons. *Earth and Planetary Science Letters*, 26(1):29–35.

Bonifacie, M., V. Busigny, C. Mével, P. Philippot, P. Agrinier, N. Jendrzejewski, M. Scambelluri, and M. Javoy
2008. Chlorine isotopic composition in seafloor serpentinites and high-pressure metaperidotites. Insights into oceanic serpentinization and subduction processes. *Geochimica et Cosmochimica Acta*, 72(1):126–139.

Boyce, J. W. and R. L. Hervig
2008. Magmatic degassing histories from apatite volatile stratigraphy. *Geology*, 36(1):63.

Boyce, J. W., Y. Liu, G. R. Rossman, Y. Guan, J. M. Eiler, E. M. Stolper, and L. A. Taylor
2010. Lunar apatite with terrestrial volatile abundances. *Nature*, 466(7305):466–9.

Boyce, J. W., S. M. Tomlinson, F. M. McCubbin, J. P. Greenwood, and A. H. Treiman
2014. The lunar apatite paradox. *Science (New York, N.Y.)*, 344(6182):400–2.

Boyce, J. W., A. H. Treiman, Y. Guan, C. Ma, J. M. Eiler, J. Gross, J. P. Greenwood, and E. M. Stolper
2015. The chlorine isotope fingerprint of the lunar magma ocean. *Science Advances*, 1:1–8.

Brenan, J.
1993a. Kinetics of fluorine, chlorine, and hydroxyl exchange in fluorapatite. *Chemical Geology*, 110:195–210.

Brenan, J.
1993b. Partitioning of fluorine and chlorine between apatite and aqueous fluids at high pressure and temperature: implications for the F and Cl content of high PT. *Earth and Planetary Science Letters*, 117:251–263.

Bunte, M. K., S. Porter, and M. S. Robinson
2011. A sortie mission to Schrödinger Basin as reconnaissance for future exploration. *Geological Society of America Special Papers*, 483:533–546.

Burnham, C. W.
1994. Development of the Burnham model for prediction of H2O solubility in magmas. *Reviews in Mineralogy and Geochemistry*, 30(1):123–129.

Burns, J. O., D. A. Kring, J. B. Hopkins, S. Norris, T. J. W. Lazio, and J. Kasper
2013. A lunar L2-Farside exploration and science mission concept with the Orion Multi-Purpose Crew Vehicle and a teleoperated lander/rover. *Advances in Space Research*, 52(2):306–320.

Butler, P.
1971. Lunar sample catalog, Apollo 15. Technical report.

Candela, P. A.
1986. Toward a thermodynamic model for the halogens in magmatic systems: An application to melt-vapor-apatite equilibria. *Chemical Geology*, 57(3-4):289–301.

Canup, R.
2008. Lunar-forming collisions with pre-impact rotation. *Icarus*, 196(2):518–538.

Canup, R. M.
2012. Forming a Moon with an Earth-like composition via a giant impact. *Science (New York, N.Y.)*, 338(6110):1052–5.

Canup, R. M., C. Visscher, J. Salmon, and B. Fegley Jr
2015. Lunar volatile depletion due to incomplete accretion within an impact-generated disk. *Nature Geoscience*, 8(12):918–921.

Carlson, I. C. and W. J. A. Walton
1978. Apollo 14 rock samples. Technical report.

Carrier, W. D.
2006. Lunar soil simulation and trafficability parameters. Technical report.

Charlier, B., G. Nowell, I. Parkinson, S. Kelley, D. Pearson, and K. Burton
2012. High temperature strontium stable isotope behaviour in the early solar system and planetary bodies. *Earth and Planetary Science Letters*, 329-330:31–40.

Chen, Y., Y. Zhang, Y. Liu, Y. Guan, J. Eiler, and E. M. Stolper
2015. Water, fluorine, and sulfur concentrations in the lunar mantle. *Earth and Planetary Science Letters*, 427:37–46.

Clayton, R. N., J. M. Hurd, T. K. Mayeda, R. Clayton, J. Hurd, and T. Mayeda
1972. Oxygen isotopic compositions and oxygen concentrations of Apollo 14 and Apollo 15 rocks and soils. *Proceedings of the Third Lunar science Conferencecience Conference*, 2:1455–1463.

Compston, W., M. Vernon, H. Berry, R. Rudowski, C. Gray, and N. Ware
1972a. Apollo 14 mineral ages and the thermal histroy of the Fra Mauro formation. *In: Lunar and Planetary Science Conference*, 3:1487–1501.

Compston, W., M. J. Vernon, H. Berry, R. Rudowski, C. M. Gray, N. Ware, B. W. Chappell, and M. Kaye
1972b. Age and Petrogenesis of Apollo 14 Basalts. *In: Lunar and Planetary Science Conference*, 3.

Crawford, I., M. Anand, C. Cockell, H. Falcke, D. Green, R. Jaumann, and M. Wieczorek
2012. Back to the Moon: The scientific rationale for resuming lunar surface exploration. *Planetary and Space Science*, 74(1):3–14.

Ćuk, M. and S. T. Stewart
2012. Making the Moon from a fast-spinning Earth: a giant impact followed by resonant despinning. *Science (New York, N.Y.)*, 338(6110):1047–52.

Czank, M., K. Girgis, A. B. Harnik, F. Laves, R. Schmid, H. Schulz, and L. Weber
1972. Crystallographic Studies of Some Apollo 14 Plagioclases. In *In: Lunar and Planetary Science Conference*, volume 3.

Dasch, E., C.-Y. Shih, B. Bansal, H. Wiesmann, and L. Nyquist
1987. Isotopic analysis of basaltic fragments from lunar breccia 14321: Chronology and petrogenesis of pre-Imbrium mare volcanism. *Geochimica et Cosmochimica Acta*, 51(12):3241–3254.

Dauphas, N., J. Chen, and D. Papanastassiou
2015. Testing Earth-Moon Isotopic Homogenization with Calcium-48. *In: Lunar and Planetary Science Conference*, 46:2436.

Dauphas, N., J. H. Chen, J. Zhang, D. A. Papanastassiou, A. M. Davis, and C. Travaglio
2014. Calcium-48 isotopic anomalies in bulk chondrites and achondrites: Evidence for a uniform isotopic reservoir in the inner protoplanetary disk. *Earth and Planetary Science Letters*, 407:96–108.

Davenport, J. D., J. Longhi, C. R. Neal, D. Bolster, and B. L. Jolliff
2014. Simulating Planetary Igneous Crystallization Environments (SPICEs): A Suite of Igneous Crystallization Programs. *In: Lunar and Planetary Science Conference*, 45.

Day, J. M., L. A. Taylor, C. Floss, A. D. Patchen, D. W. Schnare, and D. G. Pearson
2006. Comparative petrology, geochemistry, and petrogenesis of evolved, low-Ti lunar mare basalt meteorites from the LaPaz Icefield, Antarctica. *Geochimica et Cosmochimica Acta*, 70(6):1581–1600.

de Meijer, R., V. Anisichkin, and W. van Westrenen
2013. Forming the Moon from terrestrial silicate-rich material. *Chemical Geology*, 345:40–49.

de Vries, J., A. van den Berg, and W. van Westrenen
2010. Formation and evolution of a lunar core from ilmenite-rich magma ocean cumulates. *Earth and Planetary Science Letters*, 292(1-2):139–147.

Ding, L., H. Gao, Z. Deng, K. Nagatani, and K. Yoshida
2011. Experimental study and analysis on driving wheels' performance for planetary exploration rovers moving in deformable soil. *Journal of Terramechanics*, 48(1):27–45.

Doherty, A. L., J. D. Webster, B. a. Goldoff, and P. M. Piccoli
2014. Partitioning behavior of chlorine and fluorine in felsic melt-fluid(s)-apatite systems at 50 MPa and 850-950 C. *Chemical Geology*, 384:94 – 111.

Drozd, R., C. Hohenberg, C. Morgan, F. Podosek, and M. Wroge
1977. Cosmic-ray exposure history at Taurus-Littrow. *In: Lunar Science Conference*, 3:3027–3043.

Duff, E. J.
1972. Orthophosphates - XI Bromoapatite: Stability of solid solutions of bromoapatite with other calcium apatites under aqueous conditions. *Journal of Inorganic and Nuclear Chemistry*, 34(1):101–108.

Duncan, A., R. Grieve, and D. Weill
1975. The life and times of Big Bertha: lunar breccia 14321. *Geochimica et Cosmochimica Acta*, 39(3):265–273.

Dymek, R. F., A. L. Albee, and A. A. Chodos
1975. Comparative mineralogy and petrology of Apollo 17 mare basalts - Samples 70215, 71055, 74255, and 75055. *In: Lunar Science Conference*, 6:49–77.

Edgar, A. D. and L. A. Pizzolato
1995. An experimental study of partitioning of fluorine between K-richterite, apatite, phlogopite, and melt at 20 kbar. *Contributions to Mineralogy and Petrology*, 121(3):247–257.

El Goresey, A., P. Ramdohr, and L. A. Taylor
1971. The geochemistry of the opaque minerals in Apollo 14 crystalline rocks. *Earth and Planetary Science Letters*, 13:121–129.

El Goresy, A. and P. Ramdohr
1975. Subsolidus Reduction of Lunar Opaque Oxides: Evidence, Assemblages, Geochemical Relevance, and Evidence For A Late Stage Reducing Gaseous Mixture. *In: Lunar and Planetary Science Conference*, 6:245 – 247.

El Goresy, A., L. A. Taylor, and P. Ramdohr
1972. Fra Mauro crystalline rocks: Mineralogy, geochemistry, and subsolidus reduction of the opaque minerals. *In: Lunar Science Conference*, 3:333.

Elkins-Tanton, L., J. A. V. Orman, B. H. Hager, and T. L. Grove
2002. Re-examination of the lunar magma ocean cumulate overturn hypothesis : melting or mixing is required. *Earth and Planetary Science Letters*, 196:239–249.

Elkins-Tanton, L. T., S. Burgess, and Q.-Z. Yin
2011. The lunar magma ocean : Reconciling the solidification process with lunar petrology and geochronology. *Earth and Planetary Science Letters*, 304(3-4):326–336.

Elkins-Tanton, L. T., N. Chatterjee, and T. L. Grove
2003. Magmatic processes that produced lunar fire fountains. *Res. Lett*, 30(10):1–4.

Ellis, D. J. and D. H. Green
1979. An experimental study of the effect of Ca upon garnet-clinopyroxene Fe-Mg exchange equilibria. *Contributions to Mineralogy and Petrology*, 71(1):13–22.

Engel, A. E. and C. G. Engel
1970. Lunar rock compositions and some interpretations. *Science (New York, N.Y.)*, 167(3918):527–8.

Epstein, S. and J. Taylor, H. P.
1973. The isotopic composition and concentration of water, hydrogen, and carbon in some Apollo 15 and 16 soils and in the Apollo 17 orange soil. *In: Lunar Science Conference*, 4:1559.

Eugster, O., P. Eberhardt, J. Geiss, N. Grögler, M. Jungck, F. Meier, M. Mörgeli, and F. Niederer
1984. Cosmic ray exposure histories of Apollo 14, Apollo 15, and Apollo 16 rocks. *Journal of Geophysical Research*, 89(2):B498.

Evensen, N. M., V. R. Murthy, and J. Coscio, M. R.
1973. Rb-Sr ages of some mare basalts and the isotopic and trace element systematics in lunar fines. *In: Lunar Science Conference*, 4:1707 – 1724.

Fagan, A., C. Neal, A. Simonetti, P. Donohue, and K. O'Sullivan
2013. Distinguishing between Apollo 14 impact melt and pristine mare basalt samples by geochemical and textural analyses of olivine. *Geochimica et Cosmochimica Acta*, 106:429–445.

Fagan, T. J., D. Kashima, Y. Wakabayashi, and A. Suginohara
2014. Case study of magmatic differentiation trends on the Moon based on lunar meteorite Northwest Africa 773 and comparison with Apollo 15 quartz monzodiorite. *Geochimica et Cosmochimica Acta*, 133:97–127.

Fegley, B.
1991. Thermodynamic models of the chemistry of lunar volcanic gases. *Geophysical Research Letters*, 18(11):2073–2076.

Finger, L. W., S. S. Hafner, K. Schürmann, D. Virgo, and D. Warburton
1972. Distinct Cooling Histories and Reheating of Apollo 14 Rocks. *In: Lunar and Planetary Science Conference*, 3:259.

Flahaut, J., J.-F. Blanchette-Guertin, C. Jilly, P. Sharma, A. Souchon, W. van Westrenen, and D. Kring
2012. Identification and characterization of science-rich landing sites for lunar lander missions using integrated remote sensing observations. *Advances in Space Research*, 50(12):1647–1665.

Fleet, M. E.
1995. Site Preference of Rare Earth Elements in fluorapatite. *American Astronomical Society*, 80(1):329–335.

Fleet, M. E., X. Liu, and Y. Pan
2000. Site Preference of Rare Earth Elements in Hydroxyapatite [Ca10(PO4)6(OH)2]. *Journal of Solid State Chemistry*, 149(2):391–398.

Füri, E., E. Deloule, A. Gurenko, and B. Marty
2014. New evidence for chondritic lunar water from combined D/H and noble gas analyses of single Apollo 17 volcanic glasses. *Icarus*, 229:109–120.

Gancarz, A., A. Albee, and A. Chodos
1971. Petrologic and mineralogic investigation of some crystalline rocks returned by the Apollo 14 mission. *Earth and Planetary Science Letters*, 12(3):141–141.

Gancarz, A., A. Albee, and A. Chodos
1972. Comparative petrology of Apollo 16 sample 68415 and Apollo 14 samples 14276 and 14310. *Earth and Planetary Science Letters*, 16(3):307–330.

Ghiorso, M. S., M. M. Hirschmann, P. W. Reiners, and V. C. Kress
2002. The pMELTS: A revision of MELTS for improved calculation of phase relations and major element partitioning related to partial melting of the mantle to 3 GPa. *Geochemistry, Geophysics, Geosystems*, 3(5):1–35.

Ghiorso, M. S. and R. O. Sack
1995. Chemical mass transfer in magmatic processes IV. A revised and internally consistent thermodynamic model for the interpolation and extrapolation of liquid-solid equilibria in magmatic systems at elevated temperatures and pressures. *Contributions to Mineralogy and Petrology*, 119(2-3):197–212.

Ghose, S., G. Ng, and L. S. Walter
1972. Clinopyroxenes from Apollo 12 and 14: Exsolution, domain structure and cation order. *In: Lunar Science Conference*, 3:507.

Gola, A. A., B. D'Anna, K. L. Feilberg, S. R. Sellevåg, L. Bache-Andreassen, and C. J. Nielsen
2005. Kinetic isotope effects in the gas phase reactions of OH and Cl with CH3Cl, CD3Cl, and13CHCl. *Atmospheric Chemistry and Physics*, 5(9):2395–2402.

Gomes, R., H. F. Levison, K. Tsiganis, and A. Morbidelli
2005. Origin of the cataclysmic Late Heavy Bombardment period of the terrestrial planets. *Nature*, 435(7041):466–469.

Greenwood, J. P., S. Itoh, N. Sakamoto, P. Warren, L. Taylor, and H. Yurimoto
2011. Hydrogen isotope ratios in lunar rocks indicate delivery of cometary water to the Moon. *Nature Geoscience*, 4(2):79–82.

Grieve, R., G. McKay, H. Smith, and D. Weill
1975. Lunar polymict breccia 14321: a petrographic study. *Geochimica et Cosmochimica Acta*, 39(3):229–245.

Grove, T. L. and M. J. Krawczynski
2009. Lunar Mare Volcanism: Where Did the Magmas Come From? *Elements*, 5(1):29–34.

Gualda, G. a. R., M. S. Ghiorso, R. V. Lemons, and T. L. Carley
2012. Rhyolite-MELTS: a Modified Calibration of MELTS Optimized for Silica-rich, Fluid-bearing Magmatic Systems. *Journal of Petrology*, 53(5):875–890.

Guggisberg, S., P. Eberhardt, J. Geiss, N. Groegler, A. Stettler, G. M. Brown, and A. Peckett
1979. Classification of the Apollo-11 mare basalts according to /Ar-39/-/Ar-40/ ages and petrological properties. *In: Lunar and Planetary Science Conference*, 10:1–39.

Haggerty, S. E. and H. O. Meyer
1970. Apollo 12: Opaque oxides. *Earth and Planetary Science Letters*, 9(5):379–387.

Hallis, L., M. Anand, R. Greenwood, M. Miller, I. Franchi, and S. Russell
2010. The oxygen isotope composition, petrology and geochemistry of mare basalts: Evidence for large-scale compositional variation in the lunar mantle. *Geochimica et Cosmochimica Acta*, 74(23):6885–6899.

Harrison, T. M. and E. Bruce
1984. The behavior of apatite during crnstal anatexis : Equilibrium and kinetic considerations. *Geochimica et Cosmochimica Acta*, 48:1467–1477.

Hauri, E. H., A. E. Saal, M. J. Rutherford, and J. A. Van Orman
2015. Water in the Moon's interior: Truth and consequences. *Earth and Planetary Science Letters*, 409:252–264.

Hauri, E. H., T. Weinreich, A. E. Saal, M. C. Rutherford, and J. A. Van Orman
2011. High pre-eruptive water contents preserved in lunar melt inclusions. *Science (New York, N.Y.)*, 333(6039):213–5.

Helmke, P. A., L. A. Haskin, R. L. Korotev, and K. E. Ziegler
1972. Rare earths and other trace elements in Apollo 14 samples. *In: Lunar Science Conference*, 3:1275.

Henderson, P.
1970. The Significance of the Mesostasis of Basic Layered Igneous Rocks. *Journal of Petrology*, 11(3):463–473.

Herwartz, D., A. Pack, B. Friedrichs, and A. Bischoff
2014. Identification of the giant impactor Theia in lunar rocks. *Science (New York, N.Y.)*, 344(6188):1146–50.

Herzog, G., F. Moynier, F. Albarède, and A. Berezhnoy
2009. Isotopic and elemental abundances of copper and zinc in lunar samples, Zagami, Pele's hairs, and a terrestrial basalt. *Geochimica et Cosmochimica Acta*, 73(19):5884–5904.

Hess, P. and E. Parmentier
1995. A model for the thermal and chemical evolution of the Moon's interior: implications for the onset of mare volcanism. *Earth and Planetary Science Letters*, 134(3-4):501–514.

Hiesinger, H. and J. W. Head
2006. New Views of Lunar Geoscience: An Introduction and Overview. *Reviews in Mineralogy and Geochemistry*, 60(1):1–81.

Hiesinger, H., R. Jaumann, G. Neukum, and J. W. Head
2000. Ages of mare basalts on the lunar nearside. *Journal of Geophysical Research: Planets*, 105(E12):29239–29275.

Hintenberger, H., H. W. Weber, H. Voshage, H. Wänke, F. Begemann, and F. Wlotzka
1970. Concentrations and isotopic abundances of the rare gases, hydrogen and nitrogen in lunar matter. In *In: Lunar Planetary Science Conference*, volume 11, Pp. 1269 – 1282.

Hirschmann, M., A. Withers, P. Ardia, and N. Foley
2012. Solubility of molecular hydrogen in silicate melts and consequences for volatile evolution of terrestrial planets.

Hohenberg, C. M., P. K. Davis, W. A. Kaiser, R. S. Lewis, and J. H. Reynolds
1970. Trapped and cosmogenic rare gases from stepwise heating of Apollo 11 samples. In *In: Lunar Planetary Science Conference*, volume 1, Pp. 1283 – 1309.

Hollister, L., W. Trzcienski, R. Dymek, C. Kulick, P. Weigand, and R. Hargraves
1972. Igneous Fragment 14310,21 and the Origin of the Mare Basalts. *In: Lunar and Planetary Science Conference*, 3:386.

Hopkins, J.
2013. Proposed orbits for human missions to the Earth-Moon L2 region. In *International Astronomical Conference*.

Hoppe, P., S. Cohen, and A. Meibom
2013. NanoSIMS: Technical Aspects and Applications in Cosmochemistry and Biological Geochemistry. *Geostandards and Geoanalytical Research*, 37(2):111–154.

Horn, P., T. Kirsten, and E. K. Jessberger
1975. Are there 12 mare basalts younger than 3.1 b.y. unsuccessful search for a 12 mare basalts with crystallization ages below 3.1 b.y. *Meteoritics & Planetary Science*, 10:417–418.

Hovis, G. L. and D. E. Harlov
2010. Solution calorimetric investigation of fluor-chlorapatite crystalline solutions. *American Mineralogist*, 95(7):946–952.

Hovis, G. L., F. M. McCubbin, H. Nekvasil, G. Ustunisik, W. R. Woerner, and D. H. Lindsley
2014. A novel technique for fluorapatite synthesis and the thermodynamic mixing behavior of F-OH apatite crystalline solutions. *American Mineralogist*, 99(5-6):890–897.

Huang, L., N. Sturchio, T. Abrajano, L. Heraty, and B. Holt
1999. Carbon and chlorine isotope fractionation of chlorinated aliphatic hydrocarbons by evaporation. *Organic Geochemistry*, 30(8):777–785.

Hubbard, N. J., P. W. Gast, J. M. Rhodes, B. M. Bansal, H. Wiesmann, and S. E. Church
1972. Nonmare basalts: Part II. *In: Lunar Science Conference*, 3:1161.

Hughes, J. and M. Cameron
1989. Structural variations in natural F, OH , and Cl apatites. *American Mineralogist*, 74:870–876.

Hughes, J. M., M. Cameron, and K. D. Crowley
1990. Crystal structures of natural ternary apatites; solid solution in the Ca 5 (PO 4) 3 X(X = F, OH, Cl) system. *American Mineralogist*, 75(3-4):295–304.

Hughes, J. M. and J. Rakovan
2002. The Crystal Structure of Apatite, Ca5(PO4)3(F,OH,Cl). *Reviews in Mineralogy and Geochemistry*, 48(1):1–12.

Hughes, J. M. and J. F. Rakovan
2015. Structurally robust, chemically diverse: Apatite and apatite supergroup minerals. *Elements*, 11(3):165–170.

Hui, H., J. G. Oshrin, and C. R. Neal
2011. Investigation into the petrogenesis of Apollo 14 high-Al basaltic melts through crystal stratigraphy of plagioclase. *Geochimica et Cosmochimica Acta*, 75(21):6439–6460.

Hui, H., A. H. Peslier, Y. Zhang, and C. R. Neal
2013. Water in lunar anorthosites and evidence for a wet early Moon. *Nature Geoscience*, 6(3):177–180.

Humayun, M. and R. N. Clayton
1995. Precise determination of the isotopic composition of potassium: Application to terrestrial rocks and lunar soils. *Geochimica et Cosmochimica Acta*, 59(10):2115–2130.

Husain, L., J. F. Sutter, and O. A. Schaeffer
1971. Ages of crystalline rocks from fra mauro. *Science (New York, N.Y.)*, 173(4003):1235–6.

Jaffe, L. and R. Choate
1974. Unmanned Surface Traverses of Mars and Moon: Science Objectives, Payloads, Operations. *Journal of Spacecraft and Rockets*, 11(6):353–354.

James, O. B. and E. D. Jackson
1970. Petrology of the Apollo 11 ilmenite basalts. *Journal of Geophysical Research*, 75(29):5793–5824.

Jarosewich, E., J. Nelen, and J. A. Norberg
1980. Reference Samples for Electron Microprobe Analysis. *Geostandards and Geoanalytical Research*, 4(1):43–47.

Jochum, K. P., U. Weis, B. Stoll, D. Kuzmin, Q. Yang, I. Raczek, D. E. Jacob, A. Stracke, K. Birbaum, D. a. Frick, D. Günther, and J. Enzweiler
2011. Determination of Reference Values for NIST SRM 610-617 Glasses Following ISO Guidelines. *Geostandards and Geoanalytical Research*, 35(4):397–429.

Jolliff, B. L., L. A. Haskin, R. Colson, and M. H. I. Wadhwa
1993. Partitioning in REE-saturating minerals : Theory, experiment, and modellmg of whitlockite, apatite, and evolution of lunar residual magmas. *Geochimica et Cosmochimica Acta*, 57(16):4069–4094.

Karner, J. M., S. R. Sutton, J. J. Papike, C. K. Shearer, J. H. Jones, and M. Newville
2006. Application of a new vanadium valence oxybarometer to basaltic glasses from the Earth, Moon, and Mars. *American Mineralogist*, 91(2-3).

Kempl, J., P. Vroon, E. Zinngrebe, and W. van Westrenen
2013. Si isotope fractionation between Si-poor metal and silicate melt at pressuretemperature conditions relevant to metal segregation in small planetary bodies. *Earth and Planetary Science Letters*, 368:61–68.

Klein, C., J. C. Drake, and C. Frondel
1971. Mineralogical, petrological, and chemical features of four Apollo 12 lunar microgabbros. *Proceedings of the Lunar Science Conference*, 2:265–284.

Kohl, I. E., P. H. Warren, and E. D. Young
2015. Earth and Moon are Indistinguishable in Δ17O to Several Parts Per Million. *In: Lunar and Planetary Science Conference*, 46.

Konzett, J., D. Rhede, and D. J. Frost
2011. The high PT stability of apatite and Cl partitioning between apatite and hydrous potassic phases in peridotite: an experimental study to 19GPa with implications for the transport of P, Cl and K in the upper mantle. *Contributions to Mineralogy and Petrology*, 163(2):277–296.

Korotev, R. L. and J. J. Gillis
2001. A new look at the Apollo 11 regolith and KREEP. *Journal of Geophysical Research: Planets*, 106(E6):12339–12353.

Krähenbühl, U., R. Ganapathy, J. W. Morgan, and E. Anders
1973. Volatile elements in Apollo 16 samples: Implications for highland volcanism and accretion history of the moon. *In: Lunar and Planetary Science Conference*, 4:1325.

Kramer, G. Y., D. A. Kring, A. L. Nahm, and C. M. Pieters
2013. Spectral and photogeologic mapping of Schrödinger Basin and implications for post-South Pole-Aitken impact deep subsurface stratigraphy. *Icarus*, 223(1):131–148.

Krawczynski, M. J. and T. L. Grove
2012. Experimental investigation of the influence of oxygen fugacity on the source depths for high titanium lunar ultramafic magmas. *Geochimica et Cosmochimica Acta*, 79:1–19.

Kring, D. A. and D. D. Durada
2012. *A global lunar landing site study to provide the scientific context for exploration of the Moon.*, lpi contri edition. Lunar and Planetary Institute, Houston, TX, 688 p.

Kruijer, T. S., T. Kleine, M. Fischer-Gödde, and P. Sprung
2015. Lunar tungsten isotopic evidence for the late veneer. *Nature*, 520(7548):534–7.

Kusebauch, C., T. John, M. J. Whitehouse, S. Klemme, and A. Putnis
2015. Distribution of halogens between fluid and apatite during fluid-mediated replacement processes. *Geochimica et Cosmochimica Acta*, 170:225–246.

Kushiro, I. and H. Haramura
1971. Major element variation and possible source materials of apollo 12 crystalline rocks. *Science (New York, N.Y.)*, 171(3977):1235–7.

Kushiro, I., Y. Ikeda, and Y. Nakamura
1972. Petrology of Apollo 14 high-alumina basalt. *In: Lunar Science Conference*, 3:115.

Leader, M. K., R. N. Rege, N. J. Potts, A. L. Gullikson, N. M. Curran, J. K. Dhaliwal, and D. A. Kring
2014. Velocity of a rover as a function of slope of lunar terrain. *In: Lunar and Planetary Science Conference*, 46.

Lesher, C. E.
2010. Self-diffusion in Silicate Melts: Theory, Observations and Applications to Magmatic Systems. *Reviews in Mineralogy & Geochemistry*, 72:269–309.

Li, H. and J. Hermann
2015. Apatite as an indicator of fluid salinity: An experimental study of chlorine and fluorine partitioning in subducted sediments. *Geochimica et Cosmochimica Acta*, 166:267–297.

Li, Y., R. Dasgupta, and K. Tsuno
2015. The effects of sulfur, silicon, water, and oxygen fugacity on carbon solubility and partitioning in Fe-rich alloy and silicate melt systems at 3 GPa and 1600 C: Implications for core-mantle differentiation and degassing of magma oceans and reduced plane. *Earth and Planetary Science Letters*, 415:54–66.

Liu, Y., C. Floss, J. M. D. Day, E. Hill, and L. a. Taylor
2009. Petrogenesis of lunar mare basalt meteorite Miller Range 05035. *Meteoritics & Planetary Science*, 44(2):261–284.

Longhi, J.
1991. Comparative liquidus equilibria of hypersthene-normative basalts at low pressure. *American Mineralogist*, 76(5-6):785–800.

Longhi, J., D. Walker, and J. Hays
1972. Petrography and crystallization history of basalts 14310 and 14072. *Proceedings of the Lunar Science Conference*, 3.

LSPET
1970. Preliminary Examination of Lunar Samples from Apollo 12. *Science*, 167(3923):1325–1339.

LSPET
1971. Preliminary examination of lunar samples from apollo 14. *Science (New York, N.Y.)*, 173(3998):1211–1227.

Lucey, P., R. L. Korotev, J. J. Gillis, L. A. Taylor, D. Lawrence, B. A. Campbell, R. Elphic, B. Feldman, L. L. Hood, D. Hunten, M. Mendillo, S. Noble, J. J. Papike, R. C. Reedy, S. Lawson, T. Prettyman, O. Gasnault, and S. Maurice
2006. Understanding the Lunar Surface and Space-Moon Interactions. *Reviews in Mineralogy and Geochemistry*, 60(1):4829–219.

Lugmair, G. and A. Shukolyukov
1998. Early solar system timescales according to 53Mn-53Cr systematics. *Geochimica et Cosmochimica Acta*, 62(16):2863–2886.

Lupisella, M. and M. R. Bobskill
2012. NASA Human Spaceflight Architecture Team: Cis-Lunar Analysis. In *Earth and Space 2012*, Pp. 1515–1524, Reston, VA. American Society of Civil Engineers.

MacDonald, R., R. L. Smith, and J. E. Thomas
2010. Chemistry of the Subalkalic Silicic Obsidians. *U.S. Geological Survery Professional Paper 1523*, P. 214.

Magenheim, A. J., A. J. Spivack, P. J. Michael, and J. M. Gieskes
1995. Chlorine stable isotope composition of the oceanic crust: Implications for Earth's distribution of chlorine. *Earth and Planetary Science Letters*, 131(3-4):427–432.

Mark, R. K., C.-N. Lee-Hu, and G. W. Weatherill
1974. Rb-Sr age of lunar igneous rocks 62295 and 14310. *Geochimica et Cosmochimica Acta*, 38(10):1643–1648.

Mastrobuono-Battisti, A., H. B. Perets, and S. N. Raymond
2015. A primordial origin for the compositional similarity between the Earth and the Moon. *Nature*, 520(7546):212–5.

Mathez, E. a. and J. D. Webster
2005. Partitioning behavior of chlorine and fluorine in the system apatite-silicate melt-fluid. *Geochimica et Cosmochimica Acta*, 69(5):1275–1286.

Mazarico, E., G. Neumann, D. Smith, M. Zuber, and M. Torrence
2011. Illumination conditions of the lunar polar regions using LOLA topography. *Icarus*, 211(2):1066–1081.

McCubbin, F. M., E. H. Hauri, S. M. Elardo, K. E. Vander Kaaden, J. Wang, and C. K. Shearer
2012. Hydrous melting of the martian mantle produced both depleted and enriched shergottites. *Geology*, 40(8):683–686.

McCubbin, F. M., B. L. Jolliff, H. Nekvasil, P. K. Carpenter, R. a. Zeigler, A. Steele, S. M. Elardo, and D. H. Lindsley
2011. Fluorine and chlorine abundances in lunar apatite: Implications for heterogeneous distributions of magmatic volatiles in the lunar interior. *Geochimica et Cosmochimica Acta*, 75(17):5073–5093.

McCubbin, F. M., A. Steele, E. H. Hauri, H. Nekvasil, S. Yamashita, and R. J. Hemley
2010a. Nominally hydrous magmatism on the Moon. *Proceedings of the National Academy of Sciences of the United States of America*, 107(25):11223–8.

McCubbin, F. M., A. Steele, H. Nekvasil, A. Schnieders, T. Rose, M. Fries, P. K. Carpenter, and B. L. Jolliff
2010b. Detection of structurally bound hydroxyl in fluorapatite from Apollo Mare basalt 15058,128 using TOF-SIMS. *American Mineralogist*, 95(8-9):1141–1150.

McCubbin, F. M., K. E. Vander Kaaden, R. Tartèse, J. W. Boyce, S. Mikhail, E. S. Whitson, A. S. Bell, M. Anand, I. A. Franchi, J. Wang, and E. H. Hauri
2015a. Experimental investigation of F, Cl, and OH partitioning between apatite and Fe-rich basaltic melt at 1.0 to 1.2 GPa and 950 to 1000 C. *American Mineralogist*, 100(8-9):1790–1802.

McCubbin, F. M., K. E. Vander Kaaden, R. Tartèse, R. L. Klima, Y. Liu, J. Mortimer, J. J. Barnes, C. K. Shearer, A. H. Treiman, D. J. Lawrence, S. M. Elardo, D. M. Hurley, J. W. Boyce, and M. Anand
2015b. Magmatic volatiles (H, C, N, F, S, Cl) in the lunar mantle, crust, and regolith: Abundances, distributions, processes, and reservoirs. *American Mineralogist*, 100(8-9):1668–1707.

McDade, P., B. J. Wood, W. Van Westrenen, R. Brooker, G. Gudmundsson, H. Soulard, J. Najorka, and J. Blundy
2002. Pressure corrections for a selection of piston-cylinder cell assemblies. *Mineralogical Magazine*, 66(6):1021–1028.

McGee, P. E., J. L. Warner, and C. H. Simonds
1977. Introduction to the Apollo collections. Part 1: Lunar igneous rocks. Technical report.

McKay, D. S., U. S. Clanton, G. H. Heiken, D. A. Morrison, R. M. Taylor, and G. Ladle
1972. Vapor Phase Crystallization in Apollo 14 Breccias and Size Analysis of Apollo 14 Soils. *In: Lunar and Planetary Science Conference*, 3:529.

McKay, G., G. A. McKay, H. Wiesmann, B. M. Bansal, and C.-Y. Shih
1979. Petrology, chemistry, and chronology of Apollo 14 KREEP basalts. *In: Lunar and Planetary Science Conference*, 10:181–205.

Medard, E., C. A. McCammon, J. A. Barr, and T. L. Grove
2008. Oxygen fugacity, temperature reproducibility, and H2O contents of nominally anhydrous piston-cylinder experiments using graphite capsules. *American Mineralogist*, 93(11-12):1838–1844.

Meier, M. M. M.
2012. Moon formation: Earth's titanium twin. *Nature Geoscience*, 5(4):240–241.

Mest, S.
2011. The geology of Schrodinger basin: Insights from post-Lunar Orbiter daa. In *Recent Advances in Lunar Straigraphy*, D. Williams and W. Ambrose, eds., Pp. 95–115. Geological Society of America Special Paper.

Meyer, C., I. S. Williams, and W. Compston
1996. Uranium-lead ages for lunar zircons: Evidence for a prolonged period of granophyre formation from 4.32 to 3.88 Ga. *Meteoritics & Planetary Science*, 31(3):370–387.

Meyer, C., J., D. S. McKay, D. H. Anderson, and J. Butler, P.
1975. The source of sublimates on the Apollo 15 green and Apollo 17 orange glass samples. *In: Lunar and Planetary Science Conference*, 6:1673–1699.

Morbidelli, A., S. Marchi, W. Bottke, and D. Kring
2012. A sawtooth-like timeline for the first billion years of lunar bombardment. *Earth and Planetary Science Letters*, 355:144–151.

Morgan, J. W., J. C. Laul, U. Krähenbühl, R. Ganapathy, and E. Anders
1972. Major impacts on the moon: Characterization from trace elements in Apollo 12 and 14 samples. *In: Lunar and Planetary Science Conference*, 3:1377.

Neal, C. R., M. D. Hacker, G. A. Snyder, L. A. Taylor, Y.-G. Liu, and R. A. Schmitt
1994a. Basait generation at the Apollo 12 site, Part 2: Source heterogeneity, multiple melts, and crustal contamination. *Meteoritics & Planetary Science*, 29(3):349–361.

Neal, C. R., M. D. Hacker, G. A. Snyder, L. A. Taylor, Y.-G. Liu, and R. A. Schmitt
1994b. Basalt generation at the Apollo 12 site, Part 1: New data, classification, and re-evaluation. *Meteoritics & Planetary Science*, 29(3):334–348.

Neal, C. R. and G. Y. Kramer
2006. The petrogenesis of the Apollo 14 high-Al mare basalts. *American Mineralogist*, 91(10):1521–1535.

Neal, C. R., L. A. Taylor, and M. M. Lindstrom
1988. Apollo 14 mare basalt petrogenesis - Assimilation of KREEP-like components by a fractionating magma. *In: Lunar and Planetary Science Conference*, 18:139–153.

Neal, C. R., L. A. Taylor, and A. D. Patchen
1989a. High alumina (HA) and very high potassium (VHK) basalt clasts from Apollo 14 breccias. I - Mineralogy and Petrology - Evidence of crystallization from evolving magmas. *In: Lunar and Planetary Science Conference*, 19:137–145.

Neal, C. R., L. A. Taylor, R. A. Schmitt, S. S. Hughes, and M. M. Lindstrom
1989b. High alumina (HA) and very high potassium (VHK) basalt clasts from Apollo 14 breccias. II - Whole rock geochemistry - Further evidence for combined assimilation and fractional crystallization within the lunar crust. *In: Lunar and Planetary Science Conference*, 19:147–161.

Nemchin, A., M. Grange, and R. Pidgeon
2010. Distribution of rare earth elements in lunar zircon. *American Astronomical Society*, 95:273–283.

Nemchin, A., R. Pidgeon, M. Whitehouse, J. Vaughan, and C. Meyer
2008. SIMS UPb study of zircon from Apollo 14 and 17 breccias: Implications for the evolution of lunar KREEP. *Geochimica et Cosmochimica Acta*, 72(2):668–689.

Nemchin, A. A., R. T. Pidgeon, D. Healy, M. L. Grange, M. J. Whitehouse, and J. Vaughan
2009. The comparative behavior of apatite-zircon U-Pb systems in Apollo 14 breccias: Implications for the thermal history of the Fra Mauro Formation. *Meteoritics & Planetary Science*, 44(11):1717–1734.

Nicholis, M. G. and M. J. Rutherford
2009. Graphite oxidation in the Apollo 17 orange glass magma: Implications for the generation of a lunar volcanic gas phase. *Geochimica et Cosmochimica Acta*, 73(19):5905–5917.

NRC
2007. The scientific context for exploration of the Moon, Final report. Technical report, National Academies Press, Washington DC.

Nunes, P. D. and M. Tatsumoto
1973. Excess lead in rusty rock 66095 and implications for an early lunar differentiation. *Science (New York, N.Y.)*, 182(4115):916–20.

Nyquist, L. E.
1977. Lunar Rb-Sr chronology. *Physics and Chemistry of Earth*, 10:103–142.

O'Hara, M. J.
1972. Volatilization Losses from Lunar Lava 14310. *Nature*, 240(5376):95–96.

O'Sullivan, K. M., T. Kohout, K. G. Thaisen, and D. A. Kring
2011. Calibrating several key lunar stratigraphic units representing 4 b.y. of lunar history within Schrödinger basin. In *Geological Society of America Special Papers*, volume 477, Pp. 117–127.

Pan, Y. and M. E. Fleet
2002. Compositions of the Apatite-Group Minerals: Substitution Mechanisms and Controlling Factors. *Reviews in Mineralogy and Geochemistry*, 48(1):13–49.

Paniello, R. C., J. M. D. Day, and F. Moynier
2012. Zinc isotopic evidence for the origin of the Moon. *Nature*, 490(7420):376–9.

Papanastassiou, D. and G. Wasserburg
1971a. Lunar chronology and evolution from RbSr studies of Apollo 11 and 12 samples. *Earth and Planetary Science Letters*, 11(1-5):37–62.

Papanastassiou, D. and G. Wasserburg
1971b. RbSr ages of igneous rocks from the Apollo 14 mission and the age of the Fra Mauro formation. *Earth and Planetary Science Letters*, 12(1):36–48.

Papanastassiou, D., G. Wasserburg, and D. Burnett
1970. Rb-Sr ages of lunar rocks from the sea of tranquillity. *Earth and Planetary Science Letters*, 8(1):1–19.

Papike, J. J., A. E. Bence, and D. H. Lindsley
1974. Mare basalts from the Taurus-Littrow region of the moon. *In: Lunar and Planetary Science Conference*, 5:471–504.

Patiño Douce, A. E. and M. Roden
2006. Apatite as a probe of halogen and water fugacities in the terrestrial planets. *Geochimica et Cosmochimica Acta*, 70(12):3173–3196.

Pernet-Fisher, J., G. Howarth, Y. Liu, Y. Chen, and L. Taylor
2014. Estimating the lunar mantle water budget from phosphates: Complications associated with silicate-liquid-immiscibility. *Geochimica et Cosmochimica Acta*, 144:326–341.

Pichavant, M., J. V. Herrera, S. Boulmier, L. Briqueu, J. L. Joron, M. Juteau, L. Marin, A. Michard, S. M. F. Shepard, M. Treuil, and M. Vernet
1987. The Macusani glasses, SE Peru: evidence fo chemical fractionation in peraluminous magmas. *Magmatic processes: Physicochemical principles*, 1(1):359–373.

Pieters, C. M., J. Boardman, B. Buratti, A. Chatterjee, R. Clark, T. Glavich, R. Green, J. Head Iii, P. Isaacson, E. Malaret, T. Mccord, J. Mustard, N. Petro, C. Runyon, M. Staid, J. Sunshine, L. Taylor, S. Tompkins, P. Varanasi, and M. White
2009. The Moon Mineralogy Mapper (M 3) on Chandrayaan-1. *Current Science*, 96(4):500–505.

Potts, N. J., R. Tartese, M. Anand, A. A. Griffiths, W. V. Westrenen, T. J. Barrett, and I. A. Franchi
2016. Characterization of mesostasis regions in lunar basalts: Understanding late-stage melt evolution and its influence on apatite formation. *Meteoritics & Planetary Science*, P. in press.

Potts, N. J., R. Tartese, I. A. Franchi, and M. Anand
2015. Understanding the chlorine isotopic composition of apatite in lunar basalts. In *46th Lunar and Planetary Science Conference*, number 2077.

Prowatke, S. and S. Klemme
2006. Trace element partitioning between apatite and silicate melts. *Geochimica et Cosmochimica Acta*, 70(17):4513–4527.

Putirka, K. D., H. Mikaelian, F. J. Ryerson, and H. Shaw
2003. New clinopyroxene-liquid thermobarometers for mafic, evolved, and volatile-bearing lava compositions, with applications to lavas from Tibet and the Snake River Plain, Idaho. *American Mineralogist*, 88:1542–1554.

Quaide, W. and R. Wrigley
1972. Mineralogy and origin of Fra Mauro fines and breccias. *In: Lunar and Planetary Science Conference*, 3:771.

Rama Murthy, V., N. M. Evensen, B.-M. Jahn, and J. Coscio, M. R.
1972. Apollo 14 and 15 samples: Rb-Sr ages, trace elements, and lunar evolution. *In: Lunar and Planetary Science Conference*, 3:1503.

Rhodes, J. M. and D. Blanchard
1980. Chemistry of Apollo 11 low-K mare basalts. *Proceedings of the 11th Lunar Planetary Science Conference*, 11:49–66.

Rhodes, J. M. and N. J. Hubbard
1973. Chemistry, classification, and petrogenesis of Apollo 15 mare basalts. *In: Lunar and Planetary Science Conference*, 4:1127–1148.

Rhodes, J. M., H. Wiesmann, K. V. Rodgers, J. C. Brannon, B. M. Bansal, and N. J. Hubbard
1976. Chemistry, classification, and petrogenesis of Apollo 17 mare basalts. *In: Lunar and Planetary Science Conference*, 2:1467–1489.

Richet, P., Y. Bottinga, and M. Javoy
1977. A review of hydrogen, carbon, nitrogen, oxygen, sulphur, and chlorine stable isotope fractionation amoung gaseous molecules. *Annual Review Earth and Planetary Science*, 5(196):65 –110.

Ridley, W. I.
1975. On high-alumina mare basalts. *In: Lunar Science Conference*, 6:131–145.

Ridley, W. I. and R. Brett
1973. Petrogenesis of basalt 70035 - multi-stage cooling histroy. In *EOS*, volume 54, Pp. 611–612. American Geophysical Union, 2000 Florida Ave NW, Washington, DC 20009.

Ridley, W. I., R. Brett, R. J. Williams, H. Takeda, and R. W. Brown
1972. Petrology of Fra Mauro basalt 14310. *In: Lunar and Planetary Science Conference*, 3:159.

Robinson, K. L., J. J. Barnes, K. Nagashima, A. Thomen, I. A. Franchi, G. R. Huss, M. Anand, and G. J. Taylor
2016. Water in evolved lunar rocks: Evidence for multiple reservoirs. *Geochimica et Cosmochimica Acta*, 188:244–260.

Robinson, K. L. and G. J. Taylor
2014. Heterogeneous distribution of water in the Moon. *Nature Geoscience*, 7(6):401–408.

Roeder, P. and R. Emslie
1970. Olivine-Liquid Equilibrium. *Contr. Mineral. and Petrol*, 29:275–289.

Rubie, D., S. Jacobson, a. Morbidelli, D. O'Brien, E. Young, J. de Vries, F. Nimmo, H. Palme, and D. Frost
2015. Accretion and differentiation of the terrestrial planets with implications for the compositions of early-formed Solar System bodies and accretion of water. *Icarus*, 248:89–108.

Ryder, G.
1985. *Catalog of Apollo 15 rocks*. National Aeronautics and Space Administration, Lyndon B. Johnson Space Center.

Saal, A. E., E. H. Hauri, M. L. Cascio, J. a. Van Orman, M. C. Rutherford, and R. F. Cooper
2008. Volatile content of lunar volcanic glasses and the presence of water in the Moon's interior. *Nature*, 454(7201):192–5.

Saal, A. E., E. H. Hauri, J. a. Van Orman, and M. J. Rutherford
2013. Hydrogen isotopes in lunar volcanic glasses and melt inclusions reveal a carbonaceous chondrite heritage. *Science (New York, N.Y.)*, 340(6138):1317–20.

Sarafian, A. R., S. G. Nielsen, H. R. Marschall, F. M. McCubbin, and B. D. Monteleone
2014. Early solar system. Early accretion of water in the inner solar system from a carbonaceous chondrite-like source. *Science (New York, N.Y.)*, 346(6209):623–6.

Sato, M.
1976. Oxygen fugacity and other thermochemical parameters of Apollo 17 high-Ti basalts and their implications on the reduction mechanism.

Schauble, E., G. R. Rossman, and H. P. Taylor
2004. Theoretical estimates of equilibrium chromium-isotope fractionations. *Chemical Geology*, 205(1-2):99–114.

Schauble, E. A., G. R. Rossman, J. Taylor, H. P., and H. Taylor
2003. Theoretical estimates of equilibrium chlorine-isotope fractionations. *Geochimica et Cosmochimica Acta*, 67(17):3267–3281.

Schönbächler, M., D.-C. Lee, M. Rehkämper, A. N. Halliday, M. A. Fehr, B. Hattendorf, and D. Günther
2003. Zirconium isotope evidence for incomplete admixing of r-process components in the solar nebula. *Earth and Planetary Science Letters*, 216(4):467–481.

Schonfeld, E. and J. Meyer, Charles
1972. The abundances of components of the lunar soils by a least-squares mixing model and the formation age of KREEP. *In: Lunar and Planetary Science Conference*, 3:1397.

Schürmann, K. and S. S. Hafner
1972. Distinct subsolidus cooling histories of Apollo 14 basalts. *In: Lunar and Planetary Science Conference*, 3:493.

Scoon, J. H.
1971. Chemical analyses of lunar samples 12040 and 12064. *Proceedings of the Lunar Science Conference*, 2:1259–1260.

Seddio, S., J. B.L., R. Korotev, and R. Zeigler
2013. Petrology and geochemistry of lunar granite 12032 , 366-19 and implications for lunar granite petrogenesis. *American Mineralogist*, 98:1697–1713.

Seeni, A., R. Engineer, B. Schäfer, P. Manager, D. Bernhard Rebele, and D. Rainer Krenn
2008. Lunar Rover with Multiple Science Payload Handling Capability. In *59th Internation Astronautical Congress*.

Seeni, A., B. Schfer, and G. Hirzinger
2010. Robot Mobility Systems for Planetary Surface Exploration State-of-the-Art and Future Outlook: A Literature Survey. In *Aerospace Technologies Advancements*. InTech.

Shahar, A., K. Ziegler, E. D. Young, A. Ricolleau, E. A. Schauble, and Y. Fei
2009. Experimentally determined Si isotope fractionation between silicate and Fe metal and implications for Earth's core formation. *Earth and Planetary Science Letters*, 288(1-2):228–234.

Shankar, B., G. Osinski, I. Antonenko, C. Neish, and P. J. McCausland
2013. A multispectral geological study of the Schrödinger impact basin. *Canadian Journal of Earth Sciences*, 50(1):44–63.

Sharp, Z., J. Barnes, T. Fischer, and M. Halick
2010a. An experimental determination of chlorine isotope fractionation in acid systems and applications to volcanic fumaroles. *Geochimica et Cosmochimica Acta*, 74(1):264–273.

Sharp, Z. and D. Draper
2013. The chlorine abundance of Earth: Implications for a habitable planet. *Earth and Planetary Science Letters*, 369-370:71–77.

Sharp, Z. D., J. D. Barnes, A. J. Brearley, M. Chaussidon, T. P. Fischer, and V. S. Kamenetsky
2007. Chlorine isotope homogeneity of the mantle, crust and carbonaceous chondrites. *Nature*, 446(7139):1062–5.

Sharp, Z. D., C. K. Shearer, K. D. McKeegan, J. D. Barnes, and Y. Q. Wang
2010b. The chlorine isotope composition of the moon and implications for an anhydrous mantle. *Science (New York, N.Y.)*, 329(5995):1050–3.

Shearer, C. and J. Papike
1993. Basaltic magmatism on the Moon: A perspective from volcanic picritic glass beads. *Geochimica et Cosmochimica Acta*, 57(19):4785–4812.

Shearer, C., Z. Sharp, P. Burger, F. McCubbin, P. Provencio, A. Brearley, and A. Steele
2014. Chlorine distribution and its isotopic composition in rusty rock 66095. Implications for volatile element enrichments of rusty rock and lunar soils, origin of rusty alteration, and volatile element behavior on the Moon. *Geochimica et Cosmochimica Acta*, 139:411–433.

Shearer, C. K., P. C. Hess, M. A. Wieczorek, M. E. Pritchard, E. M. Parmentier, L. E. Borg, J. Longhi, L. Elkins-Tanton, C. R. Neal, I. Antonenko, R. M. Canup, A. N. Halliday, T. L. Grove, B. H. Hager, D. C. Lee, and U. Wiechert
2006. Thermal and Magmatic Evolution of the Moon. *Reviews in Mineralogy and Geochemistry*, 60(1):365–518.

Shinohara, H.
2009. A missing link between volcanic degassing and experimental studies on chloride partitioning. *Chemical Geology*, 263(1-4):51–59.

Shoemaker, E. M., M. S. Robinson, and E. M. Eliason
1994. The South pole region of the moon as seen by clementine. *Science (New York, N.Y.)*, 266(5192):1851–4.

Silver, L. and E. Stopler
1985. A thermodynamic model for hydrous silicate melts. *Journal Petrology*, 93:161–171.

Simonds, C. H., W. C. Phinney, J. L. Warner, P. E. McGee, J. Geeslin, R. W. Brown, and J. M. Rhodes
1977. Apollo 14 revisited, or breccias aren't so bad after all. *In: Lunar and Planetary Science Conference*, 2:1869–1893.

Snape, J., A. Nemchin, M. Grange, J. Bellucci, F. Thiessen, and M. Whitehouse
2016. Phosphate ages in Apollo 14 breccias: Resolving multiple impact events with high precision UPb SIMS analyses. *Geochimica et Cosmochimica Acta*, 174:13–29.

Snyder, A., C. R. Neal, A. Taylor, and A. N. Halliday
1997. Anatexis of lunar cumulate mantle in time and space : Clues from trace-element, strontium, and neodymium isotopic chemistry of parental Apollo 12 hasalts. *Geochimica et Cosmochimica Acta*, 61(13):2731–2737.

Snyder, G. A., L. E. Borg, L. E. Nyquist, and L. A. Taylor
2000. Chronology and Isotopic Constraints on Lunar Evolution. In *Origin of the earth and moon*, R. Canup and K. Righter, eds., Pp. 361–395. Tucson: University of Arizona Press.

Snyder, G. a. G., L. a. Taylor, and C. R. Neal
1992. A chemical model for generating the sources of mare basalts: Combined equilibrium and fractional crystallization of the lunar magmasphere. *Geochimica et Cosmochimica Acta*, 56(10):3809–3823.

Spera, F. J.
1992. Lunar magma transport phenomena. *Geochimica et Cosmochimica Acta*, 56(6):2253–2265.

Spilliaert, N., N. Métrich, and P. Allard
2006. SClF degassing pattern of water-rich alkali basalt: Modelling and relationship with eruption styles on Mount Etna volcano. *Earth and Planetary Science Letters*, 248(3):772–786.

Spudis, P. and C. Pieters
1991. *Global and Regional Data about the Moon in Lunar Sourcebook: A User's Guide to the Moon*. Cambridge University Press.

Srinivasan, B.
1974. Lunar breccia 14066 - Kr-81/Kr-83 exposure age, evidence for fissiogenic xenon from Pu-224 and rate of production of spallogenic Xe-126. *In: Lunar and Planetary Science Conference*, 5:2033–2044.

Steenstra, E., N. Rai, J. Knibbe, Y. Lin, and W. van Westrenen
2016. New geochemical models of core formation in the Moon from metalsilicate partitioning of 15 siderophile elements. *Earth and Planetary Science Letters*, 441:1–9.

Stettler, A., P. Eberhardt, J. Geiss, N. Grögler, and P. Maurer
1973. Ar39-Ar40 ages and Ar37-Ar38 exposure ages of lunar rocks. *In: Lunar and Planetary Science Conference*, 4:1865–1888.

Stock, M. J., M. C. S. Humphreys, V. C. Smith, R. D. Johnson, and D. M. Pyle
2014. New constraints on electron-beam induced halogen migration in apatite. *American Mineralogist*, 100(1):281–293.

Stöffler, D. and G. Ryder
2001. Stratigraphy and Isotope Ages of Lunar Geologic Units: Chronological Standard for the Inner Solar System. *Space Science Reviews*, 96(1):9–54.

Swann, G., N. Bailey, R. Batson, R. Eggleton, M. Hait, H. Holt, K. Larson, V. Reed, G. Schaber, R. Sutton, N. Trask, G. Ulrich, and H. Wilshire
1977. Geology of the Apollo 14 landing site in the Fra Mauro highlands. Technical report.

Tartèse, R. and M. Anand
2013. Late delivery of chondritic hydrogen into the lunar mantle: Insights from mare basalts. *Earth and Planetary Science Letters*, 361:480–486.

Tartèse, R., M. Anand, J. Barnes, N. A. Starkey, I. A. Franchi, and Y. Sano
2013a. The abundance, distribution, and isotopic composition of Hydrogen in the Moon as revealed by basaltic lunar samples: Implications for the volatile inventory of the Moon. *Geochimica et Cosmochimica Acta*, 122:58–74.

Tartèse, R., M. Anand, and T. Delhaye
2013b. NanoSIMS Pb / Pb dating of tranquillityite in high-Ti lunar basalts : Implications for the chronology of high-Ti volcanism on the Moon. *American Mineralogist*, 98:1477–1486.

Tartèse, R., M. Anand, K. Joy, and I. Franchi
2014a. H and Cl isotope systematics of apatite in brecciated lunar meteorites Northwest Africa 4472, Northwest Africa 773, Sayh al Uhaymir 169, and Kalahari 009. *Meteoritics & Planetary Science*, 49(12):2266–2289.

Tartèse, R., M. Anand, F. M. McCubbin, S. M. Elardo, C. K. Shearer, and I. A. Franchi
2014b. Apatites in lunar KREEP basalts: The missing link to understanding the H isotope systematics of the Moon. *Geology*, 42(4):363–366.

Tartèse, R., M. Anand, F. M. McCubbin, S. M. Elardo, C. K. Shearer, and I. A. Franchi
2014c. Apatites in lunar KREEP basalts: The missing link to understanding the H isotope systematics of the Moon. *Geology*, 42(4):363–366.

Tatsumoto, M., C. E. Hedge, B. R. Doe, and D. M. Unruh
1972. U-Th-Pb and Rb-Sr measurements on some Apollo 14 lunar samples. *In: Lunar and Planetary Science Conference*, 3:1531.

Taylor, L. A., A. Patchen, R. G. Mayne, and D.-H. Taylor
2004. The most reduced rock from the moon , Apollo 14 basalt 14053 : Its unique features and their origin. *American Mineralogist*, 89:1617–1624.

Taylor, S. R., M. Kaye, P. Muir, W. Nance, R. Rudowski, and N. Ware
1972. Composition of the lunar uplands: Chemistry of Apollo 14 samples from Fra Mauro. *In: Lunar and Planetary Science Conference*, 3:1231.

Tera, F., D. Papanastassiou, and G. Wasserburg
1974. Isotopic evidence for a terminal lunar cataclysm. *Earth and Planetary Science Letters*, 22(1):1–21.

Tollari, N., M. Toplis, and S.-J. Barnes
2006. Predicting phosphate saturation in silicate magmas: An experimental study of the effects of melt composition and temperature. *Geochimica et Cosmochimica Acta*, 70(6):1518–1536.

Touboul, M., T. Kleine, B. Bourdon, H. Palme, and R. Wieler
2007. Late formation and prolonged differentiation of the Moon inferred from W isotopes in lunar metals. *Nature*, 450(7173):1206–9.

Touboul, M., I. S. Puchtel, and R. J. Walker
2015. Tungsten isotopic evidence for disproportional late accretion to the Earth and Moon. *Nature*, 520(7548):530–3.

Treiman, A. H., J. W. Boyce, J. Gross, Y. Guan, J. M. Eiler, and E. M. Stolper
2014. Phosphate-halogen metasomatism of lunar granulite 79215: Impact-induced fractionation of volatiles and incompatible elements. *American Mineralogist*, 99(10):1860–1870.

Turner, G.
1970. Argon-40/ argon-39 dating of lunar rock samples. *Science (New York, N.Y.)*, 167(3918):466–8.

Turner, G., J. Huneke, F. Podosek, and G. Wasserburg
1971. 40Ar-39Ar ages and cosmic ray exposure ages of Apollo 14 samples. *Earth and Planetary Science Letters*, 12(1):19–35.

Turner, G., J. Huneke, F. Podosek, and G. Wasserburg
1972. Ar40-Ar30 systematics in rocks and separated minerals from Apollo 14. *In: Lunar and Planetary Science Conference*, 3:1589–1612.

Ustunisik, G., H. Nekvasil, and D. Lindsley
2011. Differential degassing of H2O, Cl, F, and S: Potential effects on lunar apatite. *American Mineralogist*, 96(10):1650–1653.

Ustunisik, G., H. Nekvasil, D. H. Lindsley, and F. M. McCubbin
2015. Degassing pathways of Cl-, F-, H-, and S-bearing magmas near the lunar surface: Implications for the composition and Cl isotopic values of lunar apatite. *American Mineralogist*, 100(8-9):1717–1727.

Valdes, M. C., M. Moreira, J. Foriel, and F. Moynier
2014. The nature of Earth's building blocks as revealed by calcium isotopes. *Earth and Planetary Science Letters*, 394:135–145.

van Kan Parker, M., P. R. Mason, and W. van Westrenen
2011. Trace element partitioning between ilmenite, armalcolite and anhydrous silicate melt: Implications for the formation of lunar high-Ti mare basalts. *Geochimica et Cosmochimica Acta*, 75(15):4179–4193.

van Kan Parker, M., C. Sanloup, N. Sator, B. Guillot, E. J. Tronche, J.-P. Perrillat, M. Mezouar, N. Rai, and W. van Westrenen
2012. Neutral buoyancy of titanium-rich melts in the deep lunar interior. *Nature Geoscience*, 5(3):186–189.

Villemant, B., G. Boudon, S. Nougrigat, S. Poteaux, and A. Michel
2003. Water and halogens in volcanic clasts: tracers of degassing processes during Plinian and dome-building eruptions. *Geological Society, London, Special Publications*, 213(1):63–79.

Wadhwa, M.
2008. Redox Conditions on Small Bodies, the Moon and Mars. *Reviews in Mineralogy & Geochemistry*, 68:493–510.

Wakita, H., R. A. Schmitt, and P. Rey
1970. Elemental abundances of major, minor and trace elements in Apollo 11 lunar rocks, soil and core samples. In *In: Lunar and Planetary Science Conference*, volume 2, Pp. 1685–1717.

Wänke, H., R. Rieder, H. Baddenhausen, B. Spettel, F. Teschke, M. Quijanorico, and A. Balacescu
1970. Major and trace elements in lunar material. In *In: Lunar and Planetary Science Conference*, volume 2, Pp. 1719–1727.

Warren, P. H. and J. T. Wasson
1979. The origin of KREEP. *Reviews of Geophysics*, 17(1):73.

Wasserburg, G. J., G. Turner, F. Tera, F. A. Podosek, and J. C. Huneke
1972. Comparison of Rb-Sr, K-Ar and U-Th-Pb Ages: Lunar Chronology and Evolution. *In: Lunar and Planetary Science Conference*, 3:788.

Watson, E.
1979. Apatite saturation in basic to intermediate magmas. *Geophysical Research Letters*, 6(12):937–940.

Watson, E., D. Wark, J. Price, and J. Van Orman
2002. Mapping the thermal structure of solid-media pressure assemblies. *Contributions to Mineralogy and Petrology*, 142(6):640–652.

Watson, E. B. and T. H. Green
1981. Apatite/liquid partition coefficients for the rare earth elements and strontium. *Earth and Planetary Science Letters*, 56:405–421.

Weber, R. C., P.-Y. Lin, E. J. Garnero, Q. Williams, and P. Lognonné
2011. Seismic detection of the lunar core. *Science (New York, N.Y.)*, 331(6015):309–12.

Webster, J., R. Kinzler, and E. Mathez
1999. Chloride and water solubility in basalt and andesite melts and implications for magmatic degassing. *Geochimica et Cosmochimica Acta*, 63(5):729–738.

Webster, J. D., C. M. Tappen, and C. W. Mandeville
2009. Partitioning behavior of chlorine and fluorine in the system apatitemeltfluid. II: Felsic silicate systems at 200MPa. *Geochimica et Cosmochimica Acta*, 73(3):559–581.

Weigand, P. W.
1973. Petrology of a course-grained Apollo-17 ilmenite basalt. In *EOS*, volume 54, Pp. 621–622. American Geophysical Union, 2000 Florida Ave NW, Washington, DC 20009.

Wenk, E., A. Glauser, H. Schwander, and V. Trommsdorff
1972. Twin laws, optic orientation, and composition of plagioclases from rocks 12051, 14053, and 14310. *Proceedings of the Lunar Science Conference*, 3.

Wiechert, U., A. N. Halliday, D. C. Lee, G. A. Snyder, L. A. Taylor, and D. Rumble
2001. Oxygen isotopes and the moon-forming giant impact. *Science (New York, N.Y.)*, 294(5541):345–8.

Wieczorek, M. A.
2006. The Constitution and Structure of the Lunar Interior. *Reviews in Mineralogy and Geochemistry*, 60(1):221–364.

Wieczorek, M. A., G. A. Neumann, F. Nimmo, W. S. Kiefer, G. J. Taylor, H. J. Melosh, R. J. Phillips, S. C. Solomon, J. C. Andrews-Hanna, S. W. Asmar, A. S. Konopliv, F. G. Lemoine, D. E. Smith, M. M. Watkins, J. G. Williams, and M. T. Zuber
2013. The crust of the Moon as seen by GRAIL. *Science (New York, N.Y.)*, 339(6120):671–5.

Wilhelms, D. E., J. F. with sections by McCauley, and N. J. Trask
1987. The geologic history of the Moon. Technical report.

Willis, J. P., A. J. Erlank, J. J. Gurney, and L. H. Ahrens
1972. Geochemical features of Apollo 15 materials. In *The Apollo 15 lunar samples*, J. Chamberlain and C. Watkins, eds., Pp. 286 – 271. The Lunar Science Institute, Houston.

Wilshire, H. G. and E. Jackson
1972. Petrology and stratigraphy of the Fra Mauro Formation at the Apollo 14 site. Technical report.

York, D., W. J. Kenyon, and R. J. Doyle
1972. 40Ar-39Ar ages of Apollo 14 and 15 samples. *In: Lunar and Planetary Science Conference*, 3:1613.

Young, E. D., I. E. Kohl, P. H. Warren, D. C. Rubie, S. A. Jacobson, and A. Morbidelli
2016. Oxygen isotopic evidence for vigorous mixing during the Moon-forming giant impact. *Science*, 351(6272):493–496.

Zambardi, T., F. Poitrasson, A. Corgne, M. Méheut, G. Quitté, and M. Anand
2013. Silicon isotope variations in the inner solar system: Implications for planetary formation, differentiation and composition. *Geochimica et Cosmochimica Acta*, 121:67–83.

Zhang, J., N. Dauphas, A. M. Davis, I. Leya, and A. Fedkin
2012. The proto-Earth as a significant source of lunar material. *Nature Geoscience*, 5(4):251–255.

Zhang, Y.
2011. "Water" in lunar basalts: the role of molecular hydrogen (H2), espeically in the diffusion of the H component. *42nd Lunar and Planetary Science Conference (2011)*, P. 1957.

Zhang, Y. and H. Ni
2010. Diffusion of H, C, and O Components in Silicate Melts. *Reviews in Mineralogy and Geochemistry*, 72(1):171–225.

List of publications

Journal Publications

Listed below are the publications which have directly resulted from my PhD work:

Potts, N. J. Lunar Interior, Halogens. *in* Lunar Encyclopaedia. *In review.*
—This is an invited article to review current understanding of lunar halogens.

Potts, N.J., Barnes, J. J., Tartése, R., Franchi, I. A., Anand, M. Chlorine isotopic signatures of Apollo 14 rocks: Evidence for widespread vapor-phase metasomatism on the lunar nearside 4 billion years ago. *To be submitted to GCA.*
—I selected the samples, collected SEM images, performed NanoSIMS analysis, and wrote the paper.

Potts, N.J., van Westrenen, W., Tartése, R., Franchi, I.A., Anand, M. A model for back-calculating melt H_2O contents in late-stage lunar melts using measured apatite abundances. *Reviewed and resubmitting to American Mineralogist.*
—I designed the experiments, synthesised all starting material, performed all experiments, mounted most of the samples, performed the SEM, NanoSIMS, and EPMA measurements. I also devised the model and wrote the paper.

Potts, N.J., Tartése, R., Anand, M., van Westrenen, W., Griffiths, A. A., Barrett, T. J., Franchi, I. A. Characterisation of mesostasis regions in mare basalts: Understanding late-stage melt evolution and its influence on apatite formation. *Accepted in MaPS.*
—I conceived the project then I obtained all of the probe data, processed the data, calculated mesostasis region compositions, completed all the petrographic modelling, and wrote the paper. Assistance was provided by a Summer Intern to collect false-colour images.

Potts, N.J., Gullikson, A. L., Curran, N. M., Dhaliwal, J. K., Leader, M. K., Rege, R. N., Kring, D. A., (2014) Robotic traverse and sample return strategies for a lunar farside mission to the Schrdinger basin. *Advances in Space Research.* **55**, pp. 1241-1254.
—I completed all the solar irradiance mapping and modelling, researched and calculated all the ConOps activities, calculated sample return weights, and wrote the paper. I also helped design traverses at East Site, provided input into North Site traverses, and assited with MatLab modelling of rover velocity study.

Conference Abstracts

Listed below are the conference abstracts which have directly resulted from my PhD work:

2015

Anand, M., Barnes, J.J., Mortimer, J. J., **Potts, N.J.,** Tartése, R., Robinson, K., Franchi, I. A., McCubbin, M., Neal, C., Taylor, J., Kring, D., van Westrenen, W., Russell, S. (2015) *Unravelling the history of water and other volatiles in the Moon using lunar samples.* COSPAR symposium, So Paulo, Brazil (invited keynote talk).

Potts, N.J., van Westrenen, W., Tartése, R., Franchi, I.A., Anand, M. (2015) *Apatite as a tool for understanding the volatile contents of late-stage lunar magmas.* Goldschmidt, 25th Anniversary, Prague, CZ. (poster).

Potts, N.J., van Westrenen, W., Tartése, R., Franchi, I.A., Anand, M. (2015) *Apatite-melt volatile partitioning under lunar conditions.* Lunar and Planetary Science Conference XLVI, Houston, TX. #1372 (poster).

Potts, N.J., Tartése, R., Franchi, I. A., Anand, M. (2015) *Understanding the chlorine isotopic composition of apatites in lunar basalts.* Lunar and Planetary Science Conference XLVI, Houston, TX. #2077 (poster).

2014

Potts, N.J., Tartése, R., Anand, M., Frnachi, I. A., van Westrenen, W., Barnes, J. J., Griffiths, A. A. (2014) *Characterization of mesostasis areas in mare basalts: Constraining melt compositions from which apatite crystallizes.* Lunar and Planetary Sciences Conference XLV, Houston, TX. #1946 (poster).

Leader, M. K., Rege, R. N., **Potts, N.J.,** Gullikson, A.L, Curran, N. M., Dhaliwal, J. K., Kring, D. A. (2014) *Velocity of a rover as a function of slope of lunar terrain.* Lunar and Planetary Science Conference XLV, Houston, TX, #2683 (poster).

Gullikson, A. L., Curran, N. M., **Potts, N.J.,** Dhaliwal, J. K., Leader, M. K., Rege, R. N., Kring, D. A. (2014) *Traverse and station options for a robotic sample return to Schrödinger basin.* Lunar and Planetary Science Conference XLV, Houston, TX, #2082 (poster).

Griffiths, A. A., Barnes, J. J., Tartése, R., **Potts, N.J.,** Anand, M. (2014) *Characterization of mesostasis areas in mare basalts: petrography and mineral chemistry.* Lunar and Planetary Science Conference XLV, Houston, TX, #1905 (poster).

Potts, N.J., Gullikson, A. L., Curran, N. M., Dhaliwal, J. K., Chang, G., Leader, M. K., Rege, R. N., Kring, D. A. (2014) *Mapping solar irradiance within Schrödinger basin for future robotic sample return missions.* Lunar and Planetary Science Conference XLV, Houston, TX, #1835 (poster).

Curran, N. M., Gullikson, A. L., **Potts, N.J.,** Dhaliwal, J. K., Leader, M. K., Rege, R. N., Kring, D. A. (2014) *A robotic sample return mission to the Northern portion of the Schrödinger basin peak ring.* Lunar and Planetary Science Conference XLV, Houston, TX, #1475 (poster).

Potts, N.J., Gullikson, A. L., Curran, N. M., Dhaliwal, J. K., Leader, M. K., Rushal, R. N., Kring, D. A. (2014) *Robotic traverse and sample return strategies for a lunar farside mission to Schrödinger basin.* Science and Challenges of Lunar Sample Return Workshop, ESA-ESTEC, The Netherlands (talk).

Anand, M., Tartése, R., Barnes, J. J., Mortimer, J. I., **Potts, N.J.,** (2014) *An assessment of volatile inventory of the Moon through analysis of returned lunar samples using a multi-proxy approach.* Science and Challenges of Lunar Sample Return Workshop, ESA-ESTEC, The Netherlands (talk).

2013

Potts, N.J., Anand, M., van Westrenen, W., Tartése, R., Franchi, I. A. (2013) *Using lunar apatite to assess the volatile inventory of the lunar interior.* NLSI Workshop Without Walls: Lunar Volatiles (Part 1) #28 (talk).

Potts, N.J., Anand, M., van Westrenen, W., Tartése, R., Franchi, I. A. (2013) *The lunar volatile budget.* Geochemistry Group Research in Progress Meeting, Milton Keynes, UK (talk).